Two-phase flows over complex surfaces : towards bridging the gap between computations and experiments with application to structured packings

Zlatko Solomenko

To cite this version:

Zlatko Solomenko. Two-phase flows over complex surfaces : towards bridging the gap between computations and experiments with application to structured packings. Other. Université de Lyon, 2016. English. NNT : 2016LYSEC047 . tel-01542094

HAL Id: tel-01542094
https://theses.hal.science/tel-01542094

Submitted on 19 Jun 2017

Numéro d'ordre : 2016LYSEC47

THÈSE de DOCTORAT DE L'UNIVERSITÉ DE LYON
Opérée au sein de l'École centrale de Lyon

École Doctorale 162
Mécanique, Énergétique, Génie Civil et Acoustique

Spécialité : Mécanique des fluides

Soutenue publiquement le 7 décembre 2016, par :

Zlatko Solomenko

Two-phase flows over complex surfaces: towards bridging the gap between computations and experiments with application to structured packings

---

Devant le jury composé de :

Christophe Josserand	Directeur de Recherches, CNRS, I. d'Alembert	Président
Alain Berlemont	Directeur de Recherches, CNRS, CORIA	Rapporteur
Adrian Daerr	Maître de Conférences, U. Paris Diderot, MSC	Rapporteur
Veronique Roig	Professeur, INPT, IMFT	Examinatrice
Peter Spelt	Professeur, UCBL, LMFA	Directeur
Michel Lance	Professeur, UCBL, LMFA	Co-directeur
Pascal Alix	Docteur-ingénieur, IFP Énergies nouvelles	Encadrant
Christine Dalmazzone	Docteur-ingénieur, IFP Énergies nouvelles	Encadrante

Abstract

The work described in this thesis is motivated by the use of structured packing columns in acid gas treatment and post-combustion CO_2 capture. In a counter-current mode, flue gases react with the liquid that flows down over metal sheets, the geometrical complexity of which allows increasing the specific interfacial area, and thereby the overall efficiency of the process. In the context of multiscale modeling of structured-packing contacting devices, the focus in this work is on the gas-liquid flows at the smallest geometrical scale of packing sheets, of the order of the liquid film thickness, aiming to improve understanding and modeling of two-phase flows and wetting phenomena in structured packings. The ultimate objective is to build up a CFD methodology to reproduce 3D two-phase flows over complex surfaces such as structured packing sheets. For this purpose, progress is necessary both in pertinent computational methods and in the adaptation of experimental methods for observing liquid film flows over complex surfaces. This thesis therefore consists of computational and experimental parts.

Flows over structured packing sheets may exhibit dry zones, and hence (moving) contact lines, the numerical simulation of which presents a computational challenge due to the disparity in length scales involved. Here, the methodology for large-scale numerical simulations of flows with moving contact lines consists in resolving the flow down to an intermediate scale and modeling effects of smaller ones. The parallelized freeware Two-Phase Level-Set has been extended for this purpose. First though, because some level-set methods have been reproached to yield mass conservation issues, an assessment is made of the mass conservation properties of a range of level-set methods. It is demonstrated that the combined use of some spatial and temporal discretization schemes allows to drastically reduce mass conservation errors in level-set methods. Having thus implemented a level-set method with satisfactory performance at such tests (and others), a novel numerical method is proposed to perform 3D large-scale simulations of flows with moving contact lines in level-set, under realistic conditions. Validation tests of axisymmetric droplet spreading in a viscous, and in an inertial regime, simulated in 3D, and sliding drops are shown to be in excellent agreement with prior experimental and numerical work. The results show that complex contact-line dynamics observed in prior experimental studies on sliding droplets can be simulated using the present large-scale methodology.

To facilitate dissemination of this work in industrial applications, a similar subgrid model has been implemented in a commercial volume-of-fluid code; results of validation tests are shown to be in excellent agreement with other work.

These computational developments are accompanied by an experimental campaign to observe liquid film flows over structured packing sheets. All experimental methods used herein are tested and validated for flat and wavy films down an inclined plane before being used for observing liquid film flows over packing sheets. The film thickness is measured at local troughs and crests of small-scale corrugations of the structured packing sheet, for different flow rates, by Chromatic Confocal Imaging. Power laws of the Reynolds number for the mean liquid film thickness are suggested, with significant differences for measurements at crests compared to that at troughs. Interface velocity measurements are also performed by PIV and PTV using hydrophobic particles. Results reveal that the liquid tends to deviate from troughs of large-scale corrugations, and seems to exhibit local extrema of the velocity magnitude corresponding to troughs and crests of small-scale corrugations. In all, an experimental database has been built up to support the development of the CFD methodology in 3D simulations of two-phase flows on a representative elementary unit of structured packing sheet.

Keywords: two-phase flows, moving contact lines, liquid film, CFD, level-set, VOF, PIV, PTV, structured packings.

Résumé

Ces travaux de thèse s'incrivent dans le cadre du traitement de gaz acides et captage CO_2 dans les colonnes à garnissages structurés. Les gaz à traiter réagissent avec un liquide s'écoulant à contre-courant sur des plaques métalliques dont la compléxité géométrique permet d'accroître l'aire d'échange, et donc l'efficacité du procédé. Dans un contexte de modélisation multi-échelles des contacteurs à garnissages structurés, les écoulements gaz-liquide à la plus petite échelle géométrique des plaques de garnissages (de l'ordre de l'épaisseur du film liquide) sont étudiés, pour améliorer la compréhension et la modélisation des écoulements diphasiques et phénomènes de mouillage dans les garnissages. L'objectif final est de développer une méthodologie CFD pour reproduire des écoulements diphasiques 3D sur des géométries complexes telles que les plaques de garnissages. Pour ce faire, il est nécessaire de progresser en méthodes numériques et de proposer des méthodes expérimentales pour observer des écoulements de film liquide sur des géométries complexes. Ces travaux comprennent une partie numérique et une partie expérimentale.

Un écoulement sur une plaque de garnissage structuré peut présenter des zones sèches, et donc des lignes de contact (dynamiques), ce qui présente un défi en simulation numérique à cause des différentes échelles de l'écoulement. La méthodologie employée ici en simulation numérique consiste à résoudre l'écoulement jusqu'à une échelle intermédiaire en modélisant les effets des plus petites échelles. Le code de calcul Two-Phase Level-Set a été utilisé et modifié dans ce but. Différentes méthodes level-set ont d'abord été testées de manière à identifier une méthode satisfaisante quant à la réduction des erreurs de conservation de masse, un problème rencontré en level-set. Il est ici montré que certaines combinaisons de schémas de discrétisation spatiale et temporelle permettent de réduire considérablement ces erreurs de conservation de masse. Après avoir réalisé de nombreux tests de validation, une nouvelle méthode numérique est proposée pour simuler les grandes échelles d'écoulements diphasiques 3D avec ligne de contact dynamique en level-set, dans des conditions réalistes. La méthode est ici validée pour des écoulements axisymétriques de gouttes simulés en 3D, en régime visqueux et en régime inertiel, et pour des écoulements de gouttes sur plan incliné. Les résultats sont en très bon accord avec d'autres travaux numériques et expérimentaux.

Afin de faciliter l'utilisation de cette méthodologie pour des applications industrielles, un modèle sous-maille similaire a été implémenté dans un code VOF commercial; les résultats sont aussi en très bon accord avec d'autres travaux.

En plus de ces développements numériques, une campagne expérimentale est mise en oeuvre pour observer des écoulements de film liquide sur une plaque de garnissage structuré. Les méthodes expérimentales employées sont d'abord testées et validées pour des écoulements de film plat ou ondulé sur plan incliné, et ensuite utilisées pour observer des écoulements de film sur des plaques de garnissage. L'épaisseur de film liquide est mesurée aux creux et aux crêtes des picots des plaques de garnissages, pour différents débits, par imagerie confocale chromatique. Des lois de puissance de l'épaisseur de film en fonction du Reynolds sont proposées; celles-ci sont très différentes suivant la position des relevés de mesure, aux creux ou aux crêtes des picots. La vitesse à l'interface de l'écoulement gaz-liquide est aussi mesurée, par PIV et PTV, en utilisant des particules hydrophobes. Les résultats montrent que le liquide a tendance à dévier du creux des canaux (corrugations), et la norme de la vitesse semblent présenter des extremums correspondant aux creux et crêtes des picots. Ces travaux expérimentaux supporteront le développement de la méthodologie CFD pour simuler des écoulements diphasiques 3D sur un élément unitaire représentatif d'une plaque de garnissage.

Mots-clés : écoulements diphasiques, lignes de contact dynamiques, film liquide, CFD, level-set, VOF, PIV, PTV, garnissages structurés.

Acknowledgements

This research was carried out at École centrale de Lyon, University of Lyon, in the Laboratoire de Mécanique des Fluides et d'Acoustique, and was sponsored by IFP Énergies nouvelles.

I first want to acknowledge Yacine Haroun, Cécile Barrère-Tricca and Alain Quignard, members of the company IFP Énergies nouvelles, who initially gave me their trust for this project.

I gratefully acknowledge the jury members for evaluating my work, especially Alain Berlemont and Adrian Daerr for going deeply through the memoir.

Many thanks to my industrial supervisors, Pascal Alix and Christine Dalmazzone for their availability and for sharing with me their knowledge in chemical engineering and physico-chemistry. I also thank Manel Fourati and Philippe Béard for the scientific discussions on structured packings and CFD.

I want to thank Michel Lance for sharing his expertise in experimental fluid mechanics and for the key discussions I had with. Also, I am deeply grateful to Peter Spelt for his availability, his patience, and for everything he has taught me, in fluid mechanics and numerics, and for being attentive to my thoughts. I thank him for sharing his passion for research. It has been a great pleasure working with him.

I thank Aurélie Mouret for welcoming me at IFP Énergies nouvelles for contact angle measurements. I thank the Lapis Lazuli team of IFP Énergies nouvelles, for teaching me how to use the experimental setup, and all other members of the company who participated in designing the setup. I also thank Alexandre Azouzi for his help in installing the experimental setup at LMFA.

I thank Valéry Botton for welcoming me at INSA Lyon, and Hatem Allouche for his advice as a former user of the inclined-plane setup, as well as Simon Dagois-Bohy. I gratefully acknowledge Nathalie Grosjean for her help as a velocimetry expert, as well as Gaby Launay and Tristan Cambonie for their advice as PIV experts. I also thank Antoine Godard for the discussions on experimental uncertainties.

I acknowledge the people from the mesocenter FLMSN, especially the PMCS2I and P2CHPD teams, for the use of computational resources.

I thank all my friends, Antoine, Aurélien, Benoit, Clément, Étienne, Félix, Guillaume, Franck, Ludovic, Maxime, Olivier, Paul, Romain, Sébastien, Simon, Xavier, Youri, Vincent, who I have always been glad to meet up with, especially during these stressful years.

I thank all the doctoral students of IFP Énergies nouvelles: Amir, Daniel, Fabien, Kévin, Leonel, Pedro, Robin, Sonia, Svetan... I appreciated the good atmosphere during my short visits to the company and I thank them for that.

I thank my mates, who are my friends now, who I shared this experience with: Annabelle the receptionist, Emmanuel the violinist, Étienne the IT master, Gaby the climbing partner, Gherardo the biker, Johannes the brewer, Quentin the traveling partner, Victor the clementine-skin pattern maker. I thank them for all the scientific discussions, and especially for all the funny moments I spent with them during these years.

I want to thank all the members of my family for their support, especially my parents, who have always believed in me and have always been there for me, whatever the decisions I have made.

I thank Dina, who always has encouraged me. She always had the words to cheer me up in difficult moments. She had a very important role in the accomplishment of this work.

Contents

List of Figures

List of Tables

Nomenclature

Abbreviations

CCI	Chromatic Confocal Imaging
CFD	Computational Fluid Dynamics
CFL	Courant-Friedrichs-Lewy
CSI	Chromatic Spectral Interferometry
DNS	Direct Numerical Simulation
FTP	Fourier Transform Profilometry
HETP	Height Equivalent to a Theoretical Plate
LIF	Light-Induced Fluorescence
LS	Level-Set
MEA	Mono-Ethanol-Amine
PIV	Particle Image Velocimetry
PSD	Position Sensing Detector
PSD	Power Spectral Density
PTV	Particle Tracking Velocimetry
REU	Representative Elementary Unit
TPLS	Two-Phase Level-Set
UDF	User-Defined Function
VOF	Volume-Of-Fluid

Greek letters

α	volume fraction

α_u	angle of channels of a structured packing sheet with respect to the horizontal direction
β	inclination angle
$\Delta\theta$	contact angle hysteresis
$\delta^r v, \delta^s v, \delta v$	random, systematic and overall uncertainties in the measurement of a variable v
ϵ	dimensionless length scale of the intermediate region
κ	curvature
λ	dimensionless slip length
λ_c	wavelength of the small-scale corrugation of a structured packing sheet
λ_u	base of the channel of a structured packing sheet
μ	dynamic viscosity
ν	kinematic viscosity
ϕ	level-set function
ψ	function that is being reinitialized to a signed distance function
ρ	density
σ	surface tension
τ	pseudo time
θ_A	advancing angle
θ_d	interface slope in the intermediate region
θ_R	receding angle
θ_w	angle in the inner region
θ_Y	Young angle
θ_{ap}	apparent angle in the outer region
ξ	smooth width
ζ	artificial pressure

Roman letters

$\hat{\mathbf{n}}$	unit normal vector
$\mathbf{g}$	gravitational acceleration
$\mathbf{S}$	rate-of-strain tensor

$\mathbf{u}$	velocity vector
A_c	amplitude of small-scale corrugations of a structured packing sheet
Bo	Bond number, $Bo = \dfrac{\rho g L^2}{\sigma}$
Ca	capillary number, $Ca = \dfrac{\mu U}{\sigma}$
d	distance from the contact line
Fr	Froude number, $Fr = \dfrac{U^2}{gL}$
g	magnitude of gravitational acceleration
h	liquid film thickness, temporal average of liquid film thickness
h	uniform grid spacing
h_u	height of the channel of a structured packing sheet
H_ξ, H_h	smoothed Heaviside function
k_G, k_L	gas-side mass transfer coefficient, liquid-side mass transfer coefficient
Ka	Kapitza number, $Ka = \dfrac{\sigma}{\rho \nu^{4/3} (g \sin \beta)^{1/3}}$
L	characteristic length
L_c	capillary length, $L_c = \sqrt{\dfrac{\sigma}{\rho g}}$
La	Laplace number, $La = \dfrac{\rho \sigma L}{\mu^2}$
Oh	Ohnesorge number, $Oh = \dfrac{\mu}{\sqrt{\rho \sigma L}}$
p	pressure
Q_G, Q_L	gas flow rate, liquid flow rate
Q_i	constant of the inner region
r	roughness coefficient
r_μ	viscosity ratio
r_ρ	density ratio
Re	Reynolds number, $Re = \dfrac{UL}{\nu}$
S_h	smoothed sign function
U	characteristic velocity

We	Weber number, $We = \dfrac{\rho U^2 L}{\sigma}$

Subscripts

CL	Contact Line
G, L, S	Gas, Liquid, Solid
iv	inviscid subregion
v	viscous subregion

Introduction

For gas sweetening and CO_2 capture, amine-based processes are often used to put the gas phase in contact with a strong base solvent, which is crucial for the design of contacting devices, hence the actual resort to structured packings to enhance the contact area between the two phases. In the scope of acid gas treatment with structured packing columns, gravity-driven liquid films flow over complex surfaces whilst being sheared by a counter-current gas flow. The larger the contact area between the two phases, the more efficient the process is expected to be, hence the use of complex surfaces with large topographical structures compared to the liquid film thickness. On the other hand, maximum wetting of the complex surface is wanted but often not achieved, hence the need to develop an optimal geometry of the complex surface that maximizes wetting and enhances the overall process efficiency.

Studying gas-liquid counter-current flows in columns equipped with structured packing, although necessary for macroscale modeling of contacting devices, is often expensive and time-consuming. Experimental campaigns generally allow for direct macroscale modeling of hydrodynamic and mass transfer parameters, but without accounting for the underlying physics, which may impact the performance of the reactor. Further development of contacting devices would therefore amount to multiscale modeling, informed by experiments. Computational Fluid Dynamics is an interesting alternative to long and expensive experimental campaigns, aiming to improve understanding and modeling of wetting of complex surfaces such as structured packing sheets, an important phenomenon in contacting devices as the interfacial area is manifestly linked to wetting of metal sheets.

Wetting phenomena involve flows with moving contact lines, however, the numerical simulation of which is a computational challenge. Flows with moving contact lines involve a large range of length scales, from the molecular scale invalidating assumptions of continuum mechanics, to the micrometric scale where viscosity starts competing with capillarity, and up to the macroscopic scale, far away from the contact line, where the interface is also affected by the entire flow. The physics occurring in the direct vicinity of moving contact lines must be modeled in order to be able to predict hydrodynamics of macroscopic systems. Macroscale models either spring from experimental or theoretical work, the latter providing details of the flow over the entire range of length scales. Hydrodynamic theories generally consider a Stokes flow on the smallest scale resolved, in the vicinity of the contact line, coupled with analysis of flows with moving contact lines on a much larger scale through matched asymptotic expansions. Such theories subsequently yield macroscale models for the interface shape in the entire contact-line region. Large-scale numerical simulations of flows with moving contact line may thus be deployed, using an existing large-scale model derived in prior asymptotic theories. The flow is resolved down to an intermediate region, accounting for effects of the under-resolved part of the flow, that is actually known from the theory. Although macroscale models for two-dimensional general flows exist, they depend on the actual geometry the flow through higher-order terms of asymptotic expansions.

A first part of this memoir presents the establishment of a computational methodology to reproduce general three-dimensional flows with moving contact lines. Numerical simulations of two-phase flows were undertaken with interface-capturing techniques, namely level-set and volume-of-fluid. An existing macroscale model for contact lines dynamics in two-dimensional flows, derived from hydrodynamic theories in prior work, was implemented in the freeware Two-Phase Level-Set and further in a commercial volume-of-fluid code to facilitate dissemination of this work in industry. Implementations were validated against prior experimental and numerical results of axisymmetric droplet spreading in both viscous and inertial regimes. Further tests against three-dimensional sliding drops in viscous regime were successful.

In the second part of this memoir, an experimental study is presented for liquid film flows over complex surfaces that are representative of structured packings. Prior experimental work of this nature is primarily limited to falling films on a planar inclined surface rather than over complex surfaces. Liquid film thickness and interface velocity measurements were carried out by chromatic confocal imaging and particle tracking velocimetry, respectively. After several validation tests, both techniques were used for quantitative characterization of liquid film flows over complex surfaces. The results are a benchmark for CFD, but also show direct connections to prior work for falling films on a planar substrate.

This thesis is organized as follows. The first chapter introduces the industrial context and presents the contribution of this work to multiscale modeling of two-phase flows in gas-liquid reactors. In the second chapter, experimental techniques for liquid film thickness measurements are reviewed and their applicability to observing liquid film flows over complex surfaces is discussed, and generalities on static contact lines and the modeling of moving contact lines are introduced. The third chapter addresses the problem of mass conservation errors encountered in numerical simulations of two-phase flows in the level-set framework. These errors are investigated, and key aspects for improving mass conservation are identified. A novel computational method for the numerical simulation of three-dimensional macroscopic flows with moving contact lines in the level-set framework is presented in the fourth chapter. Numerical simulations of flows with moving contact lines were also performed in a commercial volume-of-fluid code, for some of the same tests, gathered in Appendix B. Experimental techniques for liquid film thickness and interface velocity measurements are validated in the fifth chapter. Quantitative measurements for liquid film flows over complex surfaces are undertaken in the last chapter and comparisons are made with prior work on falling films, when possible, to discuss the reliability of the results. Finally, the main results are summarized and some perspectives are proposed.

Chapter 1

Structured packing columns and acid gas treatment

Outline

1.1 Industrial context

Mitigating greenhouse gas emissions, especially carbon dioxide emitted by fossil fuel combustion in power plants, is important for slowing down global warming. Research has been focusing on carbon capture and storage to reduce capital and operational expenditure (Raynal et al., 2013). Several techniques have been developed for optimization, amongst pre-combustion, oxygen combustion and post-combustion capture (Freund, 2003). The latter have been the main alternative for CO_2 capture in power plants as a large amount of flue gases can be treated – more than 10^6 $m^3.h^{-1}$ according to Raynal and Royon-Lebeaud (2007). It consists in separating CO_2 from flue gases by a process such as reactive absorption with a strong base. CO_2 absorption in structured packing columns with 30wt% MEA (monoethanolamine) requires a lot of energy, especially for solvent regeneration. Research has also been carried out for the development of new solvents and new packing geometries (Raynal et al., 2011).

For gas treatment in general, acid gas compounds (CO_2, H_2S, ...) must be separated to liquefy and/or transport natural gas. Gas fields contain variable amounts of acid gases that should be treated while natural gas specifications have been becoming more and more severe. Acid gas removal units must be optimized in terms of size and energy consumption. This also promotes research on new solvents and packing geometries.

The present project focuses on improving hydrodynamics modeling of two-phase flows in structured packings, aiming to enhance reliability for pieces of design and their optimization. This thesis consists of an experimental study of a liquid film flow down on commercial structured packing sheets, and the development of a CFD methodology that shall be validated from experimental observations. The main objectives are the following:

- Improvement of understanding and modeling of two-phase flows and wetting in structured packings:
    - acquisition of experimental data at local scale (liquid film thickness, interface velocity) of liquid flows over structured packing sheets;
- Development of a predictive CFD methodology that reproduces three-dimensional two-phase flows encountered in structured packings at local scale:
    - improvement of wetting modeling;
    - validation against DNS and experimental results;
    - simulation of a counter-current gas-liquid flow over a representative elementary unit (REU) of structured packing sheet.

1.2 Structured packing columns

1.2.1 Applications

Structured packing columns are increasingly used for acid gas treatment and post-combustion CO_2 capture by amine system cleaning. The process principle is presented in Figure 1.1. The gas to be treated rises and is exposed to the solvent in the absorption column. The liquid flows down on structured packing sheets whilst being sheared by the gas: this is a counter-current mode. For CO_2 capture, the absorber operates at atmospheric pressure, while for acid gas treatment the pressure can vary from several bars to more than 100 bars. Acid compounds are then extracted from the solvent within a regeneration column at moderate pressure (several bars) and high temperature (110 to 140°C) before being sent to storage or sulfur recovery unit. Structured packings have high porosity, generally higher than 90%, and low pressure drops, of the order of 10 mbar.m^{-1}. In order to maximize the absorption column efficiency, one needs to enhance gas-liquid contact by ensuring homogeneous flow over subsequent surfaces. Actually, the process efficiency is strongly dependent on geometrical characteristics of packing sheets, in a sense that it depends on the contact area and the pressure drop; an efficient process allows reaching gas specifications with reduced pressure drop. These sheets exhibit (large-scale) corrugations (Figure 1.2a) and small-scale corrugations (Figures 1.2b and 1.2c). Triangular-shaped corrugations of base λ_u and height h_u allow increasing the interfacial area between the solvent and the gas to be treated, and distributing the liquid all over metal sheets, while small-scale corrugations of wavelength λ_c and amplitude A_c may have an effect

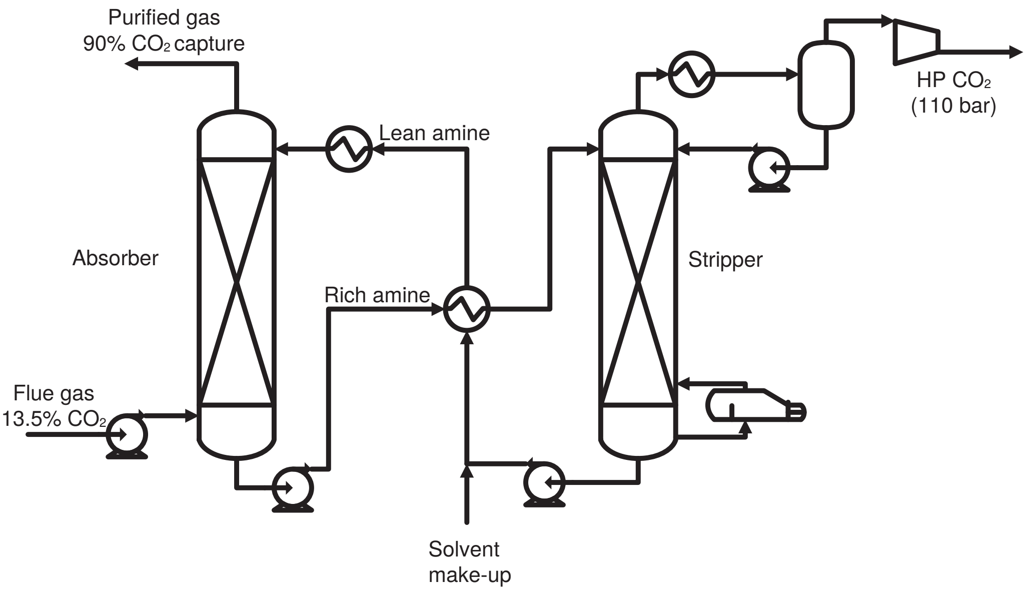

Figure 1.1: Post-combustion CO_2 capture process by amine system cleaning (from Raynal et al. (2013)).

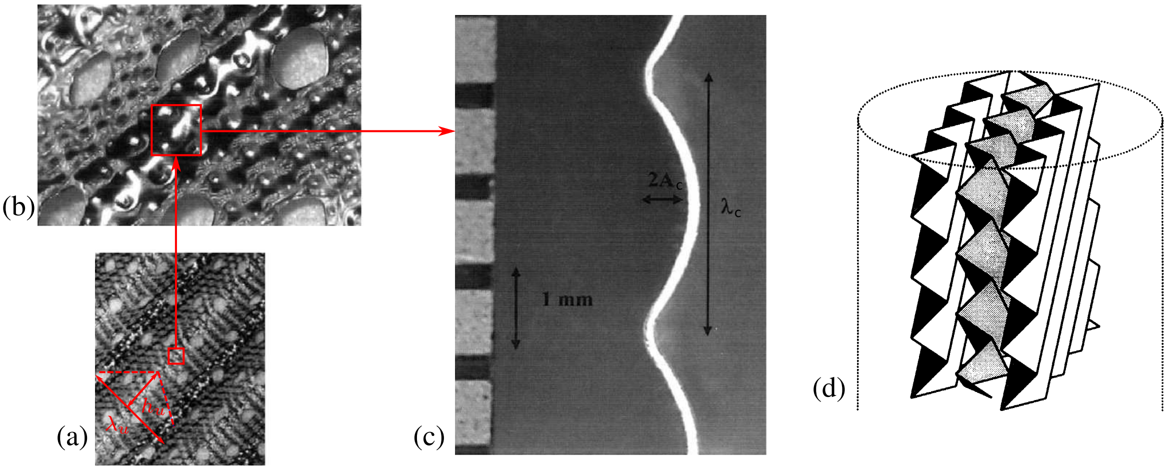

Figure 1.2: (Large-scale) corrugations (a), close view of small-scale corrugations (b), cut-view of small-scale corrugations (c) of structured packing sheets that form a packing element (d). (a), (b) and (c) are from Raynal and Royon-Lebeaud (2007), (d) is from Aroonwilas et al. (2001).

on wetting (Trifonov, 2004) and mass transfer (Kohrt et al., 2011). These two features are important for enhancing the process efficiency. Corrugations have an inclination angle with the horizontal direction $\alpha_u = \pi/3$ for a Mellapak 250X and $\alpha_u = \pi/4$ for a Mellapak 250Y (Figure 1.2d). A packing element consists of several vertical sheets that are alternated, that is to say they have an algebraic inclination angle $\pm\alpha_u$ with the horizontal direction (Figure 1.2d). A lower inclination angle induces higher pressure drop and higher separation efficiency (Figure 1.3), the latter being linked to transfer parameters (Linek et al., 1984; Raynal et al., 2013). In the industrial process, sheets are perforated in order to improve wetting. In this project, only flows over non-perforated sheets are studied to simplify observations and numerical simulations.

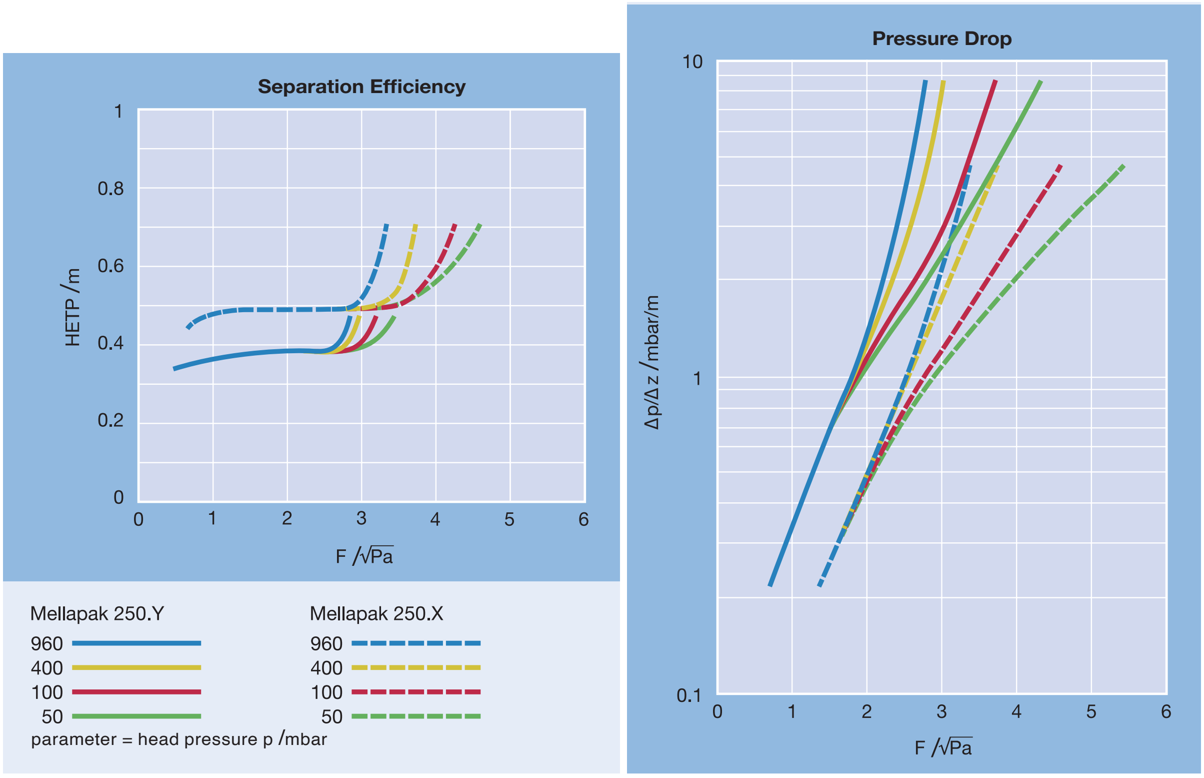

Figure 1.3: Separation efficiency (expressed in Height Equivalent to a Theoretical Plate) and pressure drop characteristics of Mellapak 250X and Mellapak 250Y structured packings (graphs from Sulzer Ltd.). $F = U_G\sqrt{\rho_G}$ (in $\mathrm{Pa}^{1/2}$) is the gas capacity factor, measure of the shear stress due to the gas flow, U_G being the gas superficial velocity at the scale of the column.

1.2.2 Design

1.2.2.1 Hydrodynamic parameters

Hydrodynamic parameters are important for designing absorbers, especially for determining the diameter of a column.

Liquid holdup

Liquid holdup macroscopically characterizes a reactor as the liquid volume in the column with respect to the total available volume. It depends on packing geometry, fluid properties, liquid load and the gas capacity factor $U_G\sqrt{\rho_G}$ (Billet and Schultes, 1999) which is an important parameter for designing structured packing as it measures the shear stress between gas and liquid. For a given liquid load, higher gas loads yield an increase in liquid holdup: this is called the holdup loading region from which liquid flow starts being inhibited (Figure 1.4). At some higher gas load, the pressure drop becomes too large and all the liquid is held up (the flooding point). Some authors (Suess and Spiegel (1992), Sidi-Boumedine and Raynal (2005), Alix and Raynal (2008)) have proposed correlations for liquid holdup that depend on packing geometry, fluid properties, liquid and gas loads.

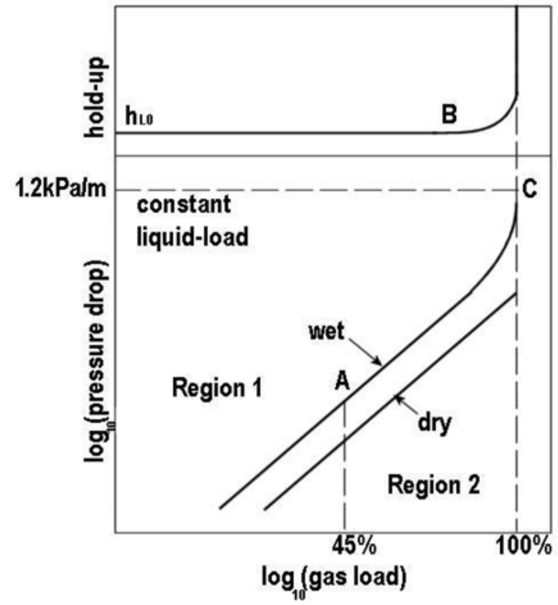

Figure 1.4: Liquid holdup and pressure drop characteristics of structured packing columns (Spiegel and Meier, 1992). A is the pressure drop loading point, B is the loading point, C is the flooding point. Units are operated in the pressure drop loading region.

Pressure drop

Operational expenditure is directly related to the pressure drop (Raynal et al., 2013). For CO_2 capture, the pressure drop in structured packing columns is typically below 2 mbar.m^{-1} at operating conditions. Packing geometry as well as loads and fluid properties influence the pressure drop. Figure 1.4 shows holdup and pressure drop characteristics for a conventional structured packing column. The pressure drop drastically increases from a gas load that is half the flooding point: that defines the pressure drop loading region, in which the gas flow enhances mass-transfer by increasing shear stresses. As a consequence, units are operated in the pressure drop loading region, generally up to about 80% of the flooding point. As mentioned above, a higher pressure drop prevents the liquid from flowing down and the liquid holdup suddenly increases to unity: this is the flooding phenomenon, that must to be avoided.

1.2.2.2 Mass transfer parameters

Mass transfer parameters are important for designing absorbers, especially for determining the height of a column.

Effective area

The specific effective area or chemical area is an important parameter in gas treatment as it is proportional to the specific molar absorption rate of gas. In structured packings, liquid flows over metal sheets and the specific wetted area is ideally equal to the specific packing area. That is not always the case as dry zones may appear even for uniformly-distributed liquid. The effective area is the dominant parameter in mass transfer (Raynal et al., 2013).

Mass transfer coefficients

Mass transfer in the vicinity of a gas-liquid interface behaves differently in gas and liquid phases. The reciprocals of mass transfer coefficients, k_L and k_G, represent liquid-side and gas-side resistances to gas absorption. These coefficients contain information in terms of hydrodynamics and packing geometry. They are important to determine the column height as most of gas treatment reactions are limited by mass transfer in the vicinity of the interface. The reader is referred to Appendices II and III of Brahem (2013) for further information on mass transfer parameters.

1.3 Multiscale modeling of two-phase flows in structured packings

The modeling of gas-liquid flows in structured packing columns can be pursued by utilizing an averaging procedure, such as volume averaging, as a generalization of the modeling of flow in porous media.

1.3.1 Pressure drop

As discussed in Section 1.2.2, the pressure drop determines operational expenditure. First predictive models for the pressure drop in structured packing columns were established empirically based on laws of Darcy-Forcheimer type, for which Ergun coefficients were determined experimentally (Billet and Schultes, 1999). Now, CFD is a very interesting alternative to long and expensive experimental campaigns. Consider a gas flow in a structured packing column. Several scales comes into play, from the small corrugations (Figure 1.2b) to the (large) corrugations (Figure 1.2a), up to the packing element (Figure 1.2d) and further to the scale of the column. Petre et al. (2003) predicted the dry pressure drop at the scale of the column by considering all energy losses due to gas-gas and gas-solid interactions at the scale of corrugations. They identified that losses due to gas-gas interactions occurring at criss-crossing junctions of channels (large-scale corrugations) mainly contribute to the overall dry pressure drop. Later, Raynal et al. (2004) observed boundary conditions influenced the numerical results and a periodic element has been worked out since then. The multiscale approach proposed by Raynal and Royon-Lebeaud (2007) for the overall (wet) pressure drop in structured packings consists in studying the liquid film flowing down on small-scale corrugations first (2D in their work), to get the liquid holdup (related to the liquid film thickness), and then the pressure drop at the scale of corrugations. These hydrodynamic parameters are further used within a porous-media-type estimate of the overall pressure drop at the scale of the column. Said et al. (2011) have studied the dry pressure drop for different Representative Elementary Units (REUs) of structured packing element and observed similar results in the dry pressure drop using different REUs.

In the presence of liquid, the gas phase undergoes further energy losses due to restriction of the gas-flow cross-section, and gas-liquid interactions. Empirical correlations have been developed for the wet pressure drop knowing the dry pressure drop (see Billet and Schultes (1999) for instance). Nowadays, numerical methodologies offer many possibilities for the prediction of wet pressure drops. Assuming that packing sheets are fully wetted, the approach of Raynal and Royon-Lebeaud (2007) may be applied, starting from a first three-dimensional simulation of a liquid film at the scale of small corrugations. A more rigorous methodology might be to directly simulate gas-liquid flows in a REU of structured packing element, such as that used by Raynal and Royon-Lebeaud (2007), but at much higher computational cost.

1.3.2 Liquid film

The approach described above for estimating the wet pressure drop requires knowledge of both the thickness and the interface velocity of the liquid film at the scale of small corrugations. The wetted area as well as the interface velocity plays a role in mass transfer. Prior work has focused on evaluating these in two-dimensional volume-of-fluid (VOF) simulations (Raynal and Royon-Lebeaud, 2007). Three dimensional simulations of liquid film flows over an REU of structured packing sheet seems unavoidable. Integral models (see Trifonov (2004) and Valluri et al. (2005) for instance), or one-fluid interface-capturing methods (VOF or level-set for instance, see Tryggvason et al. (2011) for an introduction) may be used for these. Haroun et al. (2014) carried out 3D VOF simulations of gas-liquid flows in a counter-current mode over such a REU in order to observe the liquid film thickness and the wetted area. They simulated transient flows with moving contact lines, with a computational domain initially occupied by air, and observed results strongly dependent on the value of the contact angle, which was constant in their study. Accounting for contact line dynamics would have rendered the approach even more rigorous, which might be a key point for predicting wetting of metal sheets and for improving the overall multiscale strategy. It is hoped here that the outcomes of such simulations will allow a fair comparison with experimental results, in terms of wetting, liquid film thickness, interface velocity, and will provide information and support to further development of closure laws for gas-liquid simulations at the scale of the column in the porous framework.

1.3.3 Hydrodynamics at the scale of the column

The higher the contact area, the more efficient the process is expected to be. Therefore, an optimal liquid distribution, that depends on both the distributor and the packing geometry, is wanted. In the literature, simulations of gas-liquid multiphase flows in structured packing columns have been carried out using an Euler-Euler description in the framework of porous media (Fourati et al., 2013; Soulaine et al., 2014). Results have been compared with existing experimental data such as these of Fourati et al. (2012), for instance.

In the framework of flows through porous media, continuum momentum and continuity equations can be obtained by volume averaging (Whitaker, 1973), assuming a separation of scales between the pore and system size. Such an approach has been pursued for structured packings by Iliuta et al. (2004), whose model for gas-liquid and fluid-solid interactions is mostly in the form of momentum exchange terms of Darcy-Forcheimer type, of viscous and inertial nature.

In their axisymmetric numerical simulations using Euler-Euler models in this framework, Fourati et al. (2013) obtained good agreement with their experimental results for the order of magnitude of the pressure drop (Fourati et al., 2012), but discrepancies were observed regarding liquid spreading.

The approach of Mahr and Mewes (2007, 2008) is similar but they split the liquid phase into two Eularian phases, with the same fluid properties, that can exchange mass in the vicinity of contact points of two adjacent structured packing sheets.

Soulaine et al. (2014) used the model of Mahr and Mewes (2007) and further simplified governing equations by considering creeping-flow conditions; the velocity is related to the pressure via Darcy's law and the transient dynamics are only solved in the continuity equations (gas and liquid saturations).

The work undertaken in this thesis includes numerical simulations and experiments on the three-dimensional gas-liquid flow over a REU (scale of large corrugations). The insight and results obtained may be integrated

Re_L	50–100
Re_G	500–5000
Fr	≥ 1
We	$O(1)$
r_ρ	$O(10^{-3})$
r_μ	$O(10^{-2})$
L_L/λ_c	$O(10^{-1})$
L_L/A_c	$O(1)$
L_L/h_u	$O(5 \cdot 10^{-2})$
L_L/λ_u	$O(10^{-2})$
L_G/λ_u	$O(1)$

Table 1.1: Orders of magnitude of dimensionless numbers.

in any future work on continuum modelling at the scale of the column.

1.4 Dimensionless groups

Use is made herein of dimensionless groups, as follows. The system is governed by the following variables:

- kinematic variables: U_L, U_G;
- physical properties: ρ_L, μ_L, ρ_G, μ_G, σ;
- the gravity constant: g;
- geometric variables: L_L, L_G, λ_u, h_u, λ_c, A_c.

14 variables determine the system and are combinations of 3 dimensions: mass, length and time. From the Vachy-Buckingham theorem, the system depends on 11 dimensionless numbers that are:

$$\begin{aligned} &Re_L = \frac{U_L L_L}{\nu_L}, Re_G = \frac{U_G L_G}{\nu_G}, Fr = \frac{U_L^2}{g L_L}, We = \frac{\rho_L U_L^2 L_L}{\sigma}, \\ &r_\rho = \frac{\rho_G}{\rho_L}, r_\mu = \frac{\mu_G}{\mu_L}, \frac{L_L}{\lambda_c}, \frac{L_L}{A_c}, \frac{L_L}{h_u}, \frac{L_L}{\lambda_u}, \frac{L_G}{\lambda_u}. \end{aligned} \tag{1.1}$$

Table 1.1 gathers dimensionless numbers for flows over a Mellapak 250Y sheet that is studied in the project. The liquid flow is laminar or inertial whereas the gas flow is inertial or turbulent. The Froude number Fr is greater than 1: upstream disturbances shall not affect the liquid flow downstream. The Weber number We is about 1: capillary forces have a key role in wetting, which may introduce further parameters.

Further dimensionless parameters are introduced by a contact-line model, including contact angles and a ratio of length scales that arises near a contact line, such as a dimensionless slip length.

1.5 Conclusion

The scope of this work is developing insight and modeling for the optimization of acid gas treatment processes by amine system cleaning in column equipped with structured packings. Specifically, the focus here is on wetting phenomena on structured packing sheets, at the scale of corrugations. Optimal surfaces are wanted in order to maximize wetting of packing sheets and the liquid distribution. Qualitative and quantitative observations of liquid films over packing sheets are carried out and a CFD methodology is developed to simulate such flows. The developed CFD approach can be used in the future development of closure laws for liquid-solid interactions in continuum modeling to simulate gas-liquid flows at the scale of the column, and/or for testing new packing sheet geometries in order to improve their wettability as well as the liquid distribution, to contribute to optimizing the chemical process.

Chapter 2

Literature review

Outline

In this chapter, liquid film thickness measurement techniques are reviewed first, including comparisons and an assessment of their applicability to observing liquid film flows over complex surfaces. Such flows may exhibit dry zones, and hence (moving) contact lines (three-phase junction). Generalities on contact lines are therefore presented in a second part of this chapter, notably dynamic contact line models and the computational methodology for the numerical simulation of two-phase flows with moving contact lines.

2.1 Liquid film thickness measurement techniques

Liquid flows over complex surfaces are studied throughout this thesis. In particular, thickness measurements of a liquid film flowing down on a structured packing sheet Mellapak 250Y are performed (the sheets used in the thesis do not have perforations). Raynal and Royon-Lebeaud (2007) mentioned geometrical characteristics of a Mellapak 250Y sheet. They have triangular-shaped (large-scale) corrugations with base $\lambda_u = 22.4$ mm and height $h_u = 11.6$ mm and sinusoidal-shaped small-scale corrugations with periodic length $\lambda_c = 2.8$ mm and amplitude $A_c = 0.3$ mm (Figure 1.2).
Consistently with parameters of industrial flows and previous studies (Alekseenko et al., 2008; Dietze et al., 2009; Vitry, 2011), liquid film flow thicknesses are expected to be between 200 and 1000 µm. A precision lower than 10 µm is thus preferable. Taking into account the small corrugations, it would be desirable to achieve a spatial resolution of the order of $20 \cdot 20$ µm^2. The literature on film thickness

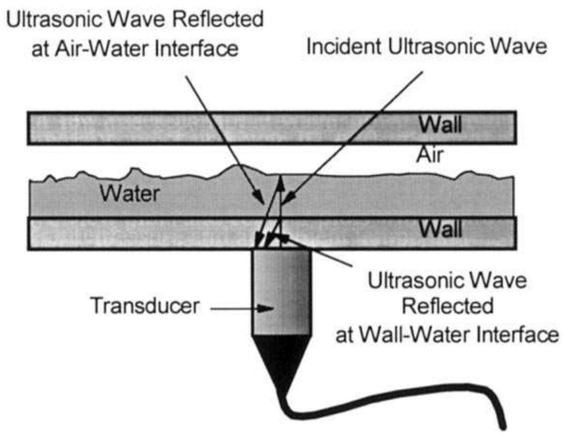

Figure 2.1: Ultrasonic measurement principle, from Kamei and Serizawa (1998).

measurements on such complex surfaces is virtually non-existent. In order to carry out these liquid film thickness measurements, existing experimental techniques are reviewed, amongst acoustic, electrical and optical methods. The present review ends with a conclusive part for selecting the best method for measuring the thickness of a liquid film flowing down on a structured packing sheet.

2.1.1 Acoustic methods

When an acoustic wave propagating in a liquid film hits an interface, this generally results in partial transmission and reflection. The acoustic wave is emitted in a solid material using a transducer, the axis of which being perpendicular to the substrate (Figure 2.1). The traveling wave is then reflected at the interface back to the probe, which gives the time that separates the emission and the reception of the wave. Knowing the sound speed and measuring the propagation time yield the liquid film thickness.

Kamei and Serizawa (1998) measured thicknesses ranging from 0.3 to 2 mm with 75-µm accuracy. They achieved a 0.9-mm-diameter resolution at a rate of 10 kHz.

This technique is non-intrusive and the spatial resolution can be enhanced by increasing the wave frequency. However, the gas-liquid interface has to be quasi-perpendicular to the transducer so that the probe receives the reflected signal. Another issue is due to large and small corrugations of structured packing sheets (Figure 1.2), which makes the application of that technique to thickness measurement of a liquid film flowing on structured packing sheets a difficult task. Indeed, the transducer must be put perpendicularly to the plate and has to be in perfect contact with it. Taking into account the small corrugations, perfect contact between the transducer and the plate cannot be achieved, hence this technique is not adequate.

2.1.2 Electrical methods

2.1.2.1 Conductance

This method is based on the conductivity of liquid media, which is proportional to the liquid volume between two measuring electrodes. Damsohn and Prasser (2009) designed a field of 1024 electrode pairs to get a thickness field. They achieved a spatial resolution of $3.12 \cdot 3.12$ mm^2 for each electrode pair with a 10-kHz data rate. They measured thicknesses from 100 to 800 µm with 5% accuracy.

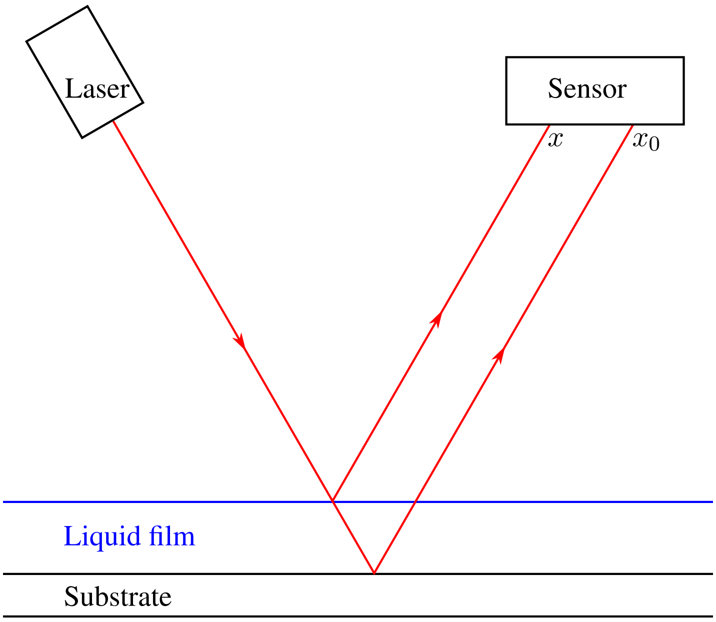

Figure 2.2: Laser triangulation principle.

This technique is easily implemented but requires modifying the solid substrate and may thus influence the hydrodynamics. The spatial resolution is equal to the inter-electrode distance and is therefore limited. Note that thicknesses higher than the inter-electrode distance cannot be measured as there is a saturation phenomenon in that case.

2.1.2.2 Capacitance

Many liquids are dielectric media. Liu et al. (2007) used electrical capacitance tomography. They measured thicknesses of a liquid flowing down inside a 15-mm-ID vertical tube by using eight electrodes. They measured thicknesses ranging from 50 to 250 µm with a 1-mm inter-electrode distance and 1-kHz acquisition frequency.

The capacitance measurement method requires modifying the solid substrate, so it is difficult to implement this for studying undulated sheets. Spatial resolution is limited by the inter-electrode distance. Besides, merely the total capacity of the multiphase flow is measured, hence corrections should be done to improve accuracy and obtain the actual film thickness.

2.1.3 Optical methods

2.1.3.1 Laser triangulation

Laser triangulation consists in observing the displacement of a light beam by a reflective interface with respect to a reference position (Figure 2.2). First, the beam is reflected at a solid substrate and goes onto the position detector. Then, another measurement is performed when there is the liquid film, which gives a new position on the detector as the laser is reflected at the free-surface. The light beam has been displaced by the liquid. Calculation using the measured displacement yields the liquid film thickness.

Gosset and Buchlin (2008) studied a viscous flow around a rotating cylinder soaked in oil. They observed the time signal of the thickness of a glycerin film at the top of the cylinder. Thicknesses ranging from 100 to 500 µm were measured with 12% accuracy and a spatial resolution of the order of the light beam

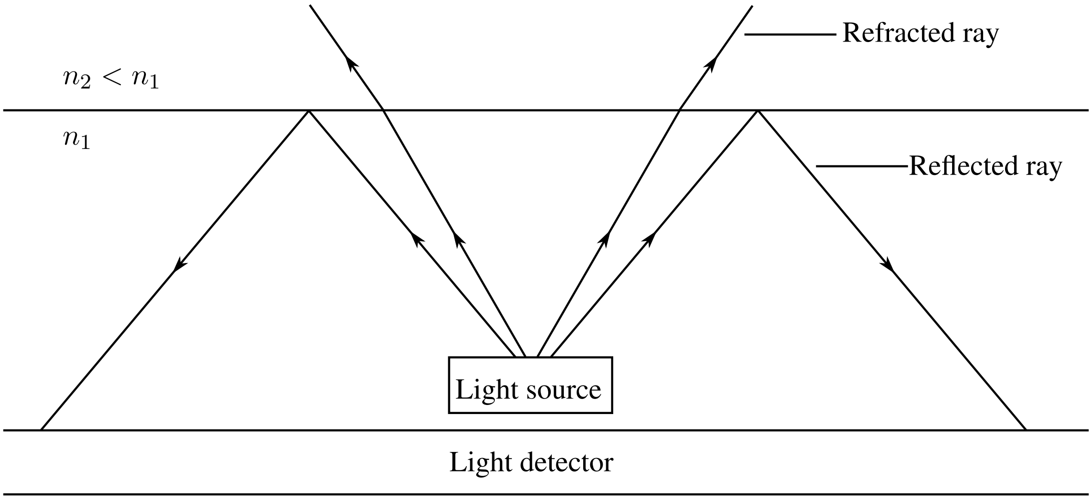

Figure 2.3: Internal reflection principle.

diameter, say 1 mm. The acquisition rate was 250 Hz. Note that they seeded a dye to render the gas-liquid interface reflective.

Measurement on curved interfaces may lead to substantial difficulties, as the interface profile itself must be determined to further deduce the height profile. This technique is basically applied when the normal to the reference reflective surface is almost the same as the normal to the gas-liquid interface. Again, it is not convenient in the case of undulated substrates, especially micro-structured ones. However, single-point measurements can be done with this technique for characterizing eventual surface waves.

2.1.3.2 Internal reflection

A light beam going through a transparent medium of index n_1 towards another medium less refringent $n_2 < n_1$ yields a total reflection at the interface of these two media when the incident angle i is higher than $\arcsin(n_2/n_1)$. If the angle of the beam emitted by the light source is high enough so that some total reflection occurs, then only part of the incident light is transmitted through the interface (Figure 2.3). The difference in light energy yields the liquid film thickness.

Several references are cited by Tibiriçá et al. (2010). Spatial resolution depends on the limit refraction angle and the kind of lighting that is used, but it is generally of the order of 1 mm. For instance, the limit refraction angle for a water-air interface is 48°, hence very small spatial resolution is not achievable. But the light comes from below the solid substrate that has to be transparent, whereas structured packing sheets are not.

2.1.3.3 Light absorption

Liquids are or can be made absorbent by seeding a dye. A dye solution is absorbent and the mix of all radiations that are not absorbed gives the dye color. Such liquids are said to be semi-transparent. When light goes through an absorbent liquid film, some light is reflected at the interface, some is absorbed by the liquid and some is transmitted. By the Beer-Lambert law, for a given light intensity I_0, the absorbed light intensity is $I_0 \exp(-\varepsilon t)$ where t is the liquid thickness along which light is absorbed and ε is the absorption coefficient which depends on the wavelength and the local dye concentration.

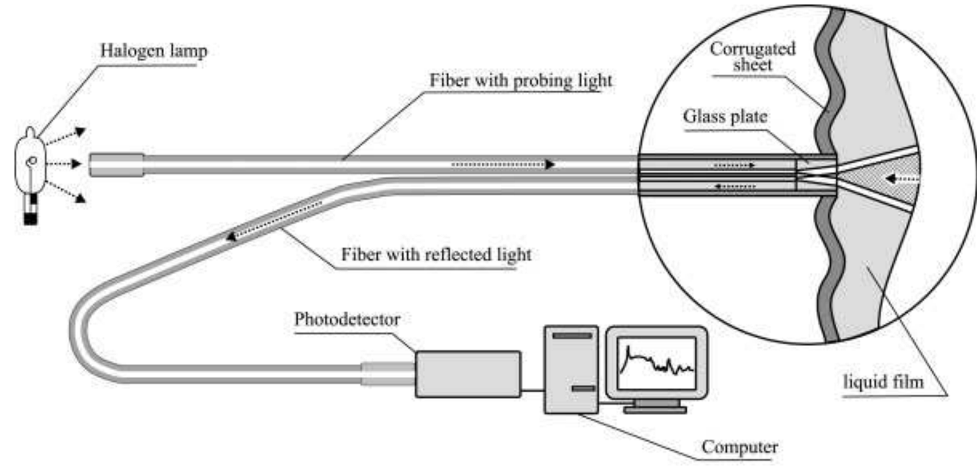

Figure 2.4: Optical-fiber measurement principle, from Alekseenko et al. (2008).

Gosset and Buchlin (2008) studied the instability of a viscous flow around a transparent rotating cylinder soaked in an oil bath. The perturbation was introduced with an air blast coming out of a nozzle. They observed the time evolution of the thickness surface field over a view field of 14 cm^2 (the spatial resolution may be reduced depending on the view field and the spatial resolution that are wanted). Thicknesses ranging from 100 to 500 µm were measured with an accuracy of 8% and a spatial resolution of 0.3 mm. They used a green light source inside the cylinder and mounted a green filter on the camera.
The considerable advantage of using a camera is that the view field, spatial resolution and acquisition frequency can be chosen. Results are accurate when the incident light is uniform. Otherwise a few corrections need to be made in a post-processing step. Lighting the system from inside as Gosset and Buchlin (2008) did is a good way to achieve uniform lighting. Note that the technique can be applied by lighting the liquid from above. It is difficult to apply such a technique to systems with substrate of complex topology, however. Indeed, the attenuation length is actually the optical path length so both profiles of the gas-liquid interface and the complex substrate must be determined. Moreover, seed particles may disturb the flow by changing the effective rheology of the particle/fluid mixture, an indication of which can be obtained from Einstein's effective viscosity of suspensions. Furthermore, dyes may modify other properties such as surface tension of the gas-liquid interface (Przadka et al., 2012).

2.1.3.4 Optical-fiber measurement

This technique does not allow investigating the flow over micro-structured substrates considering the desired resolution. As the diameter of the optical fiber is larger than the size of small corrugations, modifying the solid substrate would entirely change hydrodynamics, which is unwanted. This technique is also governed by the Beer-Lambert law. A light beam is emitted and travels within the optical fiber to strike the gas-liquid interface and then goes back to the sensor. The light energy that comes back in is compared with the light energy initially emitted by the system. The absorbed light energy is thus measured and yields the liquid film thickness. Alekseenko et al. (2008) measured thicknesses between 0.1 and 1 mm with a spatial resolution of the order of $0.4 \cdot 0.4$ mm^2. They achieved an accuracy of the order of 10 µm. The acquisition frequency was 1 kHz. The investigated plate had perforations. The optical-fiber was put under the plate so that measurements could be done through a perforation (Figure 2.4).

2.1.3.5 Diffraction

When a laser light beam goes through a liquid medium with seed particles of diameter lower than the wavelength, diffraction occurs. The intensity of scattered light is a function of the number of particles, so that light is attenuated according to Beer-Lambert law. Salazar and Marschall (1975) measured thicknesses of a liquid film ranging from 0.7 to 3 mm. Spatial resolution is of the order of the light beam, say 1 mm. High accuracy is achieved with particles of small size, smaller than 1 µm. However, the solid substrate must be transparent.

2.1.3.6 Light-induced fluorescence (LIF)

LIF techniques have been widely used to study falling films. LIF consists in seeding a fluorescent dye in the liquid. The fluorescent dye is characterized by its excitation wavelength λ_e and its re-emission wavelength $\lambda_r > \lambda_e$. The re-emitted light energy is equal to the absorbed energy. That way, thickness measurements are performed based on the Beer-Lambert law.

Vitry (2011) lighted a water film containing fluorescein with a UV light source from above. The calibration procedure allowed accounting for optical defects of the camera lens (distortion and vignetting) and spatial distribution lighting. The interface curvature was taken into account in post-processing. Thicknesses between 0.1 and 2 mm could be measured over a $328 \cdot 241$ mm^2 view field with a spatial resolution of $201 \cdot 201$ µm^2. An accuracy of 7 mm was achieved with a 150 Hz acquisition rate. Argyriadi et al. (2006) observed a liquid film flow over a corrugated wall. It was confirmed that a corrugated surface may stabilize the flow compared with a plane surface. The authors measured thicknesses ranging from 100 µm to 1 mm with respect to the corrugated wall with an accuracy below 20 µm. They had a view field of $25 \cdot 19$ mm^2 with a spatial resolution of the order of 300 µm. The acquisition frequency was 10 Hz.

High spatial and temporal resolutions can be achieved with recent high-speed cameras. The view field can be controlled so that effects of small corrugations can be observed. The same problem as for the light absorption technique is encountered when flows over complex topologies are investigated: the optical length is the measured quantity hence the substrate profile must be known. The same issues as those for the light absorption technique have to be dealt with regarding seed particles.

2.1.3.7 Photochromic dye activation

Some chemical entities initially transparent may react in the presence of a light source to form a colored product. These are called photochromic dyes. They may be used for liquid film thickness measurement via the Beer-Lambert law or as tracers for velocimetry. The reverse reaction is quasi-instantaneous but the color fading time is still finite.

Kim and Kim (2005) used photochromic dyes initially transparent that turned violet in the presence of UV rays. They observed thin liquid films between two microscope slides, and measured thicknesses ranging from 12.73 to 63.66 µm with an accuracy lower than 2 µm. Liquid films were obviously static but the technique can be applied dynamically.

Advantages and drawbacks are the same as those encountered for light absorption and LIF techniques. High spatial and vertical resolution can be achieved depending on the optics. The substrate profile must be known. Note that photochromic dyes are now less used because of safety reasons.

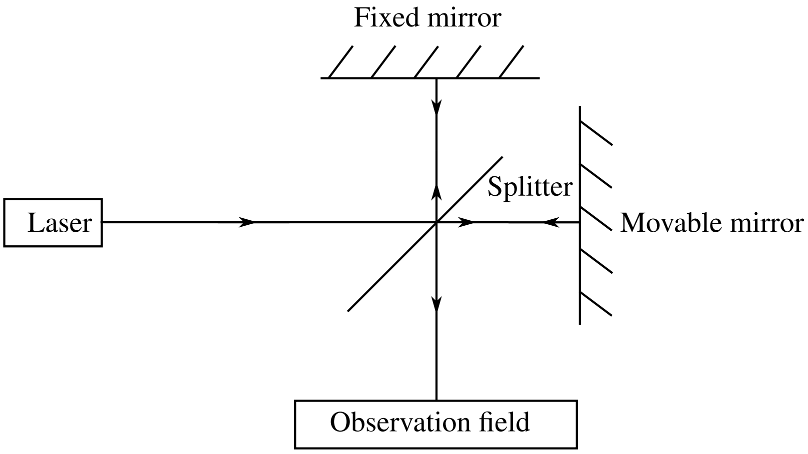

Figure 2.5: Initial configuration of the Michelson interferometer.

2.1.3.8 Interferometry

The resulting light intensity of two waves can be different from the sum of the two illuminations (interference). Interference patterns can be obtained using a beam splitter, such as in the Michelson interferometer (Figure 2.5). A light beam is split by a half-silvered mirror. Both rays strike a mirror and then interfere if some optical path difference is introduced by rotating or translating the moveable mirror. Mirrors are initially perpendicular to each other and at equal distance to the beam splitter. If the moveable mirror is translated so that it introduces a difference between the optical paths, one may observe fringes of equal inclination. If the moveable mirror is rotated, one may obtain fringes of equal thickness.

Han et al. (2011) used an interferometer to observe fringes of equal thickness. Liquid films were between 2 and 20 µm. As liquid films were very thin, the interface played the role of beam splitter. The difference in optical paths was equal to the liquid film thickness. The latter was determined from the interferogram by counting the interference fringes. They achieved a spatial resolution of $0.88 \cdot 0.66$ mm^2 with high accuracy that depended of the number of fringes. The acquisition frequency was 1 kHz.

This technique is straightforward for the measurement of very thin flat films. In that case there is no need of reference: the interference phenomenon occurs between rays that are reflected at the free-surface and those that are reflected at the solid substrate. Note that interferometry-based profilometry (temporal evolution of interface shape) can be performed. In that case, a reference state interferogram is needed. Regarding spatial resolution, the thickness is measured at a single spot which size is that of the interferogram. However, problems are encountered for curved interfaces as the light rays may not come back into the sensor.

2.1.3.9 Chromatic Confocal Imaging (CCI)

A point source of white light goes through a beam splitter and then through a lens. The image of the point source through the lens is stretched due to the chromatic aberration of a lens (Figure 2.6). Indeed, glass is dispersive and blue is deflected more than red. Light is then reflected, goes back through the lens, hits the half-silvered mirror and reaches the spectrometric sensor. The wavelength of maximal intensity on the spectrum is related to the distance of the reflective interface to the sensor. The lens has to be put such that the reflective interface intersects the stretched image of the point source of white light. A confocal

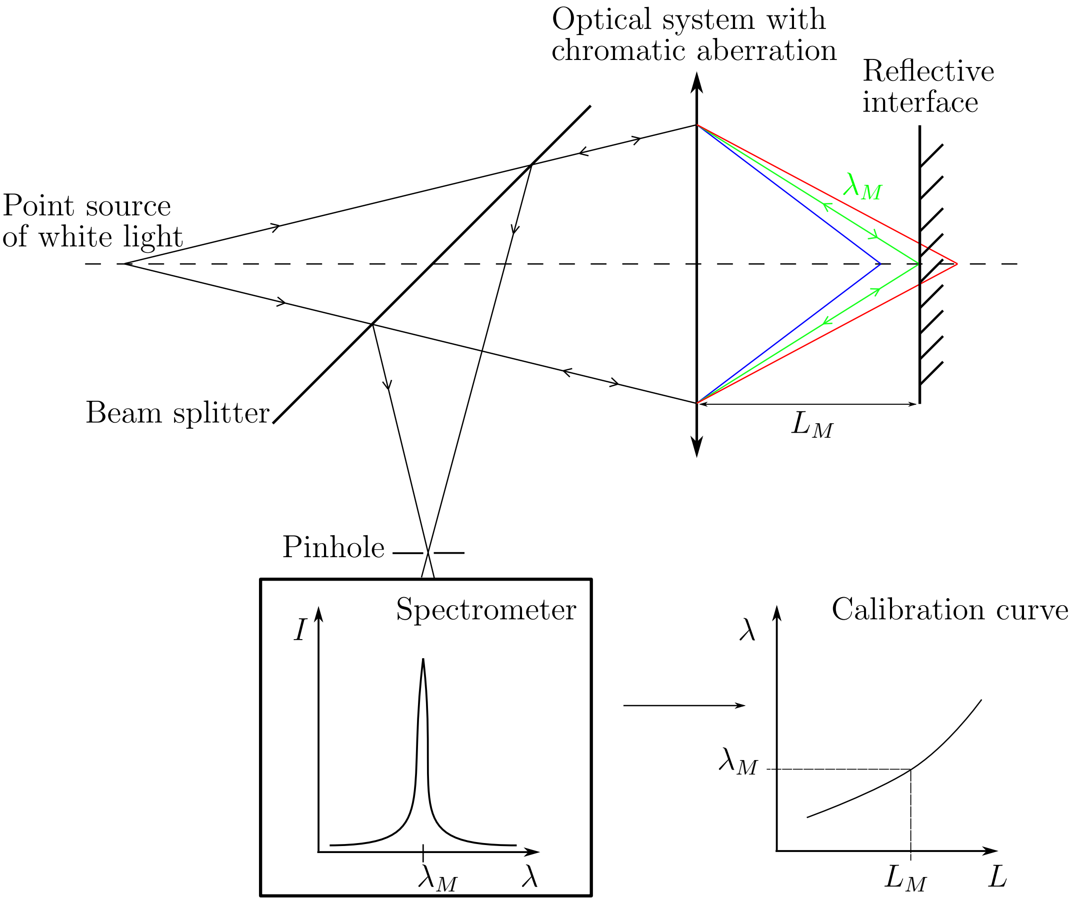

Figure 2.6: CCI technique principle.

chromatic sensor incorporates all the components. Each sensor is made for a given working distance, spatial resolution, measurement range and accuracy. The reflective interface position from the sensor is obtained via the calibration curve determined by the manufacturer.

Lel et al. (2005) used CCI for liquid films flowing down an inclined plane. They measured liquid film thicknesses ranging from 0.1 to 2 mm with an accuracy of 15 µm and an acquisition rate ranging from 1 to 4 kHz.

Dietze et al. (2009) observed liquid films flowing down inside a vertical cylindrical transparent tube with the same technique. They followed a refractive index matching procedure to avoid any refraction to occur. They measured thicknesses ranging from 200 to 700 µm with a spatial resolution of $10 \cdot 10$ µm^2, an accuracy of 4 µm and a repetition frequency of 800 Hz. The experimenter used the sensor both with and without the flowing liquid film to perform an indirect thickness measurement.

Extremely high spatial resolution is achievable with high accuracy. But this is a single-point measurement so measurements would have to be carried out at several points. Another issue is encountered whilst locating a curved interface. The optical axis of the sensor must be quasi-perpendicular to the reflective interface so that a light signal does go back into the sensor.

2.1.3.10 Chromatic Spectral Interferometry (CSI)

This is a profilometry technique. Light is reflected both at a reference mirror and at the gas-liquid interface. Fringes of equal inclination are obtained. It is based on the same principle as CCI, that is to say the

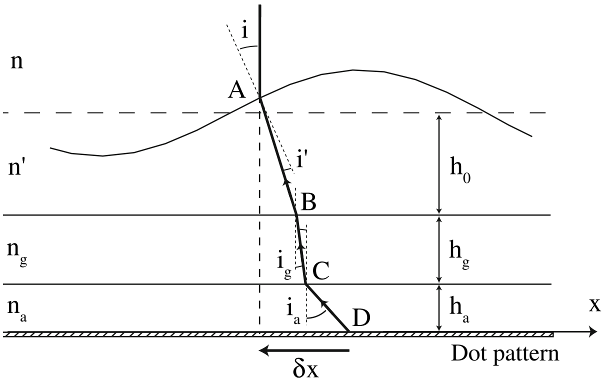

Figure 2.7: Schlieren technique principle, from Moisy et al. (2009).

chromatic aberration of a lens. Combining interferometry and CCI of white light allows achieving high accuracy (lower than 0.1 µm) whilst measuring thicknesses higher than 100 µm. This technique can be applied with a commercial sensor or with an own experimental setup. Problems due to curved interfaces may be encountered.

2.1.3.11 Schlieren

The Schlieren method is a profilometry technique that consists in observing deformations of a pattern through a dynamic interface. The reference pattern can be either carved on the substrate on which the liquid flows or put below the substrate, should the latter be transparent.

Moisy et al. (2009) observed deformations of a speckle pattern through a gas-liquid interface flowing on a transparent plane (Figure 2.7). They measured thicknesses of the order of 100 µm with a $14 \cdot 14$ cm^2 view field, a spatial resolution of $70 \cdot 70$ µm^2 and a 1-µm accuracy. They acquired 100 frames per second. They mentioned that the interface-to-pattern distance must be higher than the liquid depth to avoid rays crossing. However, rays crossing may occur also in the case of highly-curved interfaces.

2.1.3.12 Fourier Transform Profilometry (FTP)

The FTP was first introduced by Takeda and Mutoh (1983). A fringe grating is projected onto a reference plane. The same grating is then projected onto an object which profile is wanted (Figure 2.8). The image of the projected fringe grating is not the same on the reference plane as on the object. Differences between the two images are related to a phase difference between the two frames. Images are recorded and a Fourier analysis is performed to recover the phase difference, which is related to the elevation depth (Maurel et al., 2009).

Reconstruction of dynamic gas-liquid interface was carried out by Cobelli et al. (2011) who studied surface waves. Lagubeau et al. (2012) observed the spreading of a drop impacting on a liquid film with a high-speed camera. They reconstructed the height field with values ranging from 0.1 to 2 mm with a spatial resolution of $100 \cdot 100$ µm^2 and a height resolution of 20 µm. The view field was of the order of $100 \cdot 100$ mm^2. They made the gas-liquid interface reflective by seeding 300-nm particles of anatase (titanium dioxide) which is a white pigment. That dye has the characteristic of not modifying the surface tension of the gas-liquid interface (Przadka et al., 2012). The concentration of anatase particles was small, 0.2% in volume.

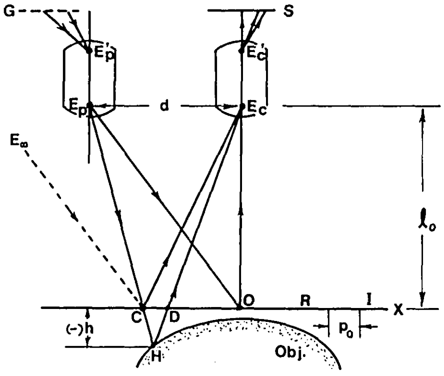

Figure 2.8: Fourier transform profilometry principle, from Takeda and Mutoh (1983).

In the end, this technique cannot be applied to measure a 500-µm liquid film flowing on a solid substrate. Indeed, such a thin liquid film cannot be made opaque (and reflective) enough for applying the technique. That was not an issue for Lagubeau et al. (2012) because the droplet was dropped onto a liquid layer that had the same concentration of reflective particles.

2.1.4 Discussion

Table 2.1 summarizes the collected information on existing thickness measurement techniques. Acoustic and electrical techniques cannot be applied because they require modifying the substrate. The same problem is encountered with optical-fiber measurements. Diffraction and internal reflection methods are dismissed because the substrate is not transparent. Any optical technique might lead to issues regarding curved-interface flows. Therefore, interferometry, CSI and Schlieren methods may be dismissed. For techniques based on the Beer-Lambert law, one may avoid these spurious aspects by calculating the interface slope (Vitry, 2011). Note that the observation area is confined with glass in the experimental setup used in Chapter 6, hence absorption of glass would have to be taken into account.

This leaves two options to be considered further. If the LIF technique is employed, lighting must be as uniform as possible, glass planarity has to be checked and corrected if necessary, and the plate must be black-tainted to avoid spurious reflections. Note that fluorescent seed particles may modify liquid and wetting properties. Tainting the plate may modify wetting properties as well. This technique has the advantage of yielding a view field. However, the exact equation of the complex surface must be determined as the reference for each run. If the CCI technique is applied, there is no need to taint the plate or to use seed particles: wetting properties are preserved but the film thickness measurement is at a single point. The CCI technique has been chosen because it does not require any modification of the geometry and will not modify any liquid property. Specifications of the CCI system are gathered in Table 2.2. Although thicknesses smaller than 500 µm are expected to be measured, observing through the glass channel imposes a minimal working distance, hence the choice of this CCI system. Problems related to distance measurement through a glass medium will be discussed in Chapter 6.

Technique	Principle	Thickness	Resolution	Issues
Ultrasonic	Speed of sound	0.3 – 2 mm	1 mm^2	Corrugated plate, resolution
Conductance	Liquid conductivity	100 – 800 µm	$3.12 \cdot 3.12$ mm^2	Support modification, resolution
Capacitance	Liquid dielectric constant	50 – 250 µm	1 mm^2	Substrate modification, resolution
LT	Reflection	100 – 500 µm	1 mm^2	Corrugated plate, resolution, curved interface
Internal reflection	Total reflection	0.01 – 2 mm	1 mm^2	Non-transparent and corrugated plate
Absorption	Beer-Lambert	$>$ 100 µm	$0.3 \cdot 0.3$ mm^2	Corrugated plate, curved interface
Optical fiber	Beer-Lambert	$>$ 100 µm	1 mm	Substrate modification
Diffraction	Beer-Lambert, particle diameter $<$ wavelength	0.7 – 3 mm	1 mm	Non-transparent and corrugated plate
LIF	Beer-Lambert	0.1 - 2 mm	$100 \cdot 100$ μm^2	Corrugated plate, curved interface
Photochromic	Beer-Lambert	12 – 64 µm	1 mm	Corrugated plate
Interferometry	Reflection at substrate and gas-liquid interface	2 – 20 µm	$0.88 \cdot 0.66$ mm^2	Curved interface
CCI	Chromatic aberration	0.1 – 2 mm	$10 \cdot 10$ μm^2	Curved interface
CSI	CCI + interferometry	0.1 - 2 mm	1μm^2	Curved interface, interface profile but not thickness
Schlieren	Speckle-pattern deformation	0.1 – 1 mm	$70 \cdot 70$ μm^2	Curved interface, interface profile but not thickness
FTP	Deformation of a projected fringe grating	0.1 – 2 mm	$100 \cdot 100$ μm^2	Penetration length

Table 2.1: Summary of liquid film thickness measurement methods.

Measuring range	Minimum working distance	Spot diameter	Axial accuracy	Maximum tilt	Acquisition rate
10000 µm	66.9 mm	51 µm	0.9 µm	±12°	0.1 – 2 kHz

Table 2.2: Specifications of the CCI system, STIL OP-10000.

2.2 Contact lines

Throughout the thesis, flows with moving contact lines are considered. A contact line is a three-phase junction, in the present context, this refers to the intersection of two separate fluid phases and a solid substrate. Contact lines are observed for any liquid flow over a substrate exhibiting dry zones. Flows over structured packing sheets may involve moving contact lines. A brief introduction is presented here. Macroscale modeling of flows with moving contact lines is discussed further in Chapter 4.

2.2.1 Static contact lines

Let σ_{LS} and σ_{GS} be the energy per unit area of liquid-solid and gas-solid interfaces, respectively, and σ denote the energy per unit area or surface tension of the gas-liquid interface. If the contact line is moved with a positive infinitesimal displacement dx between two steady states (Figure 2.9), liquid-solid and gas-liquid interfaces gain energies $\sigma_{LS}dxdy$ and $\sigma\cos\theta_Y dxdy$, respectively, while the gas-solid interface loses an energy $\sigma_{GS}dxdy$. Young's equation (Young, 1805) expresses energy conservation at the contact line:

$$\sigma_{GS} = \sigma_{LS} + \sigma\cos\theta_Y. \tag{2.1}$$

The Young angle θ_Y is a theoretical angle for homogeneous substrates. In reality, any solid surface exhibits heterogeneities, that can either be of a geometrical or chemical nature and viewed as some kind of roughness. A review of roughness effects on wetting phenomena is available in Quéré (2008).

2.2.1.1 Roughness

Contact angle hysteresis

The apparent contact angle θ_{ap} is often different from the Young angle θ_Y because of local pieces of roughness of the substrate. A contact line that would advance on a perfectly smooth, clean substrate may remain pinned in reality because of geometrical or chemical heterogeneities until it reaches a maximum angle called the advancing contact angle θ_A, above which motion occurs. The receding contact angle θ_R is the minimum angle below which the contact line can be receded. The contact angle hysteresis $\Delta\theta = \theta_A - \theta_R$ increases with the substrate roughness and can have a value close to θ_A in some cases.

Wenzel model

Roughness modifies the contact angle. Wenzel (1936) assumed the liquid to fit perfectly the substrate topography (Figure 2.10). In this case, a positive infinitesimal displacement dx of the contact line leads to gains $r\sigma_{LS}dxdy$ and $\sigma\cos\theta_{ap}dxdy$ of energy of liquid-solid and gas-liquid interfaces, respectively, and a loss $r\sigma_{GS}dxdy$ of energy of the gas-solid interface. Here, r is a roughness coefficient that corresponds to the ratio of the actual to the projected area. Energy conservation yields:

$$r\sigma_{GS} = r\sigma_{LS} + \sigma\cos\theta_{ap}. \tag{2.2}$$

The Wenzel equation that defines the substrate roughness is then obtained from (2.1) and (2.2):

$$\cos\theta_{ap} = r\cos\theta_Y. \tag{2.3}$$

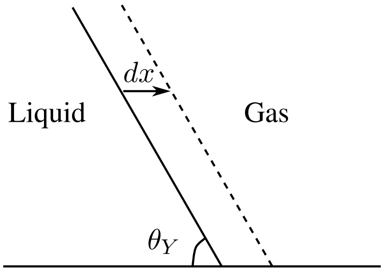

Figure 2.9: Infinitesimal displacement on a smooth substrate.

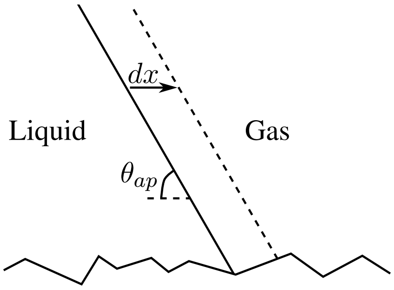

Figure 2.10: Infinitesimal displacement on a rough substrate.

From (2.3), roughness enhances the wettability of a hydrophilic solid. Indeed, $\theta_{ap} < \theta_Y$ for a rough ($r > 1$) and hydrophilic ($\theta_Y < \pi/2$) substrate. Likewise, the rougher a solid, the more hydrophobic: $\theta_{ap} > \theta_Y$ for a rough and hydrophobic ($\theta_Y > \pi/2$) substrate.
The assumptions of the Wenzel model are very restrictive. In particular, (2.3) is not valid in the case of a very rough ($r \gg 1$) substrate. That would involve complete wetting or complete drying, which is not observed experimentally. Moreover, roughness does not necessarily enhance wetting on a hydrophilic substrate. The Wenzel model is generally valid for low receding contact angles (Quéré, 2008) and a droplet size large compared with microstructures (Wolansky and Marmur, 1999). If the size of a droplet is of the same order as that of microstructures, then the Wenzel equation is modified (Swain and Lipowsky, 1998).

Cassie model for smooth but heterogeneous substrates

Consider a smooth surface that has a two-material composition (Figure 2.11). f_1 and f_2 denote the fraction of materials 1 and 2, respectively, θ_1 and θ_2 denote the static angles of pure materials 1 and 2. The Cassie equation for the resulting contact angle is:

$$\cos\theta_{ap} = f_1 \cos\theta_1 + f_2 \cos\theta_2. \tag{2.4}$$

This model is not of interest for structured packing sheets which are made of one material. Note that the Cassie and Wenzel models are sometimes combined for modeling substrates that are rough and chemically heterogeneous.

Cassie-Baxter model for superhydrophobic substrates

For a highly-hydrophobic substrate made of microstructures, Cassie and Baxter (1944) assumed that part of the solid remains dry, that is to say the liquid does not fit everywhere the substrate (Figure 2.12). In

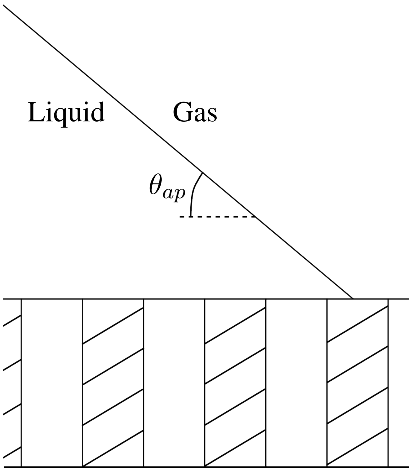

Figure 2.11: Static contact line on a smooth substrate made of two materials.

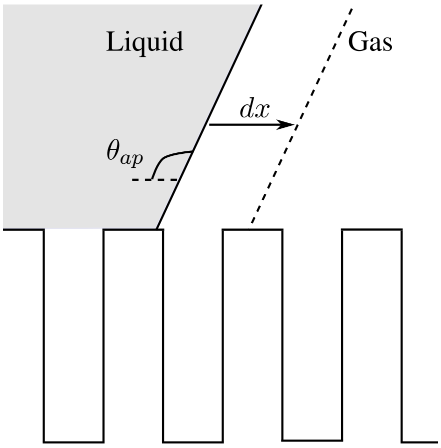

Figure 2.12: Infinitesimal displacement on a super-hydrophobic substrate.

that case, if f_S denotes the fraction of solid in contact with liquid, a positive infinitesimal displacement dx leads to gains $f_S\sigma_{LS}dxdy$ and $\sigma\big((1-f_S)+\cos\theta_{ap}\big)dxdy$ of energy of liquid-solid and gas-liquid interfaces respectively and a loss $f_S\sigma_{GS}dxdy$ of energy of the gas-solid interface. The resulting energy conservation reads:

$$f_S\sigma_{GS} = f_S\sigma_{LS} + \sigma\big((1-f_S)+\cos\theta_{ap}\big). \tag{2.5}$$

(2.1) and (2.5) yield:

$$\cos\theta_{ap} = f_S - 1 + f_S\cos\theta_Y. \tag{2.6}$$

The fraction of solid in contact with liquid f_S may not be uniform. From (2.6), an increase in f_S yields a decrease in θ_{ap}: the rougher the substrate, the more hydrophobic.

Superhydrophilic substrates

For a highly-hydrophilic solid made of microstructures, there is no dry zone between the drop and the substrate but there may be a precursor film (Quéré, 2008). Let f_S be the fraction of microstructures. A positive infinitesimal displacement dx of the contact line leads to gains $f_S\sigma_{LS}dxdy$ and $\sigma\cos\theta_{ap}dxdy$ of energy of liquid-solid and gas-liquid interfaces respectively and losses $f_S\sigma_{GS}dxdy$ and $(1-f_S)\sigma dxdy$

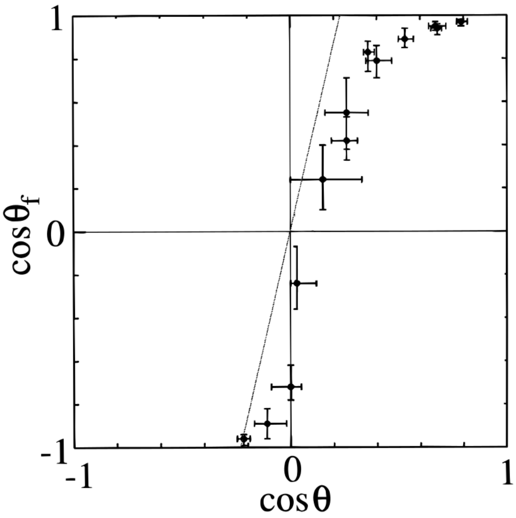

Figure 2.13: Experimental results of Onda et al. (1996): cosine of the apparent angle against cosine of Young angle for water droplets on different surfaces.

of energy of the gas-solid and gas-liquid interfaces. From energy conservation,

$$f_S\sigma_{GS} + (1 - f_S)\sigma = f_S\sigma_{LS} + \sigma\cos\theta_{ap}. \tag{2.7}$$

Then (2.1) and (2.7) yield:

$$\cos\theta_{ap} = 1 - f_S + f_S\cos\theta_Y. \tag{2.8}$$

From (2.8), θ_{ap} increases with f_S: the rougher the substrate, the more hydrophilic.

Application to structured packing sheets

In this project, small corrugations of structured packing sheets are not considered as pieces of roughness because the thickness of the liquid film flowing over structured packing sheets is of the order of the amplitude of small corrugations, $A_c = 0.3$ mm. However, structured packing sheets are made of stainless steel, a material that may exhibit a hysteresis behavior, as observed in Chapter 5. Stainless steel sheets have a hydrophilic behavior for the cases investigated there, with static angles lower than $\pi/2$. Structured packing sheets should then be considered as hydrophilic substrates with $\cos\theta_Y > 0$.

Onda et al. (1996) observed the change in apparent contact angle due to rough substrates. They varied the Young angle using different liquids. Their results, shown in Figure 2.13, can be represented by (2.3) for angles θ close to $\pi/2$ and by (2.8) for angles θ close to 0. For the systems studied in Chapter 5, Wenzel model might be suitable for characterizing static contact angles on stainless steel sheets, as no super-hydrophilic behavior has been observed there.

On the validity of Wenzel model

According to the Wenzel equation (2.3), roughness enhances wetting in the case of a hydrophilic substrate. Cox (1983) demonstrated that wetting may either be enhanced or inhibited depending on spatial variations of roughness. He determined that wetting is enhanced for a liquid spreading parallel to grooves and inhibited for a liquid spreading perpendicularly to grooves. Savva et al. (2011) conducted a statistical study considering a random function for modeling roughness. They demonstrated that roughness inhibits

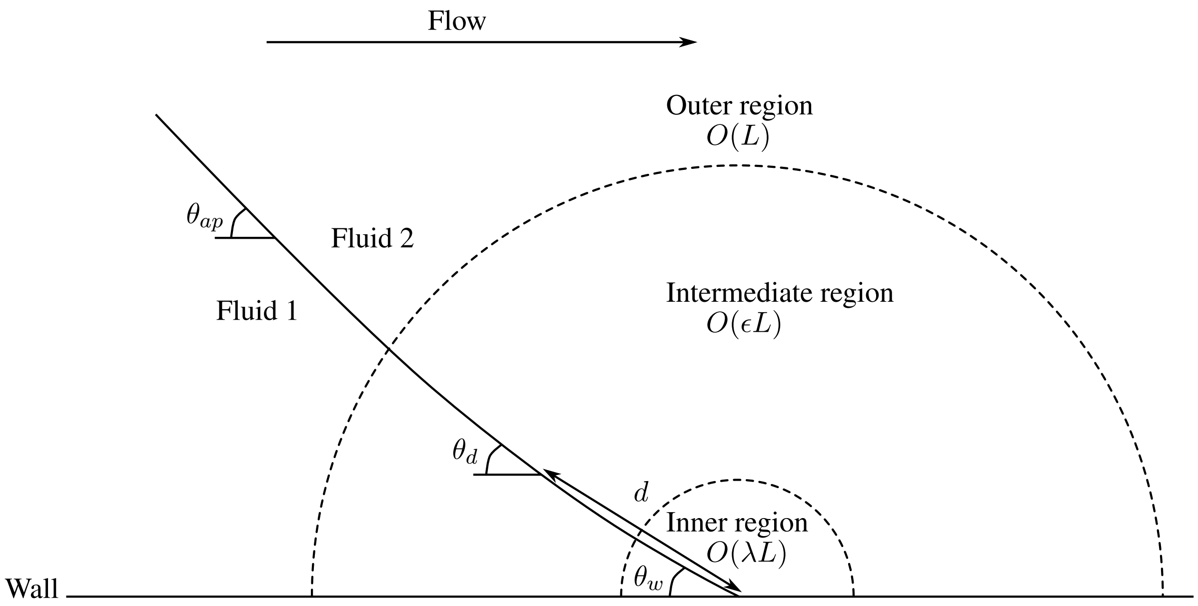

Figure 2.14: Length scales and contact angles involved in the description of moving contact lines.

spreading of a hydrophilic-fluid droplet. Therefore, roughness may have to be taken into account. As suggested by Sui et al. (2014), contact angle hysteresis is a basic way to represent roughness. Numerically, roughness would reflect the presence of structures that are smaller than the scale of the flow that is resolved next to wall boundaries.

2.2.2 Moving contact lines

2.2.2.1 The moving contact line paradox

In hydrodynamics, a no-slip condition is usually used at wall boundaries. Moffatt (1964) showed that this condition leads to a singularity at the moving contact line because both shear stress and pressure next to the wall are inversely proportional to the distance from the contact line. Snoeijer and Andreotti (2013) reviewed existing models that have been developed to get around this problem. Sui et al. (2014) have taken an interest in using such models to simulate flows with moving contact lines.

2.2.2.2 Contact angles and length scales

In order to describe microscopic or mesoscopic models that allow circumventing the moving contact line singularity, several length scales must be defined. Three length scales are generally considered in compliance with asymptotic models developed by Hocking and Rivers (1982) and by Cox (1986) for viscous regimes (Figure 2.14). The theory of Cox (1986) is presented in detail in Section 2.2.2.3.

2.2.2.3 Modeling of moving contact lines

Microscopic models

This section briefly describes contact line models that have been developed for a proper description of the physics in the immediate vicinity of a moving contact line, in the inner region. These microscopic models, reviewed by Bonn et al. (2009) and by Snoeijer and Andreotti (2013), allow alleviating the contact line

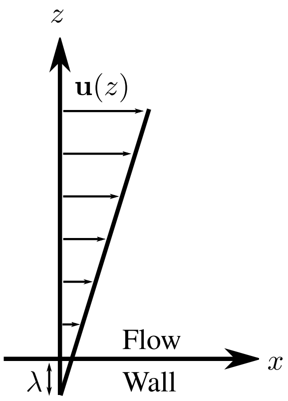

Figure 2.15: Slip length definition.

singularity. However, they have been worked out at very small scales so their use for direct numerical simulation of macroscopic flows would require a huge computational effort. Nevertheless, characteristic length scales of such physics are needed for the development of asymptotic methods used for describing larger scales. The review presented here is not exhaustive, the reader is referred to the above-mentioned reviews for a more complete and detailed account.

Slip model

A common model is to assume the existence of slip (Dussan V., 1979), at a scale that is typically nanometrical, such that the no-slip boundary condition for the velocity field is replaced by a slip condition (Figure 2.15):

$$u(x,0) - U_{wall} = \lambda \frac{\partial u}{\partial z}(x,0). \tag{2.9}$$

Here the microscopic length scale λ corresponds to the slip length, which is the characteristic length scale over which slip occurs.

Different slip length models have been developed, from statistical physics for example. More information can be found in the review of Snoeijer and Andreotti (2013). Although this approach alleviates the singularity in the wall shear stress, a weak singularity in the pressure remains - this is logarithmic in the distance to the contact line (Huh and Mason, 1977).

Kinetic model

In (2.1), a force per unit length $\sigma \cos\theta_Y$ acts on the contact line. When the latter starts moving, the effective force per unit length becomes $\sigma(\cos\theta_Y - \cos\theta_d)$. As a drag force, it should be related to the viscosity and the contact line velocity. The general trend can be captured by introducing the coefficient ι that may depend on θ_w (Sui et al., 2014), such as the contact line speed reads:

$$U_{CL} = \iota \frac{\sigma}{\mu}(\cos\theta_Y - \cos\theta_d). \tag{2.10}$$

The force per unit length $\sigma(\cos\theta_Y - \cos\theta_d)$ is referred to as the unbalanced Young force acting on the contact line.

Precursor film model

At small contact angles, a precursor film may form ahead of the contact line due to inter-molecular interaction forces (de Gennes, 1985). This model has been widely used for simulating moving contact lines in the lubrication theory (Troian et al., 1989; Bertozzi and Brenner, 1997; Kalliadasis, 2000; Kondic and Diez, 2001; Grigoriev, 2005). This model easily allows getting around the contact line stress singularity since the contact line has either been eliminated (when assuming the entire solid to be wetted by the film) or, if the precursor film is of finite extent, its thickness reduces down to molecular scales near its edge where continuum theory is no longer expected to apply. As the precursor film is about 10 nm, its consideration in numerical simulation leads to same leading-order results as with a slip length of the same order (see references in the review of Sui et al. (2014)).

Macroscale models

The various contact-line models summarized above generally introduce some very small physical length scale (slip length, precursor thickness, etc.). Numerical simulations of flows with moving contact lines based on any of these for realistic cases will necessarily be extremely expensive due to the resulting large range of length scales. It is therefore of interest to formulate a macroscale model wherein the flow on a scale that can be resolved numerically for applications does account for the influence of microscopic hydrodynamics; in particular, for the possibly strong interface curvature near a moving contact line. A straightforward way to simulate a macroscopic flow with moving contact lines is to impose a constant contact angle value as boundary condition, equal to the static angle, but that would only be useful for a very small capillary number based on the contact line speed, wherein the interface is not expected to be strongly curved near the contact line. To formulate a macroscale model, hydrodynamic theories such as that of Hocking and Rivers (1982) for axisymmetric droplet spreading or that of Cox (1986) for two-dimensional flows can be used as a basis. Cox (1986) first developed an asymptotic theory for moving contact lines in viscous regime, and further extended his work to more rapid flows, in inertial regime (Cox, 1998).

Viscous regime

In the viscous theory of Cox (1986), three length scales are considered (Figure 2.14). The outer (macroscopic) region is located far away from the contact line. Let λ and ϵ be the length scales of the inner (microscopic) region and the intermediate (mesoscopic) region, respectively, made dimensionless with a length scale of the overall flow (see below), such as $\lambda \ll \epsilon \ll 1$. The interface slope at a point located in the inner region is denoted by θ_w. The interface slope at a point located in the intermediate region, at a distance d from the contact line, is denoted by θ_d. The apparent contact angle, that is the angle that the gas-liquid interface profile extrapolated from the outer region makes with the substrate, is denoted by θ_{ap}. The length scale λ of the inner region, is a characteristic length scale associated with the physics that occurs in the immediate vicinity of the contact line, on which the stress singularity is curtailed. Henceforth this is referred to herein as the slip length (Figure 2.14).

In the inner region, the interface slope θ_w is often taken as practically constant and assumed equal to the static contact angle (Huh and Scriven, 1971). Comparison against asymptotic theories does suggest that in fact this angle may depend on the contact-line speed (Sui and Spelt, 2013b), but this does not break down the theory discussed here (see further discussion below). Cox (1986) suggested that θ_w should first be taken equal to the advancing contact angle θ_A when hysteresis is accounted for, in the case of a rough substrate.

In the intermediate region, viscous bending affects the interface slope; mathematically, this region is usually required in order to match the interface shape in the outer region to that in the inner region. Far away from the contact line, in the outer region, a no-slip boundary condition applies and the interface profile depends on that of the intermediate region; more recently this has been found to be an overlap region by Sibley et al. (2015) who identified this overlap by considering higher orders in Ca_{CL} for the interface slope solutions in the inner and outer regions. According to the theory of Cox (1986), the intermediate length scale is $\epsilon = O(1/|\ln\lambda|)$. The existence of the intermediate region has been proved throughout several experiments carried out by Ngan and Dussan V. (1989), Dussan V. et al. (1991), Shen and Ruth (1998), Ramé et al. (2004). These authors determined characteristic length scales $O(10\ \mu\text{m})$ for the intermediate region and $O(1\ \text{nm})$ for the inner region.

The outer region is the region located far away from the contact line, wherein the apparent angle is affected by the interface slope in the intermediate region, the macroscale flow geometry, the contact-line speed, and the slip law that is used. Its length scale may be the size of a drop, the thickness of a liquid film, or the capillary length which is the distance from the contact line over which capillary effects competes with gravity effects. The length scale of the outer region should then be the minimum of the geometric scale (drop size or film thickness) and the capillary length, although the choice of this length scale may be arbitrary for three-dimensional flows.

Contact angles of different scales are asymptotically linked to each other by a function of the contact line speed. The capillary number $Ca_{CL} = \mu U_{CL}/\sigma$ and the Reynolds number $Re_{CL} = LU_{CL}/\nu$ are assumed to be small: $Ca_{CL} \ll 1$ and $Re_{CL} \ll 1$. Capillary forces dominate viscous forces which dominate inertial forces. Gravity forces are assumed to be small when compared to capillary forces, that is for a small Bond number $Bo = \rho g L^2/\sigma$. The substrate is supposed to be planar. This theory was experimentally demonstrated to be valid up to the limit $Ca_{CL} \leq 0.1$ (Chen et al., 1995; Lavi and Marmur, 2004). The analysis Cox (1986) results in the following relationship between the local dynamic angle θ_d located at a distance d from the contact line in the intermediate region, the microscopic contact angle θ_w, and the contact-line speed,

$$g(\theta_d, r_\mu) = g(\theta_w, r_\mu) + Ca_{CL}\ln\left(\frac{d}{\lambda}\right) + Ca_{CL}Q_i + O(Ca_{CL}^2), \tag{2.11}$$

with

$$g(\theta, r_\mu) = \int_0^\theta \frac{(x^2 - \sin^2 x)(\pi - x + \sin x\cos x)r_\mu + [(\pi - x)^2 - \sin^2 x](x - \sin x\cos x)}{2\sin x[(x^2 - \sin^2 x)r_\mu^2 + 2(x(\pi - x) + \sin^2 x)r_\mu + (\pi - x)^2 - \sin^2 x]}. \tag{2.12}$$

The coefficient Q_i in (2.11) depends on the viscosity ratio $r_\mu = \mu_2/\mu_1$, the contact angle θ_w in the inner region and the slip law that is used. That term is often left out for simplification if the slip length is not extremely small, although in practice this may have an important quantitative effect as argued by Sui and Spelt (2013a). It is known for $r_\mu = 0$ in axisymmetric flows from the work of Hocking and Rivers (1982). Otherwise, it can be determined by comparison with experimental or DNS results. As θ_w is often assumed equal to the advancing angle for an advancing contact line (Cox, 1986), the dynamic angle is larger than the advancing angle for an advancing contact line. The analysis of Cox (1986) that results in (2.11) is not dependent on the direction of contact-line motion, and therefore covers also receding contact lines, for which the dynamic angle is smaller than the receding angle.

Some experiments have flagged up that the microscopic angle may depend on the contact line velocity (Sheng and Zhou, 1992; Ramé et al., 2004). For instance, Sheng and Zhou (1992) developed a dynamic model for the wall angle that notably allowed Sui and Spelt (2013b) to accurately simulate, using a realistic value for the slip length, the rapid droplet spreading experiment of Ding et al. (2012). An important concern with this approach is, however, that the value of the coefficient Q_i in (2.11) is not known a priori for general flows. A sensitivity study of results obtained to the value of this parameter should normally be conducted.

The key idea in large-scale computations is to only resolve the flow down to some point in the contact-line region, and to obtain the angle between the interface and substrate there from the above theory. The theory itself has been developed by matching interface shapes in the various regions. A discussion of the notion that macroscopic flow depends only on the hydrodynamics of the intermediate region through the interface slope is in Kafka and Dussan V. (1979). For these reasons, it is expected that it is sufficient to resolve the flow down to the intermediate region by modeling effects of the inner region on the intermediate region from (2.11); the application of the computational work in this thesis can be considered to be a test of the validity of these assertions.

Equation (2.11) determines the dynamic angle θ_d that has to be implemented as boundary condition at a point that is at a distance d from the contact line. For a slip length $O(1\text{ nm})$, there is practically no change in the hydrodynamics of the outer region while the dynamic angle θ_d is being imposed at the distance from the contact line between $O(10\text{ nm})$ and $O(10\text{ µm})$ (Kafka and Dussan V., 1979). Ngan and Dussan V. (1989) located the intermediate region at a distance from the contact line $O(10\text{ µm})$. In their numerical simulations, Dupont and Legendre (2010) imposed a contact angle θ_d calculated from a simplified version of (2.11), obtained from the theory of Ngan and Dussan V. (1989) by setting $d = 10$ µm. That boundary condition was taken independent of the grid spacing whereas (2.11) gives the interface slope at any location d. This was taken into account in simulations performed by Sui and Spelt (2013b). They imposed a contact angle function of the uniform grid spacing h as boundary condition and approximated the distance d in (2.11) by:

$$d = \frac{h}{2\sin\big((\theta_d + \theta_w)/2\big)}. \tag{2.13}$$

Mesh-dependent boundary conditions still lead to grid convergence (Afkhami et al., 2009; Sui and Spelt, 2013b). Maglio and Legendre (2014) also used a mesh-dependent boundary condition by approximating the distance d in (2.11) by $h/2$.

Inertial regime

The inertial theory of Cox (1998) proposes a macroscale model for flows wherein inertial effects have to be accounted for when compared to viscous forces: $Re_{CL} \gg 1$. Capillary forces still dominate viscous forces: $Ca_{CL} \ll 1$. It is assumed that the boundary layer is laminar and no flow separation occurs. Cox (1998) works out two different cases. First, he considered flows wherein viscous effects are entirely negligible with respect to inertial effects: $1 \ll \lambda^{-1} \ll Re_{CL}$. Thus there is an inertial regime everywhere including in the inner region as $\lambda Re_{CL} \gg 1$. Next, Cox considered the case of a flow wherein the inner regime is viscous and the outer regime is inertial: $1 \ll Re_{CL} \ll \lambda^{-1}$. This latter condition is often met in the case of aqueous flows down an incline and is of interest here.

The intermediate region is further divided into a viscous subregion and an inviscid subregion. These match in a transitional zone located at a distance d^* from the contact line. Cox (1998) chooses the corresponding Reynolds number Re^* such as:

$$d^* = \frac{Re^*}{Re}. \tag{2.14}$$

The interface slope θ_d in the viscous sublayer at a distance d from the contact line is still obtained from the viscous regime equation of Cox (1986):

$$\forall d \in [\alpha\lambda, d^*], g(\theta_d, r_\mu) = g(\theta_w, r_\mu) + Ca_{CL} \ln\left(\frac{d}{\alpha\lambda}\right) + Ca_{CL} Q_i + O(Ca_{CL}^2). \tag{2.15}$$

The constant $\alpha = O(1)$ represents effects of the inviscid subregion on the viscous subregion. Sui and Spelt (2013a) suggested that $Re^* = O(1)$ and found good agreement with experimental benchmark by setting a Reynolds number $Re^* = 0.37$ for rapid droplet spreading. The interface slope θ^* in the matching transitional zone is obtained from the viscous regime equation:

$$g(\theta^*, r_\mu) = g(\theta_w, r_\mu) + Ca_{CL} \ln\left(\frac{d^*}{\lambda}\right) + Ca_{CL} Q_i + O(Ca_{CL}^2). \tag{2.16}$$

The interface slope θ_d in the inviscid subregion at a distance $d > d^*$ to the contact line reads

$$g_{iv}(\theta_d) - g_{iv}(\theta^*) = Ca_{CL}\left(h_{iv}(\theta_d) - h_{iv}(\theta^*) + \ln\left(\frac{d}{d^*}\right)\right) + O(Ca_{CL}^2), \tag{2.17}$$

with

$$h_{iv}(\theta) = -2\ln\left(\sin\frac{\theta}{2}\right) + 2\int_{\pi}^{\theta} \frac{x}{1-\cos x} dx, \tag{2.18}$$

and

$$g_{iv}(\theta) = 1.53161(\theta - \sin\theta). \tag{2.19}$$

Practically, one first assumes that the first grid cell next to the wall is in the viscous subregion and calculates the boundary angle θ_d from (2.11) before checking $d < d^*$, where d and d^* are obtained from (2.13) and (2.14), respectively. If $d > d^*$, then the interface slope θ^* in the matching transitional zone needs to be calculated from (2.16) and the boundary angle θ_d in the inviscid subregion is calculated from (2.17)–(2.19).

On the validity of macroscale models

In the above macroscale models for viscous and inertial regimes, gravity is not accounted for. It is therefore assumed that gravity effects are negligible compared to capillary effects, i.e. for a small Bond number $Bo = \rho g L^2/\sigma$, where L is the macroscale. For a gas-liquid flow with a 500-µm water film, $Bo = 0.03$. Thus, for the work in this thesis, the intermediate region is not sensitive to gravity effects and the above macroscale model can be applied.

Another concern is the fact that the model of Cox (1986) was developed in two dimensions, and its validity in three dimensions is uncertain. It is true though that the theory of Cox (1986) agrees with the model of Hocking and Rivers (1982), the latter being for axisymmetric droplet spreading with very small viscosity ratio. It is possible to assess the significance of variation in the third dimension a posteriori: if one assumes the theory of Cox (1986, 1998) in three dimensions, then in the results obtained the magnitude in transverse variations (parallel to the substrate) of the interface slope should be small compared to the vertical variations (normal to the substrate), that is, in spherical coordinates (r, ω, φ),

$$\left|\frac{1}{r\sin\omega}\frac{\partial\theta}{\partial\varphi}\right| \ll \left|\frac{1}{r}\frac{\partial\theta}{\partial\omega}\right|. \tag{2.20}$$

Finally, models of Hocking and Rivers (1982) and that of Cox (1986) are for spreading on a planar substrate. For a sinusoidal substrate, with amplitude A_c and small corrugation λ_c, the interface profile in the intermediate region remains unchanged for $\epsilon L \ll \lambda_c$ and $\epsilon L \ll A_c$, which is the case of structured packing sheets.

Discussion

For simulating liquid film flows of 200 to 500 µm with moving contact lines, one may want to use a general macroscale model such as that of Cox (1986, 1998) described in Section 2.2.2. The dynamic boundary angle can be implemented with (2.11) or (2.17) to resolve the flow down to the intermediate region - which is quite large compared to the inner region. The methodology consists in starting calculations on a coarse computational grid and doing convergence tests. As the wavelength of small corrugations $\lambda_c = 2.8$ mm is large compared with the size of first-layer cells, these small corrugations shall not be numerically considered as pieces of roughness. All small corrugations should normally be taken into account in the computational domain geometry. Contact angle hysteresis may also have to be considered to account for pieces of roughness that are not visible, i.e. that are small compared with small corrugations. Hysteresis depends on the material of the substrate and fluid properties so its measurement shall be performed on a flat plate made of the same material, and using the same fluids. Practically, a simple model of hysteresis is to set the wall angle in the macroscale model equal to the advancing (resp. receding) angle for an advancing (resp. receding) contact line.

2.3 Conclusion

Existing experimental methods for liquid film thickness measurement have been reviewed and their applicability to observing liquid film flows over structured packing sheets have been discussed. The CCI technique has been selected as a non-intrusive single-point measurement technique for its high spatial resolution and the fact that it does not require any modification of the substrate geometry, nor the use of any additive substance to the liquid; curved gas-liquid interfaces may be problematic though, as with any other optical method.

For simulating flows with moving contact lines, the methodology consists in resolving the flow down to an intermediate scale while accounting for effects of smaller scales in the dynamic contact angle model. In particular, the angle (interface slope in the intermediate region) to impose as a boundary condition depends on the angle that the interface makes with the substrate in the inner region, the length scale of the inner region (the slip length), and the contact line speed. General macroscale models based on asymptotic theories of Cox (1986, 1998) for viscous and inertial regimes will be used here, keeping in mind that these were developed in two dimensions.

Chapter 3

Numerical simulations of two-phase flows in the level-set framework

Outline

The asymptotic theory of Cox (1986, 1998) provides moving contact line models for both viscous and inertial regimes. These can be implemented in two-phase flows solvers in order to account for contact line dynamics. The freeware TPLS (Two-Phase Level-Set) of Ó Náraigh et al. (2014) has been extended for the purpose. That is presented in the next chapter. But first, mass conservation errors, which are commonly encountered in level-set methods, have been analyzed and solutions have been proposed to remedy this problem.

3.1 Introduction

Level-set methods are widely used for the numerical simulation of two-phase flows (see for instance, Osher and Fedkiw (2006)). In these, as in other interface-capturing methods such as volume-of-fluid and diffuse-interface methods, interfaces are evolved through a scalar field that is defined throughout the domain (see Tryggvason et al. (2011) for an introduction). In level-set, the instantaneous interface is defined precisely, at a constant value (usually zero) of this scalar ’level-set’ function, which is continuous at interfaces. Level-set for interfaces in two-phase flows is used either in conjunction with a continuous surface tension formulation (see Sussman et al. (1994), for example), wherein the governing equations of motion for the fluids (with different fluid properties) are combined into one set, or a ghost-fluid approach, to account for interface conditions (Osher and Fedkiw, 2006). In the former, this is attractive because of ease of implementation and convenience for the representation of surface tension; in the latter, they provide the basis for prescribing interface conditions at a sharp interface.

For application in two-phase flows, the level-set function ϕ is generally chosen to be the signed distance to the interface (Sussman et al., 1994), as it is herein, although a smoothed Heaviside function has been proposed also (Olsson and Kreiss, 2005). That is, at any point in the flow, $|\phi|$ is equal to the distance to the nearest interface, and the sign of ϕ is different in each fluid, such that ϕ varies only gradually across an interface. An advantage of this is that the normal vector and curvature of an interface are readily obtained from ϕ.

The following evolution equation can be deduced from kinematical compatibility (see Section 1.10 in Pozrikidis (2011), for instance),

$$\frac{\partial \phi}{\partial t} + \mathbf{u} \cdot \nabla \phi = 0, \tag{3.1}$$

where $\mathbf{u}$ is a velocity field that for flow without phase change is simply the fluid velocity field; with phase change, it should be modified to account for the rate of phase change. The argument from kinematical compatibility is that (3.1) applies only at interfaces. Using it throughout the flow generally, which is commonly done, results in the level-set function ceasing to be a distance function, since the velocity field is a priori not uniform in the direction perpendicular to the interface.

For this reason, after having evolved the solution of the level-set function from (3.1) over one timestep, it is 'reinitialized' to verify the eikonal equation $|\nabla \phi| = 1$. Several methods have been developed for solving this equation, such as fast-marching methods (Sethian, 2001), fast-sweeping methods (Zhao, 2005) and reinitialization methods based on the iterative solve of a Hamilton-Jacobi equation (Sussman et al., 1994). The latter are of interest here because they are straightforward to implement and to parallelize. The Hamilton-Jacobi equation that is solved iteratively reads

$$\frac{\partial \psi}{\partial \tau} + \text{sign}(\psi)\big(|\nabla \psi| - 1\big) = 0, \tag{3.2}$$

subject to the initial condition that ψ is equal to the advected level-set function ϕ. After integration of ψ over pseudo time τ, the result is transferred to the level-set function ϕ.

A first concern with such methods is that the solution of (3.2) may move the zero level-set, leading to mass conservation issues, as the zero level-set should only move by the advection equation (3.1). Several methods, discussed in the next section, have been proposed in order to perform the redistancing (or reinitialization) by minimizing interface displacement, hence reducing interface distortion and improving mass conservation. Some authors already observed better reinitialization of the level-set function by using higher-order schemes for spatial or temporal discretization (du Chéné et al., 2008; Min, 2010). However, a comparison of different reinitialization methods has not been reported in the literature, and is the main first objective of this study, addressed in Section 3.3.1.

A second concern investigated herein is the performance of a two-phase flow solver in the absence of capillary forces and with only weak dissipation. It is established in Section 3.3.2 that Rayleigh-Taylor instability may, in some level-set methods, exhibit numerical distortion of the interface.

Finally, a well-known issue is the presence of parasitic currents around interfaces in two-phase flow simulations with a one-fluid formulation, not only in level-set (Scardovelli and Zaleski, 1999; Francois et al., 2006; Meland et al., 2007; Popinet, 2009; Abadie et al., 2015). These are due to numerical methods used to account for the pressure jump across the interface. A priori, the accuracy whereby interface curvature is determined may be improved by a better reinitialization of the level-set function, but it seems not to be known whether this significantly reduces parasitic currents. If curvature is less accurate, it seems more probable to get higher curvature gradients, hence parasitic currents of higher magnitude. Section 3.3.3 compares different reinitialization methods and aims to identify those, or the key elements of those that result in satisfactory mass conservation, reduced interface distortion (without surface tension) and reduced parasitic currents.

Discretization and reinitialization methods tested in this work are first presented in some detail. Results follow, notably for tests in three-dimensional systems, with a first series of tests for a translating sphere, without a Navier-Stokes solver. Some reinitialization methods, identified as mass-conservative, are then tested for Rayleigh-Taylor instability to check their ability of not giving rise to numerical distortion of the interface. Finally, parasitic currents are quantified for a static bubble and a translating bubble, to identify which reinitialization methods may lead to reduced parasitic currents.

3.2 Computational methods

The various methods used to solve the advection equation (3.1), the reinitialization (3.2), the coupling to the Navier-Stokes equations and the numerical method to resolve the latter, are presented below. The methods are presented for a uniform grid. Throughout the numerical approximation of the solution at time t_n and location (x_i, y_j, z_k) is denoted by a superscript ^{n} and subscript $_{i,j,k}$. The timestep is denoted by Δt, the uniform grid spacing by h.

3.2.1 Advection equation

The main purpose of solving the advection equation (3.1) is to accurately advect the level-set function in the vicinity of the interface. Equation (3.1) is discretized using high-order spatial and temporal discretization methods. The spatial discretization can be either using the non-conservative equation, or after rewriting (3.1) in conservative form first, for incompressible flows, upon using that the velocity field is divergence free. In either case, the pertinent version of a fifth-order weighted-essentially-non-oscillatory (WENO5) scheme is typically used. The results presented in this study were obtained with the conservative form of (3.1) and the WENO5 scheme of Jiang and Shu (1996) in space, summarized in Section A.1; the same WENO5 scheme can be used for the non-conservative form to directly compute $\nabla\phi$ at cell faces. For temporal discretization, a third-order Adams-Bashforth method is used (Butcher (2000); the second-order version is not recommended (Sengupta and Dipankar, 2004)) that gets a numerical approximation to the advection term A at time $n + \frac{1}{2}$ knowing its value at times n, $n-1$, $n-2$:

$$\frac{\phi^{n+1} - \phi^n}{\Delta t} = \tfrac{23}{12}A^n - \tfrac{4}{3}A^{n-1} + \tfrac{5}{12}A^{n-2}. \tag{3.3}$$

3.2.2 Temporal discretization of the reinitialization equation

Once the updated level-set function $\phi_{i,j,k}^{n+1}$ has been determined from the advection equation, this is used as the initialization for solving the Hamilton-Jacobi equation (3.2). We denote by $\psi_{i,j,k}^{m}$ the updated value at pseudo-time $\tau^m = m\Delta\tau$, where $\Delta\tau$ is the pseudo-time step, which is therefore subject to the initial condition $\psi_{i,j,k}^{0} = \phi_{i,j,k}^{n+1}$ obtained from the advection equation. After completion, the result is transferred back to $\phi_{i,j,k}^{n+1}$.

To assess the significance of the order used for the temporal discretization of the Hamilton-Jacobi equation (3.2), the following three temporal discretizations for that are tested: first-order forward Euler method (FE), total variation-diminishing second-order Runge-Kutta method (TVD RK2) and the latter's third-order counterpart (TVD RK3) (Shu and Osher, 1988). These are briefly recalled in Section A.2.

3.2.3 Spatial discretization of the reinitialization equation

Several discretizations of the second term in (3.2) (the numerical Hamiltonian) are tested in subsequent sections. These aim to amount to upwinding procedures such that information propagates away from the interface, whilst the level-set function is not modified in the direct vicinity of interfaces. These methods are recalled below. Reference is made to the set of cells Γ within a distance of one grid spacing from the zero level-set. This set is defined formally by considering all grid cells $\mathcal{C}_{i,j,k}$ in the computational domain Ω, and for each all neighboring cells $\mathcal{C}_{I,J,K}$,

$$\Gamma = \{\mathcal{C}_{i,j,k} \in \Omega : \min_{(I,J,K)\in v_{i,j,k}} (\psi_{i,j,k}^{0}\psi_{I,J,K}^{0}) < 0\}, \tag{3.4}$$

with

$$v_{i,j,k} = \{(i-1,j,k),(i+1,j,k),(i,j-1,k),(i,j+1,k),(i,j,k-1),(i,j,k+1)\}. \tag{3.5}$$

3.2.3.1 Method of Sussman et al. (1994) and fix of Russo and Smereka (2000)

The iterative procedure to solve the Hamilton-Jacobi equation reads here:

$$\psi_{i,j,k}^{m+1} = \begin{cases} \psi_{i,j,k}^{m} - \Delta\tau/h\big(\mathrm{sign}(\psi_{i,j,k}^{0})|\psi_{i,j,k}^{m}| - d_{i,j,k}\big) & \text{if } \mathcal{C}_{i,j,k} \in \Gamma, \\ \psi_{i,j,k}^{m} - \Delta\tau \mathrm{sign}(\psi_{i,j,k}^{0})\big(|G\psi_{i,j,k}^{m}| - 1\big) & \text{otherwise}, \end{cases} \tag{3.6}$$

where $G\psi$ is a numerical approximation of $\nabla\psi$, specified below. Just before starting the iterative procedure, the target distance for cells in the band of cells around the interface is determined as $d_{i,j,k} = \psi_{i,j,k}^{0}/|G\psi_{i,j,k}^{0}|$. Russo and Smereka (2000) proposed computing an approximation of the target distance by using the maximum change in $\psi_{i,j,k}^{0}$ in each direction:

$$d_{i,j,k} = h\frac{\psi_{i,j,k}^{0}}{\delta_{i,j,k}^{0}}, \tag{3.7}$$

with

$$\begin{aligned} \delta_{i,j,k}^{0} = \max\Big(&|\psi_{i,j,k}^{0} - \psi_{i-1,j,k}^{0}|, |\psi_{i+1,j,k}^{0} - \psi_{i,j,k}^{0}|, |\psi_{i,j,k}^{0} - \psi_{i,j-1,k}^{0}|, \\ &|\psi_{i,j+1,k}^{0} - \psi_{i,j,k}^{0}|, |\psi_{i,j,k}^{0} - \psi_{i,j,k-1}^{0}|, |\psi_{i,j,k+1}^{0} - \psi_{i,j,k}^{0}|, \\ &\sqrt{(\psi_{i+1,j,k}^{0} - \psi_{i-1,j,k}^{0})^2 + (\psi_{i,j+1,k}^{0} - \psi_{i,j-1,k}^{0})^2 + (\psi_{i,j,k+1}^{0} - \psi_{i,j,k-1}^{0})^2}\Big/2, \epsilon\Big), \end{aligned} \tag{3.8}$$

where $\epsilon \ll 1$ is set equal to h in this work. Outside the interfacial band ($\mathcal{C}_{i,j,k} \notin \Gamma$), Godunov's scheme selects the upwind derivative to compute $|G\psi^m|$, needed for use in (3.6):

$$|G\psi^m| = \begin{cases} \sqrt{\max(a_P^2, b_M^2) + \max(c_P^2, d_M^2) + \max(e_P^2, f_M^2)} \text{ if } \psi^0 \geq 0, \\ \sqrt{\max(a_M^2, b_P^2) + \max(c_M^2, d_P^2) + \max(e_M^2, f_P^2)} \text{ if } \psi^0 < 0, \end{cases} \tag{3.9}$$

with $\cdot_P = \max(\cdot, 0)$ and $\cdot_M = \min(\cdot, 0)$, $a = D_x^- \psi^m$, $b = D_x^+ \psi^m$, $c = D_y^- \psi^m$, $d = D_y^+ \psi^m$, $e = D_z^- \psi^m$, $f = D_z^+ \psi^m$.

A simple version of this method uses first-order upwinding for these one-sided derivatives. Without any special measures in the interfacial band, but replacing the sharp sign function by a smoothed version (specified below, see Equation (3.12)), the spatial discretization outlined above then corresponds to the original method of Sussman et al. (1994); the measures in the interfacial band, with first-order upwinding, is the basic version of the subcell fix proposed by Russo and Smereka (2000).

Russo and Smereka (2000) underlined that the basic version of their method can be extended to higher-order schemes, by using their original first-order subcell fix (3.7)–(3.8) but higher-order methods outside the interfacial band. In that approach, for a cell outside the interfacial band of grid cells the right-sided and left-sided derivatives of the level-set function can be obtained by using the optimal fifth-order WENO reconstruction of Jiang and Shu (1996), that was generalized to solve Hamilton-Jacobi equations by Jiang and Peng (2000). The fifth-order reconstruction is presented in Section A.3.

Higher-order subcell fixes can be constructed by using the interface position in the calculation of right-sided and left-sided derivatives (Min and Gibou, 2007; du Chéné et al., 2008). The method of Min and Gibou (2007) is based on ENO2 constructions, that of du Chéné et al. (2008) on a WENO5 scheme. Both methods use the interface position in the stencils selected for computing right-sided and left-sided derivatives. These methods were not tested here because their implementation has been found comparatively complex.

3.2.3.2 High-order constrained reinitialization of Hartmann et al. (2010)

This consists in adding a forcing term in the original form of the discretized reinitialization equation, to pin the zero level-set,

$$\frac{\psi^{m+1} - \psi^m}{\Delta\tau} + \text{sign}(\psi^0)\big(|G\psi^m| - 1\big) = \omega \delta_F^m F^m, \tag{3.10}$$

where ω is a weighting factor, which is set to 0.5, given the test results of Hartmann et al. (2010). The iterative procedure (3.10) advances by a predictor-corrector scheme, to determine the right-hand side term. At each pseudo-time step, the level-set function is first predicted at each grid cell in the entire domain with the original reinitialization equation,

$$\tilde{\psi}_{i,j,k}^{m+1} = \psi_{i,j,k}^m - \Delta\tau S_h(\psi_{i,j,k}^0)\big(|G\psi_{i,j,k}^m| - 1\big), \tag{3.11}$$

where S_h denotes the smoothed sign function,

$$S_h(\psi_{i,j,k}^0) = \frac{\psi_{i,j,k}^0}{\sqrt{(\psi_{i,j,k}^0)^2 + h^2}}. \tag{3.12}$$

Once the forcing term has been determined, as detailed below, the predicted level-set function $\tilde{\psi}$ is corrected at each cell in order to pin the zero level-set:

$$\psi^{m+1}_{i,j,k} = \tilde{\psi}^{m+1}_{i,j,k} + \Delta\tau\omega\delta_{F}{}^{m}_{i,j,k}F^{m}_{i,j,k}. \tag{3.13}$$

The forcing term is computed for cells in the interfacial band. The forcing term F^m is applied only at cells that keep the same neighbors across the interface during reinitialization (Hartmann et al., 2010), so that δ^m_F in (3.10) reads:

$$\delta_{F}{}^{m}_{i,j,k} = \begin{cases} 1 & \text{if } \tilde{\upsilon}^m_{i,j,k} = \tilde{\upsilon}^0_{i,j,k}, \\ 0 & \text{otherwise,} \end{cases} \tag{3.14}$$

with

$$\tilde{\upsilon}^m_{i,j,k} = \{(I,J,K) \in \upsilon_{i,j,k} : \psi^m_{i,j,k}\psi^m_{I,J,K} < 0\}, \tag{3.15}$$

and $\upsilon_{i,j,k}$ defined in (3.5). For the high-order constrained reinitialization HCR1 of Hartmann et al. (2010) the forcing term reads

$$^{1}F^{m}_{i,j,k} = \frac{1}{h}\left(-\psi^m_{i,j,k} + \frac{\psi^0_{i,j,k}}{N} \sum_{(I,J,K)\in\tilde{\upsilon}^0_{i,j,k}} \frac{\psi^m_{I,J,K}}{\psi^0_{I,J,K}} \right), \tag{3.16}$$

where N is the number of neighbors to $\mathcal{C}_{i,j,k}$ across the interface. For the high-order constrained reinitialization HCR2 of Hartmann et al. (2010) the forcing term is

$$^{2}F^{m}_{i,j,k} = \frac{1}{h}\left(-\psi^m_{i,j,k} + \left(\psi^0_{i,j,k}\Big/ \sum_{(I,J,K)\in\tilde{\upsilon}^0_{i,j,k}} \psi^0_{I,J,K}\right) \sum_{(I,J,K)\in\tilde{\upsilon}^0_{i,j,k}} \psi^m_{I,J,K} \right). \tag{3.17}$$

The optimal fifth-order WENO reconstruction of Jiang and Peng (2000) and Godunov's method are used in $|G\psi^m|$ as discussed in the preceding subsection.

3.2.3.3 Interface-preserving algorithm of Sussman and Fatemi (1999)

This method also uses a source term in the Hamilton-Jacobi equation,

$$\frac{\partial\psi}{\partial\tau} + \operatorname{sign}(\psi)\big(|\nabla\psi| - 1\big) = \lambda\delta(\psi^0)|\nabla\psi^0|, \tag{3.18}$$

where the coefficient λ is selected such that the total volume of a fluid is not changed over any fixed volume of the two-phase flow. In discretized form,

$$\frac{\psi^{m+1} - \psi^m}{\Delta\tau} + \operatorname{sign}(\psi^0)\big(|G\psi^m| - 1\big) = \lambda\delta_h(\psi^0)|G\psi^0|, \tag{3.19}$$

where $\delta_h(\psi) = H'_h(\psi)$ is the smoothed delta function and use is made of the smoothed Heaviside function,

$$H_h(\psi) = \begin{cases} 0 & \text{if } \psi \le -h, \\ \frac{1}{2}\left(1 + \frac{\psi}{h} + \frac{1}{\pi}\sin\left(\frac{\pi}{h}\psi\right)\right) & \text{if } |\psi| < h, \\ 1 & \text{if } \psi \ge h; \end{cases} \tag{3.20}$$

λ, which is not constant during the reinitialization, is specified below. Equation (3.19) can be solved iteratively with a predictor-corrector scheme. At each pseudo-time step, the level-set function at any point in the domain is first predicted from the original reinitialization equation,

$$\tilde{\psi}^{m+1}_{i,j,k} = \psi^m_{i,j,k} - \Delta\tau\big(2H_h(\psi^0_{i,j,k}) - 1\big)\big(|G\psi^m_{i,j,k}| - 1\big), \tag{3.21}$$

and then corrected, for cells in the interfacial band, to preserve the interface shape,

$$\psi^{m+1}_{i,j,k} = \tilde{\psi}^{m+1}_{i,j,k} + \Delta\tau\lambda_{i,j,k}\delta_h(\psi^0_{i,j,k})|G\psi^0_{i,j,k}|, \tag{3.22}$$

with a correction factor that reads

$$\lambda_{i,j,k} = -\frac{\int_{\mathcal{C}_{i,j,k}} \delta_h(\psi^0)(\tilde{\psi}^{m+1} - \psi^0)/\Delta\tau}{\int_{\mathcal{C}_{i,j,k}} \delta_h^2(\psi^0)|G\psi^0|}. \tag{3.23}$$

Integration over a cell $\mathcal{C}_{i,j,k}$ centered at (x_i, y_j, z_k) can be done with a 27-point stencil:

$$\int_{\mathcal{C}_{i,j,k}} f = \frac{h^3}{78}\left(52 f_{i,j,k} + \sum_{l=-1}^{1}\sum_{m=-1}^{1}\sum_{n=-1}^{1} \alpha_{l,m,n} f_{i+l,j+m,k+n}\right), \tag{3.24}$$

where $\alpha_{l,m,n} = 0$ if $l = m = n = 0$, and $\alpha_{l,m,n} = 1$ otherwise.

In this work, $|G\psi^m_{i,j,k}|$ is calculated with the WENO5 reconstruction of Jiang and Peng (2000) and Godunov's method. $|G\psi^0_{i,j,k}|$ in the correction step (4.24) is computed by first-order upwinding along with Godunov's scheme.

3.2.4 Navier-Stokes solver

For each time step, after advection and reinitialization of the level-set function, a single set of Navier-Stokes equations is solved throughout the entire computational domain for incompressible flow,

$$\rho\left(\frac{\partial \mathbf{u}}{\partial t} + (\mathbf{u}\cdot\nabla)\mathbf{u}\right) = -\nabla p + \frac{1}{Re}\nabla\cdot\left(\mu\big(\nabla\mathbf{u} + (\nabla\mathbf{u})^T\big)\right) + \frac{1}{ReCa}\kappa\nabla H_\xi + \frac{1}{Fr}\rho\hat{\mathbf{g}}, \tag{3.25}$$

and

$$\nabla\cdot\mathbf{u} = 0, \tag{3.26}$$

wherein the smoothed Heaviside function (3.20) is used to approximate the change in density and viscosity across the interface:

$$\begin{aligned} \rho &= H_\xi + \frac{\rho_1}{\rho_0}(1 - H_\xi), \\ \mu &= H_\xi + \frac{\mu_1}{\mu_0}(1 - H_\xi). \end{aligned} \tag{3.27}$$

The smooth width ξ is here set equal to $1.5h$, $Re = \rho_0 LU/\mu_0$ is the Reynolds number that compares inertial effects to viscous effects, $Ca = \mu_0 U/\sigma$ is the capillary number that compares viscous effects to capillary effects, and $Fr = U^2/(gL)$ is the Froude number that compares inertial to gravitational effects; $\hat{\mathbf{g}}$ is the unit gravity vector. The curvature $\kappa = -\nabla\cdot(\nabla\phi/|\nabla\phi|)$ is computed as the divergence of the normal vector in this work. The continuum surface model of Brackbill et al. (1992) is used to account for the normal stress discontinuity across the interface. The last term in (3.25) is required in a single-fluid formulation to cancel out a singular contribution from the divergence of the stress, the normal stress being discontinuous across interfaces.

The system (3.25)-(3.26) is solved with a standard projection method (see, for instance, Tryggvason et al. (2011)), with a semi-implicit viscous solve of a Helmholtz equation for the temporary velocity, followed by the solve of a Poisson equation for the artificial pressure in order for $\mathbf{u}^{n+1}$ to satisfy (3.26). Details of the corresponding spatial and temporal discretization are given in the work of Ó Náraigh et al. (2014) and in Section A.4. The detailed spatial discretization of the surface tension term is postponed to Section 3.3.3 where parasitic currents are investigated.

Method	Spatial discretization	Temporal discretization
RS-RK2	First-order upwinding with fix of Russo and Smereka (2000)	TVD RK2
RS-W5-RK2	WENO5 scheme with fix of Russo and Smereka (2000)	TVD RK2
HCR1-W5-RK2	WENO5 scheme with fix HCR1 of Hartmann et al. (2010)	TVD RK2
HCR2-W5-RK2	WENO5 scheme with fix HCR2 of Hartmann et al. (2010)	TVD RK2
SF-W5-FE	WENO5 scheme with fix of Sussman and Fatemi (1999)	Forward Euler
SF-W5-RK2	WENO5 scheme with fix of Sussman and Fatemi (1999)	TVD RK2
W5-RK2	WENO5 scheme	TVD RK2
NR	–	–

Table 3.1: Reinitialization methods tested in this work.

3.3 Results and discussion

In this section, different combinations of spatial and temporal discretization schemes are tested for a translating sphere, without the Navier-Stokes solver, to investigate mass conservation of the level-set method on its own. Subsequently, the methods are tested for Rayleigh-Taylor instability without surface tension to observe whether higher-order methods allow reducing parasitic interfacial waves; all methods are compared both qualitatively and quantitatively. Finally, parasitic currents that arise when solving a static-bubble or a translating-bubble problem are reported.

For quantitative comparisons, use is made in the following of the mass $M(t)$ of one of the fluids at time t, that is determined approximately by integrating the smoothed Heaviside function over the computational domain:

$$M(t) = \frac{1}{L_x L_y L_z} \int_0^{L_x} \int_0^{L_y} \int_0^{L_z} H_\xi(\phi(x,y,z,t))dxdydz, \tag{3.28}$$

and the mass loss at time t is

$$\Delta(t) = 1 - M(t)/M(0). \tag{3.29}$$

The various methods presented in the preceding section are referred to using the acronyms RS-RK2, RS-W5-RK2, RS-W5-RK2, HCR1-W5-RK2, HCR2-W5-RK2, SF-W5-FE, SF-W5-RK2, W5-RK2 and NR, where RS, W5 and SF stands for the modified method of Russo and Smereka (2000), the WENO5 scheme of Jiang and Peng (2000) and the algorithm of Sussman and Fatemi (1999), respectively. The case W5-RK2 is just the original method (Sussman et al., 1994), with a smoothed signed function as (3.12). The case NR is without reinitialization. The different methods are summarized in Table 3.1.

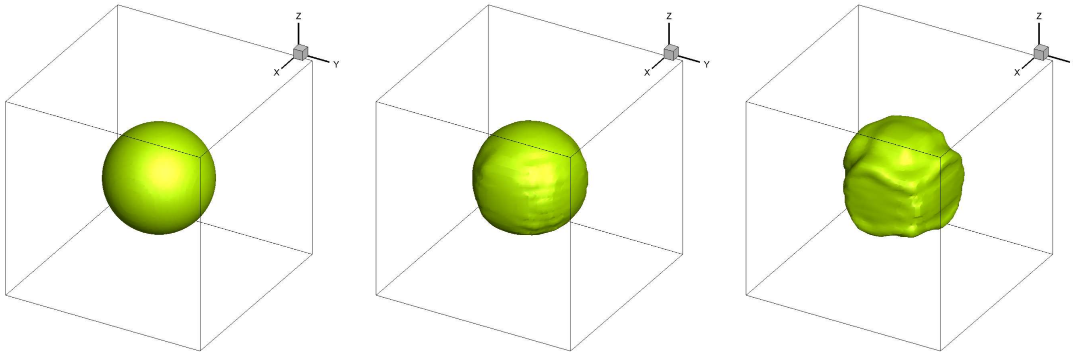

(a) $t^* = 0$ (b) $t^* = 2$ (c) $t^* = 10$

Figure 3.1: Time evolution of the interface shape with RS-RK2.

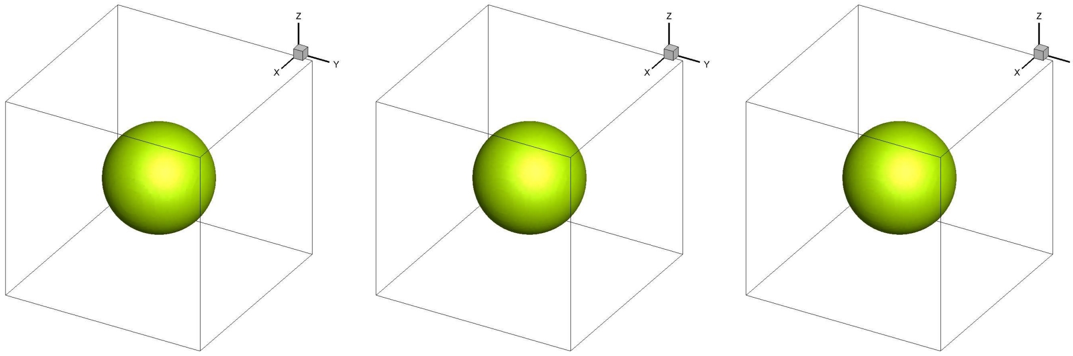

(a) $t^* = 0$ (b) $t^* = 2$ (c) $t^* = 10$

Figure 3.2: Time evolution of the interface shape with all methods using the WENO5 scheme.

3.3.1 Translating sphere

Reinitialization methods are tested first for a sphere that moves at constant velocity $(U, V, W) = (1, 0.5, 0)$. The computational domain is a cube of linear dimension $4R$, where R is the radius of the sphere; periodic boundaries are used in the first two directions, and wall boundaries for the remaining z-direction. The grid spacing is $h = R/15$. The Courant-Friedrichs-Lewy (CFL) number defined as $CFL_x = U\Delta t/h$ is set to 0.1. In all simulations, reinitialization is performed at each time-step with $N_{it} = 30$ iterations and a pseudo time-step $\Delta\tau = 0.3h$. The choice of these two parameters is discussed in Section 3.3.1.2. Eight methods are tested here: RS-RK2, RS-W5-RK2, HCR1-W5-RK2, HCR2-W5-RK2, SF-W5-FE, SF-W5-RK2, W5-RK2 and NR.

3.3.1.1 Qualitative results

Figure 3.1 presents the instantaneous shapes at times $t^* = (U/(8R))t$ obtained with RS-RK2. The interface exhibits oscillations at early times and is considerably affected at later times. Figure 3.2 presents instantaneous shapes obtained in all other methods (those that use a WENO5 scheme and NR), as no difference is qualitatively observed between them: the interface does not exhibit any unwanted pattern and still looks like a sphere at later times.

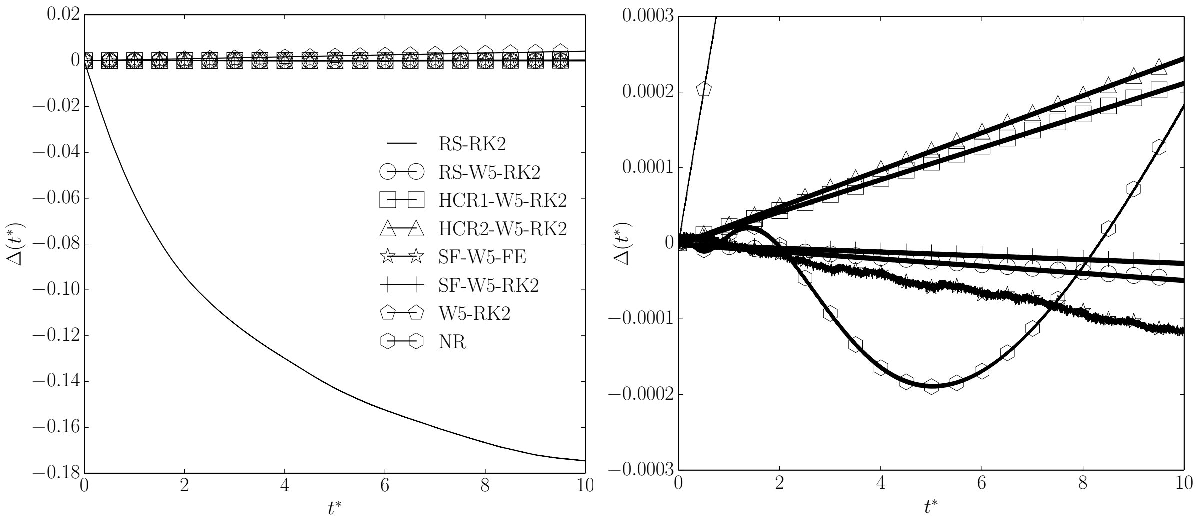

Figure 3.3: Mass loss Δ as a function of time $t^* = (U/(8R))t$. On the left-hand side, cases wherein the WENO5 scheme is used overlap (except for W5-RK2). A close-up view is thus presented on the right-hand side.

Method	Mass loss
RS-RK2	$-1.7 \cdot 10^{-1}$
RS-W5-RK2	$-5.2 \cdot 10^{-5}$
HCR1-W5-RK2	$2.1 \cdot 10^{-4}$
HCR2-W5-RK2	$2.4 \cdot 10^{-4}$
SF-W5-FE	$-1.2 \cdot 10^{-4}$
SF-W5-RK2	$-2.8 \cdot 10^{-5}$
W5-RK2	$4.1 \cdot 10^{-3}$
NR	$1.8 \cdot 10^{-4}$

Table 3.2: Mass loss for the translating sphere test; $t^* = 10$.

3.3.1.2 Quantitative results

Mass loss against time is presented in Figure 3.3, with a close-up view on cases that use the WENO5 scheme, for which mass conservation is considerably improved. Note that the method W5-RK2, for which there is no particular fix next to the interface, performs worse than other methods using the WENO5 and the case NR without reinitialization. A further comparison between all cases in the close-up view of Figure 3.3 shows that mass conserves better with the method SF-W5-RK2. The mass loss at $t^* = 10$ is presented in Table 3.2. As expected, higher-order temporal discretization methods performs better than a simple FE method. The method SF-W5-RK3 was tested but it did not yield further improvement in mass conservation. Effects of parameters N_{it} and $\Delta\tau$ on mass loss are presented in Table 3.3 for the method SF-W5-RK2. The results are converged for $N_{it} \geq 8$. Better results are obtained with $\Delta\tau = 0.3h$.

The effect of the timestep on mass loss is reported in Figure 3.4. The method SF-W5-RK2 yields better mass conservation when decreasing the timestep, in contrast with RS-W5-RK2, HCR1-W5-RK2 and HCR2-W5-RK2. This is due to the fact that the subcell fix of SF-W5-RK2 aims to preserve mass

N_{it}	Mass loss ($\Delta\tau = 0.15h$)	Mass loss ($\Delta\tau = 0.3h$)
1	$-4.2 \cdot 10^{-5}$	$-3.4 \cdot 10^{-5}$
2	$-3.9 \cdot 10^{-5}$	$-2.8 \cdot 10^{-5}$
4	$-3.6 \cdot 10^{-5}$	$-2.7 \cdot 10^{-5}$
8	$-3.6 \cdot 10^{-5}$	$-2.8 \cdot 10^{-5}$
16	$-3.6 \cdot 10^{-5}$	$-2.8 \cdot 10^{-5}$
30	$-3.6 \cdot 10^{-5}$	$-2.8 \cdot 10^{-5}$

Table 3.3: Effects of parameters N_{it} and $\Delta\tau$ with the method SF-W5-RK2 for the translating sphere test; $t^* = 10$.

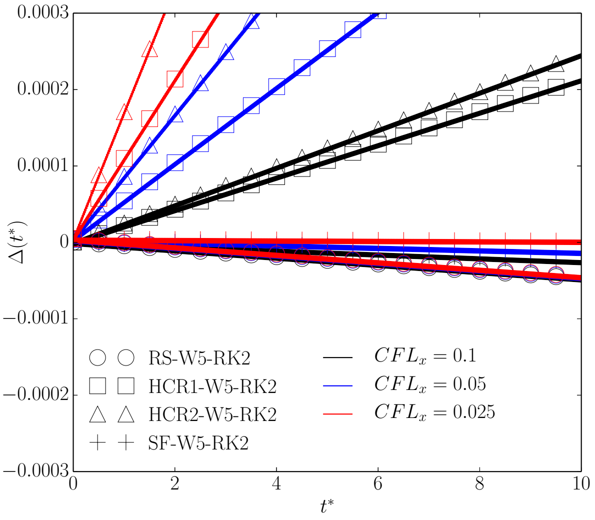

Figure 3.4: (Color online) Mass loss as a function of time for different timesteps.

explicitly, whereas the subcell fix of RS-W5-RK2 just makes use of a different stencil, and that of HCR1-W5-RK2 and HCR2-W5-RK2 is computed with an interpolation method, which does not guarantee mass conservation. When decreasing the timestep, the mass loss rate is nearly unchanged with RS-W5-RK2 but is increased with HCR1-W5-RK2 and HCR2-W5-RK2.

3.3.2 Rayleigh-Taylor instability

This classical benchmark test for two-phase flow solvers is used here to assess the performance of level-set methods coupled with a Navier-Stokes solver for two-phase flows with density contrast, but in the absence of surface tension; accounting for surface tension introduces its own difficulties, investigated in the next subsection. In this test, the interface is initially a cosine of small amplitude $y(x) = d\big(2+0.1\cos(2\pi x/d)\big)$, where d is the domain width and $4d$ is the domain height. No-slip is imposed at the bottom and top boundaries, and periodicity is imposed in the other direction. The density of the heaviest fluid is denoted by ρ_h, that of the lightest by ρ_l, and g denotes the gravitational acceleration, the viscosities are equal. Two parameters are mainly involved in Rayleigh-Taylor instability without viscosity contrast and without surface tension: the Atwood number $A = (\rho_h - \rho_l)/(\rho_h + \rho_l)$ and the Reynolds number $Re = \rho_h d\sqrt{gd}/\mu$. The case $(A, Re) = (0.5, 3000)$ was studied by Ding et al. (2007), following the early simulation at the same A value in the inviscid limit by Tryggvason (1988) and those by Guermond and Quartapelle (2000) which showed that at large Re the interface shape remained different from that inviscid result. In the present work, the uniform grid spacing is $h = d/192$ and the dimensionless time step, scaled by $(d/g)^{1/2}$, is set to $5 \cdot 10^{-4}$. Unlike the inviscid Rayleigh-Taylor instability, for which the linear theory predicts a growth rate proportional to the square root of the wavenumber (Rayleigh, 1883), accounting for viscosity induces damping, especially for large wavenumbers. From Menikoff et al. (1977), it can be deduced that in the case investigated here, the growth rate of the initial wave is about half that of the most unstable wavelength ($\lambda_m \simeq 0.1$ for the case investigated), and is more than 4 times larger than the growth rate of a wavelength of the size of the grid spacing used herein. Therefore, the linear theory predicts that small waves will not have time to grow and such a grid spacing should be sufficient to obtain converged results in terms of the amplitude of the perturbation (which has been verified for the case SF-W5-RK2, see Figure 3.6 below for qualitative results), allowing for quantitative comparison with prior work. In all simulations, reinitialization is performed at each time-step with $N_{it} = 30$ iterations and a pseudo timestep $\Delta\tau = 0.3h$. Effects of the parameter N_{it} on the results are presented in Section 3.3.2.2. Five methods are tested here: RS-RK2, RS-W5-RK2, RS-W5-RK3, HCR1-W5-RK2, and SF-W5-RK2.

3.3.2.1 Qualitative results

We first present in Figure 3.5 the results obtained with SF-W5-RK2, which compare very well with results of Guermond and Quartapelle (2000) (see their Figure 2, note their different definition for Re) and those of Ding et al. (2007) (see their Figure 6). Effects of the grid spacing are shown in Figure 3.6: results are converged for the grid spacing $h = 1/192$ used herein. In the results obtained with RS-RK2 (Figure 3.7), oscillations were observed at the interface, primarily at the descending tip at later times. These are not observed in prior work cited above for this case. With higher-order spatial discretization of the reinitialization step, RS-W5-RK2, these oscillations are seen in Figure 3.8 to be reduced, but the interface still exhibits large waves at later times along the sides of the descending heavy fluid, which is also not observed in prior work. The use of a higher-order temporal discretization scheme, RS-W5-RK3, is seen to result in only little difference (compare Figure 3.9 with Figure 3.8 for RS-W5-RK2). But with HCR1-W5-RK2 (Figure 3.10) and SF-W5-RK2 (Figure 3.5), the interfacial waves are absent altogether. These results suggest that it is the first-order fix of the algorithm of Russo and Smereka (2000) that gives rise to parasitic oscillations; this may be due to the fact that a one-dimensional stencil may often be used for the computation of the target distance in (3.7)–(3.8), whereas the subcell fix of the method of Sussman and Fatemi (1999) makes use of the integrated smoothed Heaviside function and that of Hartmann et al. (2010) is an interpolation method, which a priori accounts for multidimensionality.

3.3.2.2 Quantitative results

Mass loss, time signals of which are presented in Figure 3.11, is reduced with SF-W5-RK2, and even more so with HCR1-W5-RK2. Before $t = 2.25$, when the flow does not present any under-resolved structure, all methods yield good mass conservation, with a mass variation below 0.1%. Table 3.4 gives the mass loss at a later time. HCR1-W5-RK2 performs better than all other methods here. HCR1-W5-RK2 and SF-W5-RK2 are quantitatively compared against prior tests in Figure 3.12, where positions of the tip and the trough of the interface are given as a function of time. Good quantitative agreement is achieved against benchmark results. Note that Tryggvason (1988) used inviscid fluids, hence the differences observed in

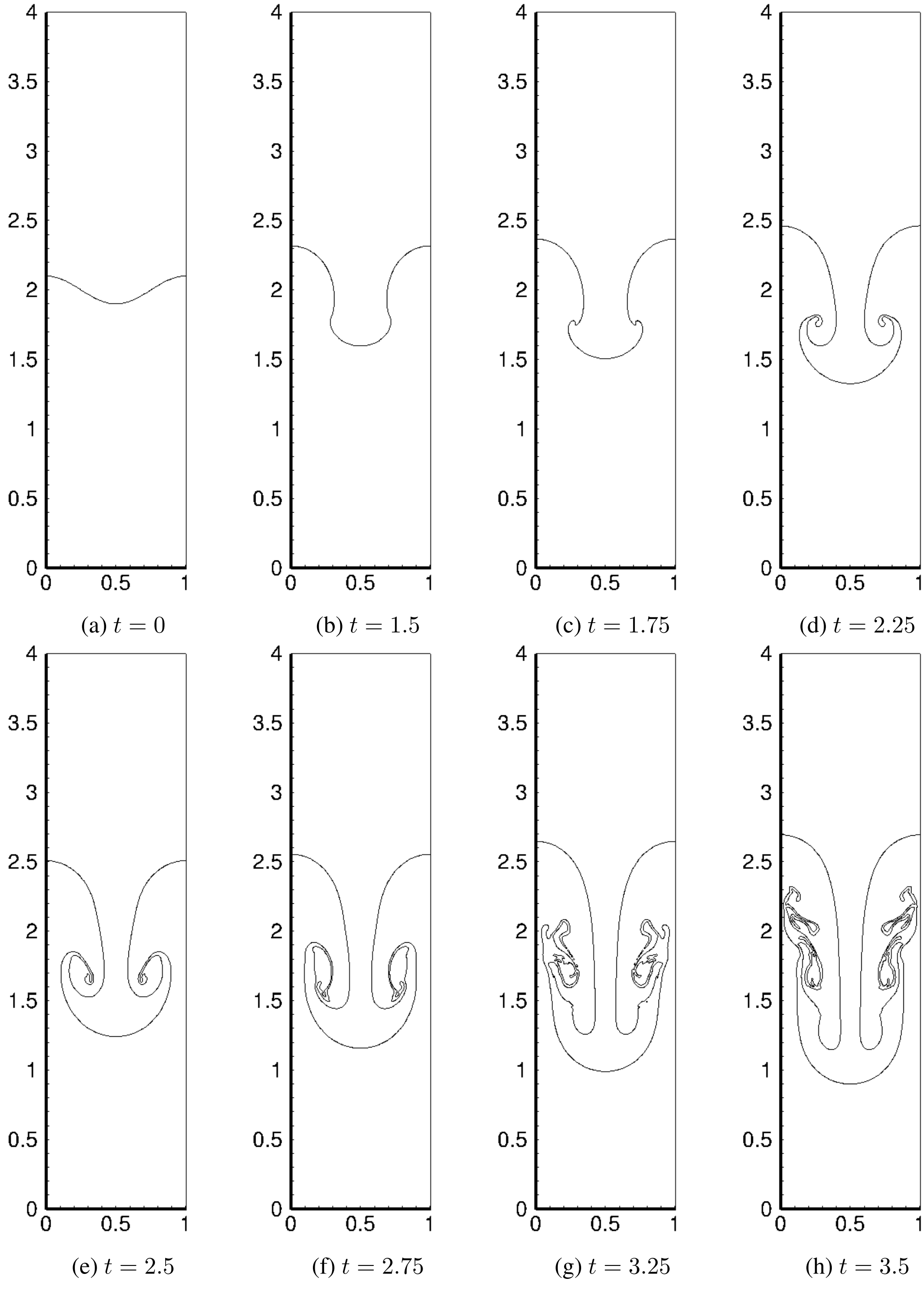

(a) $t = 0$ (b) $t = 1.5$ (c) $t = 1.75$ (d) $t = 2.25$

(e) $t = 2.5$ (f) $t = 2.75$ (g) $t = 3.25$ (h) $t = 3.5$

Figure 3.5: Instantaneous shapes with SF-W5-RK2 for Rayleigh-Taylor instability.

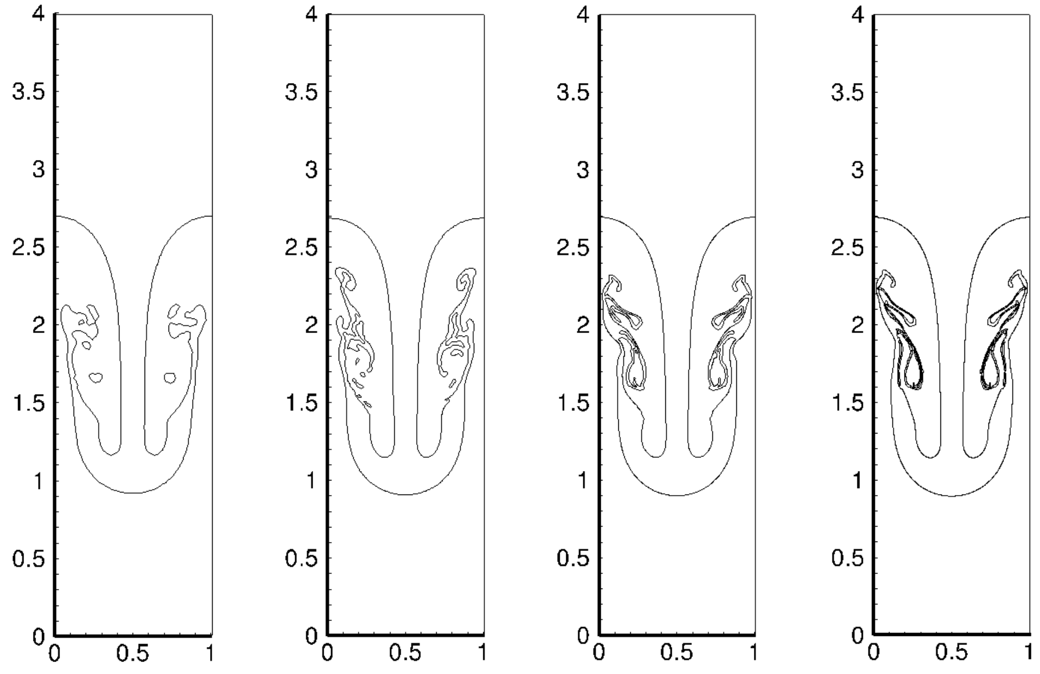

(a) $h = 1/48$ (b) $h = 1/96$ (c) $h = 1/192$ (d) $h = 1/384$

Figure 3.6: Dependence of the shape on the grid spacing with SF-W5-RK2 for Rayleigh-Taylor instability; $t = 3.5$.

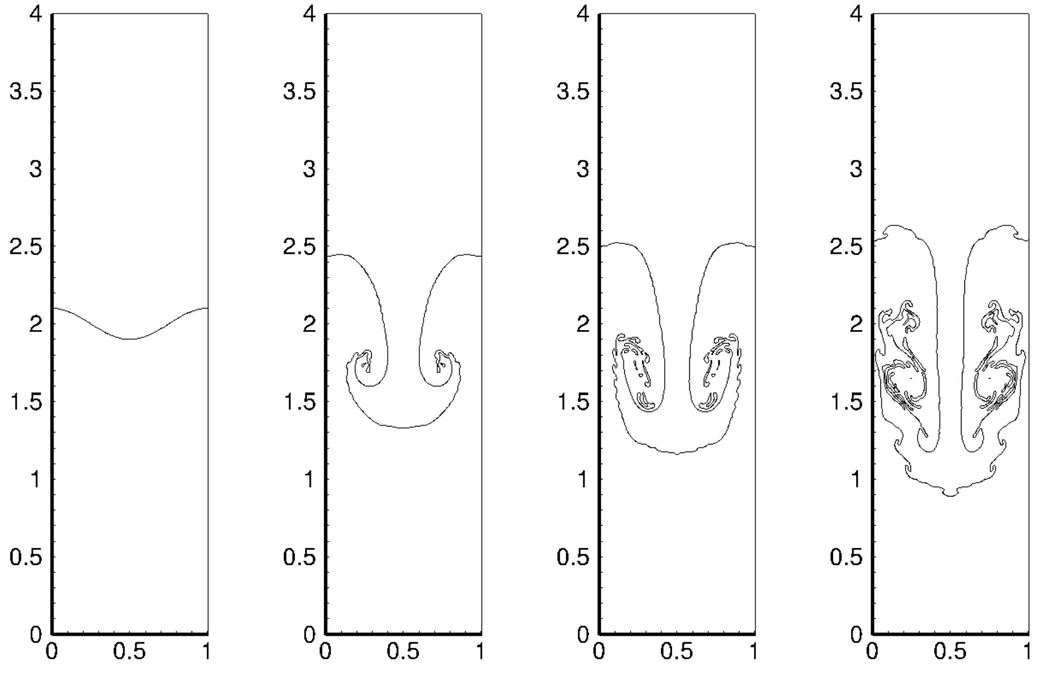

(a) $t = 0$ (b) $t = 2.25$ (c) $t = 2.75$ (d) $t = 3.5$

Figure 3.7: Instantaneous shapes with RS-RK2 for Rayleigh-Taylor instability.

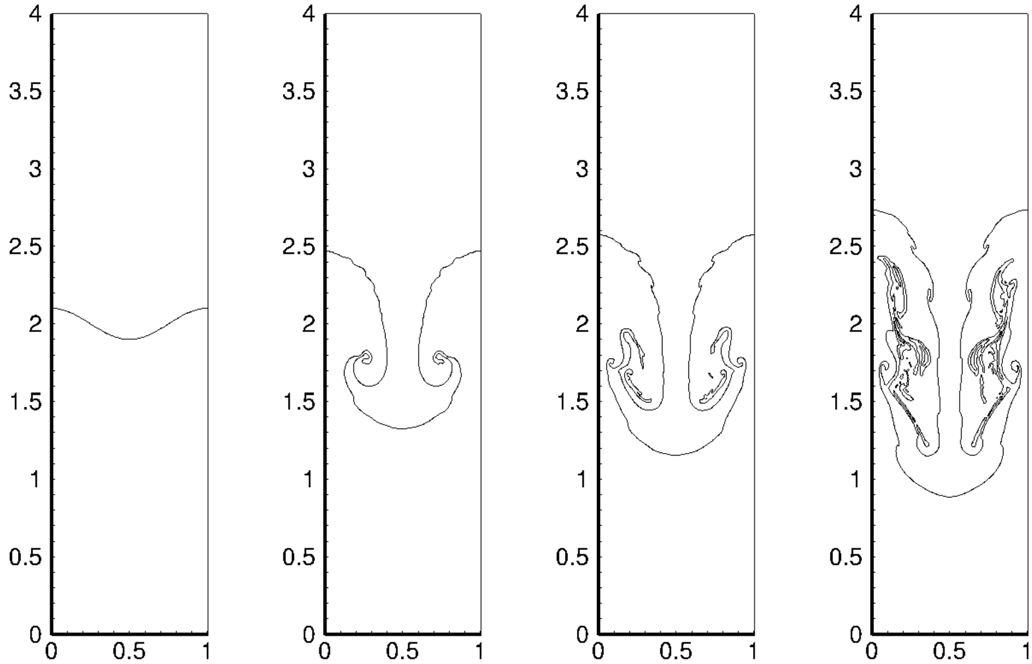

(a) $t = 0$ (b) $t = 2.25$ (c) $t = 2.75$ (d) $t = 3.5$

Figure 3.8: Instantaneous shapes with RS-W5-RK2 for Rayleigh-Taylor instability.

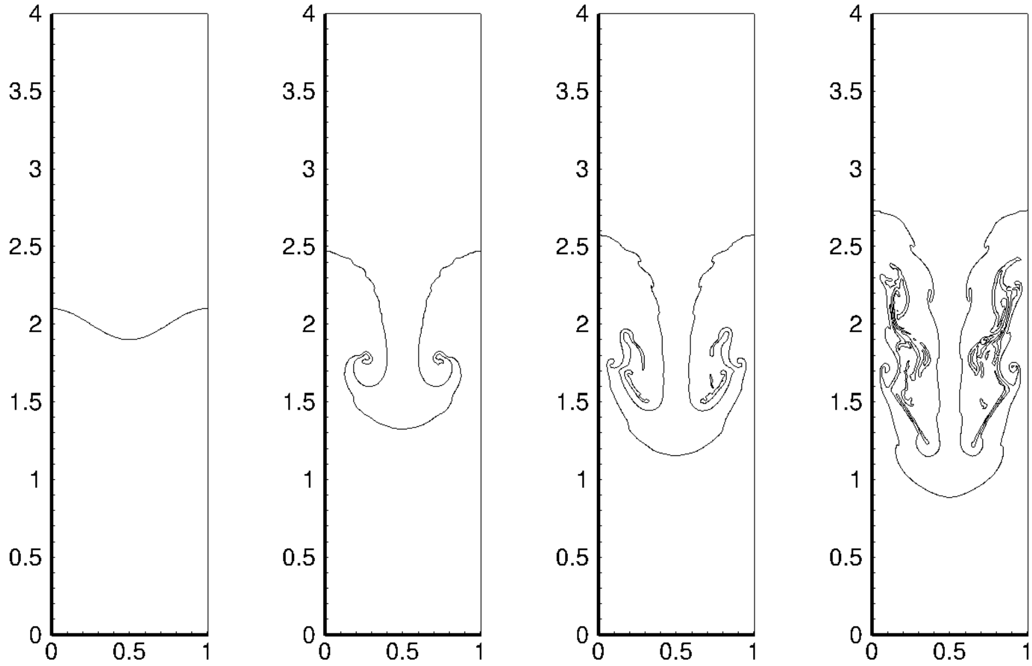

(a) $t = 0$ (b) $t = 2.25$ (c) $t = 2.75$ (d) $t = 3.5$

Figure 3.9: Instantaneous shapes with RS-W5-RK3 for Rayleigh-Taylor instability.

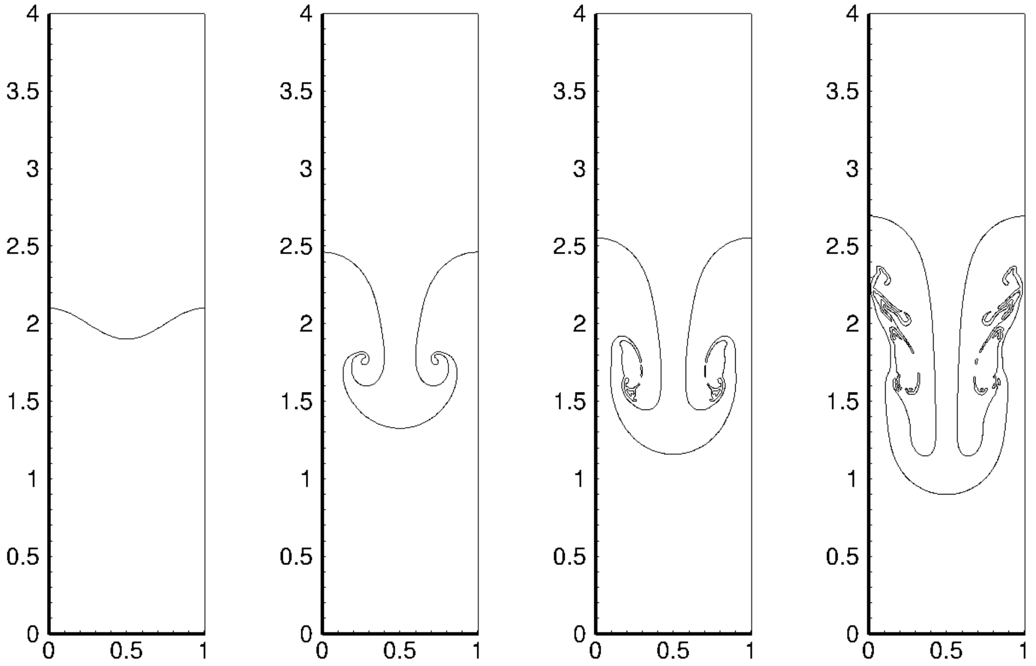

(a) $t = 0$ (b) $t = 2.25$ (c) $t = 2.75$ (d) $t = 3.5$

Figure 3.10: Instantaneous shapes with HCR1-W5-RK2 for Rayleigh-Taylor instability.

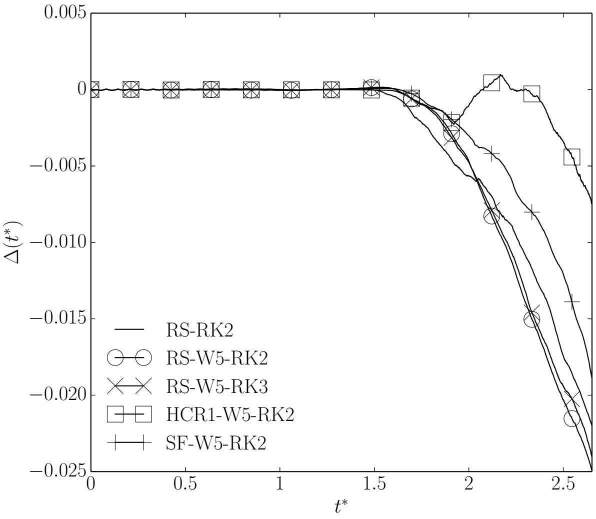

Figure 3.11: Mass loss Δ as a function of time $t^* = t\sqrt{A}$ for Rayleigh-Taylor instability.

this work, using a large but still finite Reynolds number. Note also that good quantitative agreement was obtained with all reinitialization methods here, but not qualitatively, as discussed above in Section 3.3.2.1. The effect of the parameter N_{it} was tested and no qualitative difference was observed in the results for $N_{it} \geq 1$. Quantitative effects of this parameter on mass loss and the amplitude of the perturbation are reported in Table 3.5. The results remain virtually unchanged for $N_{it} \geq 8$.

3.3.3 Parasitic currents

Final tests aim to identify which higher-order reinitialization method performs best in reducing the maximum magnitude of parasitic currents. These arise around interfaces when solving the Poisson

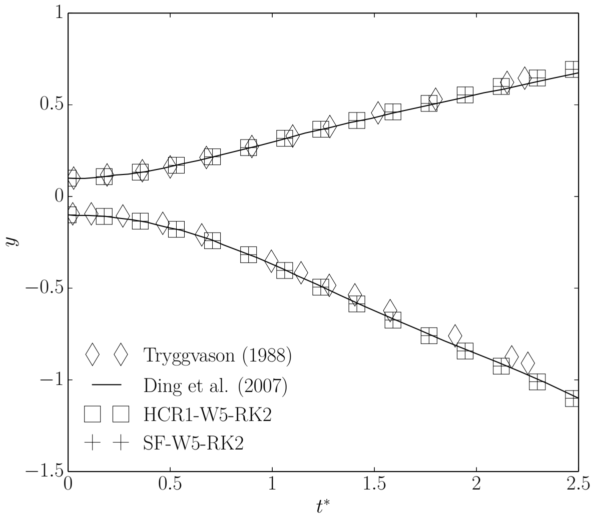

Figure 3.12: Position of the tip and the trough as a function of time $t^* = t\sqrt{A}$ for Rayleigh-Taylor instability.

Method	Mass loss
RS-RK2	$-1.6 \cdot 10^{-2}$
RS-W5-RK2	$-1.9 \cdot 10^{-2}$
RS-W5-RK3	$-1.9 \cdot 10^{-2}$
HCR1-W5-RK2	$-3.0 \cdot 10^{-3}$
SF-W5-RK2	$-1.1 \cdot 10^{-2}$

Table 3.4: Mass loss for Rayleigh-Taylor instability; $t = 3.5$.

N_{it}	Mass loss	Amplitude of the perturbation
1	$-1.3 \cdot 10^{-2}$	1.79235
2	$-1.2 \cdot 10^{-2}$	1.79334
4	$-1.2 \cdot 10^{-2}$	1.79381
8	$-1.1 \cdot 10^{-2}$	1.79396
16	$-1.1 \cdot 10^{-2}$	1.79414
30	$-1.1 \cdot 10^{-2}$	1.79394

Table 3.5: Effect of the parameter N_{it} with SF-W5-RK2 for Rayleigh-Taylor instability; $(\Delta\tau, t) = (0.3h, 3.5)$.

equation for the artificial pressure in the context of the projection method, whilst represents the normal stress discontinuity. Thus, parasitic currents are the result of inconsistent discretization of the normal to the interface with that of the pressure gradient and numerical errors in curvature computation (Renardy and Renardy, 2002; Francois et al., 2006; Meland et al., 2007; Popinet, 2009). The reader is referred to the recent work of Abadie et al. (2015) for further information on parasitic currents.

Capillarity is accounted for here using the Continuum Surface Force (CSF) model (Brackbill et al., 1992), that is, by a source term in the momentum equation (3.25), as recalled in the introduction. For the particular case of a static bubble, the artificial pressure is the solution of the Poisson equation

$$\nabla \cdot \left(\frac{1}{\rho} \nabla p \right) = \nabla \cdot \left(\frac{1}{ReCa} \frac{\kappa}{\rho} \nabla H_\xi \right). \tag{3.30}$$

Computing the capillary forces with the gradient of the smoothed Heaviside function rather than with the smoothed Dirac delta function has been shown to reduce the maximum magnitude of parasitic currents (Meland et al., 2007). In (3.30), a consistent discretization of the gradient of the smoothed Heaviside function with that of the pressure gradient yields, in 1D:

$$\frac{\dfrac{p_{i+1}-p_i}{\rho_{i+\frac{1}{2}}} - \dfrac{p_i-p_{i-1}}{\rho_{i-\frac{1}{2}}}}{\Delta x^2} = \frac{\dfrac{\kappa_{i+\frac{1}{2}}}{\rho_{i+\frac{1}{2}}}\big((H_\xi)_{i+1}-(H_\xi)_i\big) - \dfrac{\kappa_{i-\frac{1}{2}}}{\rho_{i-\frac{1}{2}}}\big((H_\xi)_i-(H_\xi)_{i-1}\big)}{ReCa\Delta x^2} \tag{3.31}$$

With such a consistent discretization, the maximum magnitude of parasitic currents is very small when imposing the exact curvature ($Ca_{\max} = 1.9 \cdot 10^{-14}$ with SF-W5-RK2 for the two-dimensional case of the static bubble, investigated below). Therefore, in any simulation, the only contribution to parasitic currents comes from the computation of the curvature $\kappa = -\nabla \cdot (\nabla\phi/|\nabla\phi|)$, discretized here as the divergence of the normal vector.

Two test cases are considered in this section, that are based on those that have been used extensively with other methods in prior work, in 2D, notably by Popinet (2009) and Abadie et al. (2015). 3D results are also presented in this work.

3.3.3.1 Static bubble

The first test is for a static bubble of diameter D at the center of a square domain (in 3D, discussed in this section, a cubic domain is used) of linear dimension $5D/2$ and no gravity. Unlike in previous work, not just one quarter of the domain is resolved, but the entire domain, thus symmetry across the bubble is not imposed. The upper and lower boundaries are symmetry boundaries, the left and right boundaries are periodic (in 3D, periodicity is also imposed in the third direction). The Laplace number that compares capillary with viscous forces is set to $La = \rho\sigma D/\mu^2 = 12000$, where σ is the surface tension; the density and viscosity are equal for both fluids. The grid spacing is set to $h = 5D/128$ and the timestep, scaled by the inertial capillary time $\sqrt{\rho D^3/\sigma}$, is set to 10^{-3}. In all simulations, reinitialization is performed at each time-step with $N_{it} = 30$ iterations and a pseudo time-step $\Delta\tau = 0.3h$. The effect of the parameter N_{it} on the results is discussed at the end of this section. Three methods are tested: RS-W5-RK2, HCR1-W5-RK2 and SF-W5-RK2. A typical pressure field obtained for a static bubble is shown in Figure 3.13. The error in the pressure jump is here within 0.3%. Despite a relatively good representation of the normal stress discontinuity, parasitic currents arise (Figure 3.14), with maximum magnitude very close to the interface. 2D and 3D quantitative results of maximum magnitude of parasitic currents and mass loss

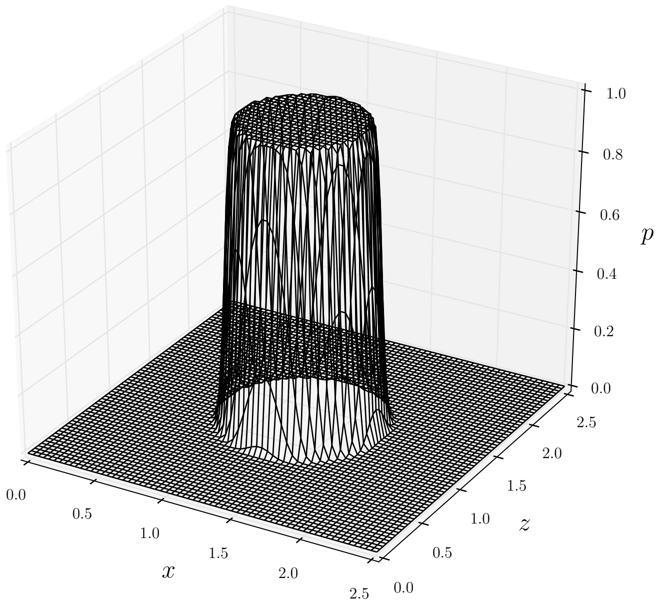

Figure 3.13: Pressure field for a 2D static bubble, normalized by $2\sigma/D$, obtained with the method SF-W5-RK2; $(La, t) = (12000, 30)$.

Method	$Ca_{\max}$	Mass loss
RS-W5-RK2 (2D)	$4.5 \cdot 10^{-5}$	$-9.7 \cdot 10^{-3}$
HCR1-W5-RK2 (2D)	$5.0 \cdot 10^{-5}$	$-3.4 \cdot 10^{-3}$
SF-W5-RK2 (2D)	$5.0 \cdot 10^{-5}$	$-2.3 \cdot 10^{-3}$
RS-W5-RK2 (3D)	$1.0 \cdot 10^{-4}$	$-4.3 \cdot 10^{-2}$
HCR1-W5-RK2 (3D)	$1.1 \cdot 10^{-4}$	$-2.2 \cdot 10^{-2}$
SF-W5-RK2 (3D)	$1.1 \cdot 10^{-4}$	$-2.2 \cdot 10^{-2}$

Table 3.6: Maximum magnitude of parasitic currents and mass loss for the static bubble; $(La, t) = (12000, 30)$.

are shown in Figure 3.15. The time signal of the maximum magnitude of parasitic currents exhibits discontinuities (which might be due to the use of the max operator in Equation (3.8)), while those obtained with HCR1-W5-RK2 and SF-W5-RK2 overlap and do not present discontinuities. SF-W5-RK2 performs better than HCR1-W5-RK2 in conserving mass, while mass conservation is worse with RS-W5-RK2. Results would look even worse with RS-RK2, so those are not presented here. Quantitative results at $t = 30$ are reported in Table 3.6. 2D results in terms of maximum magnitude of parasitic currents are very close to those obtained by (Abadie et al., 2015) with their methods LS-CCSF and LS-SSF (see their Figure 3). In 3D, it is now seen for this case, the maximum magnitude of parasitic currents is doubled and the mass gain increases nearly by an order of magnitude. Finally, the effect of the parameter N_{it} on mass loss is reported in Table 3.7 for the method SF-W5-RK2-3D; the parameter N_{it} has no effect on the maximum magnitude of parasitic currents for this case. The results are virtually unchanged for $N_{it} \geq 8$.

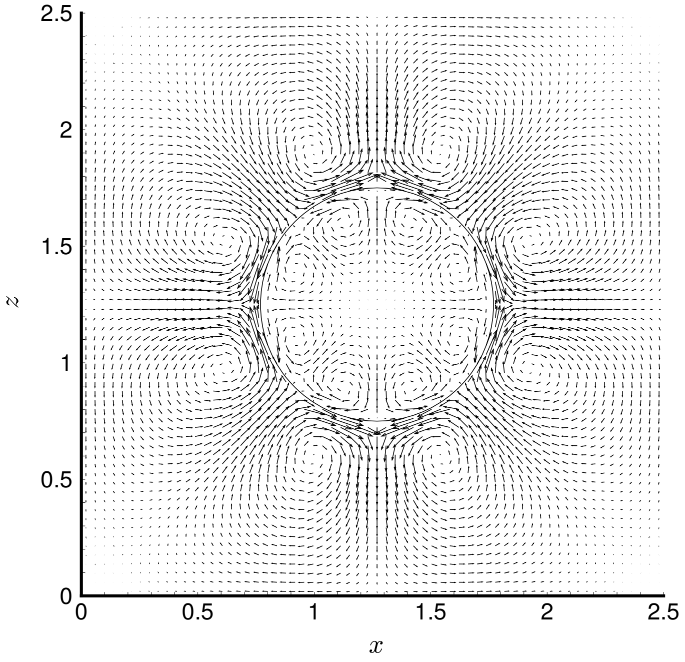

Figure 3.14: Velocity field for a 2D static bubble with SF-W5-RK2; $(La, t) = (12000, 30)$.

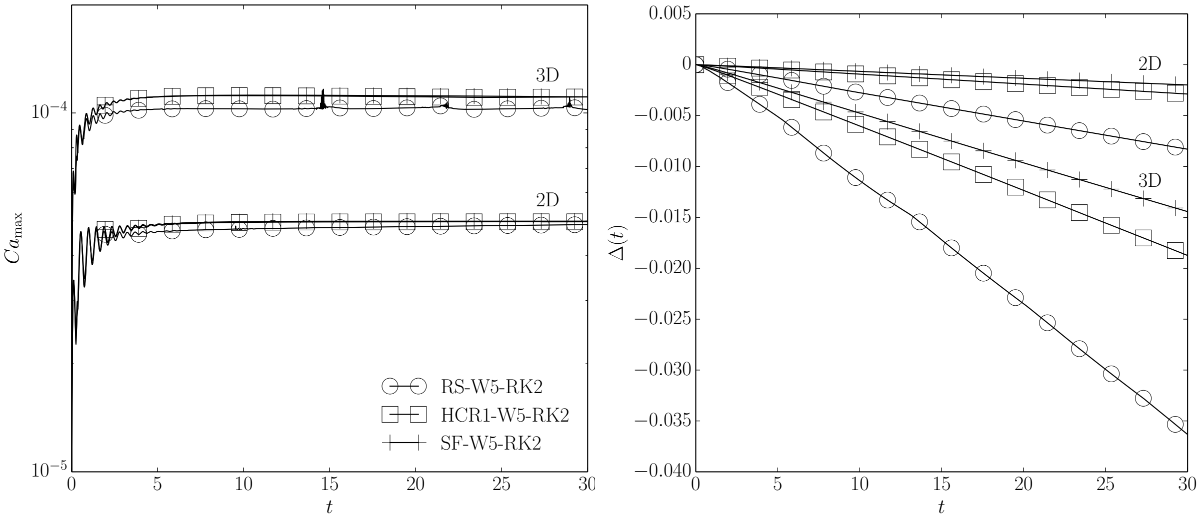

Figure 3.15: Capillary number $Ca_{\max}$ based on the maximum speed of parasitic currents and mass loss Δ and as a function of time for the static bubble; $La = 12000$.

N_{it}	Mass loss
1	-0.0152
2	-0.0159
4	-0.0165
8	-0.0168
16	-0.0168
30	-0.0168

Table 3.7: Effect of the parameter N_{it} for a 3D static bubble with the method SF-W5-RK2; $(La, t, \Delta\tau) = (12000, 30, 0.3h)$.

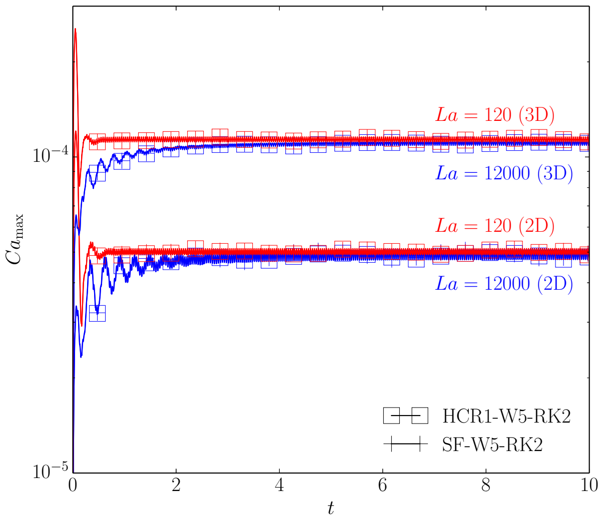

Figure 3.16: (Color online) Capillary number based on the maximum magnitude of parasitic currents as a function of time for the translating bubble.

3.3.3.2 Translating bubble

For the same setup a uniform initial velocity is now imposed in x-direction, U, to assess whether the performance of the methods is affected by that. Given the absence of walls this should persist. U introduces a further dimensionless group, for instance, a Weber number $We = \rho D U^2/\sigma$, which is set to 0.4 as in prior (2D) work (Popinet, 2009; Abadie et al., 2015); several values of La are tested. The timestep, here scaled by D/U, is set to $5 \cdot 10^{-4}$ for $La \in \{120, 1200, 12000\}$ and to $5 \cdot 10^{-5}$ for $La \in \{12, 24, 60\}$. Some 2D and 3D results are shown in Figure 3.16 for methods HCR1-W5-RK2 and SF-W5-RK2. The mass loss rate (not shown) quickly levels off as soon as the maximum magnitude of parasitic currents does, as for the static bubble. All results, in terms of maximum magnitude of parasitic currents and mass loss rate, in 2D and in 3D, are plotted against La in Figure 3.17. The values of the maximum magnitude of parasitic currents are akin to those obtained by Abadie et al. (2015). However, magnitudes have been found almost independent of the Laplace number within the range of investigation. In 3D, the parasitic velocities are increased by half an order of magnitude. Besides, the absolute value of mass loss rate is generally lower in 2D than in 3D (Figure 3.17), and reaches lower values for lower Laplace numbers with SF-W5-RK2. The mass loss rate with HCR1-W5-RK2 is way higher than with SF-W5-RK2 for $La \in \{12, 24, 60\}$. To investigate whether this is due to the fact that a smaller timestep was used for these Laplace numbers, further simulations were performed for $La = 120$, with both methods, to identify the effect of the timestep on the mass loss rate. Results are reported in Figure 3.18. The timestep has nearly no effect on the mass loss rate with SF-W5-RK2, whereas it increases when the timestep is reduced with HCR1-W5-RK2. That observation is consistent with results of the sensitivity study to the timestep done in Section 3.3.1.2.

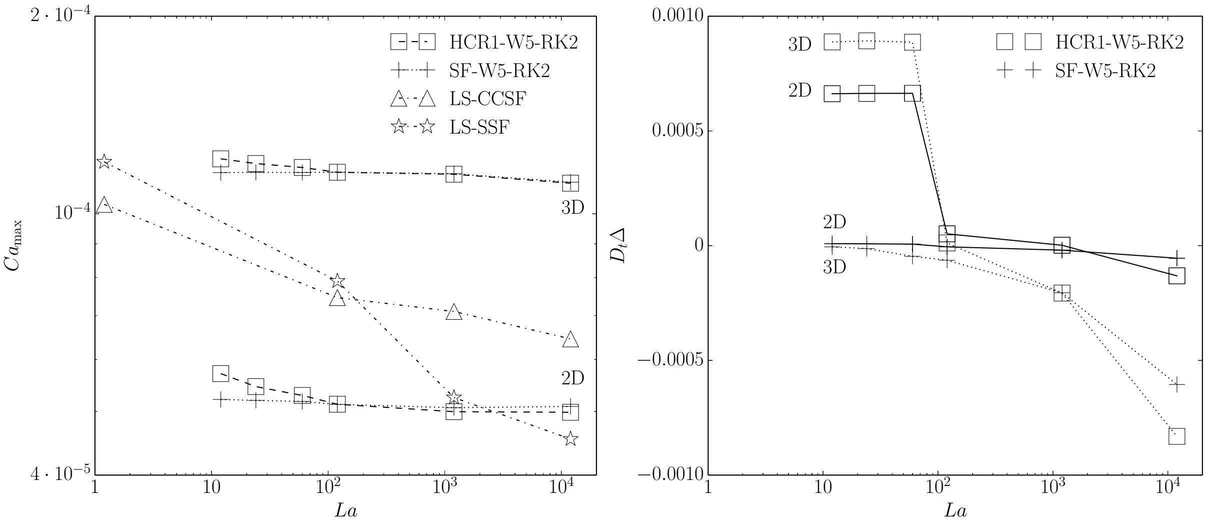

Figure 3.17: Capillary number based on the maximum speed of parasitic currents and mass loss rate as a function of the Laplace number for the translating bubble. Results with LS-CCSF and LS-SSF were obtained for a 2D translating bubble by Abadie et al. (2015).

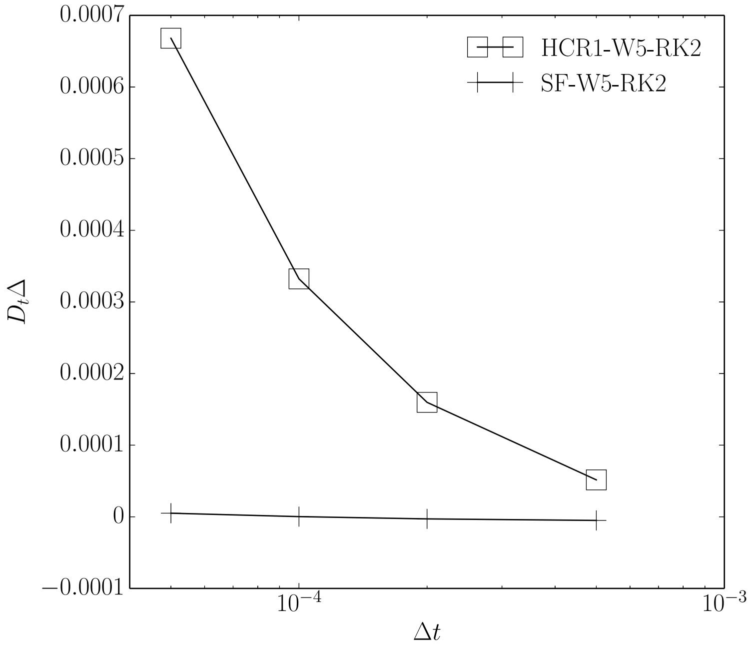

Figure 3.18: Dependence of the mass loss rate on the timestep for the 2D translating bubble; $La = 120$.

3.4 Conclusions

Different combinations for spatial and temporal discretization of the reinitialization equation have been tested for a translating sphere, Rayleigh-Taylor instability, and parasitic currents (static bubble and translating bubble). Several conclusions can be drawn from this work. For temporal discretization of the reinitialization equation:

- TVD RK2 improves mass conservation compared to first-order forward Euler.
- TVD RK3 does not result in further improvement in mass conservation.
- Mass conservation may be quantitatively affected by the timestep, depending on the method that is used for spatial discretization of the reinitialization equation.

For spatial discretization of the reinitialization equation:

- A high-order spatial discretization scheme is necessary to avoid mass loss and interface distortion. In all methods presented here, the combination of TVD RK2 for temporal discretization and WENO5 for spatial discretization has shown improvement in mass conservation.
- In absence of capillary forces, the modified algorithm of Russo and Smereka (2000), RS-W5-RK2, tested here yields parasitic interfacial waves in some solutions of the Navier-Stokes equations. Note that using higher-order subcell fixes, as proposed by du Chéné et al. (2008), may reduce these artificial oscillations. This was not tested here because implementation was found to be complex, and anticipate that the computational cost may be a concern, especially in 3D. No parasitic oscillations have been observed in the absence of surface tension for the high-order constrained reinitialization of Hartmann et al. (2010), HCR1-W5-RK2, nor for the method based on the interface-preserving algorithm of Sussman and Fatemi (1999), SF-W5-RK2.
- Regarding parasitic currents, it was found that a consistent discretization of the capillary force with that of the pressure gradient reduces the maximum magnitude of parasitic currents (as previously observed by Francois et al. (2006) using volume-of-fluid methods), and drastically improves mass conservation. The present tests have shown good agreement with prior (2D) work of Abadie et al. (2015). In 3D, the maximum magnitude of parasitic currents is increased by half an order of magnitude. There is nearly no mass loss due to parasitic currents with SF-W5-RK2, and even less when reducing the timestep, in contrast with HCR1-W5-RK2.

Finally, the predictor-corrector scheme of Sussman and Fatemi (1999) seems to be the most promising method here, when combined with TVD RK2 for temporal discretization and the optimal fifth-order WENO reconstruction for spatial discretization. Indeed, the method SF-W5-RK2 performs very well at conserving mass for a simple translation test on a coarse grid. The two methods, HCR1-W5-RK2 and SF-W5-RK2, have shown very good agreement with results of prior work on Rayleigh-Taylor instability, as well as on static-bubble and translating-bubble tests. In the end, two reinitialization methods that are straightforward to implement have been shown to pass several benchmark tests and are seen as very good candidates for accurate interface capturing with satisfactory mass conservation, with a preference for SF-W5-RK2 for which mass conservation is improved by decreasing the timestep, in contrast with HCR1-W5-RK2. The method SF-W5-RK2 was chosen for the rest of the thesis.

Chapter 4

Numerical simulation of two-phase flows with moving contact lines

Outline

The previous chapter focused on general problems encountered in level-set methods, especially mass conservation errors, that can be reduced with the method of Sussman and Fatemi (1999). Here, a new way of implementing (any) macroscale models in the level-set framework is presented. The method, fully detailed in this chapter, is validated for viscous and inertial droplet spreading. It also accounts for contact-angle hysteresis, and results are presented for three-dimensional flows of sliding drops.

4.1 Introduction

Many applications involve spreading and wetting phenomena, such as acid gas treatment with contacting devices, microfluidics, coating films, inkjet printing (Bonn et al., 2009). Any motion of the contact (or triple) line occurring therein poses several formidable challenges. Using a no-slip condition at the wall would result in a stress singularity in the vicinity of a moving contact line (Moffatt, 1964; Huh and Scriven, 1971). This has provoked consideration of the circumstances at a nanometer scale about a contact line and various models (slip, kinetic, precursor film and diffuse interface, amongst others) have been formulated for moving contact lines (for a review see Snoeijer and Andreotti (2013)). The main challenge for implementation in a computational method for two-phase flows, which is the main subject of this chapter, is that these models involve a large range of length scales: from the scale of, for instance, the size of a droplet, down to a length scale that is nanometric, in line with the original notion that different physical behavior mostly enters close to a contact line. Despite this different physical behavior occurring only at such a small scale, the flow behavior is affected also on a scale much larger than this nanometric region, and the interface is strongly curved accordingly, unless the capillary number based on the contact-line speed is very small. For instance, a slip model allows for the flow to slip at a nanometric scale, the slip length (Dussan V., 1979). During the spreading of a droplet of radius L, unless very slow, the flow and interface shape are affected significantly on a length scale $L/\ln(1/\lambda)$, where λL is the (dimensional) slip length (Hocking and Rivers, 1982; Cox, 1986): that is, over a region that is usually only an order of magnitude smaller than the drop size. Therefore, on the one hand, an ordinary discretization of a droplet without consideration of contact lines already enters such a scale, whereas on the other, simulations under realistic conditions wherein such flows are resolved down to a realistic slip length (or other small length scale) are not feasible, due to the disparity in length scales. It is therefore of interest to couple the computational method with analysis that represents the unresolved flow behavior. Such an approach is usually referred to as a large-scale (or macroscale) model (for a review see Sui et al. (2014)).

If no part of the contact-line region is resolved numerically at all, the above strategy suggests to impose a relation between an apparent contact angle and the contact-line speed (for example, see Spelt (2005); Fang et al. (2008)). Under these restrictions, no special measures are made to accommodate contact-line motion, the only effect of the physical behavior at smaller scales enters through this relation for an apparent angle. In other words, the flow corresponds to the solution for the 'outer region' in asymptotic analysis such as that of Cox (1986), at a scale much larger than the region affected significantly by the contact line. This introduces some difficulties. On the one hand, the resolution should remain coarse compared to the contact-line region (wherein the interface is curved), whereas on the other hand, the overall flow should be well resolved, which can over-restrict the possible numerical resolution. Furthermore, a suitable relation for the apparent angle would be needed, whereas no universally valid model is available for any flow in an outer region. For instance, Cox (1986) assumes that the far field (viewed from the contact line) corresponds to a wedge flow.

Beyond such a limited approach, the interface shape in any part of the contact-line region is required, for coupling with the computational method. For this purpose, prior asymptotic theory can be made use of. For example, the detailed theory of Cox (1986) (not just his result for a sole apparent contact angle) provides a first approximation of the interface slope as a function of the local distance to the contact line, the capillary number, the viscosity ratio, and the ratio of length scales, λ. The theory is discussed, with its extensions to higher order and accounting for inertial effects in the next section.

The formulation of such an approach for three-dimensional flows is here considered in the context of level-set methods, a specific class of interface-capturing methods for two-phase flows, that is presented below in Section 4.3.1. For an interface-capturing method based on finite volumes, one usually defines the scalar variable at cell centers. The approach set out above would amount to the following in this context. In practical applications part of the contact-line region will be resolved numerically. In this region, the interface is strongly curved, thus for a given grid spacing, the distance between the contact line and the center of grid cells adjacent to the substrate is first estimated. This distance can then be used in the theoretical relation between the interface slope at this distance and the contact-line speed, which is then imposed through either the slope of the interface at this first grid cell, or by the contact-line speed.

Several such large-scale methods coupled with hydrodynamic theories have been developed previously. In the level-set framework, Sui and Spelt (2013b) simulated axisymmetric droplet spreading both for viscous and inertial regimes. They validated their large-scale simulations against direct numerical simulations (DNS, wherein the entire flow is resolved) of droplet spreading in viscous regime performed by Sui and Spelt (2013a), and experiments of Ding et al. (2012) on droplet spreading with inertial effects. In their method, Sui and Spelt (2013b) imposed a contact angle boundary condition coupled with the contact line speed. The level-set function at the wall would be set in order to be consistent with the calculated contact line position. The extension to three dimensions is a priori not straightforward, as the coupling with the quasi-two-dimensional theory must be imposed along the direction of the contact-line speed, which is not aligned with the computational grid. Still in the level-set framework, Luo et al. (2016) recently proposed to impose the macroscale model through the curvature, their 2D level-set method has lead to good agreement with prior analytical, numerical and experimental results, but they have not presented 3D results. In the volume-of-fluid framework, Afkhami et al. (2009) developed a numerical contact angle model from the theory of Cox (1986), developing the important notion that the numerical angle to be imposed should depend on the size of the first grid cell next to the wall, but requiring as input an apparent contact angle value in the outer region in transient simulations. Using that same model, Dupont and Legendre (2010) simulated two-dimensional droplet spreading and droplet sliding. Later Maglio and Legendre (2014) performed three-dimensional volume-of-fluid simulations of sliding drops. They compared their numerical results against the experiment of Le Grand et al. (2005). They obtained good agreement regarding the onset of motion and they could simulate the different sliding regimes. However, their results lead them to believe that viscous forces were under-predicted in some cases for which they have not obtained good quantitative agreement for sliding speeds.

A level-set method is developed herein for the simulation of three-dimensional flows with moving contact lines, coupled with hydrodynamic theory, without having to resolve the flow down to the slip length, for regimes of contact-line motion that are either primarily viscous or with inertial effects in part of the contact-line region. Part of this work includes the removal of numerical problems that may arise near the wall boundary when solving the Hamilton-Jacobi equation in the redistance step. Della Rocca and Blanquart (2014) proposed a modified reinitialization equation for the first layer of cells above the substrate but they have not used a macroscale model. Another aspect concerns the theory of Cox (1986, 1998), that was developed in two dimensions, and its use in three dimensions remains uncertain. This work presents a numerical tool to investigate the possible use of macroscale models in three dimensions. Finally, this work is pioneering regarding three-dimensional flows with contact angle hysteresis in the level-set framework.

The problem is formulated in Section 4.2, wherein the macroscale models for both viscous and inertial regimes and the computational methodology to make use of these are summarized. The numerical methods for implementation of such models in the level-set framework is presented in Section 4.3. The code is validated against axisymmetric droplet spreading in both viscous and inertial regimes in Section 4.4, tested against the experiment of Ding et al. (2012) for droplet spreading in inertial regime, and against experiments of Podgorski et al. (2001) and Le Grand et al. (2005) for sliding droplets in viscous regime.

4.2 Problem formulation

In this section the overall formulation of the two-phase flow method without contact lines is first recalled. The contact-line model is presented subsequently: first for cases wherein contact-line motion is rather slow such that no inertial effects arise in the contact-line region; in the final subsection, the contact-line model for cases wherein inertial effects do enter the contact-line region is formulated.

4.2.1 Formulation for the bulk two-phase flow

Consider a three-dimensional flow of two fluids governed by the incompressible Navier-Stokes equations (4.1) and (4.2), without phase change. A single set of equations is used in dimensionless form: the momentum equation

$$\rho\left(\frac{\partial \mathbf{u}}{\partial t} + (\mathbf{u}\cdot\nabla)\mathbf{u}\right) = -\nabla p + \frac{1}{Re}\nabla\cdot\Big(\mu\big(\nabla\mathbf{u} + (\nabla\mathbf{u})^T\big)\Big) + \frac{1}{ReCa}\kappa\nabla H_\xi + \frac{Bo}{ReCa}\rho\hat{\mathbf{g}}, \qquad (4.1)$$

and the conservation of mass

$$\nabla\cdot\mathbf{u} = 0. \qquad (4.2)$$

These equations are accompanied by an interface-capturing technique to evolve interfaces, for which a level-set method is used, the presentation of which is deferred to Section 4.3.1. The dimensionless local density and viscosity are not constant but follow from the level-set function (see Section 4.3.1). The boundary conditions of each fluid at an interface with the other fluid, namely continuity of velocity, a discontinuity in normal stress due to surface tension, and continuity of tangential stress, can be shown to be satisfied by this formulation (Tryggvason et al., 2011). In particular, the jump in normal stress leads to a singularity in the first two terms of the right-hand side of (4.1) that is compensated by the third term, where κ is the interface curvature and H_ξ is the local volume fraction of one of the two fluids which is also inferred from the interface-capturing method. Precise definitions of these quantities derived from the level-set function are given in Section 4.3.1. In (4.1), the Reynolds number $Re = \rho_0 LU/\mu_0$ compares inertial to viscous effects, the capillary number $Ca = \mu_0 U/\sigma$ is the ratio of viscous to capillary forces, the Bond number $Bo = \rho_0 g L^2/\sigma$ compares gravity to capillary forces and $\hat{\mathbf{g}}$ denotes the unit gravity vector. The governing equations (4.1) and (4.2) are resolved in a rectangular domain. The bottom boundary is a planar solid boundary that is intersected by interfaces, the intersection lines being the contact lines. The contact-line models used and corresponding boundary conditions on the solid substrate are presented in the next subsections. The top boundary is also a planar solid boundary. The computational domain has periodic boundaries in the other two directions.

4.2.2 Theory for contact-line motion dominated by viscous/capillary effects

Cases wherein the Reynolds number based on the contact-line speed $Re_{CL} = LU_{CL}/\nu$ is small are considered first, regardless of which viscosity of the two fluids is used. The capillary number $Ca_{CL} =$

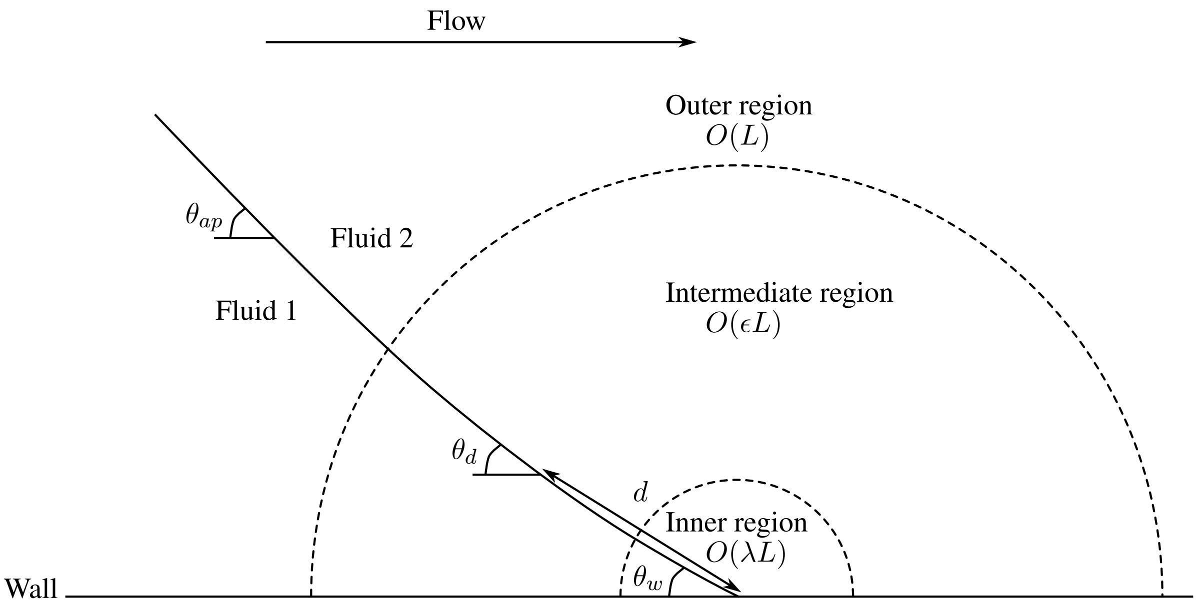

Figure 4.1: Angles and length scales involved in asymptotic theories of flows with moving contact lines. The curved solid line represents the interface.

$\mu U_{CL}/\sigma$ is assumed to be small also (again, for both viscosities), but not necessarily excessively so, as $Ca_{CL}|\ln\lambda|$ may be $O(1)$. Thus, capillary forces dominate viscous forces which dominate inertial forces. Gravity is assumed to be small compared to capillary forces. The theory summarized below has been demonstrated experimentally to be valid up to $Ca_{CL} \leq 0.1$ (Chen et al., 1995; Lavi and Marmur, 2004).

Classical analyses consider flows near contact lines at different length scales (e.g., Cox (1986)), see Figure 4.1. In an 'outer problem', the flow is analyzed at a typical linear dimension L that corresponds to that of the overall flow (such as a radius of a spreading droplet). At this scale, the flow is subject to the boundary conditions without contact lines (such as a no-slip condition). The theoretical problem is to formulate the angle that the interface makes with the substrate, the 'apparent angle' θ_{ap}. This involves matching to the solution of the 'inner problem', which is the flow considered at the small scale introduced by the contact-line model, denoted herein by λL. Here, λ shall be referred to as the dimensionless slip length, although the analysis of Cox (1986) is not necessarily restricted to this contact-line model. At this small scale, the actual contact angle θ_w applies at the contact line, which is often assumed equal to the static contact angle (Huh and Scriven, 1971). Some experimental results suggest that θ_w may depend on the contact-line speed (Ramé et al., 2004), for instance, a dependency on a capillary number based on the contact-line speed (Sheng and Zhou, 1992; Sui and Spelt, 2013b).

Viewed from the contact line, the solution of the inner problem applies up to a distance of $O(\lambda L)$ (the inner region), and that of the outer problem beyond a distance of $O(L)$ (the outer region). The matching between these regions is at an intermediate scale, $\epsilon = O(L/|\ln\lambda|)$, unless the contact-line speed is very small (e.g., Cox (1986)). In the original analyses, this is treated as a separate, 'intermediate region'; more recently this has been found to be an overlap region by Sibley et al. (2015) who identified this overlap by considering higher orders in Ca_{CL} for the interface slope solutions in the inner and outer regions. The predicted shape of the intermediate region has been confirmed experimentally by Ngan and Dussan V. (1989), Dussan V. et al. (1991), Shen and Ruth (1998), Ramé et al. (2004).

The interface shape predicted in the overlap (or intermediate) region is that of key interest here, as the outer region is resolved numerically, whereas the inner region is only resolved in DNS which is beyond the reach of computations for realistic systems. The asymptotic relationship between the local dynamic angle θ_d located at a distance d from the contact line in the overlap region and the actual contact angle θ_w is

$$g(\theta_d, r_\mu) = g(\theta_w, r_\mu) + Ca_{CL} \ln\left(\frac{d}{\lambda}\right) + Ca_{CL} Q_i + O(Ca_{CL}^2), \tag{4.3}$$

with

$$g(\theta, r_\mu) = \int\limits_0^\theta \frac{(x^2 - \sin^2 x)(\pi - x + \sin x \cos x) r_\mu + [(\pi - x)^2 - \sin^2 x](x - \sin x \cos x)}{2 \sin x [(x^2 - \sin^2 x) r_\mu^2 + 2(x(\pi - x) + \sin^2 x) r_\mu + (\pi - x)^2 - \sin^2 x]}. \tag{4.4}$$

The interface slope at a distance d from the contact line is therefore obtained from the implicit relation (4.3). The coefficient Q_i therein is often left out for simplicity if the slip length is not extremely small, but it may otherwise have an important quantitative effect (Sui and Spelt, 2013a). In principle, it depends on the viscosity ratio $r_\mu = \mu_2/\mu_1$, the contact angle θ_w in the inner region, the slip law that is used, and the flow geometry. For droplet spreading and dewetting, $Q_i - 1$ was tabulated by Hocking and Rivers (1982) for $r_\mu = 0$, corresponding to $Q_i(\alpha)$ in their Table 1. The determination of Q_i for other problems may necessitate comparison with experimental or DNS results, and/or a sensitivity test. An example of an application wherein this arises is presented in Section 4.4.3.

4.2.3 Theory for contact-line motion with inertial effects

Inertial effects first enter the contact-line region depicted in Figure 4.1 from the larger scales, upsetting the analysis outlined in the previous subsection, although not to the extreme extent that inertia would enter at the very small scale of the inner problem. Thus the case with $1 \ll Re_{CL} \ll \lambda^{-1}$ is considered, following one of the cases analyzed by Cox (1998). Capillary forces still dominate viscous forces: $Ca_{CL} \ll 1$. It is assumed that the boundary layer is laminar and no flow separation occurs and that the flow is quasi-steady. The overlap/intermediate region discussed in the previous subsection is now divided into a viscous subregion and an inviscid subregion. These match in a transitional zone located at a distance d^* from the contact line. Cox (1998) defined the corresponding Reynolds number Re^* such that

$$d^* = \frac{Re^*}{Re}. \tag{4.5}$$

The interface slope θ_d in the viscous subregion at a distance d from the contact line is still obtained from the viscous regime equation of Cox (1986), i.e., (4.3). Cox (1998) included a constant $O(1)$ in the argument of the logarithm (which could be absorbed in Q_i anyway), but reasonable results were obtained by Sui and Spelt (2013a) when setting this to unity, as it shall be done herein. Cox (1998) suggested that $Re^* = O(1)$ and Sui and Spelt (2013a) found good agreement with a benchmark test by setting $Re^* = 0.37$ for rapid droplet spreading. The interface slope θ^* in the matching transitional zone is obtained from the viscous regime equation:

$$g(\theta^*, r_\mu) = g(\theta_w, r_\mu) + Ca_{CL} \ln\left(\frac{d^*}{\lambda}\right) + Ca_{CL} Q_i + O(Ca_{CL}^2). \tag{4.6}$$

The interface slope θ_d in the inviscid subregion at a distance $d > d^*$ from the contact line reads:

$$g_{iv}(\theta_d) - g_{iv}(\theta^*) = Ca_{CL}\left(h_{iv}(\theta_d) - h_{iv}(\theta^*) + \ln\left(\frac{d}{d^*}\right)\right) + O(Ca_{CL}^2), \tag{4.7}$$

with

$$h_{iv}(\theta) = -2\ln\Big(\sin\frac{\theta}{2}\Big) + 2\int\limits_{\pi}^{\theta} \frac{x}{1-\cos x}dx \tag{4.8}$$

and

$$g_{iv}(\theta) = 1.53161(\theta - \sin\theta). \tag{4.9}$$

4.2.4 Outline of use of the above theories in large-scale computations

The computational method developed in the subsequent section aims to resolve numerically contact-line regions down to an intermediate scale (fully resolving at the inner scale (DNS) being too costly computationally). As set out in the next section, this requires from the theories summarized above the angle between the interface and the substrate at a distance from the contact line that corresponds to the smallest resolved scale (in the present approach, the first grid point at which the level-set function is adjacent to the substrate).

In the present approach, at any time, the resolved angle between interface and substrate θ_d and the corresponding distance from the contact line d are determined from the numerical simulation (i.e., the level-set function). The contact-line speed is obtained from substitution of these in the appropriate theoretical expression: first use (4.3), then calculate d^* from (4.5). If $d < d^*$, the first grid point is in the viscous subregion and the boundary angle θ_d is that obtained with (4.3). If $d > d^*$, then the interface slope θ^* in the matching transitional zone needs to be calculated from (4.6) and the boundary angle θ_d in the inviscid subregion is calculated from (4.7)–(4.9).

The approach outlined here supposes that prescription of the interface slope somewhere in an overlap/intermediate region suffices for the determination of the flow on a larger scale. Some evidence in support of this hypothesis is available. This is the approach underlying the asymptotic analyses, wherein the interface shape is matched between the various regions, and is a point discussed further by Kafka and Dussan V. (1979), who argue that the macroscopic flow is affected by inner dynamics through the interface slope in the overlap region. Thus, consistent with the analyses, the flow is resolved down to a point in the intermediate length scale by modeling effects of the inner region on the intermediate region from (4.3).

For a slip length $O(1\text{ nm})$, there is practically no change in the hydrodynamics of the outer region if the dynamic angle θ_d is being imposed at the distance from the contact line between $O(10\text{ nm})$ and $O(10\ \mu\text{m})$ (Kafka and Dussan V., 1979). Ngan and Dussan V. (1989) located the intermediate region at a distance from the contact line $O(10\ \mu\text{m})$. Further support for this approach is the good agreement obtained in prior work for axisymmetric flows Sui and Spelt (2013b). Beyond these arguments, the present work puts the above hypothesis to the test for three-dimensional flows.

4.3 Numerical method

4.3.1 The level-set method

The method is briefly recalled here; the reader is referred to the previous chapter for further details.

The level-set method (e.g., Sussman et al. (1994)) allows simulating two-phase flows with a one-fluid model. It consists in locating the interface with a signed distance function that is continuous. The level-set function is denoted by ϕ in this work. Let Ω^+ (resp. Ω^-) be the phase where the level-set function is positive (resp. negative). Any cell that is part of the domain $\Omega = \Omega^+ \cup \Omega^-$ is denoted by $\mathcal{C}_{i,j,k}$. The interface, located at the zero of the level-set function, moves with the fluid, which suggests that the evolution of the level-set function is given by the following advection equation:

$$\frac{\partial \phi}{\partial t} + \mathbf{u} \cdot \nabla \phi = 0. \tag{4.10}$$

A priori, the velocity field changes in the direction perpendicular to the interface, so the solution of this transport equation does generally not remain a distance function; for the level-set function, (4.10) only applies at interfaces. Using this transport equation in spite of this, then necessitates enforcing the condition $|\nabla \phi| = 1$ so that the level-set function is still a distance function. The Hamilton-Jacobi equation can be solved iteratively to maintain a distance function:

$$\frac{\partial \psi}{\partial \tau} + \mathrm{sign}(\psi)(|\nabla \psi| - 1) = 0. \tag{4.11}$$

with an initialization field $\psi^0 = \tilde{\phi}$ that is the scalar obtained from the advection equation (4.10). The level-set method suffers from mass conservation issues in some cases because of the redistance step that is usually carried out with the Hamilton-Jacobi equation (4.11). Several methods (Russo and Smereka, 2000; Sussman and Fatemi, 1999; Hartmann et al., 2010; Min and Gibou, 2007; du Chéné et al., 2008) have been developed in order to perform the redistancing by minimizing the displacement of the interface, hence improving mass conservation. Further details on the resolution of the Hamilton-Jacobi equation in general can be found in the previous chapter, and for flows with contact lines in the next subsection.

After the redistance step, the incompressible Navier-Stokes equations for Newtonian fluids without phase change are resolved. The one-fluid formulation of the Navier-Stokes equations given by (4.1) and (4.2) is used. The smoothed Heaviside function H_ξ is used to approximate the continuity of fluid properties at the interface by smoothing them over a length often taken as $\xi = 1.5h$, where h is the uniform isotropic grid spacing (Sussman et al., 1994). The smoothed Heaviside function reads:

$$H_\xi(\phi) = \begin{cases} 1 & \text{if } \phi > \xi, \\ \frac{1}{2}\left(1 + \frac{\phi}{\xi} + \frac{1}{\pi}\sin\left(\frac{\pi\phi}{\xi}\right)\right) & \text{if } |\phi| \leq \xi, \\ 0 & \text{if } \phi < -\xi, \end{cases} \tag{4.12}$$

Fluid properties are then calculated as:

$$\begin{aligned} \rho &= H_\xi + r_\rho(1 - H_\xi), \\ \mu &= H_\xi + r_\mu(1 - H_\xi), \end{aligned} \tag{4.13}$$

where r_ρ and r_μ denote density and viscosity ratios, respectively. The curvature κ is calculated accurately with the level-set function,

$$\kappa = -\nabla \cdot \left(\frac{\nabla \phi}{|\nabla \phi|}\right). \tag{4.14}$$

and is herein limited to $1/h$.

The flow solver is based on the Two-Phase Level-Set (TPLS) freeware of Ó Náraigh et al. (2014). The advection equation (4.10) is treated with the optimal fifth-order weighted essentially non-oscillatory (WENO5) reconstruction of Jiang and Shu (1996) in space and a third-order Adams-Bashforth method in time (Butcher, 2000). The Navier-Stokes equations (4.1) and (4.2) are solved with a standard projection method, wherein diffusive terms are treated with a Crank-Nicolson scheme and other terms are calculated with a third-order Adams-Bashforth method. Further details and comparisons of the computational method against analysis for other two-phase flow problems can be found in the work of Ó Náraigh et al. (2014) and in the previous chapter.

4.3.2 Contact angle implementation and redistancing

In this section it is proposed to use the level-set function for implementing the macroscale model, that is to say imposing a contact-line velocity that is consistent with the interface slope predicted by asymptotic theories. For the redistance step, the Hamilton-Jacobi equation (4.11) is discretized using an upwinding procedure so that information propagates away from the interface. Let $\mathcal{P}_k$ be the set of the cells located at $z = (k-1/2)\Delta z$ (Figure 4.2). Boundary conditions of the level-set function next to the wall are imposed by using a set of ghost cells $\mathcal{P}_0$, the wall being equidistant from planes $\mathcal{P}_0$ and $\mathcal{P}_1$. If the level-set function at ghost cells is updated at each pseudo-time step of the redistance step by extrapolation, some information goes to the substrate. In Figure 4.2, information should always go to the wall boundary for the acute side Ω^+ and should always go away from the wall boundary for the obtuse side Ω^-. Della Rocca and Blanquart (2014) emphasized the fact that extrapolation of the level-set function to the ghost cells leads to a numerical problem in the obtuse side. Indeed, in the obtuse side, some information goes to the wall boundary when the level-set function is extrapolated to the ghost cells $\mathcal{C}_{i,j,k} \in \mathcal{P}_0$ and some goes away from the wall at the next pseudo-time step of the redistance step as information is supposed to come from the interface according to the upwinding procedure. As a consequence, the level-set function eventually goes to zero next to the wall after a few time steps. In this case, the obtuse side is known as the blind spot. The main issue here is to populate the blind spot (Della Rocca and Blanquart, 2014), especially for three-dimensional flows.

In this work, a new algorithm is proposed to populate the blind spot avoiding the numerical problem mentioned above. As the contact line is part of the flow, the level-set function at ghost cells $\mathcal{C}_{i,j,k} \in \mathcal{P}_0$ should be advected by the flow rather than be obtained by extrapolation, the latter leading to a loss of information. The following algorithm is thus implemented:

Step 1

At all cells but the ghost cells, the level-set function is advected by using the advection equation (4.10). At ghost cells, it is advected by using another advection equation, wherein the macroscale model is used:

$$\frac{\partial \phi}{\partial t} + U_{CL}\hat{\mathbf{n}}_{CL} \cdot \nabla \phi = 0. \tag{4.15}$$

The direction of motion $\hat{\mathbf{n}}_{CL}$ is directly obtained from the level-set function,

$$\hat{\mathbf{n}}_{CL} = -\frac{\partial_x \phi \hat{\mathbf{e}}_x + \partial_y \phi \hat{\mathbf{e}}_y}{\sqrt{(\partial_x \phi)^2 + (\partial_y \phi)^2}}, \tag{4.16}$$

and the contact line speed is calculated from the macroscale model, knowing the interface slope θ at cells $\mathcal{C}_{i,j,k} \in \mathcal{P}_1$ from the level-set function,

$$\cos\theta = -\frac{\partial_z \phi}{|\nabla \phi|}. \tag{4.17}$$

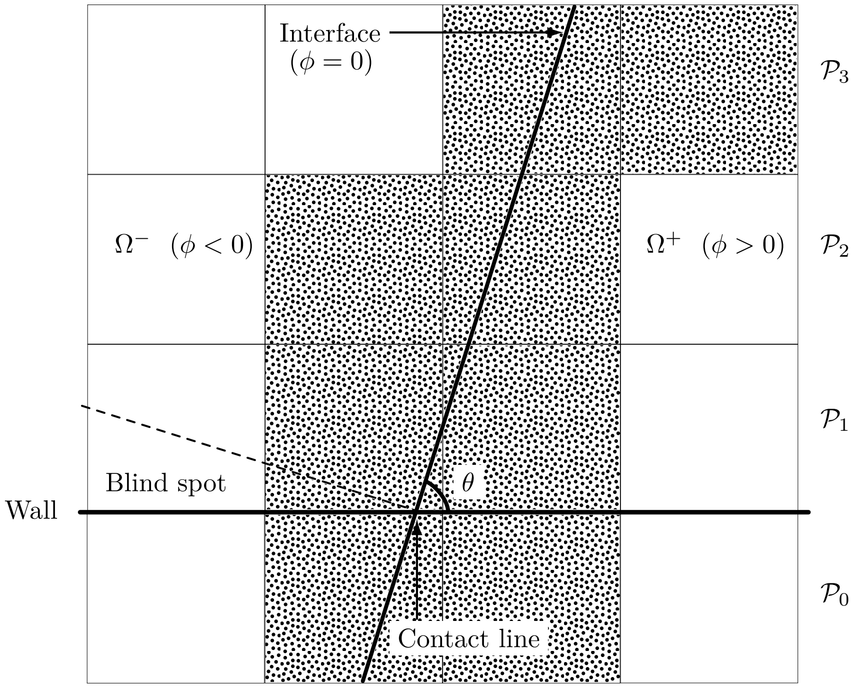

Figure 4.2: Illustration of the blind spot and definition of designations. Here, the obtuse side corresponds to Ω^- and the acute side corresponds to Ω^+. The blind spot is delimited by the wall and the dashed line. The ghost plane $\mathcal{P}_0$ is located at $z = -\Delta z/2$. The dotted cells that are within a distance of one grid spacing from the zero level-set are part of the set Γ.

Rather than using finite-difference centered schemes, though suitable here, it is preferred to approximate the gradient of the level-set function in (4.16) – (4.17) by computing the level-set function at cell corners, similarly to the computation of the mean curvature with the cell-based discrete divergence operator (Sussman et al., 1999). After that, the local slope θ is extended off the interface to all cells $\mathcal{C}_{i,j,k} \in \mathcal{P}_1$ by using the following equation:

$$\frac{\partial \theta}{\partial \tau} + \text{sign}(\phi) \frac{\nabla \phi}{|\nabla \phi|} \cdot \nabla \theta = 0. \tag{4.18}$$

In (4.18), $\nabla \theta$ is computed by first-order upwinding and the level-set normal is calculated with a second-order centered scheme. The pseudo time step $\Delta \tau$ is there set to $0.3h$. Extending the local slope off the interface has the key role of allowing for the ghost cells $\mathcal{C}_{i,j,k} \in \mathcal{P}_0$ to be given the value of the local slope at the interface. Such an extension method has notably been used in ghost-fluid methods (Fedkiw et al., 1999). The interface slope θ is then used to provide the contact line speed from the macroscale model by applying the method outlined in Section 4.2.4, which makes use of Equations (4.3)–(4.4) in the viscous regime or Equations (4.3)–(4.9) in the inertial regime, with a distance to the contact line d approximated as $h\big/\big(2\sin\big((\theta_d + \theta_w)/2\big)\big)$. The level-set function can now be advected by using (4.15). The next step consists in reinitializing the level-set function before it is used by the Navier-Stokes solver.

Remark

The contact-line speed U_{CL} in (4.15) is determined numerically by the procedure outlined above. This introduces small discretization error, so it may be necessary in some cases to apply some filtering of the contact line velocity components. Ideal low-pass filtering is used for that purpose only for three-dimensional sliding drops. For the contact line velocity component $f_{i,j}$, the value obtained after low-pass filtering reads

$$\bar{f}_{i,j} = \frac{1}{9} \sum_{l=-1}^{1} \sum_{m=-1}^{1} f_{i+l,j+m}. \tag{4.19}$$

Step 2

The level-set function at ghost cells undergoes a special numerical treatment during the reinitialization step. First, the set of cells Γ that are within a distance of one grid spacing from the zero level-set is determined (Figure 4.2):

$$\Gamma = \{\mathcal{C}_{i,j,k} \in \Omega : \min_{(I,J,K) \in \upsilon_{i,j,k}} (\phi_{i,j,k}\phi_{I,J,K}) < 0\}, \tag{4.20}$$

with

$$\upsilon_{i,j,k} = \{(i-1,j,k),(i+1,j,k),(i,j-1,k),(i,j+1,k),(i,j,k-1),(i,j,k+1)\}. \tag{4.21}$$

The level-set function at ghost cells $\mathcal{C}_{i,j,k} \in \mathcal{P}_0 \cap \Gamma$ is pinned during the redistance step. Other ghost cells $\mathcal{C}_{i,j,k} \in \mathcal{P}_0 \backslash (\mathcal{P}_0 \cap \Gamma)$ are given a linearly extrapolated value. This way, the pinned ghost cells act as a boundary condition for the level-set function. At all other cells $\mathcal{C}_{i,j,k} \in \Omega \backslash \mathcal{P}_0$ the level-set function is updated with the algorithm of Sussman and Fatemi (1999) with an initialization field ψ^0 equal to the advected field obtained from (4.10). That authors proposed adding a correction term to the original reinitialization equation (4.11) in order to preserve the interface shape. Let ψ^m be the updated value at pseudo-time $\tau^m = m\Delta\tau$, where $\Delta\tau$ is the pseudo-time step. In a semi-discretized form, the modified reinitialization equation reads:

$$\frac{\psi^{m+1} - \psi^m}{\Delta\tau} + \text{sign}(\psi)(|G\psi^m| - 1) = \lambda\delta_h(\psi^0)|G\psi^0|, \tag{4.22}$$

where $G\psi$ is a numerical approximation of $\nabla\psi$, $\delta_h = H'_h$ is the smoothed delta function, with H_h defined in Equation (4.12), and λ is a correction factor that will be detailed below. (4.22) is here solved iteratively with a predictor-corrector scheme. For all cells but the ghost cells, ψ^{m+1} is first predicted from the original reinitialization equation,

$$\tilde{\psi}^{m+1}_{i,j,k} = \psi^m_{i,j,k} - \Delta\tau\big(2H_h(\psi^0_{i,j,k}) - 1\big)\big(|G\psi^m_{i,j,k}| - 1\big), \tag{4.23}$$

and then corrected to preserve the interface shape,

$$\psi^{m+1}_{i,j,k} = \tilde{\psi}^{m+1}_{i,j,k} + \Delta\tau\lambda_{i,j,k}\delta_h(\psi^0_{i,j,k})|G\psi^0_{i,j,k}|, \tag{4.24}$$

with a correction factor that reads

$$\lambda_{i,j,k} = -\frac{\int_{\mathcal{C}_{i,j,k}} \delta_h(\psi^0)(\tilde{\psi}^{m+1} - \psi^0)/\Delta\tau}{\int_{\mathcal{C}_{i,j,k}} \delta_h^2(\psi^0)|G\psi^0|}. \tag{4.25}$$

Integration over a cell $\mathcal{C}_{i,j,k}$ can be done with a 27-point stencil:

$$\int_{\Omega_{i,j,k}} f = \frac{h^3}{78}\left(52 f_{i,j,k} + \sum_{l=-1}^{1} \sum_{m=-1}^{1} \sum_{n=-1}^{1} \alpha_{l,m,n} f_{i+l,j+m,k+n}\right), \tag{4.26}$$

where $\alpha_{l,m,n} = 0$ if $l = m = n = 0$, $\alpha_{l,m,n} = 1$ otherwise. In the prediction equation (4.23), temporal discretization is done with a total-variation-diminishing second-order Runge-Kutta method (Shu and Osher, 1988) and $|G\psi^m_{i,j,k}|$ is calculated with a WENO5 scheme of Jiang and Peng (2000). $|G\psi^0_{i,j,k}|$ in the correction equation (4.24) is computed by first-order upwinding and Godunov method.

Remark

Pinning the level-set function at ghost cells $\mathcal{C}_{i,j,k} \in \mathcal{P}_0 \cap \Gamma$ during the redistance step is not sufficient to avoid the numerical problem related to the blind spot mentioned above. From experience, it is possible to avoid this by setting divided differences of the WENO5 scheme to zero whenever they are supposed to be calculated using values of the level-set function that have been extrapolated to the ghost cells. That way, after extrapolation to the ghost cells, information is enforced not to go back up in the blind spot and the numerical problem does not prevail anymore.

4.4 Results and discussion

The 3D code is tested against two axisymmetric cases of droplet spreading: first in the viscous regime, then in the inertial regime. Finally, three-dimensionnal simulations of sliding droplets in viscous regime with contact angle hysteresis are performed.

4.4.1 Axisymmetric droplet spreading in viscous regime

The algorithm is first validated against DNS results of Sui and Spelt (2013a). Those authors simulated axisymmetric droplet spreading in the viscous regime. The dynamic angle θ_d is obtained herein from (4.3) with $\theta_w = \pi/6$, $Q_i = -0.7$, $\lambda = 10^{-4}$, $r_\mu = 0.1$, $r_\rho = 0.1$. For axisymmetric droplet spreading in the viscous regime, the parameter Q_i in (4.3) is in fact known for small viscosity ratio r_μ, from the theoretical analysis of Hocking and Rivers (1982). Those authors tabulated values of $Q_i - 1$, denoted by $Q_i(\alpha)$ in their Table 1, hence the value herein chosen for the parameter Q_i. In (4.1), the Reynolds number Re and the Ohnesorge number $Oh = \sqrt{Ca/Re}$ are set to 5 and 0.1 respectively. Velocities are scaled by the initial downward velocity and lengths are normalized by the droplet diameter $2R$. The initial state is a spherical cap with a contact angle of $\pi/3$. The time is normalized by the viscous time $\rho R^2/\mu$. Simulations are performed on three uniform grids, $h \in \{1/64, 1/128, 1/256\}$, with $\Delta t/h$ fixed, set to $256 \times 5.0 \cdot 10^{-6}$ here. In Figure 4.3, results are compared against DNS (Sui and Spelt, 2013a) and results of macroscale simulations that Sui and Spelt (2013b) performed with an axisymmetric code. Results appear to converge for both the drop base radius and the contact line speed. The contact line speed compares very well with the DNS results as well. Note that Sui and Spelt (2013b) showed grid convergence could not be achieved for the drop base radius as a function of time when considering a constant contact angle equal to the static angle for the entire simulation, and spreading would be over-estimated there. This test finally shows that contact line dynamics affects wetting at the macroscale, and that through the higher-order term $Ca_{CL}Q_i$ of (4.3). Indeed, Sui and Spelt (2013b) showed spreading would be under-estimated without that term.

4.4.2 Axisymmetric droplet spreading in inertial regime

Ding et al. (2012) experimentally studied rapid spreading of water drops. Air was the surrounding gas. Authors identified a regime for droplet ejection, referred to as second-stage pinch-off. The flow is qualitatively described in the next paragraph. The dynamic angle θ_d is here obtained from (4.3) or (4.7) with $\theta_w = 23°$, $Q_i = -0.99$, $Re^* = 0.37$, $r_\mu = 0.05$, $r_\rho = 0.001$. Sui and Spelt (2013b) determined a slip length of 10^{-16} m by fitting the experimental results to the inertial theory of Cox (1998). They showed that using such an unrealistic slip length and a constant wall angle θ_w allowed

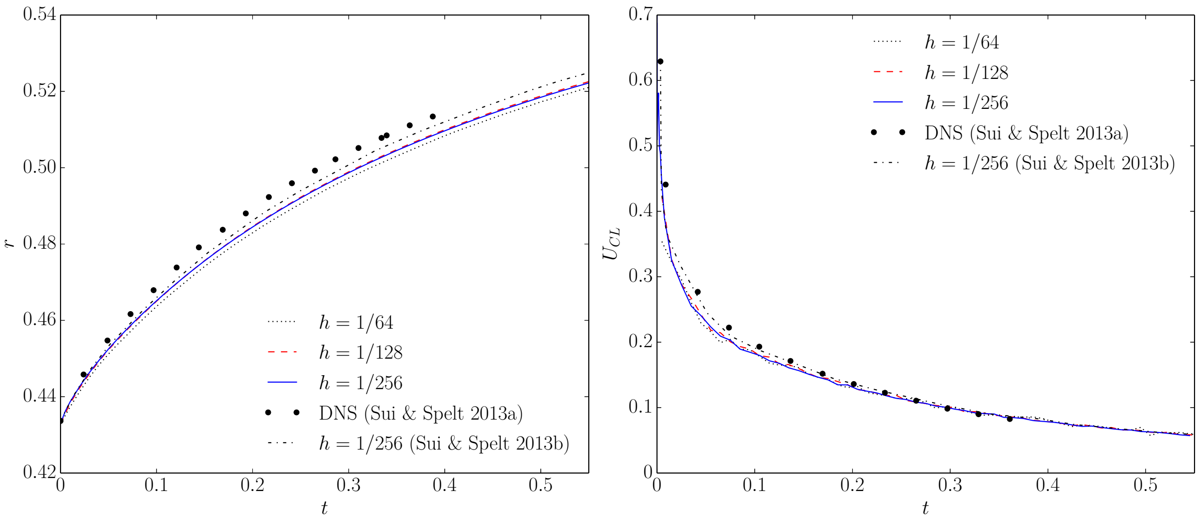

Figure 4.3: Drop base radius and contact line speed as a function of time for viscous spreading.

getting the same results as with a realistic slip length 10^{-9} m and a dynamic wall angle. A slip length of 10^{-16} m is used in this work. Sui and Spelt (2013b) performed their simulations with a Weber number $We = ReCa$ equal to 0.033 and $Oh = 0.006$ based on an initial downward velocity 0.079 m.s^{-1} and an initial drop radius $3.85 \cdot 10^{-4}$ m. Based on the actual initial drop radius $3.055 \cdot 10^{-4}$ m, We and Oh in (4.1) are here set to 0.027 and 0.0067, respectively. The smooth width is set to $2.5h$ to ensure convergence of the pressure solver. The initial level-set function is a spherical droplet that touches the wall $\phi(x, y, z) = R - \left(x^2 + y^2 + \left(z - R\sqrt{1 - 1/16}\right)^2\right)^{1/2}$. The grid spacing, normalized by the drop radius, is $h = 1/90$. The time step, made dimensionless by the inertial-capillary time $\sqrt{\rho R^3/\sigma}$, is set to $1.25 \cdot 10^{-5}$.

Qualitative results presented in Figure 4.4 compare very well with the experiment of Ding et al. (2012) and numerical results of Sui and Spelt (2013b). When the water drop initially hits the solid substrate (Figure 4.4a), the interface is strongly curved next to the contact line as the contact angle at the wall is equal to θ_w (Figure 4.4b). As a consequence, a train of capillary waves travels from the contact line (Figure 4.4c) up to the top of the drop (Figure 4.4d) and then travels back down to the contact line (Figures 4.4e – 4.4g). A pinching neck forms (Figure 4.4h) but there is no droplet pinch-off yet, but rather the neck re-expands (Figure 4.4i): a capillary wave starts traveling from the re-expanding neck (Figure 4.4j) to the contact line, yielding to the formation of another pinching neck (Figure 4.4k), a smaller one, that further leads to droplet ejection (Figure 4.4l). As in the experiment, a second-stage droplet pinch-off is observed. Sui and Spelt (2013b) showed that the use of a constant contact angle equal to θ_w lead to a first-stage pinch-off. In that case there would be ejection of a droplet from the first pinching neck.

Figure 4.5 shows very good quantitative agreement with experimental and numerical results of Ding et al. (2012) and Sui and Spelt (2013b) respectively. The train of capillary waves reaches the contact line around $t = 1$. The other capillary wave coming from the re-expanding neck reaches the contact line after $t = 2$. Sui and Spelt (2013b) mentioned that the first grid cell next to the wall was in the inviscid subregion for velocities higher than 1.3 with parameters $(h, We, Oh) = (1/100, 0.033, 0.006)$. The algorithm implemented here allows getting the same results. However, for the parameters $(h, We, Oh) = (1/90, 0.027, 0.0067)$ used here, the first grid cell next to the wall is in the inviscid subregion for velocities

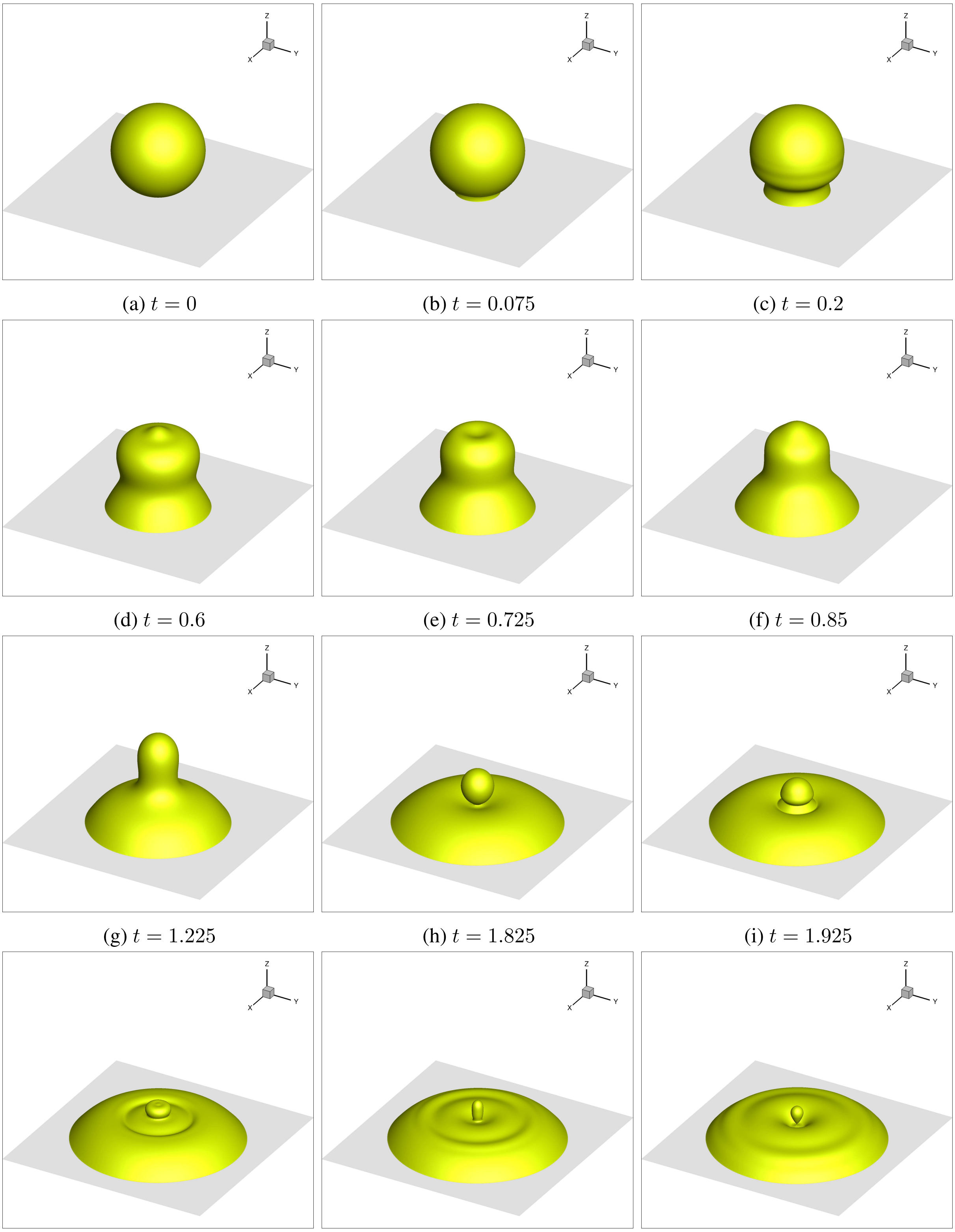

(a) $t = 0$ (b) $t = 0.075$ (c) $t = 0.2$

(d) $t = 0.6$ (e) $t = 0.725$ (f) $t = 0.85$

(g) $t = 1.225$ (h) $t = 1.825$ (i) $t = 1.925$

(j) $t = 2$ (k) $t = 2.075$ (l) $t = 2.15$

Figure 4.4: Rapid spreading of a water drop leading to a second-stage droplet pinch-off.

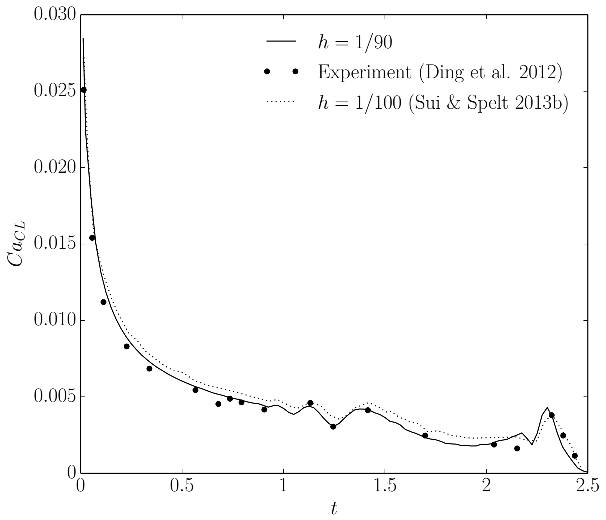

Figure 4.5: Capillary number based on the contact line speed as a function of time for rapid spreading.

higher than 1.47, corresponding to capillary numbers higher than 0.00162. This test case shows that contact line dynamics qualitatively affects the flow at the macroscale and it has to be taken into account to simulate macroscopic flows with moving contact lines.

4.4.3 Sliding drop in viscous regime

Podgorski et al. (2001) and then Le Grand et al. (2005) experimentally studied viscous drops sliding down an inclined plane. They observed different regimes referred to as oval, corner, cusp and pearling regimes. For small inclinations angles, oval drops are observed. When the inclination angle is increased, the curvature locally increases at the back of the drop, leading to cornered shapes, and further to cusp shapes. By increasing the inclination angle further, the drop stretches and a tail forms, that leads to a capillary instability resulting in droplet pinch-off, or pearling. The experimental results were found to be in good quantitative agreement with the viscous theory of Cox (1986).

The experiments of Le Grand et al. (2005) were simulated by Maglio and Legendre (2014), who performed macroscale simulations by using the theory of Cox (1986) with a volume-of-fluid method. They obtained good qualitative and quantitative agreement for the most viscous fluids. However, the sliding speeds they obtained in their simulations for the fluid 47V10 were higher than in the experiment. They suggested this discrepancy to come from the fact that only the large-scale viscous dissipation was taken into account by numerically resolving the flow only down to the intermediate region, and not that of the inner region. Hitherto, such pearling drops have not been obtained in the level-set framework. The numerical results presented here demonstrates the efficiency of the computational method to account for contact angle hysteresis in three dimensions. Note that the asymptotic theory of Cox (1986) was developed in two dimensions, and its use in three dimensions for strongly curved contact lines remains uncertain, which forms a further motivation of the present case study.

The first case simulated here is from the experiment of Le Grand et al. (2005), with the fluid 47V10. The dynamic angle θ_d is obtained from (4.3) with $\theta_{w,A} = 50.5°$, $\theta_{w,R} = 45.5°$, a droplet volume $V = 6$ mm^3, a slip length $\lambda V^{1/3} = 10^{-9}$ m (consistent with the experiment), $Q_i = 0$, $r_\mu = 0.001$ and $r_\rho = 0.001$. Initially, the drop is a spherical cap with a contact angle equal to $\theta_{w,A} - 0.5°$. For given fluid

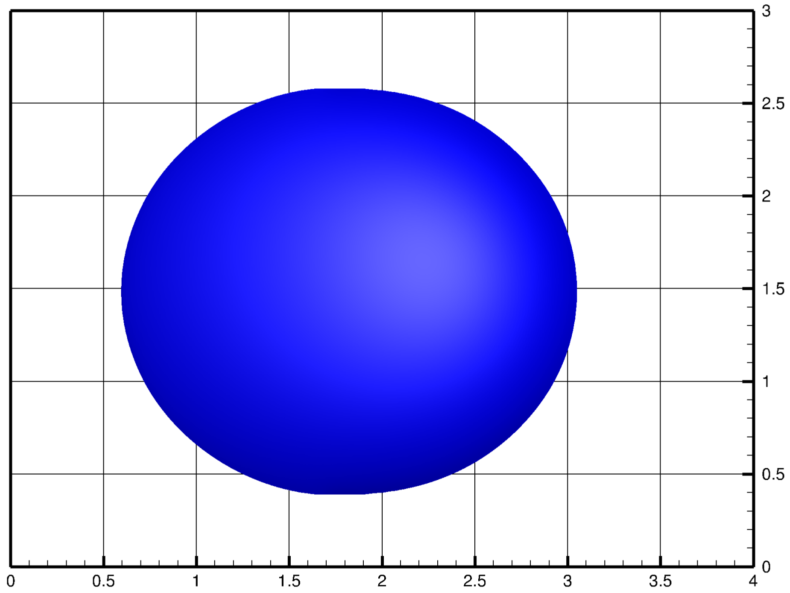

(a) Top view.

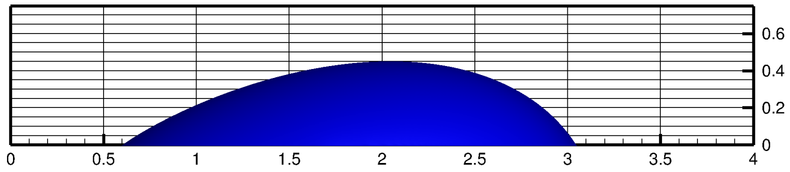

(b) Side view.

Figure 4.6: Qualitative results for the oval sliding drop; $(Bo \sin\alpha, t) = (0.65, 1.5)$. Flow is from left to right.

properties, the flow is governed by a single parameter that is the inclination angle α. Let Bo be the Bond number $Bo = \rho V^{2/3} g/\sigma$. $Bo \sin\alpha$ is here set to 0.65. The time is normalized by the viscous time scale $\rho V^{2/3}/\mu$. Three grids were used, with grid spacing $h \in \{1/48, 1/72, 1/108\}$ and $\Delta t/h$ fixed, here equal to $108 \times 2.5 \cdot 10^{-6}$.

The oval regime was observed (see Figure 4.6), which is consistent with the experiment. Time signals of droplet height, base length, base width and speed are plotted in Figure 4.7. Results are nearly independent of the grid spacing and very close to the experimental data, with geometrical and speed data within 10% from the experiment.

For the same initial conditions, the parameter $Bo \sin\alpha$ is now set to 0.90, for which Le Grand et al. (2005) observed the corner regime. Simulations were done on two grids, $h \in \{1/48, 1/72\}$, and $\Delta t/h = 72 \times 5 \cdot 10^{-6}$. As in the experiment, the corner regime is obtained (Figure 4.8). In Figure 4.9, geometrical data and sliding speed are within 10% from experimental data. It can be noted that the speed is now lower than in the experiment. This may be due to the fact that the macroscale model used here was developed for vanishingly small Bond numbers, $Bo \ll 1$. In reality, the interface slope in the intermediate region may have increased at the front and decreased at the tail of the drop compared to

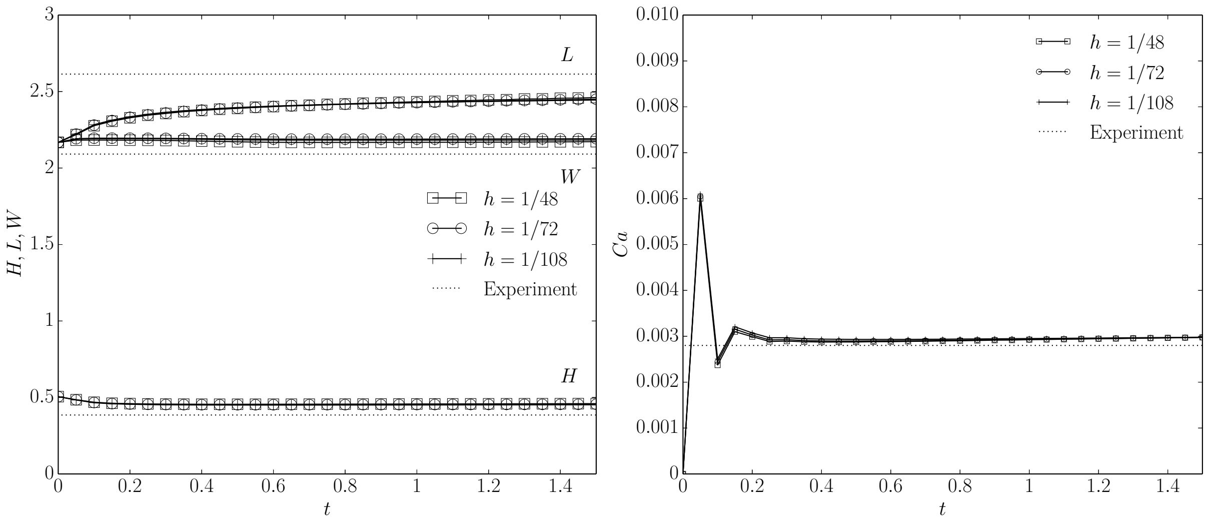

(a) Height, base length and base width against time.

(b) Speed against time.

Figure 4.7: Quantitative results for the oval sliding drop; $Bo \sin\alpha = 0.65$.

the oval regime, yielding a higher sliding speed compared to the numerical results obtained using the gravity-free macroscale model.

The case simulated next is from the experiment of Podgorski et al. (2001), with the fluid 47V10. The dynamic angle θ_d is obtained from (4.3) with $\theta_{w,A} = 52°$, $\theta_{w,R} = 42°$, a droplet volume $V = 8$ mm^3, a slip length $\lambda V^{1/3} = 10^{-8}$ m (consistent with the experiment), $r_\mu = 0.001$ and $r_\rho = 0.001$. Initially, the drop is a spherical cap with a contact angle equal to $\theta_{w,A} - 0.5°$. $Bo \sin\alpha$ is here set to 1.69. The time step is $5 \cdot 10^{-6}$ and the grid spacing is $h = 1/60$. Mass loss was checked and the mean shift of the interface, computed as the difference between the current volume and the initial volume divided by the current interface area, was lower than one grid spacing at the time of second pinchoff.

Qualitatively, the simulation is in agreement with the experiment as a pearling drop is observed (Figure 4.10). Quantitatively, as shown in Figure 4.11, the sliding speed has a value within 15% from the experimental speed. The lower values at time 2.275 and 3.05 in Figure 4.11 are direct consequences of the first and second pinch-offs. Such differences with the experimental results were expected. First, because of the point made above: at $O(1)$ values of Bo, the contact-line region is expected to be affected by gravity, which is still an open area. Using a macroscale model that accounts for gravity may improve the accuracy of numerical predictions. Secondly, the (effective) slip length is a parameter that depends on the coefficient Q_i of the higher-order term in (4.3). That coefficient depends on the flow geometry and is not known a priori for general flows. Sui and Spelt (2013a) showed that term may have to be taken into account. Thirdly, the asymptotic theory of Cox (1986), developed for general two-dimensional flows, although consistent with the axisymmetric hydrodynamic theory of Hocking and Rivers (1982), remains valid in three dimensions only for small contact line curvature. Indeed, Snoeijer et al. (2005) showed that the contact line curvature has a non-negligible effect on the flow, while the theory of Cox (1986) does not account for this. In spite of these limitations, the theory does give satisfactory results for a realistic slip length, and that without accounting for gravity, nor for higher-order terms (coefficient Q_i).

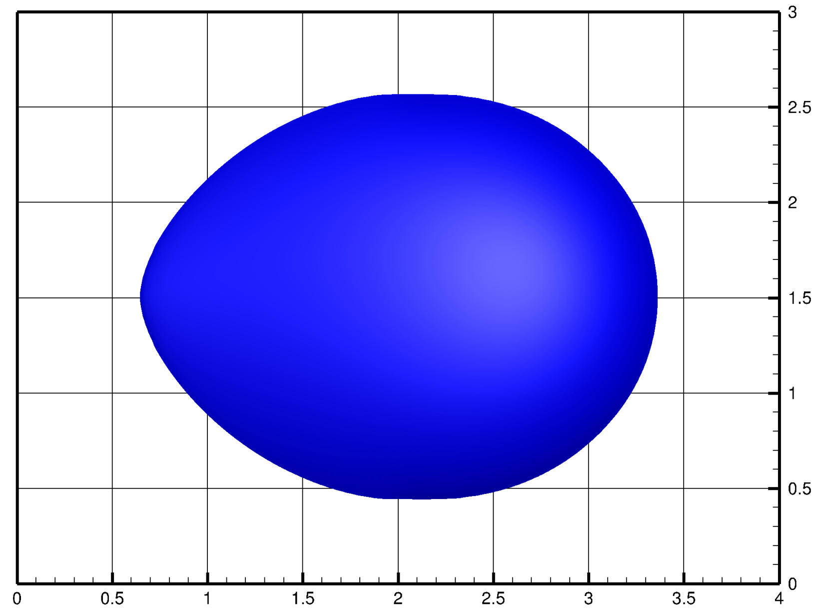

(a) Top view.

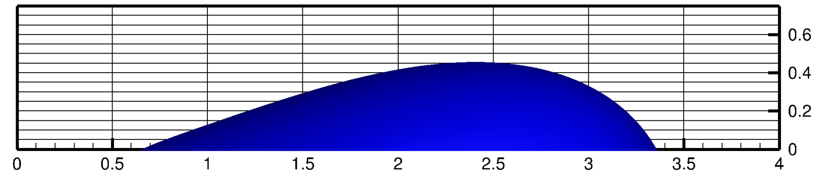

(b) Side view.

Figure 4.8: Qualitative results for the corner-regime drop; $(Bo \sin\alpha, t) = (0.90, 2.0)$. Flow is from left to right.

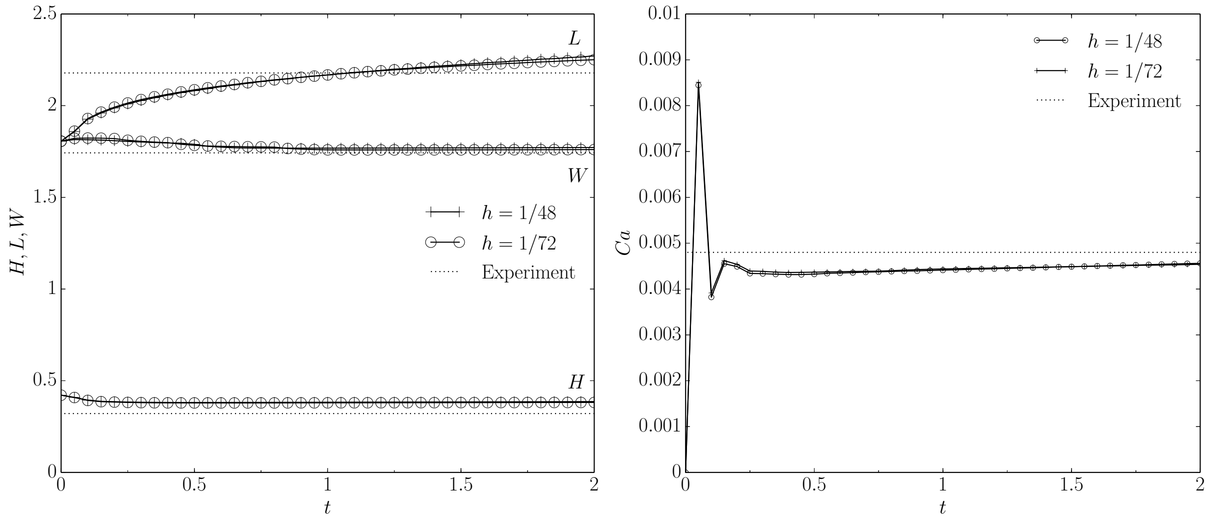

(a) Height, base length and base width against time.

(b) Speed against time.

Figure 4.9: Quantitative results for the corner-regime sliding drop; $Bo \sin\alpha = 0.90$.

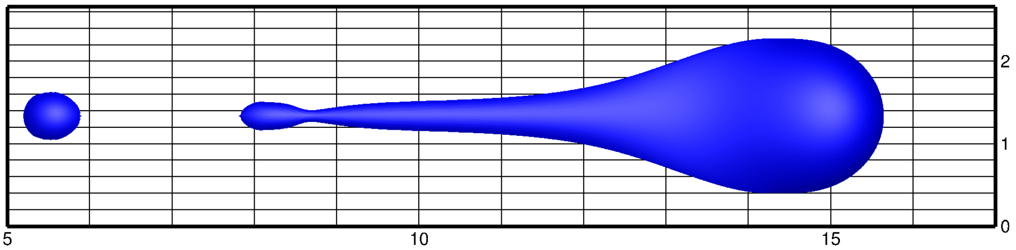

(a) Top view; $t = 2.95$.

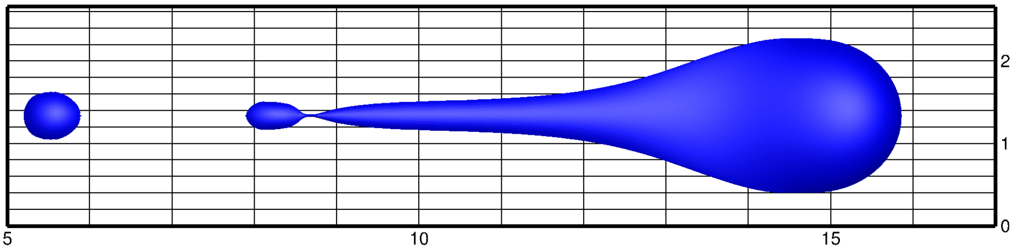

(b) Top view; $t = 3.00$.

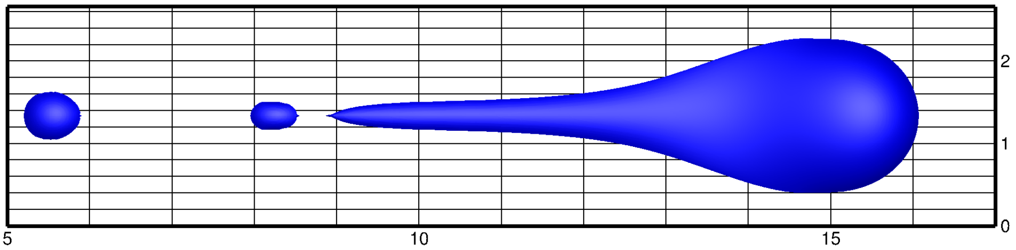

(c) Top view; $t = 3.05$.

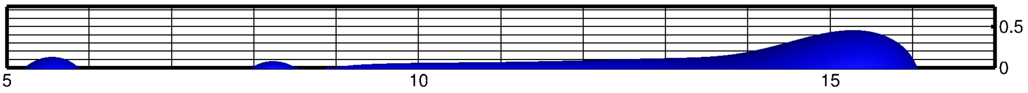

(d) Side view; $t = 3.05$.

Figure 4.10: Qualitative results for the pearling drop; $Bo \sin \alpha = 1.69$. Flow is from left to right.

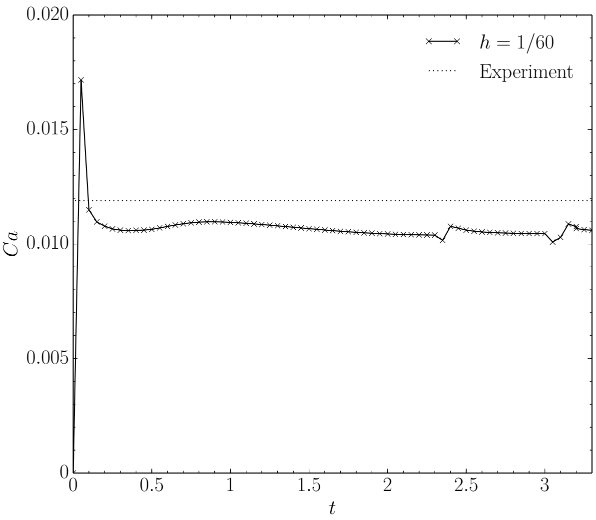

Figure 4.11: Speed of the pearling drop against time. $Bo \sin \alpha = 1.69$. The dashed line is the experimental speed at steady state.

4.5 Conclusion

A new level-set method has been developed to simulate three-dimensional macroscopic flows with moving contact lines. Along with the asymptotic theory of Cox (1986, 1998) as macroscale model, the code reproduces accurately axisymmetric droplet spreading in both viscous and inertial regimes for which excellent qualitative and quantitative agreement have been obtained. The numerical method allows simulating three-dimensional sliding drops with contact angle hysteresis, for which the code has again showed good agreement with experimental results. This new method is seen as an efficient numerical tool to investigate the use of asymptotic theories in three dimensions and to predict wetting in all kind of processes. For flows with moving contact lines with significant effects of gravity, the results indicate that further generic (analytical and/or DNS) work is needed. It is believed that the method can further be used for the simulation of more complex flows such as liquid films with moving contact lines, and for the extension of macroscale models to more complicated physical systems involving non-flat substrates, Marangoni stresses (Sui and Spelt, 2015), etc...

To facilitate dissemination of this work in industrial applications, the macroscale model of Cox (1986, 1998) was implemented in a commercial volume-of-fluid code, and successfully tested against the axisymmetric inertial spreading and the three-dimensional oval drop of Section 4.4.2 and Section 4.4.3, respectively. Results are gathered in Appendix B.

Chapter 5

Experimental methodology

Outline

To characterize flows with moving contact lines such as those considered herein require data on advancing angles for advancing contact lines, alongside data on receding angles for receding contact lines. The first section presents contact angle measurements. Comparison with experimental results available in the literature supports the experimental procedure. In the second section, liquid film thickness measurements by Chromatic Confocal Imaging (CCI), used in the next chapter, are carried out and compared with the analytical solution of a flat film down an inclined plane. Measurements are further validated for wavy films by simultaneous measurements with another technique. Interface velocity measurements are also validated for the flat film, and further tested for a wavy film.

Uncertainty analyses are presented in Appendix C.

5.1 Measurement of contact angle hysteresis with a Drop Shape Analyser

5.1.1 Experimental apparatus

The KRUSS Drop Shape Analyzer 100 is used for contact angle measurement. The apparatus consists of an optical system with camera and arm to deposit the droplet down on the substrate with a needle that has

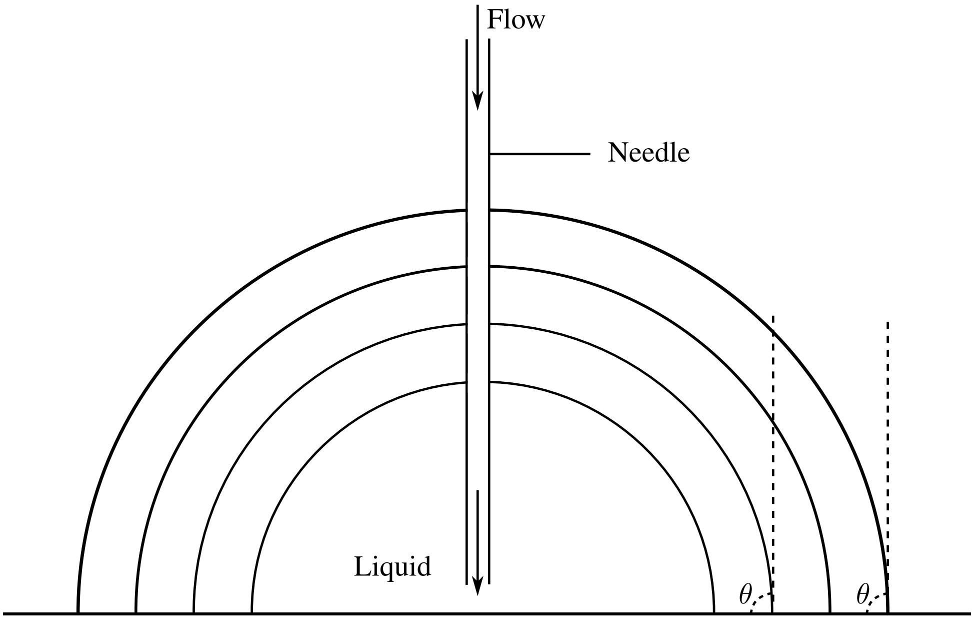

Figure 5.1: Advancing angle measurement technique. Liquid is added at very low flow rate. The advancing angle is the mean angle over the period of contact line slow motion.

an outer diameter of 206 $\pm$ 0.5 µm. The resolution is about 210.0 ± 0.7 pix/mm. Advancing angles are measured by adding some liquid to an initial droplet at a flow rate of the order of 1 µL/min (Figure 5.1). As some liquid is added, the droplet grows with static contact lines; the angle increases until it reaches the advancing angle and the contact lines start advancing slowly. Receding angles are measured by removing some volume from the droplet (Figure 5.2). Receding contact angle measurements with this technique are less accurate than advancing angle measurements, notably because of limits in spatial resolution here (in the case of small receding angles) and evaporation at the contact line. Moreover, the volume is smaller in that case and the presence of the needle may affect the curvature next to the contact line. Measurements may be disrupted by:

- evaporation: the measurement time must be such that the evaporated volume is small compared to the droplet volume, especially for receding angle measurements;
- temperature: that question comes in as the temperature is not controlled, and the air temperature may be different from one measurement to another due to heating of the lamp. However, a change in the contact angle with temperature is expected to be of the order of $-0.1°.\mathrm{K}^{-1}$ for the system investigated here (Bernardin et al., 1997), hence the fact that the temperature is not controlled is not problematic for reproducibility of measurements.
- gravity: for a droplet size of the order of the capillary length, $L_c = \sqrt{\sigma/\rho g}$, the bigger the droplet, the more flattened it becomes;
- meniscus effect: an apparent angle is measured here so if the droplet is too small, then the curvature at the contact line may lead to erroneous measurements. The droplet must be big enough so that the curvature next to the contact line is not affected by the needle.

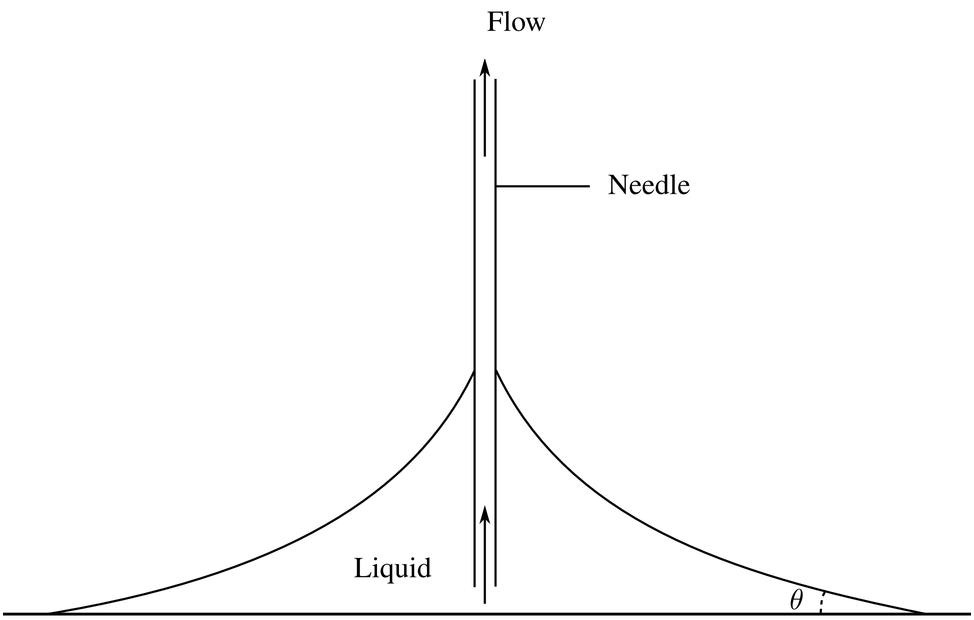

Figure 5.2: Receding angle measurement technique. Liquid is withdrawn at moderate flow rate. The receding angle corresponds to the angle for which motion starts.

Measurement are performed automatically with the software by locally fitting the interface shape next to the contact line to a general equation of the form $ax^2 + by^2 + cxy + dx + ey + f = 0$. The slope then yields the apparent angle. As previously done by Lam et al. (2001) the advancing angle is here measured as the apparent angle observed when advancing the contact line at small capillary number Ca_{CL}. Lam et al. (2001) pointed out that receding angle measurements may have to be done at higher flow rates, especially for volatile liquids. However, one may want to check that $Ca_{CL} \ll 1$, so that the apparent angle (the one that is measured) can be assumed equal to the wall angle, consistently with asymptotic theory such as that of Cox (1986).

The droplet radius should be of the same order but less than the capillary length: in that case one may think there is no gravity effect on the droplet and the droplet size is big enough so that the needle does not affect the curvature next to the contact line. Meanwhile, spreading isotropicity must be checked at all time.

5.1.2 Experimental procedure

5.1.2.1 Cleaning procedure

Stainless steel samples are first cleaned with acetone to remove dirt and then rinsed with distilled water before being dried in an oven at 40°C. For measurements, tap water is preferred over distilled water despite the presence of impurities because it is thought that the composition of distilled water would quickly evolve when in contact with air, whereas tap water is already stable.

5.1.2.2 Advancing angle

Let $L_c = \sqrt{\sigma/\rho g}$ be the capillary length of a liquid, which is the length scale over which capillarity competes with gravity. Some liquid is added progressively to the initial droplet. The droplet must be large enough for the distance d from the needle to the contact line to be larger than the capillary length, $d > L_c$. Indeed, when the contact line is advancing, one does not want the curvature next to the contact line to be modified by the presence of the needle. Besides, a flattened droplet is unwanted, and the condition for the Bond number $(d/L_c)^2 < 1$ is required. In practice, the droplet has an initial volume $V_0 \gtrsim 10$ µL, so that $Bo \lesssim 1$ and $d \lesssim L_c$.

5.1.2.3 Receding angle

Some liquid is removed progressively from the initial droplet that should be such that $d > L_c$ when motion occurs, so that the curvature next to the contact line is not modified by the presence of the needle. In practice the droplet is initially such that $d \lesssim L_c$ to make use of the maximum spatial resolution of the DSA.

5.1.3 Results

Angles are first obtained for tap water on PMMA samples and on stainless steel samples, and compared with the results of Dupont (2007). The mean advancing angles are obtained by time-averaging contact angles measured for contact lines advancing at low capillary number Ca_{CL}. A typical evolution of the contact angle against time is presented in Figure 5.3: the contact line is initially stationary, some liquid is added to the droplet, the contact angle increases (Figure 5.3a) until it reaches the advancing value θ_A and the contact line starts advancing (Figures 5.3b and 5.3c). From Figure 5.3c, the capillary number Ca_{CL} is of the order of 10^{-7} and the difference of the wall angle with respect to the apparent angle can be estimated using the theory of Cox (1986):

$$\frac{\theta_w}{\theta_{ap}} - 1 = \frac{3Ca_{CL}}{\theta_w^3} \ln \lambda, \tag{5.1}$$

where λ is the dimensionless slip length. For the cases investigated, with a realistic slip length of 10^{-9} m, $\lambda = 10^{-6}$ and $3Ca_{CL} \ln \lambda = -4 \cdot 10^{-6}$, so it can be considered that the wanted wall angle, if not extremely small, is equal to the measured apparent angle.

For receding angle measurements, the contact line must move faster, especially for volatile liquids (Lam et al., 2001). The receding angle θ_R is here identified as the angle when the contact line starts receding (Figure 5.4).

Results presented in Table 5.1, that were obtained from 5 sets of measurements, compare well with prior results, thus validating the experimental procedure. Results obtained with sodium hydroxide on stainless steel are provided in Table 5.2: as expected, wetting is enhanced by adding sodium hydroxide to water - with a molar concentration of 0.1 mol.L^{-1} in sodium hydroxide, the advancing angle is here about 10° lower than with tap water. Note that random uncertainties are higher for measurements on stainless steel samples compared to PMMA samples, probably because of roughness effects. Although one may point out that the number of samples for receding angle measurements (5 to 12 here) is relatively small compared to the number of samples of advancing angle measurements (a few hundreds), yielding an increase in random uncertainty compared to a normal distribution, the values of overall uncertainties may not be expected to go below that obtained for advancing angle measurements. Further sets of receding angle measurements should be carried out here in order to reduce random uncertainties though.

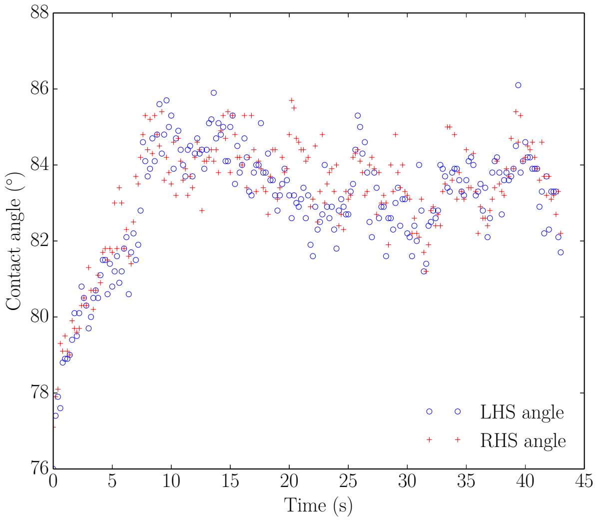

(a) Left-hand side and right-hand side advancing angles against time.

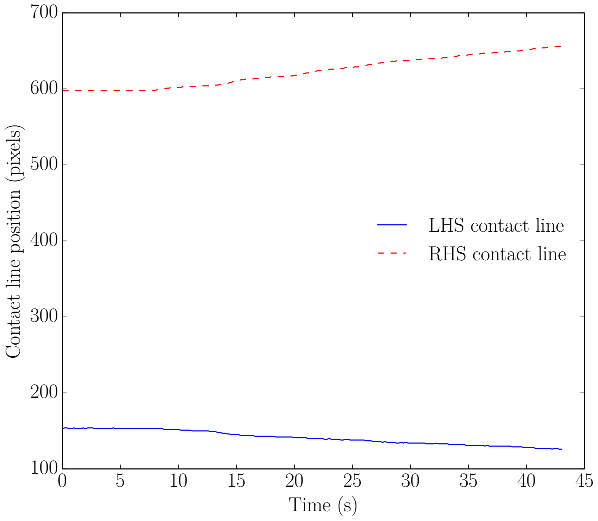

(b) Left-hand side and right-hand side positions against time.

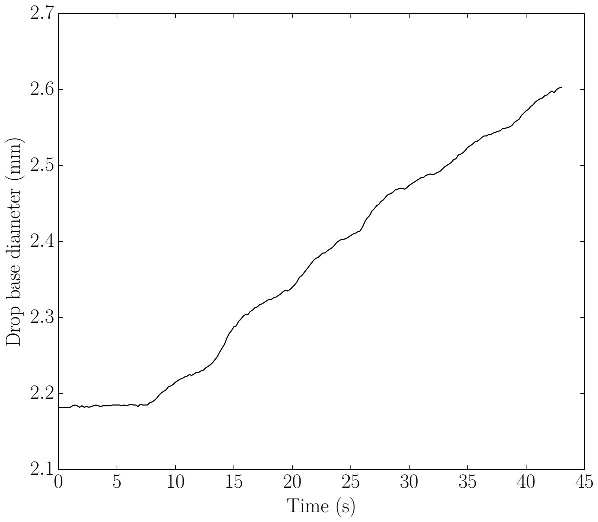

(c) Drop base diameter against time.

Figure 5.3: Advancing contact angle measurement by adding-volume technique.

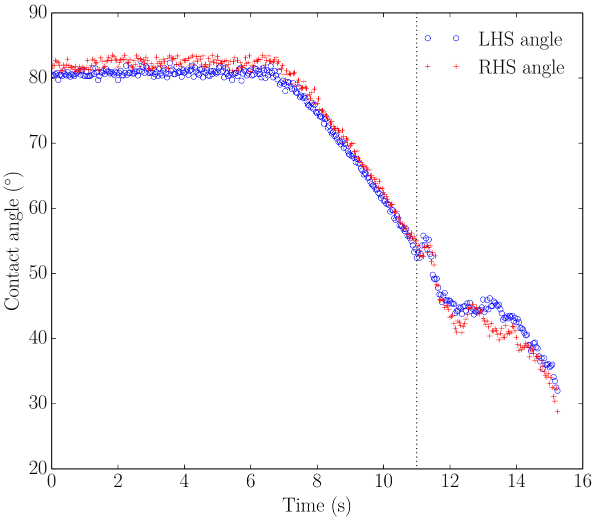

(a) Left-hand side and right-hand side advancing angles against time.

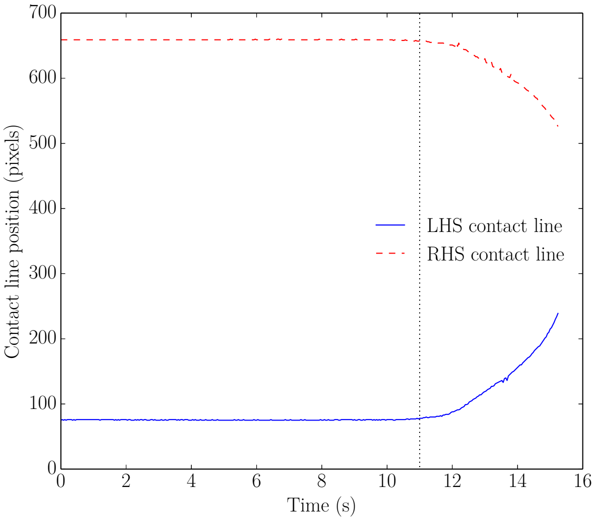

(b) Left-hand side and right-hand side positions against time.

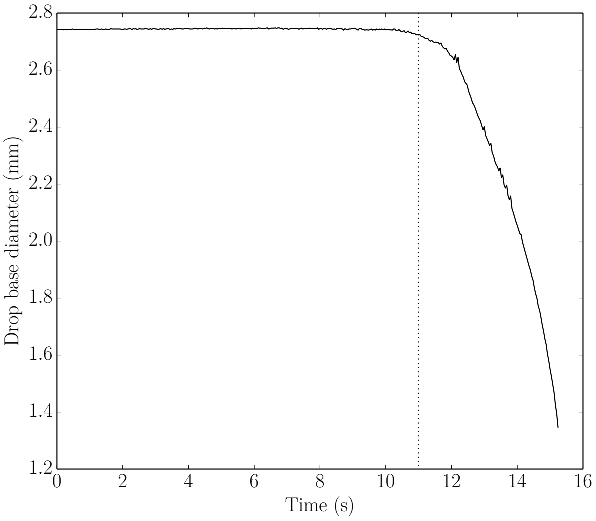

(c) Drop base diameter against time.

Figure 5.4: Receding contact angle measurement by removing-volume technique. The dotted line indicates the beginning of the receding motion, corresponding to a contact angle θ_R.

		PMMA	Stainless steel
Dupont (2007)	θ_A (°)	~ 85	~ 90
	θ_R (°)	~ 45	~ 20
Current work	θ_A (°)	82.9 ± 3.7	84.0 ± 8.2
	θ_R (°)	52.0 ± 4.0	15.9 ± 10.5

Table 5.1: Experimental values of advancing and receding angles of water.

	Water	NaOH 0.1 mol/L
θ_A (°)	84.0 ± 8.2	73.1 ± 7.7
θ_R (°)	15.9 ± 10.5	14.5 ± 8.8

Table 5.2: Experimental values of advancing and receding angles on stainless steel.

5.2 Inclined plane

5.2.1 Introduction

The CCI technique is validated in the case of a liquid film down an inclined plane. The experimental setup of Allouche (2014) is used for this purpose. The liquid flows down an inclined glass plane of $2000 \cdot 464$ mm^2. The inclination can be varied up to $15°$ with an accuracy of $0.035°$ allowed by a motorized stand. The liquid flows in a closed loop. It is fed from the downstream tank to the inlet via a volumetric pump with helical lobes. The fluid temperature is directly measured in the tank using a thermocouple, with an accuracy of 0.1°C. The volume flow rate is known from an electromagnetic flowmeter with an accuracy of 0.5 mL.s^{-1}. Flat-film and then wavy-film thicknesses are observed. For wavy films, a vibrating pot introduces a disturbance with controlled frequency for generating surface waves at the inlet. Such a forcing is of common practice in order to get rid of natural noise by generating a monochromatic surface wave (Chang, 1994).

5.2.2 Liquid film thickness measurement by Chromatic Confocal Imaging

5.2.2.1 Flat film

In this subsection, flat films are observed and compared with the analytical (Nusselt) solution. The liquid film thickness is measured with the CCI system (Figure 5.5). The Nusselt velocity profile of a flat film down an inclined plane is

$$u(y) = 3U_N \frac{y}{h_N}\left(1 - \frac{y}{2h_N}\right), \tag{5.2}$$

where h_N is the film thickness, U_N is the bulk velocity,

$$U_N = \frac{h_N^2 g \sin\beta}{3\nu}, \tag{5.3}$$

and β denotes the inclination angle. The pressure field is

$$p(y) = p(h_N) + \rho g(h_N - y)\cos\beta. \tag{5.4}$$

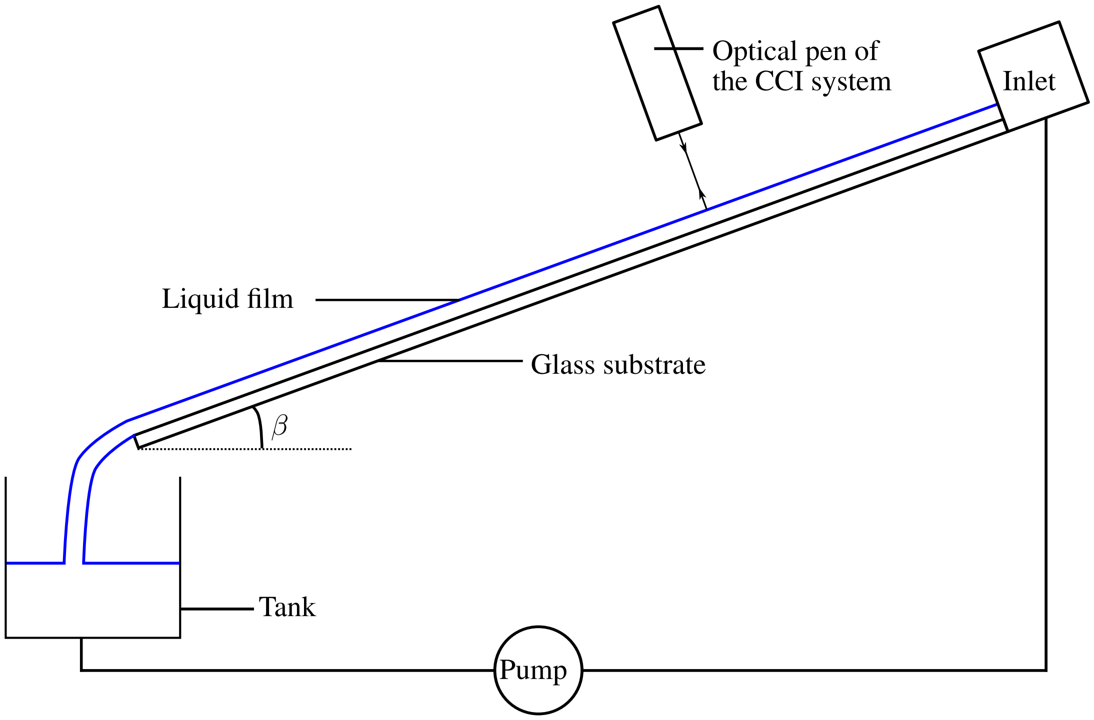

Figure 5.5: Schematic of the experimental setup for measuring the thickness of a flat film.

The system is described by two dimensionless parameters: the Reynolds number $Re = U_N h_N/\nu$, and the Kapitza number Ka, often preferred to the Weber number $We = \rho h_N U_N^2/\sigma$ in order to compare inertial to capillary forces, for its dependence on fluid properties and inclination angle only:

$$Ka = \frac{\sigma}{\rho\nu^{4/3}(g\sin\beta)^{1/3}}. \tag{5.5}$$

Note the Kapitza number actually satisfies $Ka = (3Re)^{2/3}/(3Ca)$, with a capillary number $Ca = We/Re$. The smaller the Kapitza number, the more stable the flow. Therefore, the more viscous the fluid, the easier the observation of a flat film. Charogiannis et al. (2015) have studied liquid films with water-glycerine mixtures. The mixture they used for observing flat films was 80%wt in glycerine, yielding Kapitza numbers of 14 to 20 in their setup. Here, the inclination angle was set to 10°. For a fluid temperature of 22.3°C, dynamic viscosity and density were determined to be 60.5 ± 1.4 cP and 1176.8 ± 4.2 kg.m^{-3} respectively. With a surface tension of 62.0 N.m^{-1} (not measured), the corresponding Kapitza number was 23. A flat film was then observed for five different Reynolds numbers. For each Reynolds number, several sets of $1,000$ data points with a 200-Hz acquisition rate were carried out. Parameters of the sets of measurements are provided in Table 5.3. Measurements are compared with the analytical solution in Figure 5.6. Excellent agreement is achieved against the analytical solution, with relative errors for the mean experimental values within 2 % from the analytical solution.

μ (mPa.s)	60.5 ± 1.4				
ρ (kg.m^{-3})	1176.8 ± 4.2				
b (mm)	464 ± 1				
β (°)	10.0 ± 0.1				
Q (mL.s^{-1})	40 ± 2	80 ± 2	121 ± 2	159 ± 2	203 ± 2
Re	$1.7 \pm 5.5\%$	$3.4 \pm 3.4\%$	$5.1 \pm 2.9\%$	$6.7 \pm 2.7\%$	$8.5 \pm 2.5\%$

Table 5.3: Experimental parameters along with uncertainties due to systematic and random errors; the uncertainty in the Reynolds number is determined from the flat-film analytical solution.

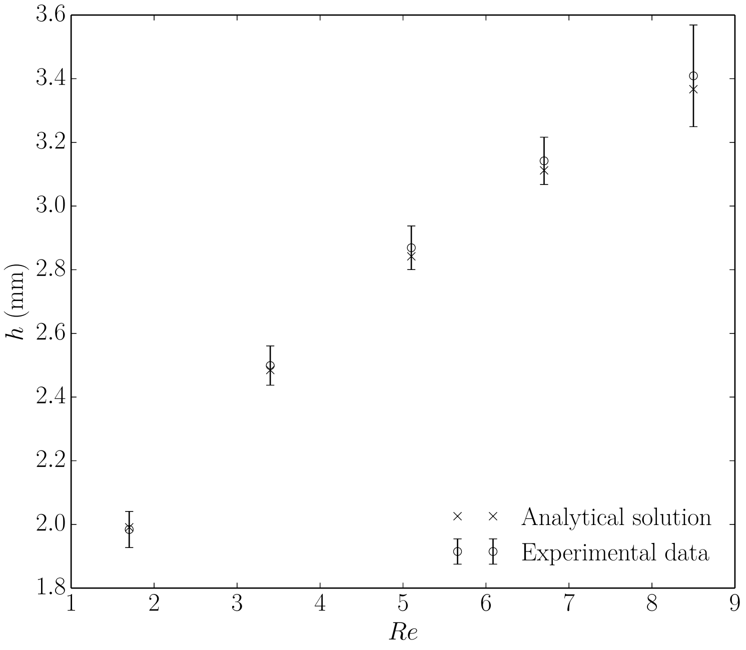

Figure 5.6: Comparison of experimental film thicknesses against the flat-film analytical solution. Uncertainty bars account for the accuracy of the CCI system, the eventual tilt of the optical pen with respect to the normal to the interface, uncertainties in the measurement of parameters of the system, and random uncertainties in film thickness measurements.

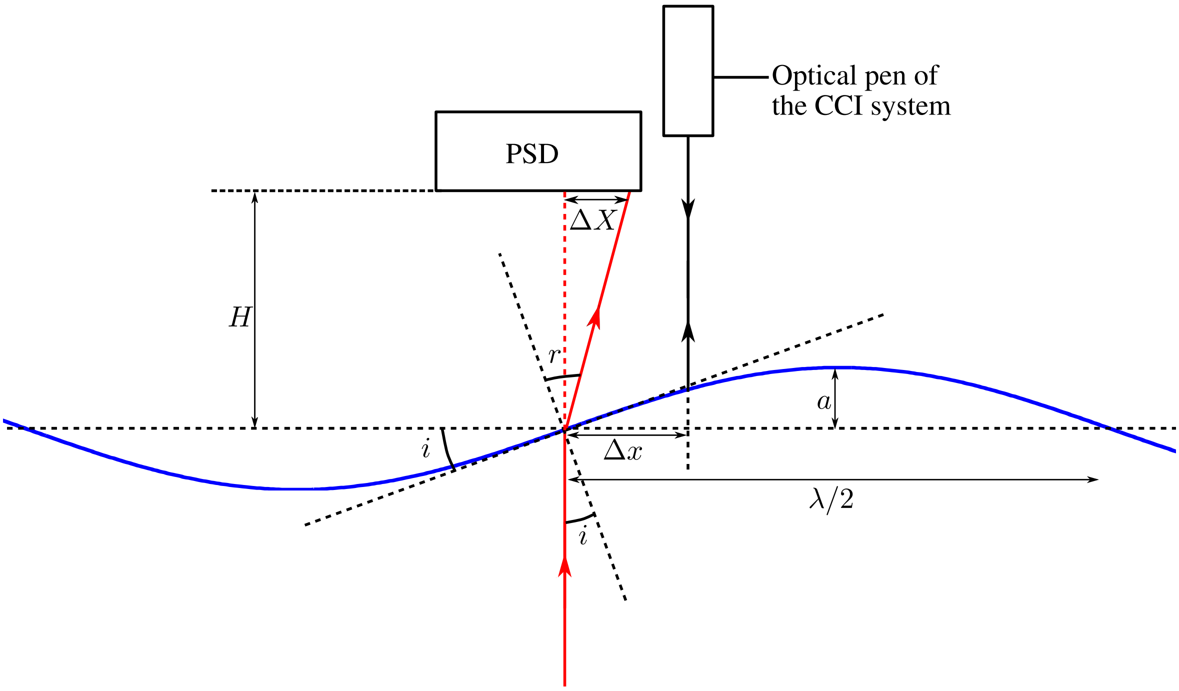

Figure 5.7: Comparison of PSD and CCI techniques on measuring the amplitude of a wave.

5.2.2.2 Wavy film

This subsection aims to compare both experimental techniques, that with the CCI system and that using the Position Sensing Detector (PSD), on measuring the amplitude of a two-dimensional wave resulting from a one-dimensional streamwise disturbance with frequency $f = \omega/(2\pi)$. The CCI system gives the height $h(x_0, t) = s_0(t)$ at the position x_0 whereas the PSD indirectly gives the slope $\partial_x h(x_1, t) = \alpha s_1(t)/H$ at the position $x_1 = x_0 + \Delta x$ (Figure 5.7), where α is the coefficient of proportionality of the PSD (in m.V^{-1}) determined in a prior calibration step and H is the distance of the sensor from the interface. It is recalled here that the PSD returns the voltage corresponding to the abscissa of the Laser beam on the sensor. The two time signals, that of the CCI and the voltage, can be written as:

$$s_i(t) = C_i \cos(\omega t - \phi_i), i \in \{0, 1\}. \tag{5.6}$$

Synchronous demodulation techniques are used for getting the phase difference of the two signals. These can be recast as

$$s_i(t) = A_i \cos(\omega t) + B_i \sin(\omega t), i \in \{0, 1\}, \tag{5.7}$$

with

$$A_i = C_i \cos(\phi_i), B_i = C_i \sin(\phi_i), i \in \{0, 1\}. \tag{5.8}$$

Amplitudes are obtained by integrating time signals over n periods:

$$\begin{aligned} A_i &= \frac{2}{nT} \int_0^{nT} s_i(t) \cos(\omega t) dt, i \in \{0, 1\}, \\ B_i &= \frac{2}{nT} \int_0^{nT} s_i(t) \sin(\omega t) dt, i \in \{0, 1\}, \end{aligned} \tag{5.9}$$

a_{PSD} (µm)	45.3 ± 2.8	50.3 ± 3.1	47.6 ± 3.0	50.0 ± 3.1	53.5 ± 3.3
a_{CCI} (µm)	45.3 ± 1.3	45.4 ± 1.3	47.4 ± 1.4	46.5 ± 1.4	50.0 ± 1.4
λ (cm)	10.0 ± 0.1	11.1 ± 0.1	10.4 ± 0.1	10.8 ± 0.1	11.6 ± 0.1

Table 5.4: Comparison of measurement techniques on measuring a wavy-film amplitude; $\beta = 15°$, $Re = 8.0$, $\nu = 5.61 \cdot 10^{-5}$ m^2.s^{-1}.

which yields the phases,

$$\phi_i = \arctan\left(\frac{B_i}{A_i}\right), i \in \{0, 1\}, \tag{5.10}$$

hence the wavelength

$$\lambda = 2\pi \frac{x_1 - x_0}{\phi_1 - \phi_0}. \tag{5.11}$$

Let X be the position of the Laser beam on the PSD and H the distance between the reflective interface and the PSD. n is the refractive index of the fluid and the wave amplitude reads

$$C_1 = \frac{\lambda \Delta X}{(n-1) 2\pi H}. \tag{5.12}$$

The linear PSD has been calibrated to get the displacement ΔX from the voltage at the terminals of the sensor. Five sets of measurements were carried out. Each run consisted in acquiring 5,000 samples at a rate of 1 kHz. The forcing frequency was set to 6 Hz. The refractive index was not measured there but was approximated to be 1.44 ± 0.01 after measuring viscosity, density, and comparing them to the tabulated values gathered by the Glycerine Producers' Association (1963). Table 5.4 gathers amplitudes and wavelength obtained in each set. The uncertainty analysis is detailed in Appendix C. The uncertainty in the measurement of a_{PSD} is mainly due to uncertainties in the wavelength λ and the distance H from the sensor to the interface. The relative error in the mean amplitude measured with the CCI system with respect to the mean amplitude measured with the PSD sensor, is always within 10%, thus validating the experimental procedure.

5.2.3 Interface velocity measurement of a liquid film

In this section well-known particle-imaging techniques (Particle Image Velocimetry and Particle Tracking Velocimetry; see Adrian (1991) for a review) are tested for measuring the projection of the free-surface velocity field in a plane normal to the optical axis of the digital camera used for the purpose. Measurements are first performed for a flat film and compared to Nusselt analytical solution. A further test is considered to check whether these techniques can be applied in the presence of waves.

5.2.3.1 Particle Image Velocimetry

In PIV, local comparisons of two successive images taken at times t_0 and $t_1 = t_0 + \Delta t$ are carried out with cross-correlation techniques. The displacement (in pixels) of a pattern of seed particles corresponds to the maximum of the correlation function. The cross-correlation operation consists in multiplying a local pattern of a reference intensity field $I_0(x, y)$ with that of the intensity field $I_1(x + \Delta x, y + \Delta y)$ and searching for the couple $(\Delta x, \Delta y)$ that maximizes the correlation function. The velocity is then obtained knowing the time difference between the two successive images, Δt, and the scale factor, determined in a prior calibration step. The reader may refer to, for instance, the book of Raffel et al. (1998) for further information on PIV fundamentals. Below, PIV measurements are performed by cross-correlating two frames of single exposure, with a maximum acquisition rate of 15 Hz here. The software DaVis 8.2.2 from LaVision Inc. has been used for acquisition and post-processing. In PIV, the calibration procedure introduces a systematic uncertainty. Another systematic uncertainty, that depends on the cross-correlation algorithm that is used, is due to the accuracy in the determination of a displacement, which basically ranges from 0.04 to 0.1 pixel (Stanislas et al., 2008).

5.2.3.2 Particle Tracking Velocimetry

While PIV is well suited for high image density (high concentration of particles, typically 10 particles within an interrogation window), PTV is often preferred for low image density. There, Lagrangian tracking is carried out: the velocity is obtained knowing the time difference Δt and determining particle centers at times t_0 and $t_1 = t_0 + \Delta t$. The cross-correlation algorithm of Brevis et al. (2011) has been used here. Particles are detected in the second frame and interrogation windows are chosen to coincide with particle centers for subsequent cross-correlation operations. PTV is often used in addition to PIV aiming to reach a better spatial resolution in the velocity field (Charogiannis et al., 2015). PTV algorithms can still be used for relatively high image density, keeping in mind that such conditions may increase systematic errors in the determination of particle centers due to particle overlapping (Guezennec et al., 1994). This is one of the main drawbacks in PTV compared to PIV, even though efforts have been made to alleviate this problem. As in PIV, the calibration procedure introduces a systematic uncertainty. A further uncertainty is found in the determination of particle centers, the accuracy of which is typically of the order of 0.1 pixel (Udrea et al., 1996).

5.2.3.3 Setup

The setup for observing flat or wavy liquid films is presented in Figure 5.8. The light source is a pulsed Laser B-PIV 200-15 from Litron Lasers Ltd., with a wavelength of 532 nm and a maximum pulse repetition rate of 15 Hz. In order to get a viewfield of 1 to 2 cm^2, particles are illuminated with the Laser beam spot, magnified to reach a diameter of a few centimeters. Frame pairs are recorded with an imager sCMOS camera from LaVision Inc., with 6.5-µm pixels, a CCD chip size of 2560×2160 pixels and a 16-bit digital output. Tracers are fluorescent red polyethylene microspheres from Cospheric LLC, with a density of 0.995 g/cm^3 and size ranging from 10 to 45 µm. Calibration was performed via a scaling procedure using a ruler. The apparent pixel size was about $7.0 \pm 0.5\%$ µm/pix for all cases presented in this subsection. A typical frame is shown in Figure 5.9.

5.2.3.4 Flat film

Flat films are observed first, and results are compared with the Nusselt solution. The temporal resolution ranges from 450 to 1350 µs to yield displacements of about 12 pixels. The acquisition rate is set to 15 Hz. Velocity vectors are obtained in 32×32 interrogation windows. In PIV, a multi-pass processing procedure is used, without window overlap. In the multi-pass processing, vectors are deleted when having a peak ratio lower than 1.2, and when the difference to average is 1.5 times the local standard deviation. The

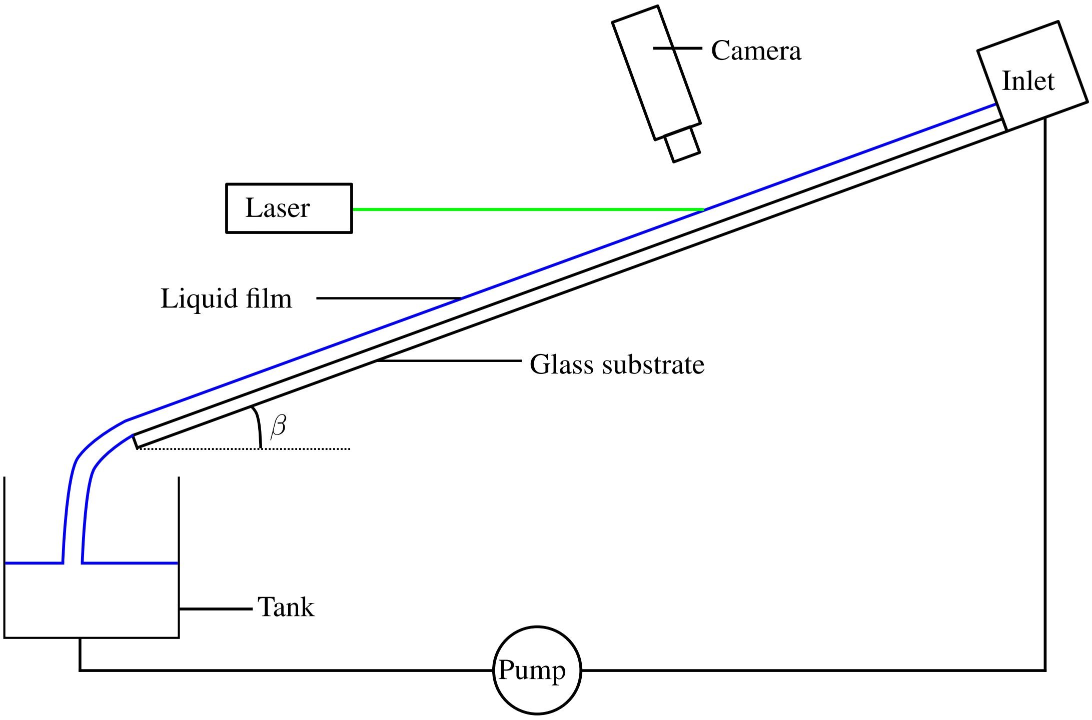

Figure 5.8: Schematic of the experimental setup for measuring the interface velocity of a flat or a wavy film.

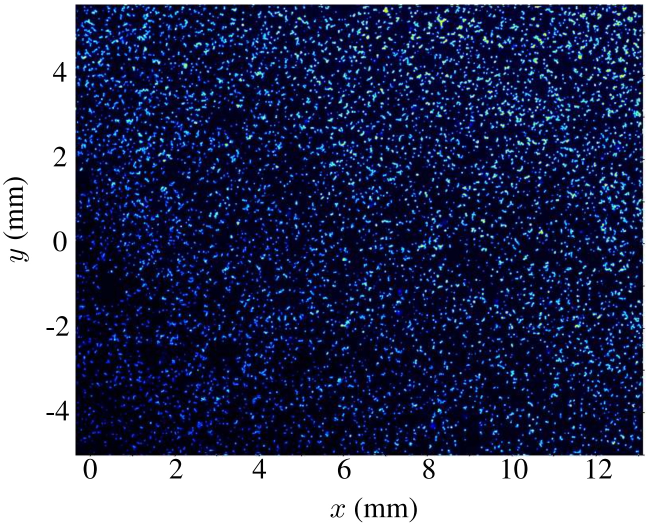

Figure 5.9: Typical frame of single exposure in PIV measurements.

$\nu \cdot 10^6$ (m^2.s^{-1})	$53.1 \cdot \pm 1.2$	53.1 ± 1.2	53.1 ± 1.2	51.4 ± 3.1	53.5 ± 3.3
Q (mL.s^{-1})	40 ± 2	79 ± 2	120 ± 2	160 ± 2	201 ± 2
Re	$1.7 \pm 5.5\%$	$3.3 \pm 3.4\%$	$5.0 \pm 2.8\%$	$6.7 \pm 2.7\%$	$8.4 \pm 2.6\%$

Table 5.5: Experimental parameters along with uncertainties due to systematic and random errors; the uncertainty in the Reynolds number is derived from the flat-film analytical solution.

mean displacement is here obtained from several image pairs by summing cross-correlation functions,

$$R_{i,j}^{tot}(x,y) = \frac{1}{N}\sum_{k=1}^{N} R_{i,j}^{k}(x,y), \tag{5.13}$$

where N is the number of frame pairs and $R_{i,j}^k$ is the cross-correlation function of an image pair with intensity fields I_0^k and I_1^k at the pixel $p_{i,j}$ for the pair of frames k,

$$R_{i,j}^{k}(x,y) = \sum_{l=i-N_x}^{i+N_x} \sum_{m=j-N_y}^{j+N_y} I_0^k(l,m) I_1^k(l+x, m+y), \tag{5.14}$$

with $2N_x + 1$ and $2N_y + 1$ the number of pixels within the interrogation window in x- and y- directions, respectively.

In PTV, the cross-correlation algorithm of Brevis et al. (2011) has been used.

Experimental parameters for all sets of measurements are given in Table 5.5. Image pairs have been post-processed by both PIV and PTV. Figure 5.10 presents the mean velocity field obtained for a Reynolds number $Re = 1.7$: the flow is uniform, with measured velocities ranging from 6.64 to 6.74 cm.s^{-1} for PIV measurements and from 5.2 to 7.4 cm.s^{-1} for PTV measurements. Such large range of velocities in PTV measurements may be due to some particle overlapping, as high density images have been post-processed here. Figure 5.11 compares experimental velocities to the corresponding analytical solutions. Results obtained by PIV and PTV are very close to the analytical solutions. The analytical solution for the highest three Reynolds numbers is outside the uncertainty interval, whatever the technique, PIV or PTV. This is thought to be a problem with focus: if the particles are not exactly in the focal plane but a little bit farther from the camera, the displacements are underestimated. However, each experimental velocity is within 3% from the corresponding analytical solution, which sounds promising for subsequent tests to support the reliability of these velocimetry techniques.

5.2.3.5 Wavy film

This subsection reports a feasibility test of free-surface velocity measurement with waves of small amplitude. A disturbance is introduced at the inlet and the wavy film is observed a few tens of centimeters farther downstream. Figure 5.12 presents the mean velocity fields obtained by PIV and PTV when the acquisition system was synchronized with the forcing frequency, here set to 6 Hz. Part of the wave is observed and, as expected, the interface velocity profile is one-dimensional. That test further supports the reliability of these techniques.

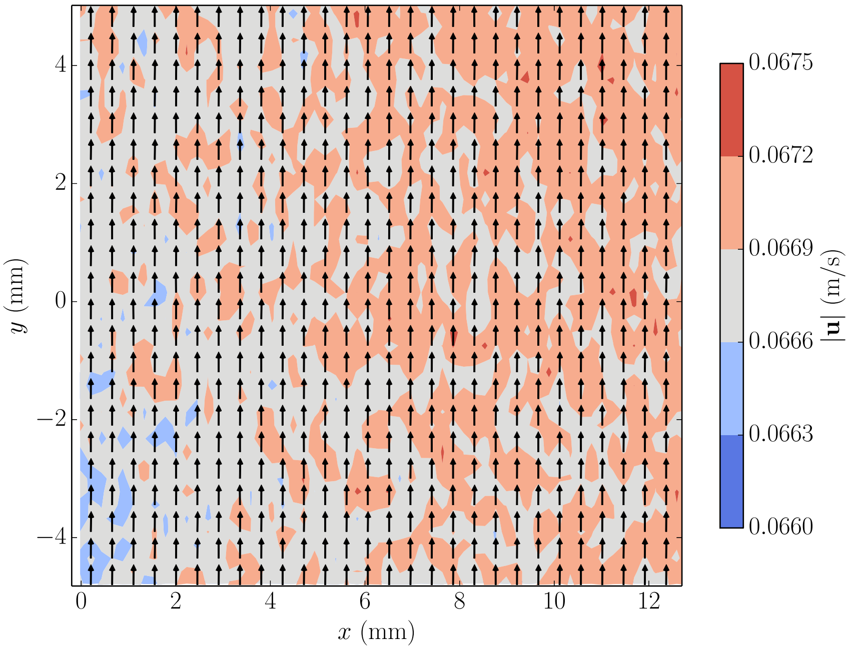

(a) Velocity field obtained by PIV.

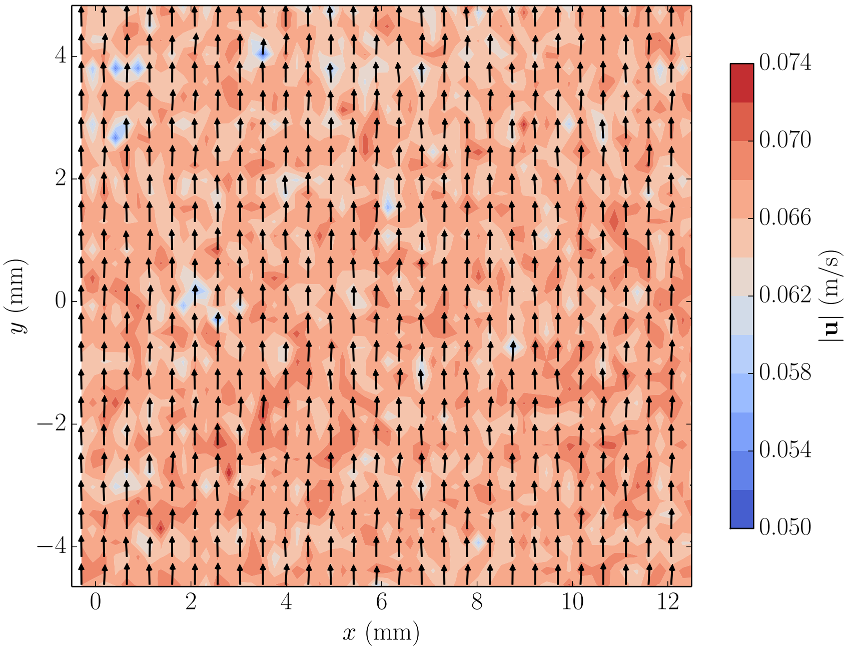

(b) Velocity field obtained by PTV.

Figure 5.10: Mean velocity field of a flat film obtained from a full sequence of image pairs. $\beta = 10°$, $Re = 1.7$, $\nu = 5.31 \cdot 10^{-5}$ m^2.s^{-1}.

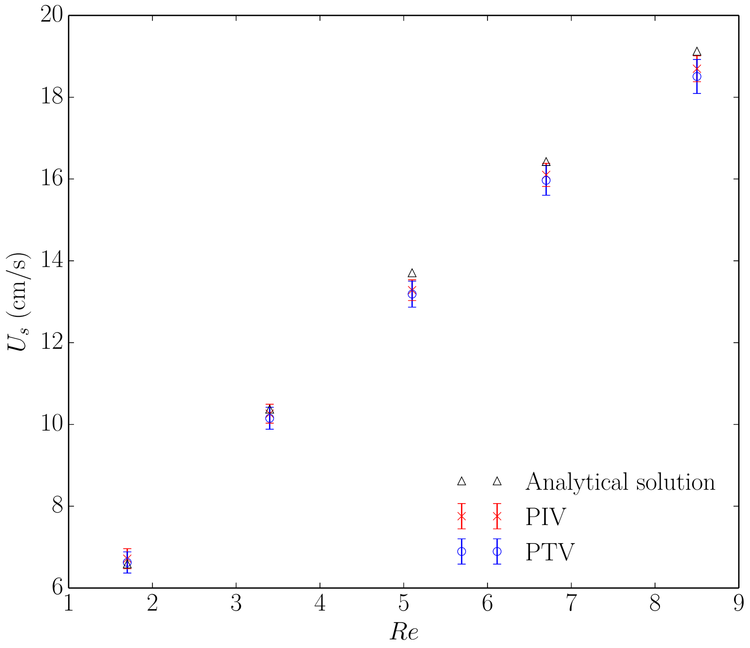

Figure 5.11: Comparison of experimental free-surface velocities against the flat-film analytical solution. Uncertainty bars accounts for the scaling procedure, the accuracy of the cross-correlation algorithm, uncertainties in the measurement of parameters of the system, and random uncertainties introduced in the space-averaging procedure.

5.3 Conclusion

An experimental procedure has been presented and validated for measuring advancing and receding contact angles, needed for characterisation of flows with moving contact lines. Results compare well with experimental data from prior work. Liquid film thickness by CCI and interface velocity measurements by PIV and PTV have also been undertaken. Good agreement with the analytical solution of a flat film has been achieved for all techniques. Further wavy-film tests have shown promising results: the CCI technique yields similar results to the PSD technique for measuring the amplitude of a wavy film, and velocimetry results obtained by particle-imaging techniques, PIV and PTV, are consistent with expectations for a flow subject to one-dimensional streamwise disturbances.

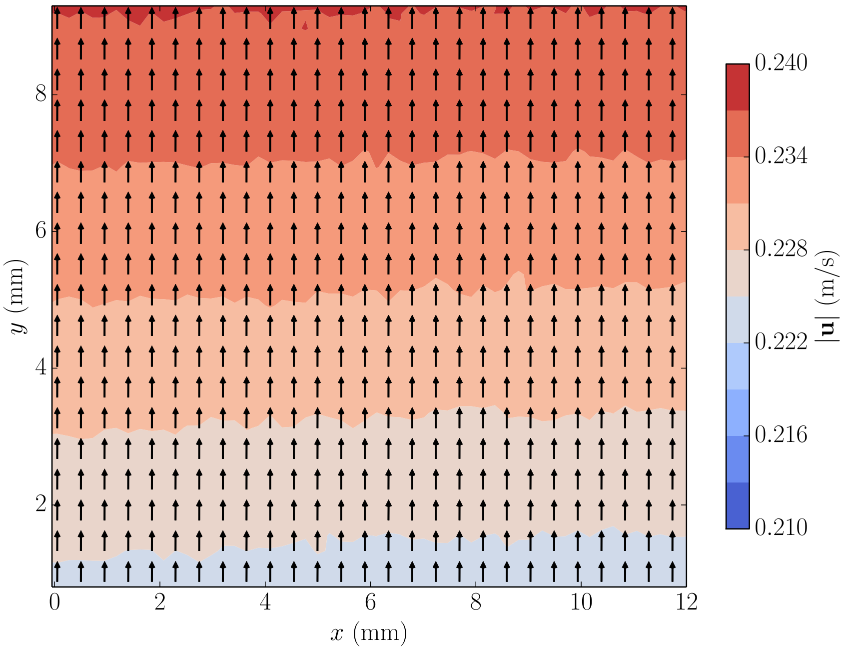

(a) Velocity field obtained by PIV.

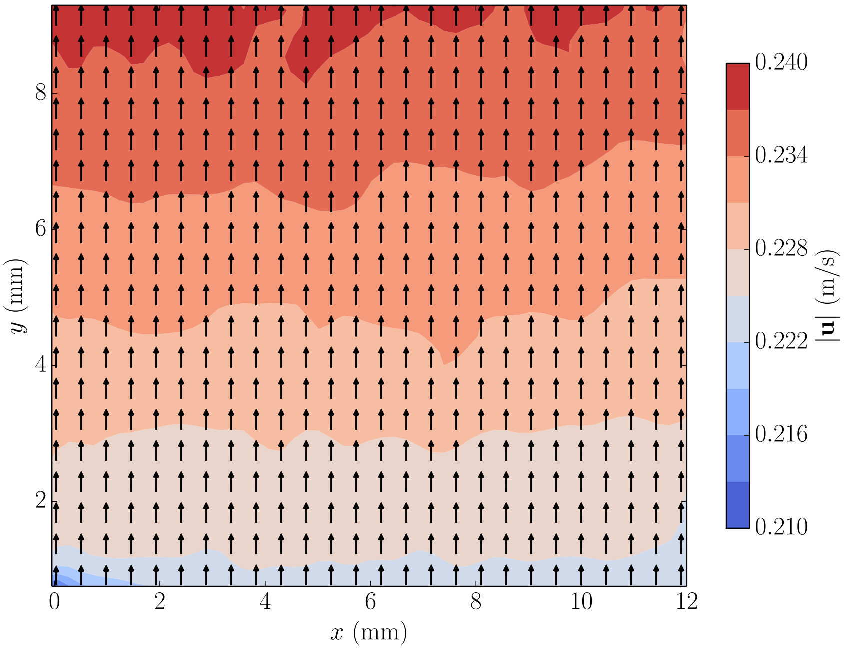

(b) Velocity field obtained by PTV.

Figure 5.12: Mean velocity field of a wavy film obtained by PIV. The forcing frequency and the acquisition rate are set to 6 Hz. $\beta = 15°$, $Re = 8.1$, $\nu = 5.52 \cdot 10^{-5}$ m^2.s^{-1}.

Chapter 6

Liquid film flows over structured packing sheets

Outline

Characterizing the flow over a Representative Elementary Unit (REU) of structured packing sheet is one of the main objectives of this thesis. The subject of this chapter is experimentally obtaining quantitative information on both liquid film thickness and velocity field, also with the aim of validating the CFD methodology. Further details of the experimental methods used here are presented in Chapter 5.

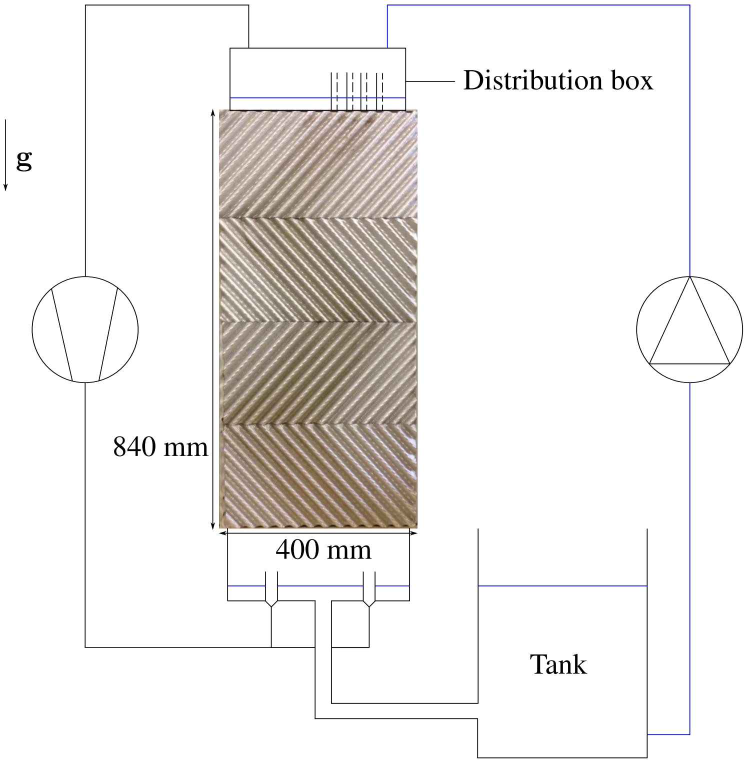

Figure 6.1: Schematic of the experimental apparatus.

6.1 Experimental setup

6.1.1 Apparatus

Figure 6.1 presents the schematic of the experimental apparatus designed for observing flows over packing sheets. The observation area is made of four $210 \cdot 400$ mm^2 non-perforated packing sheet pieces. The distribution box consists of several tubes perforated at the same levels. At steady state, when the distribution box is fed with liquid at some given flow rate, the liquid is drained out of the distribution box through the perforated tubes, providing equal flow rates into the channels (large corrugations) via the use of modular injectors plugged to the perforated tubes. The liquid loop consists of a pumping system and a tank. The counter-current gas flow, whenever it is turned on, is confined in the observation area within a glass channel of size $840 \cdot 400 \cdot 25$ mm^3. Gas and liquid temperature are controlled with an exchanger.

6.1.2 Preliminary observations

This section presents preliminary qualitative observations of liquid flows without the counter-current gas flow. Some dye is added to tap water to visualize the flow. Figure 6.2 presents qualitative results obtained when increasing the liquid flow rate, starting with a dry metal sheet. Four channels are fed with liquid so that wall effects do not disturb the flow. At low flow rates, the flow is essentially gravity-driven and rivulets are observed, shapes of which, for given fluid properties, are only functions of the flow rate and the static angle. Rivulets start merging from 40 L.h^{-1}. For higher flow rates, inertial forces increase, allowing for the formation of a liquid film that seems to follow the direction of channels (large corrugations) of the metal sheet. Maximum wetting seems to be achieved for flow rates $Q_L \geq 100$ L.h^{-1}.

Figure 6.3 presents qualitative results obtained when decreasing the liquid flow rate, starting from a large flow rate that gives a liquid-film regime with maximum wetting. Dewetting starts being observed at the first two packing sheet pieces from the top for flow rates $Q_L \leq 80$ L.h^{-1}, and at the third packing sheet piece from the top for flow rates $Q_L \leq 40$ L.h^{-1}. Decreasing the flow rate starting from a liquid-film regime does not lead back to the rivulet regime: the system exhibits a hysteresis behavior, partly due to the presence of small-scale corrugations that remain filled with liquid. In this work, the third packing sheet piece from the top has been chosen as the observation area, where the flow is assumed to have developed for flow rates $Q_L \geq 60$ L.h^{-1}. For such flow rates, liquid films are observed and the Reynolds number will be defined based on the total flow rate and the inlet width b corresponding to the four channels fed with liquid:

$$Re_L = \frac{Q_L}{b\nu_L}, \tag{6.1}$$

where b is approximated as

$$b = N_{\text{channels}} \frac{2\sqrt{h_u^2 + (\lambda_u/2)^2}}{\sin \alpha_u}. \tag{6.2}$$

Tap water at 20 ± 1.0 °C will be the working fluid for all subsequent measurements and all sets of measurements will be carried out decreasing the liquid flow rate, starting from a value $Q_L = 225$ L.h^{-1}.

6.1.3 Outline of local measurements

In the following sections, results of local measurements of liquid film thickness and interface velocity are reported. Although measurements in the presence of a counter-current gas flow were anticipated, through the glass channel, thickness measurements have first been performed by Chromatic Confocal Imaging (CCI) without counter-current gas flow, so that there was no need for observing through the glass channel. Results of interface velocity measurement are also reported for that configuration. Difficulties related to observing through the glass channel are then discussed and subsequent results of liquid film thickness measurements are compared to those obtained without the glass channel. In Figure 6.4 it is shown how the camera or the CCI system is arranged in order for its optical axis to be perpendicular to the mean plane of a large-scale triangular corrugation. The term mean plane is employed here because of the presence of small corrugations.

6.2 Liquid film thickness measurement without the glass channel

6.2.1 Setup

The CCI system has been validated in Chapter 5 for a flat and then a wavy liquid film down an inclined plane. The technique is now applied to measure the thickness of a liquid film flowing down a REU of structured packing sheet. First sets of measurements are here carried out without the counter-current gas flow; the optical pen of the CCI system is arranged the same way as the camera for subsequent velocity measurements, as shown in Figure 6.4. The liquid film thickness is measured indirectly, first acquiring the signal corresponding to the dry substrate, then the signal corresponding to the reflective gas-liquid interface.

A first problem that arises with the setup concerns light reflection at a complex surface. The optical axis of the CCI system is arranged perpendicularly to the packing sheet channel but the small corrugations constrain the experimentalist to carry out measurements close to crests and troughs of small corrugations

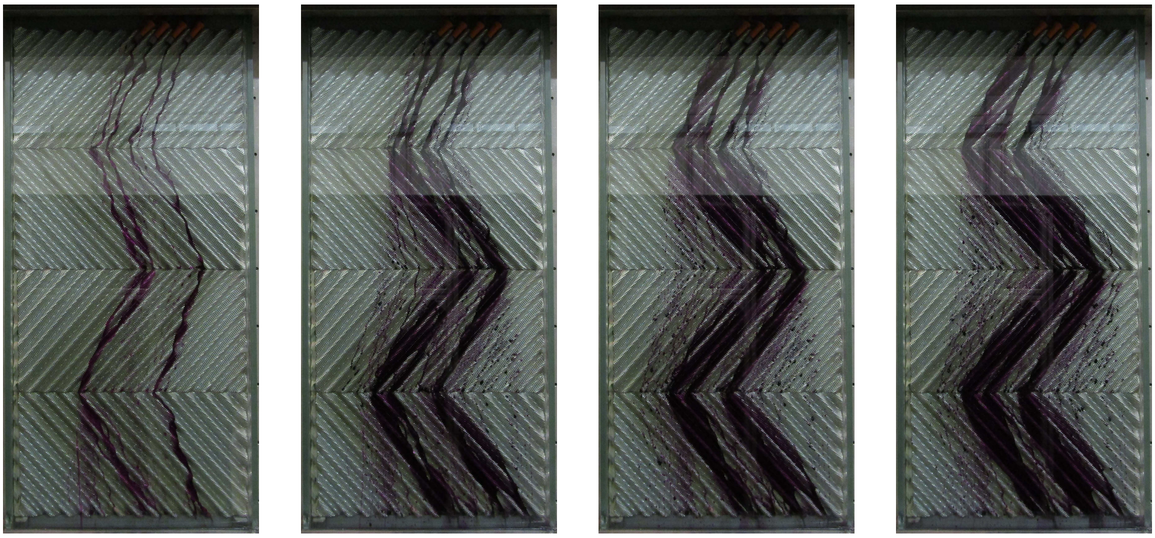

(a) $Q_L = 15$ L.h^{-1} (b) $Q_L = 35$ L.h^{-1} (c) $Q_L = 40$ L.h^{-1} (d) $Q_L = 50$ L.h^{-1}

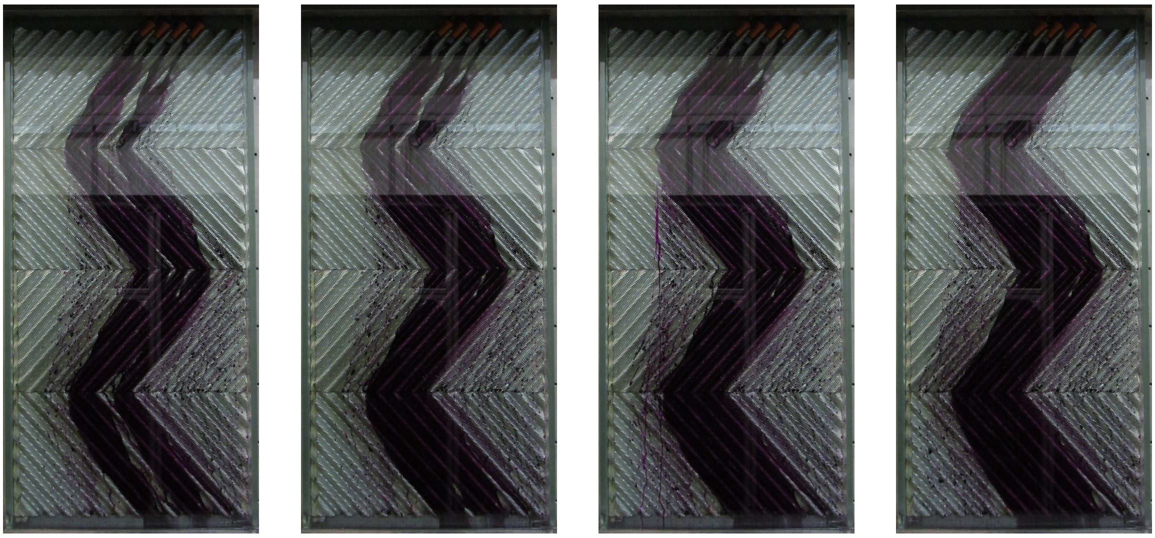

(e) $Q_L = 60$ L.h^{-1} (f) $Q_L = 70$ L.h^{-1} (g) $Q_L = 80$ L.h^{-1} (h) $Q_L = 100$ L.h^{-1}

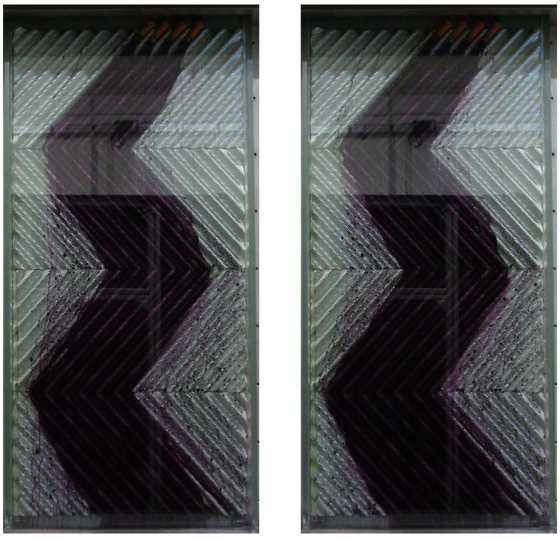

(i) $Q_L = 175$ L.h^{-1} (j) $Q_L = 300$ L.h^{-1}

Figure 6.2: Preliminary observations, increasing the flow rate.

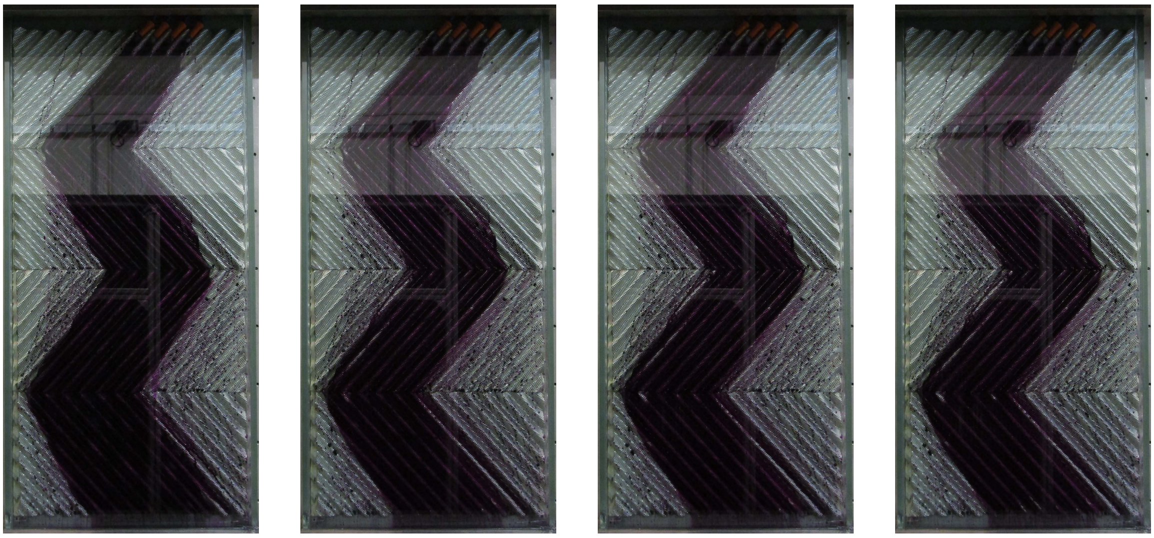

(a) $Q_L = 300$ L.h^{-1} (b) $Q_L = 80$ L.h^{-1} (c) $Q_L = 70$ L.h^{-1} (d) $Q_L = 60$ L.h^{-1}

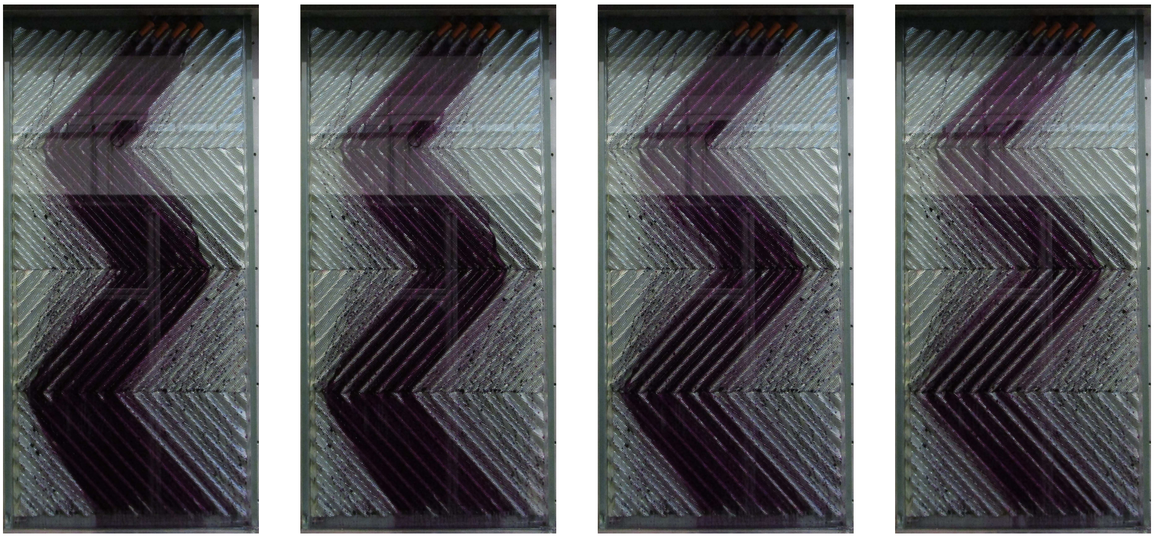

(e) $Q_L = 40$ L.h^{-1} (f) $Q_L = 25$ L.h^{-1} (g) $Q_L = 15$ L.h^{-1} (h) $Q_L = 10$ L.h^{-1}

Figure 6.3: Preliminary observations, decreasing the flow rate.

(Figure 6.5), so that the reflected light ray does get back to the sensor. Indeed, the maximum tilt of the CCI system with respect to the reflective surface must be lower than 12°. For the record, characteristics of the CCI system are given in Table 2.2.

6.2.2 Film thickness statistics

In this subsection, statistical characteristics of a liquid film flowing down a packing sheet are investigated. Examples of time signals are presented in Figure 6.6 for different Reynolds numbers. The acquisition rate was 1 kHz. The maximum film thickness increases with the Reynolds number, so does the standard deviation from the time-average film thickness. Correlations of the time-average liquid film thickness function of the Reynolds are wanted here. Some prior studies of statistical characteristics of liquid film flowing down a flat plate are listed in Table 6.1. Although these studies are not for a liquid film over corrugations, they provide experimental data of statistical characteristics to be compared with current results.

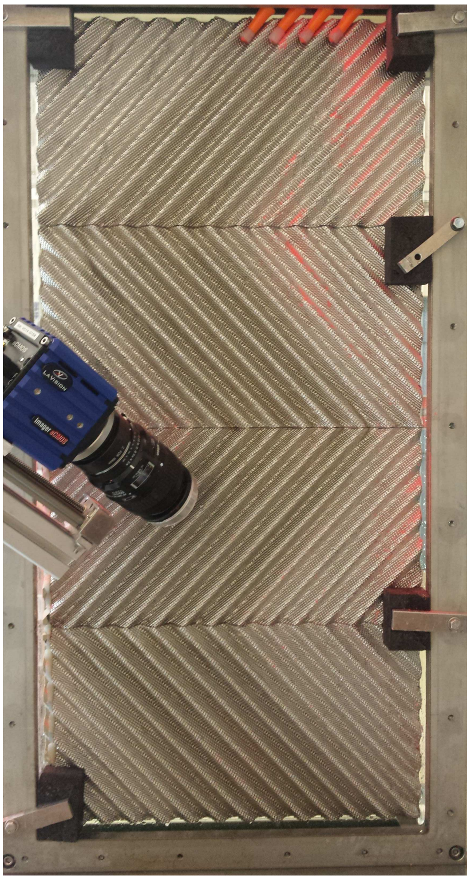

Figure 6.4: Experimental setup for interface velocity measurements. For liquid film thickness measurements, the optical pen of the CCI system replaces the camera.

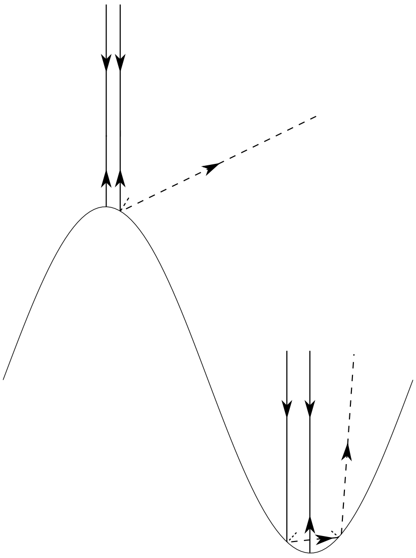

Figure 6.5: Liquid film thickness measurement on a complex geometry with a CCI system. Solid lines are for incident rays coming from the sensor and reflected rays going back to it. Dashed lines are for reflected rays not going back to the sensor; measurements are thus limited to near-trough and near-crest regions.

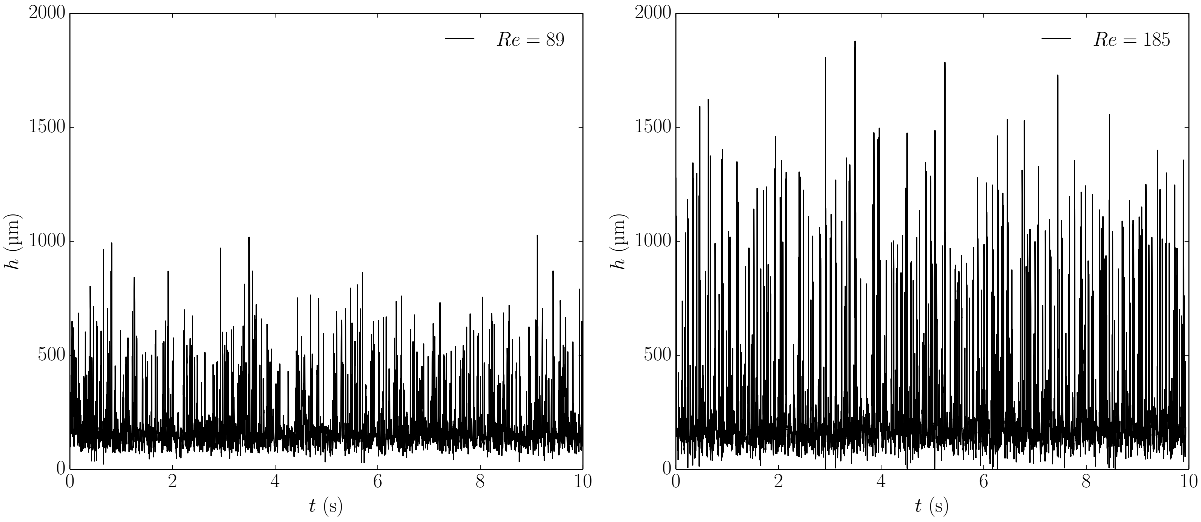

Figure 6.6: Time signals of the liquid film thickness measured at a small-corrugation trough.

Authors	Fluid	β (°)	Technique
Moran et al. (2002)	Silicone oil	45	Photochromic
Ambrosini et al. (2002)	Water	45–90	Capacitance
Drosos et al. (2004, 2006)	Water, alcoholic solutions	90	Conductance
Lel et al. (2005)	Silicone oils	13–90	CCI
Zhou et al. (2009)	Water	49–90	CCI

Table 6.1: Non-exhaustive list of prior experimental studies of statistical characteristics of liquid film flowing down a flat plate and corresponding liquid film thickness measurement technique. β is the inclination angle.

Quantitative results for the time-average liquid film thickness at troughs and crests are presented in Figure 6.7a. Results are also presented in Figure 6.7b where they are normalized by $(g \sin \alpha_c/\nu^2)^{-1/3}$ as is customarily done for direct comparison with the Nusselt solution (Lel et al., 2005). Measurement uncertainties are mainly in the systematic uncertainty due to eventual tilt of the sensor, and random uncertainties (see Section C.4.1 for calculation details of uncertainties). A curve of the form $h^* = a(1 + Re^b)$ is fitted to the normalized liquid film thickness at troughs as it has been observed that the troughs remain filled with liquid when surrounding crests undergo dewetting. A curve of the form $h^* = aRe^b$ is fitted to the normalized liquid film thickness at crests as it has been observed that the crests are not wetted for a zero liquid flow rate. The mean of the sum of squared residuals and the correlation coefficient of each curve fit are gathered in Table 6.2. Correlation coefficients suggest that good fits have been obtained in this range of Reynolds numbers. The power law at troughs is very close to the $1/3$ power law of the flat film solution, suggesting that the velocity at troughs may be reasonably predicted with the flat-film solution. The exponent of the power law is more than twice higher at crests than the $1/3$ exponent of the flat film, suggesting a different velocity profile, with increased shear stresses. The flat-film solution over-predicts the results obtained here. This may be due to the presence of small-scale corrugations, which locally modifies the hydrodynamics. Vlachogiannis and Bontozoglou (2002) observed that the liquid film thickness may be locally lower than the Nusselt film thickness, depending on the shape of corrugations.

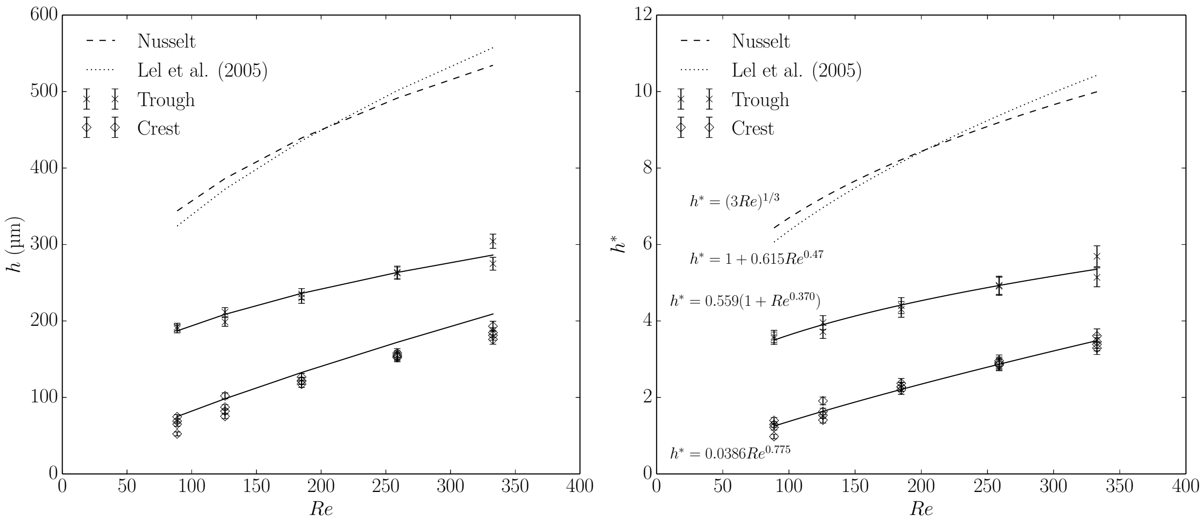

Figure 6.7: Time-average film thickness. $h^* = h(g \sin \alpha_c/\nu^2)^{1/3}$ is the normalized thickness.

Location	Equation	$\sqrt{SSR}/M$	r^2
Trough	$0.559(1 + Re^{0.370})$	0.0470	0.954
Crest	$0.0386Re^{0.775}$	0.0293	0.974

Table 6.2: Results of non-linear curve fits.

Moreover, a phase shift between the interface shape and the wall may be the reason why the thickness is lower than Nusselt's at troughs.

For these same sets of measurements, standard deviations, reported in Figure 6.8a, increase with the Reynolds number (in this range) as observed in prior work by Drosos et al. (2004) (see their Figure 7). Normalized standard deviations, reported in Figure 6.8b, seem to exhibit a local maximum for a Reynolds number of the order of 1000. Extrapolating the results to higher Reynolds number lets suggest that an increase in the Reynolds number yields a decrease in the normalized standard deviation; that is consistent with results reported by Yu et al. (1995) for water films down an inclined plane.

6.2.3 Power spectral density

Power Spectral Density (PSD) analysis have been carried out in prior studies of falling films down an inclined flat plane, by Drosos et al. (2004) for instance, and it is of interest here to observe the influence of small-scale corrugations, if any, on power density spectra. Haroun (2008) observed mass transfer enhancement with large waves in his numerical simulations. PSD analysis is thus of interest for industrial purposes as well. PSDs were estimated by Fourier transforming the auto-correlation function (Welch, 1967). 80,000 samples were used with a sampling frequency of 1 kHz.

Spectra corresponding to crest and trough measurements are reported in Figure 6.9 for different Reynolds numbers. The analysis reveals rather broad spectra, suggesting the presence of three-dimensional structures at the interface. For the smallest Reynolds number studied here, $Re = 89$, there is no noticeable peak corresponding to a specific frequency. For larger Reynolds numbers, spectra exhibit a peak, corresponding to a modal frequency of about 9 Hz. Results are here very close to that obtained with inclined-plane

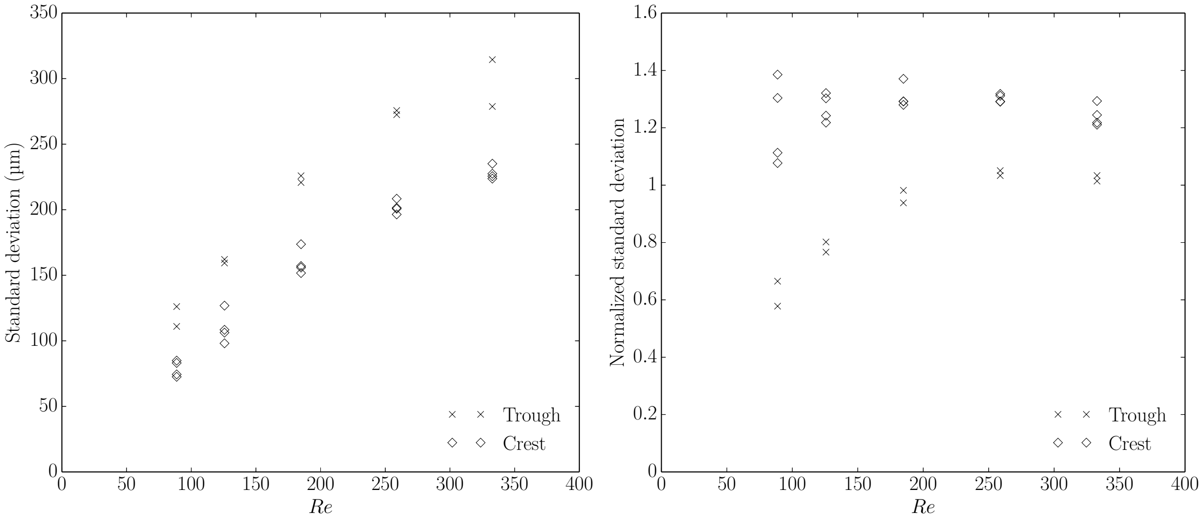

Figure 6.8: Standard deviations and standard deviations normalized by the time-average film thickness.

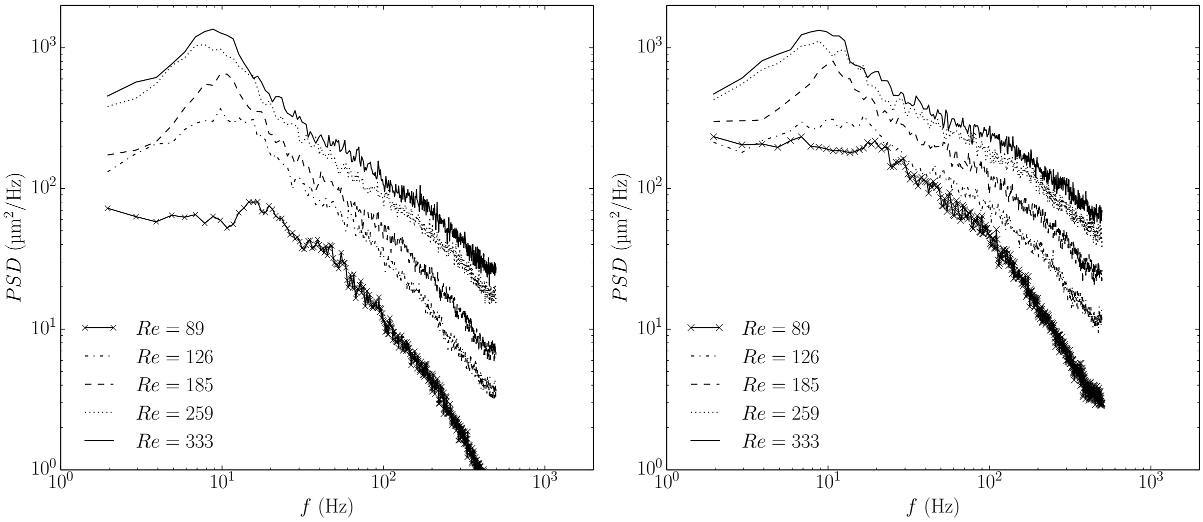

(a) Crest measurement.

(b) Trough measurement.

Figure 6.9: Power spectral density of the liquid film thickness.

configurations by Ambrosini et al. (2002) and Drosos et al. (2004) regarding the modal frequency which is about 8 to 10 Hz, suggesting that the presence of small corrugations does not have quantitative effects on interfacial structures of the flow. The higher the Reynolds number, the sharper the peak: large waves carry even more energy with increasing Reynolds number. These large waves are not necessarily that of highest amplitudes, as shown by Zadrazil et al. (2014) with their vertical annular flow configuration. A small dependency on the Reynolds number is noticeable for the modal frequency that seems to slightly decrease with increasing Reynolds number. Zadrazil et al. (2014) also noticed that slight decrease in the modal frequency with increasing the Reynolds number.

Differences between spectra at trough and crest are not significant at low frequencies, especially for Reynolds numbers $Re \geq 185$. Differences between crest and trough spectra are more noticeable at higher frequencies (larger than 20 Hz); at the modal frequency the density power has roughly the same value for trough and crest measurements (for $Re \geq 185$) so smaller waves carry more energy at troughs, where the

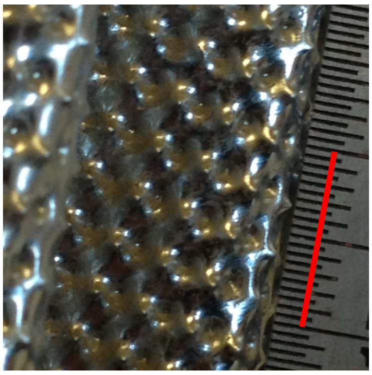

Figure 6.10: Typical observation area for interface velocity measurements, corresponding to the upper face of a large-scale triangular corrugation. The red segment is one centimeter long.

mean thickness is higher compared to that at crests. For a similar Reynolds number, the exponent of the power law decay is smaller at crests than at troughs, which is consistent with the fact that the spectra look almost identical for lower frequencies while the mean film thickness is higher at troughs, so the frequency spectrum at troughs must be broader than at crests. Another explanation could be given from the fact that the film thickness locally decreases in the vicinity of a crest, yielding a local decrease in the Weber number and hence stabilization of smallest waves, explaining a lower cutoff frequency and a narrower spectrum at crests compared to that at troughs. Note that time signals in Figure 6.9 are piecewise continuous: discontinuities quantitatively affect the estimate of power density spectra at higher frequencies (power law decays) but the modal frequency is correct because its estimate results from continuous parts of the time signal.

6.3 Interface velocity measurement without the glass channel

6.3.1 Setup

As reported in Chapter 5, the use of hydrophobic fluorescent particles has enabled measurement of the interface velocity of a flat film and further observed the one-dimensionality of the interface velocity field of a 2D wavy film by PIV and PTV. It is attempted here to apply one of these techniques to a liquid film flow down a REU of structured packing sheet. The camera aims at the REU, in the direction perpendicular to the liquid film flow inside a channel (Figure 6.4), i.e. perpendicular to the upper face of the large-scale triangular corrugation (Figure 6.10). Hydrophobic particles are dusted at the top of the geometry, just after the inlet. Particles that do not stick to the interface are blown away in order not to hinder observations. As in Chapter 5, the same pulsed Laser is used, with a repetition rate of 15 Hz. Particles are illuminated with the beam spot, magnified to reach a diameter of a few centimeters. Calibration was again carried out by using a ruler carefully deposited on the upper face of the large-scale triangular corrugation (Figure 6.11). The apparent pixel size was $10.8 \pm 0.5\%$ µm/pix. A typical frame that is exploitable is shown in Figure 6.12.

Compared to the inclined-plane tests of Chapter 5, it was difficult to obtain uniform concentrations of particles in the observation area. However it was possible to track particles with such low concentrations, and get several velocity vectors from an image pair. The PTV algorithm of Brevis et al. (2011), successfully tested for flat and wavy falling films down an inclined plane in Chapter 5, was used for the purpose.

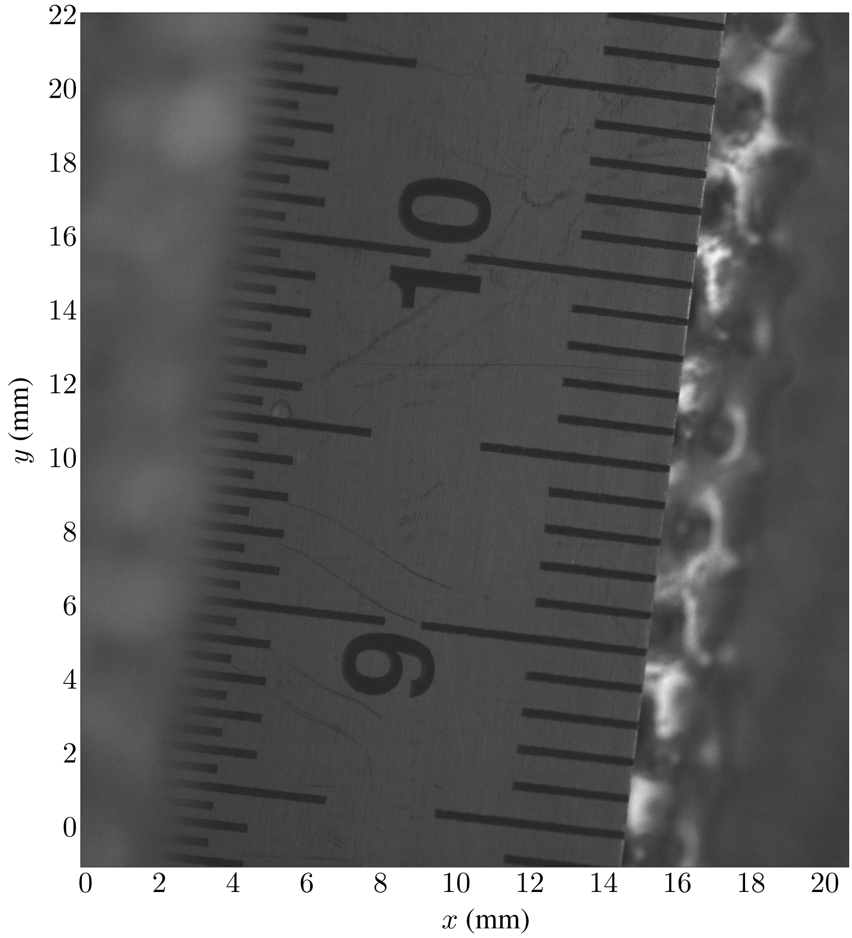

Figure 6.11: Calibration procedure. The ruler is deposited on the upper face of the large-scale triangular corrugation.

6.3.2 Results and discussion

Results presented here are for the flow rate $Q_L = 125$ L.h^{-1}, or $Re = 185$. The temporal resolution was set to 250 µs, yielding displacements in the range 8–20 pixels. Velocity vectors were obtained from different image pairs, to yield a mean velocity field that was interpolated on a grid. Figure 6.13 shows the mean interface velocity field, corresponding to the boxed area of Figure 6.14. The spatial resolution for the vector field in Figure 6.13 is 32 pixels, corresponding to 346 µm. In processing image pairs, particles were located by indicating the maximum size of a particle and the minimum intensity threshold emitted by a particle, so that there were no outliers due to eventual ill-focused particles. No post-processing was applied but deleting a few vectors directed upwards. Some vectors still seem to be erroneous, like that with smallest magnitude at $(x, y) = (8.8, 30.1)$ mm, an error that must be due to an incorrect evaluation of a particle center (Guezennec et al., 1994).

It can be observed in Figure 6.13 that the flow does not follow the channels of large-scale corrugations, but is essentially directed downwards. The crest at $(x, y) = (8.7, 30.8)$ mm seems to correspond to a local maximum of the velocity magnitude. The trough at $(x, y) = (7.7, 35.3)$ mm seems to correspond to a local minimum of the velocity magnitude. Depending on the shape of corrugations and flow parameters (Pozrikidis, 1988), and consistently with an increase (resp. decrease) in the wall shear stress next to crests

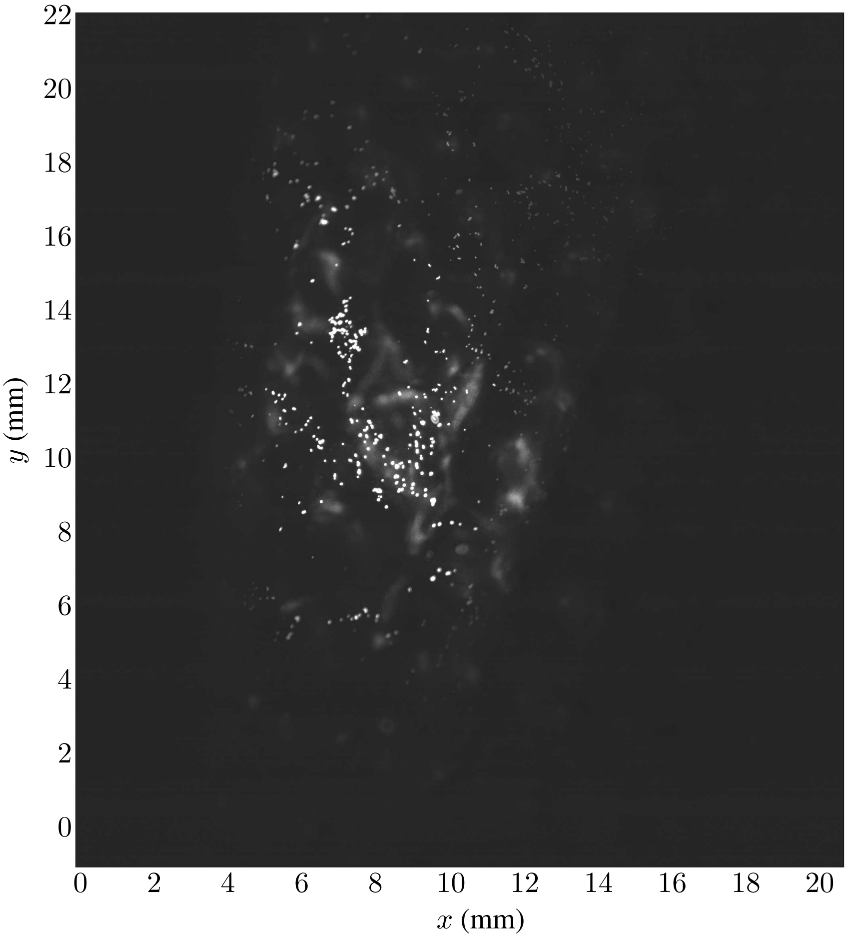

Figure 6.12: Typical frame exploitable in PTV. Troughs and crests of small-scale corrugations are underneath hydrophobic particles.

(resp. troughs) with respect to that of the flat film, it is possible to observe local maxima of the velocity field next to crests, and local minima next to troughs; that behavior seems even more intense with larger differences in the liquid film thickness between troughs and crests of periodic corrugations (Trifonov, 1999). On the other hand, looking at the entire velocity field, it seems unclear whether some features of small-scale corrugations locally affect the interface velocity field. That would be consistent with power spectral densities of liquid film thickness reported in Section 6.2.3, the modal frequency wherein having the same value at troughs and crests. In Figure 6.13, the velocity magnitude globally seems to decrease with decreasing y. The upper part of the velocity field in Figure 6.13 is closer to the trough of large-scale triangular corrugations, for which the local inclination angle with the horizontal reaches $\pi/2$, hence explaining the presence of higher velocity magnitudes there. Calculating a space-average velocity magnitude does not make any sense here since the flow is clearly not uniform.

But it is still possible to locally compare the results with the flat-film analytical solution. Large-scale triangular corrugations make an angle $\alpha_c = \pi/4$ with the horizontal and their half top angle, $\arctan\big(\lambda_u/(2h_u)\big)$, is also of the order $\pi/4$. Therefore, this suggests a comparison of local velocity magnitudes for $y \leq 32$ mm with the flat-film analytical solution corresponding to an angle $\pi/4$, which actually is of the order of 0.65 m.s^{-1}. Using the flat-film solution clearly over-predicts the velocity magnitude for $y \leq 32$ mm, which is consistent with the fact that the flat-film thickness solution would over-predict the

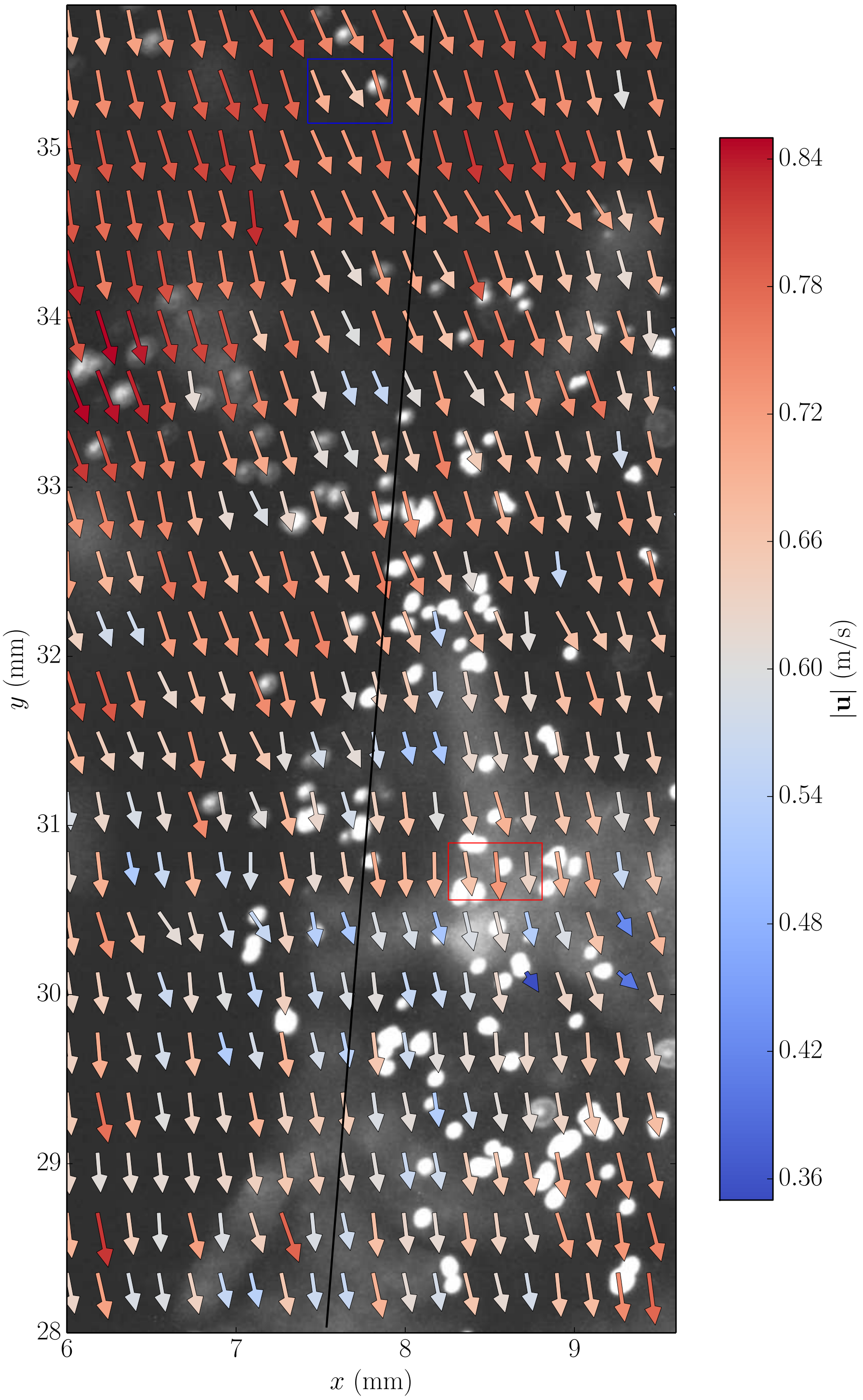

Figure 6.13: Local mean interface velocity field obtained by PTV; $Re = 185$. The image in the background was used amongst all image pairs selected for the construction of this mean velocity field. The straight line indicates the direction of the channel (large-scale triangular corrugation). The blue and red boxed areas seem to correspond to local extrema of the velocity magnitude.

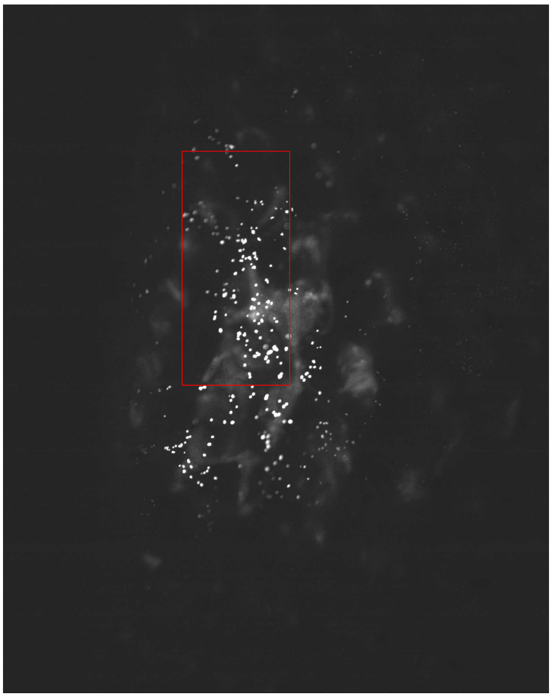

Figure 6.14: Typical frame exploitable in PTV. Troughs and crests of small-scale corrugations are underneath hydrophobic particles. A velocity field corresponding to the boxed area was constructed in Figure 6.13.

thickness, as observed in Section 6.2. Further up in Figure 6.13, for $y \geq 32$ mm, it would seem more appropriate to compare velocity magnitudes with that of a vertical flat film, which is of the order of 0.73 m.s^{-1}. The flat-film solution clearly under-predicts largest velocity magnitudes, given that the upper left of Figure 6.14 does not correspond exactly to the trough of large-scale triangular corrugations yet, and one would expect the solution of a vertical film to over-estimate the velocity magnitudes there.

6.4 Liquid film thickness measurement through the glass channel

6.4.1 Difficulties

Having investigated the case of falling films, in this section, liquid film thickness measurements in the presence of a counter-current gas flow are presented. For that, the gas flow is confined in a glass channel as explained in Section 6.1. A difficulty arises due to optical dispersion in use of the same CCI system for measuring the liquid film thickness through the glass. Considering the particular case with optical axis of the optical pen perpendicular to the glass, that leads to a deformation of the measuring range (image of the white light point source by the optical pen) along the optical axis. The measured distance is thereby modified, and the modification is a function of the wavelength. That may be corrected when knowing the glass thickness and the dispersion curve of the glass, i.e. the dependence of the refractive index on the

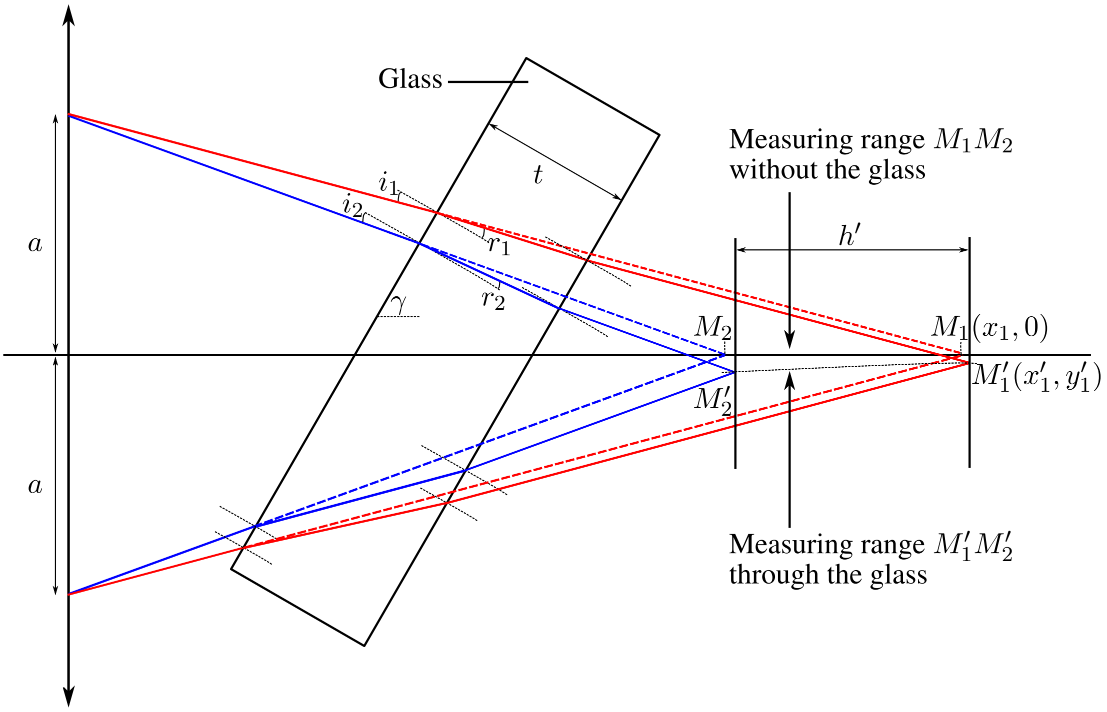

Figure 6.15: Modification of the measuring range of the CCI system by interposition of a transparent medium of width t and refraction index n. a is the size of the chromatic lens. The x-axis coincides with the optical axis of the optical pen.

wavelength (see Figure 7 of Dietze et al. (2009)). For the particular case of a liquid film flowing down over a packing metal sheet, distance measurement through the glass that makes an angle γ with the optical axis of the optical pen are further affected in a sense that the measuring range deviates from the optical axis (see Figure 6.15).

An idea to get around that problem is to use a pair of compensating prisms, in order for the optical axis of the optical pen to be perpendicular to the transparent medium. Such a procedure was attempted, first measuring the refractive index of the glass to use prisms made of a glass with the same refractive index, then choosing the angle of prisms adequately – the angle that the optical axis of the optical pen makes with the normal to the glass channel is $\arctan(2h_u/\lambda_u) \simeq \pi/4$. Unfortunately, light attenuation through the glass was even more pronounced with the pair of prisms and the signal detected by the sensor was too weak for accurate distance measurement, even by maximizing the exposure time.

Several alternatives are worth considering:

- Asking the manufacturer for a CCI system specifically designed to carry out measurements with an angle γ through a transparent medium. This may be dismissed straight away as the system would be designed for a fixed angle γ, which is not wanted, should observations of liquid films over other geometries be foreseen;
- Using a more powerful light source and a pair of prisms, and correcting distance measurement signals, as done by Dietze et al. (2009);
- Carrying out measurements through the glass, not correcting the signals but accurately estimating systematic uncertainties.

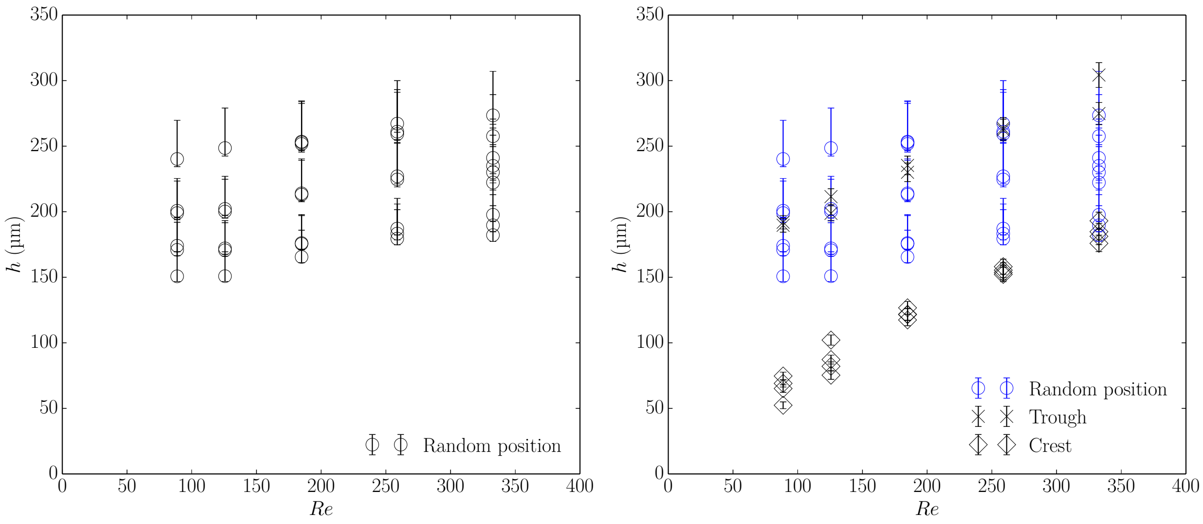

(a) Random-position measurement.

(b) Comparison with glass-free results.

Figure 6.16: Time-average film thickness for measurements through the glass channel and comparison with glass-free results previously obtained at troughs and crests.

Although using a more powerful light source and the pair of prisms appears to be the more rigorous approach, to set up in due time, preliminary tests were conducted without correcting time signals but accounting for the deviation of the measuring range in calculations of systematic uncertainty. The acquisition rate had to be lowered down to 200 Hz (against 1 kHz for prior measurements in Section 6.2) to have enough illumination going back to the CCI sensor, the glass channel itself participating to light attenuation. For the sake of clarity, calculation of the systematic uncertainty introduced by such a procedure is detailed in Section C.4.2. As the functional relationship of the CCI system (the wavelength seen by the sensor as a function of the distance) is not provided by the manufacturer, thicknesses could not be corrected, and are here reported as they were displayed by the CCI system, with an additional positive uncertainty, added to account for the deviation of focusing points along the optical axis of the optical pen. The positive, mean relative uncertainty was used in calculations, determined in Section C.4.2, corresponding to the error in a thickness measurement over the entire measuring range. This mean relative uncertainty in the thickness measurement was determined to be 0.083, corresponding, for instance, to a maximum uncertainty of 23 µm in a thickness of 275 µm. For the same thickness, the lateral deviation between the two focusing points (that of the reference substrate and that of the gas-liquid interface) is 33 µm, which sounds reasonable given that the corrugations have amplitude and wavelength of 0.3 mm and 2.8 mm, respectively.

6.4.2 Results

A further difficulty arose in positioning the optical pen in order for the measuring range to intersect the solid substrate, the lateral deviation between the two extreme focusing points, $y'_{\mathrm{red}} - y'_{\mathrm{blue}}$ being of the order of 1.2 mm (see Section C.4.2 for details). As a consequence, it was not possible to know with certitude to which location the signal corresponded – a trough or a crest. Figure 6.16 presents qualitative results that were obtained though. Results are also compared with glass-free results of Section 6.2. Good agreement is obtained whenever the glass-free values are within uncertainty bars of through-glass values. All trough values lie within uncertainty intervals of through-glass values, which sounds promising. However, some through-glass values do not correspond to any glass-free value, of a trough or a crest. This is thought to be due to the deviation of focusing points away from the optical axis of the optical pen, the deviation being different for the reference point (solid substrate) and the dynamic point (reflective interface). This may lead to inaccurate results. That may be the reason why no through-glass values have been found to correspond to crest glass-free values. Finally, such a procedure is not reliable and it seems necessary to use a more powerful light, along with a pair of compensating prisms to prevent the measuring range deviating from the optical axis.

6.5 Conclusion

Local measurements of liquid film thickness were carried out at troughs and crests of small-scale corrugations by CCI. Results revealed that, at the center of the upper face of large-scale corrugations, the liquid film thickness at troughs and crests of small corrugations were smaller than that predicted by the flat-film analytical solution. In that same area, measurements of interface velocity magnitude, carried out by PTV for a single value of the Reynolds number though, were also found to be smaller than that of the flat-film analytical solution, which was consistent with the film thickness. Higher velocity magnitudes were measured closer to the trough of the large-scale corrugation, where the flat-film solution would under-predict it. Liquid film thicknesses higher than the flat-film solution are expected there. A local maximum (resp. minimum) of velocity magnitude was observed next to a small-corrugation crest (resp. trough), for these specific flow conditions, consistently with an increase (resp. decrease) in the wall shear stress next to the crest (resp. trough) (Pozrikidis, 1988). Power density spectra were found broader at troughs than at crests, suggesting that capillary effects locally stabilize smallest waves at crests. Regarding the mean liquid film thickness, a power law close to the flat film solution was found at troughs, suggesting that the flat-film solution may give reasonable prediction of the flow at troughs. The power law was found higher at crests, suggesting a different velocity profile with increased shear stresses.

Further experimental and numerical work is needed to identify and characterize different regimes. Anticipating measurements with a counter-current gas flow, liquid film thicknesses were measured, still for a falling film, through the glass channel (designed to confined the gas flow), by CCI. The additional systematic uncertainty for measuring film thicknesses through the glass channel was quantified, and discrepancies were obtained from the glass-free case, as expected, mainly due to lateral deviation (function of the wavelength) of the measuring range of the CCI system. Using a pair of compensating prisms and a more powerful light source would certainly allow to alleviate these discrepancies. For future transient simulations of three-dimensional liquid film flows with moving contact lines, it is proposed to test the macroscale model for first fingering instabilities (Huppert, 1982), and further on liquid film flows over structured packing sheets, accounting for small-scale corrugations in the computational geometry.

Conclusions and perspectives

The work presented in this thesis consists of two main strands of research. One of these concerns the development and use of a CFD methodology for the numerical simulation of three-dimensional large-scale flows. Key here is the use of an available (2D) large-scale model for contact line dynamics in two-phase flow solvers, which has resulted in a numerical tool for use in investigations of wetting phenomena on complex surfaces. The second strand of research was to develop an experimental methodology to perform quantitative measurements of liquid film thickness and interface velocity on such a geometry, aiming to characterize different flow regimes while providing experimental data. Both these two strands were necessary to bridge the gap between experiments and CFD of liquid film flows over structured packing sheets.

The development of numerical methods for the simulation of two-phase flows with moving contact lines was undertaken in the framework of interface-capturing methods for two-phase flows. Using the freeware TPLS as a basis, key steps for reducing mass conservation errors in level-set methods were identified and implemented, in Chapter 3. A new computational method for level-set simulations of flows with moving contact lines in 3D was developed and validated against numerical and experimental benchmark tests, in Chapter 4. 3D tests suggest that available 2D macroscale models are potentially usable for 3D flows with moving contact lines. The macroscale model was further implemented in a commercial volume-of-fluid solver to facilitate dissemination of this work in industry, so that the macroscale model can be tested in numerical simulation of flows with moving contact lines over complex surfaces, such as structured packing sheets.

Likewise, the experimental methods suitable for quantitative characterization of liquid films flowing down complex surfaces were deployed and validated using basic tests. Experimental techniques were used further to perform liquid film thickness and interface velocity measurements of liquid film flowing down a representative elementary unit of structured packing sheet. Different regimes were identified and differences from the flat-film analytical solution were analyzed.

Specifically, the approach in the first (numerical) part of the thesis, is mainly based on a level-set method for numerical simulations of two-phase flows with moving contact lines. Different existing reinitialization methods therein were implemented in the otherwise pre-existing in-house code (TPLS) and tested first against standard benchmarks wherein the Navier-Stokes solver is not used such as a translating sphere. This has established that the Hamilton-Jacobi equation used in reinitialization may be accurately solved with a TVD RK2 scheme in time and a WENO5 scheme in space. Two other tests were carried out wherein the Navier-Stokes equations are resolved. It was demonstrated that Rayleigh-Taylor instability without capillary forces could be accurately simulated using the near-interface fix of Hartmann et al. (2010) (HCR1-W5-RK2) or that of Sussman and Fatemi (1999) (SF-W5-RK2). Additional tests for a static and then a translating bubble, for which the magnitude of parasitic currents was found to be as low as that reported in the recent literature on other interface-capturing codes, suggest finally that SF-W5-RK2 is the most promising method amongst those tested here for reduced mass conservation errors in level-set. That particular reinitialization method was used thereafter in this thesis. The computational method was extended subsequently to account for contact line dynamics in simulating flows with moving contact lines. A new numerical method was developed, for 3D flows, that basically consists in advecting the contact line with the velocity corresponding to the actual interface slope in the first cell next to the wall, the velocity magnitude being obtained from theory (the macroscale model). Axisymmetric droplet spreading in a slow, viscous regime and then in a more rapid (inertial) regime wherein inertial effects arise in the contact-line region were simulated and found to compare very well with prior DNS and experimental work. Further tests were conducted for sliding droplets down an inclined plane. Results were qualitatively consistent with experiments of Podgorski et al. (2001) and Le Grand et al. (2005), which comforts the potential use of the macroscale model in 3D, for qualitative agreement at the macroscale at least, even in the presence of highly-curved contact lines. Although quantitative results for the geometry and the speed of the drops were very satisfactory, they do suggest that the viscous model Cox (1986), developed with negligible gravity, may not be suitable for flows in the presence of significant effects of gravity (Bond number values $Bo \geq 1$). These results therefore call for further DNS and theoretical investigation to account for gravity in theoretical (macroscale) models. Overall, contact-line dynamics quantitatively affects spreading and it may affect the flow qualitatively up to its macroscale in some cases. Finally, the macroscale model was implemented also in a commercial volume-of-fluid code, albeit in a different way due to restrictions on the modifications users can make. Qualitative and quantitative agreement was obtained for axisymmetric spreading in the inertial regime. The single sliding-drop test that was conducted also compared satisfactorily with experimental results and numerical results obtained with TPLS.

In the second (experimental) part, specifically, liquid film thicknesses were measured by Chromatic Confocal Imaging, which is a non-intrusive single-point measurement technique; velocity measurements were carried out by particle tracking using hydrophobic fluorescent particles. Validation tests were performed for a two-dimensional viscous liquid film flowing down an inclined plane, comparing against the flat-film analytical solution, for which very good agreement was obtained. A further test was conducted for a two-dimensional wavy film, introducing a wave using a vibrating pot. There, the amplitude of the wave could be measured simultaneously, with success, by Chromatic Confocal Imaging and using a Position Sensing Device to relate the displacement of the Laser beam spot to the wave amplitude. The interface velocity fields obtained using particle tracking and particle imaging algorithms were two-dimensional, as expected, and compared well to each other. The validated techniques were then tested for falling films down the upper face of a large-scale triangular corrugation of structured packing sheet. Observations were made in the center of that area, between the trough and the summit of the large-scale triangular corrugation. Liquid film thickness was measured at troughs and crests of small-scale corrugations, evidencing larger thicknesses at troughs. For Reynolds numbers in the range $89 - 333$, the film thickness was found to be over-predicted by the corresponding flat-film solution, based on the angle of large-scale triangular corrugations. This may be due to the presence of small-scale corrugations, which locally modifies the hydrodynamics. Such a behavior has already been observed (Vlachogiannis and Bontozoglou, 2002). The local interface velocity magnitude in the corresponding observation area was found to be under-predicted by the flat-film solution next to the trough of the large-scale triangular corrugation, but over-predicted further away from that trough. The velocity magnitude seems to exhibit maxima at crests and minima at troughs; this would be consistent with an increase in the wall shear stress next to crest, and a decrease next to troughs, with respect to the flat film. Results of liquid film thicknesses were fitted to power laws of the Reynolds number. The exponent at troughs was found to be very close to the that of the flat film, suggesting that the flat-film solution may be suitable for predicting flow behavior at troughs. At crests, the exponent was found to be significantly higher than for the flat-film solution, suggesting a different velocity profile with increased shear stresses. Power density spectra of the liquid film thickness estimated at troughs and crests were found to be rather broad, suggesting the presence of three-dimensional interfacial structures. Narrower spectra were obtained at crests, with lower cutoff frequency than at troughs, suggesting that capillary effects tends to stabilize the smallest interfacial structures at crests. For the purpose of making quantitative measurements for a liquid film sheared by a counter-current gas flow, similar measurements through a transparent medium were made. The time signal was found to be modified by optical defects. For counter-current systems, using the Chromatic Confocal Imaging system with a more powerful light source and a compensating pair of prisms may yield accurate liquid film thickness measurement through the glass channel.

The experimental and computational developments presented here will be key in numerical simulations of three-dimensional liquid film flows (with moving contact lines) over a representative elementary unit of structured packing sheets. Guidelines are proposed here to continue the development and validation of such a CFD methodology. As discussed in Chapter 1, the flow at the scale of large corrugations is desired (Raynal and Royon-Lebeaud, 2007; Said et al., 2011; Soulaine, 2012). As Haroun et al. (2014) observed strong dependence of wetting on the contact angle in numerical simulations, it is proposed here to account for contact line dynamics in the simulations. As underlined in this memoir, contact-line dynamics has quantitative effects and even sometimes qualitative effects on the flow up to the macroscale. The macroscale model of Cox (1986, 1998), developed for general two-dimensional flows, has been implemented and validated against two-dimensional and axisymmetric flows in this thesis, and been tested successfully against three-dimensional sliding drops. The next step is, of course, to validate the model for liquid film flows with moving contact lines, on a rather basic case first, for which experimental and theoretical results are available. The fingering instability is perfectly suited for this purpose. In his seminal work, Huppert (1982) observed viscous liquid films of constant volume flowing down an inclined plane. In the lubrication approximation, that is for a thin viscous film, he first derived a similarity solution for the height profile of the two-dimensional flow in the outer region, with negligible gravitational effects ($Bo \ll 1$). After the two-dimensional flow had developed, Huppert (1982) observed the development of small disturbances at the moving contact line, that would grow in time to form saw-tooth or rivulet patterns, referred to as fingers. Since then, fingers have been studied extensively, experimentally (de Bruyn, 1992; Veretennikov et al., 1998; Johnson et al., 1999) and theoretically or numerically (Troian et al., 1989; Bertozzi and Brenner, 1997; Kalliadasis, 2000; Kondic and Diez, 2001). Prior numerical work, essentially in the lubrication approximation, consisted in perturbing the contact line of a base-state flow, and observe the formation and evolution of fingers, using results from experiments and the linear theory for qualitative and quantitative comparisons. It is proposed here to adopt the same methodology, but using the full Navier-Stokes equations and the macroscale model of Cox (1986). For that, two-dimensional liquid films with moving contact line would be simulated first, in a two-dimensional channel with no-slip condition at bottom and top boundaries, the analytical profile of a liquid film in a channel (Fourati et al., 2013; Schmidt et al., 2016) prescribed at the inlet, and an outflow condition for the remaining boundary. When the base state has been reached, the domain can be extended in the third (transverse) direction (with periodic boundary) and the contact line be perturbed with a single mode. The growth of the perturbation can then be compared to theoretical (Bertozzi and Brenner, 1997), numerical (Kondic and Diez, 2001), and experimental results (Johnson et al., 1999). If the general macroscale model of Cox (1986) happens to give satisfactory results to predict the linear growth of fingers, then this can be used for further three-dimensional simulations of flows with moving contact lines on complex surfaces. The CFD methodology consists in resolving the macroscale and part of the intermediate region, influenced by the inner dynamics only, that is typically a few tens of microns. Therefore, for simulations of flows with moving contact lines on structured packing sheets with small-scale corrugations of $\lambda_c = 2.8$ mm, the corrugations must be taken into account in the computational geometry. Experimental data of liquid film thickness and interface velocity will be used to support the CFD methodology.

In future experimental work, it would then be interesting to observe the effect of the counter-current gas flow in the liquid film thickness, on the power law of liquid film thicknesses (function of the Reynolds number), and on power density spectra as well. For that, the CCI system may be used with a more powerful light source and a pair of compensating prisms to observe the flow through the glass channel. Interface velocity measurements may be foreseen as well, using compensating prisms. Regarding PSD spectra of the liquid film thickness, it is expected that the counter-current gas flow will impact the modal frequency, while increasing the energy of the signal, as observed by Drosos et al. (2006) and Zadrazil et al. (2014), in different configurations though, for a flow down an inclined flat plane and a vertical annular flow, respectively. Another interesting aspect would be to undertake wave celerity measurements, as done by Drosos et al. (2004) for instance, by cross-correlating time signals of two optical pens, and see the impact, if any, of small corrugations on dispersion curves compared to the flat-film case, bearing in mind that wavy films may be beneficial or detrimental to mass transfer under some circumstances.

Bibliography

T. Abadie, J. Aubin, and D. Legendre. On the combined effects of surface tension force calculation and interface advection on spurious currents within volume of fluid and level set frameworks. *Journal of Computational Physics*, 297(0):611 – 636, 2015.

R. J. Adrian. Particle-imaging techniques for experimental fluid mechanics. *Annual Review of Fluid Mechanics*, 23(1):261–304, 1991.

S. Afkhami, S. Zaleski, and M. Bussmann. A mesh-dependent model for applying dynamic contact angles to vof simulations. *Journal of Computational Physics*, 228(15):5370 – 5389, 2009.

S. Alekseenko, D. Markovich, A. Evseev, A. Bobylev, B. Tarasov, and V. Karsten. Experimental investigation of liquid distribution over structured packing. *AIChE journal*, 54(6):1424–1430, 2008.

P. Alix and L. Raynal. Liquid distribution and liquid hold-up in modern high capacity packings. *Chemical Engineering Research and Design*, 86(6):585–591, 2008.

M. H. Allouche. *Étude théorique et expérimentale de la stabilité de l'écoulement de films de fluide non Newtonien sur plan incliné*. PhD thesis, Université Claude Bernard Lyon I, 2014.

W. Ambrosini, N. Forgione, and F. Oriolo. Statistical characteristics of a water film falling down a flat plate at different inclinations and temperatures. *International Journal of Multiphase Flow*, 28(9): 1521–1540, 2002.

K. Argyriadi, M. Vlachogiannis, and V. Bontozoglou. Experimental study of inclined film flow along periodic corrugations: The effect of wall steepness. *Physics of Fluids (1994-present)*, 18(1):012102, 2006.

A. Aroonwilas, P. Tontiwachwuthikul, and A. Chakma. Effects of operating and design parameters on CO_2 absorption in columns with structured packings. *Separation and Purification Technology*, 24(3): 403–411, 2001.

J. D. Bernardin, I. Mudawar, C. B. Walsh, and E. I. Franses. Contact angle temperature dependence for water droplets on practical aluminum surfaces. *International Journal of Heat and Mass Transfer*, 40(5): 1017–1033, 1997.

A. L. Bertozzi and M. P. Brenner. Linear stability and transient growth in driven contact lines. *Physics of Fluids (1994-present)*, 9(3):530–539, 1997.

R. Billet and M. Schultes. Prediction of mass transfer columns with dumped and arranged packings: updated summary of the calculation method of Billet and Schultes. *Chemical Engineering Research and Design*, 77(6):498–504, 1999.

D. Bonn, J. Eggers, J. Indekeu, J. Meunier, and E. Rolley. Wetting and spreading. *Review of Modern Physics*, 81:739–805, May 2009.

J. Brackbill, D. B. Kothe, and C. Zemach. A continuum method for modeling surface tension. *Journal of Computational Physics*, 100(2):335–354, 1992.

R. Brahem. *Étude de l'effet d'échelle sur les plateaux à clapets de colonnes d'absorption*. PhD thesis, Toulouse, INPT, 2013.

W. Brevis, Y. Niño, and G. Jirka. Integrating cross-correlation and relaxation algorithms for particle tracking velocimetry. *Experiments in Fluids*, 50(1):135–147, 2011.

J. Butcher. Numerical methods for ordinary differential equations in the 20th century. *Journal of Computational and Applied Mathematics*, 125(1–2):1 – 29, 2000. Numerical Analysis 2000. Vol. VI: Ordinary Differential Equations and Integral Equations.

A. Cassie and S. Baxter. Wettability of porous surfaces. *Transactions of the Faraday Society*, 40:546–551, 1944.

H. Chang. Wave evolution on a falling film. *Annual Review of Fluid Mechanics*, 26(1):103–136, 1994.

A. Charogiannis, J. S. An, and C. N. Markides. A simultaneous planar laser-induced fluorescence, particle image velocimetry and particle tracking velocimetry technique for the investigation of thin liquid-film flows. *Experimental Thermal and Fluid Science*, 68:516 – 536, 2015.

Q. Chen, E. Ramé, and S. Garoff. The breakdown of asymptotic hydrodynamic models of liquid spreading at increasing capillary number. *Physics of Fluids*, 7(11):2631–2639, 1995.

P. Cobelli, V. Pagneux, A. Maurel, and P. Petitjeans. Experimental study on water-wave trapped modes. *Journal of Fluid Mechanics*, 666:445–476, 2011.

R. G. Cox. The spreading of a liquid on a rough solid surface. *Journal of Fluid Mechanics*, 131:1–26, 1983.

R. G. Cox. The dynamics of the spreading of liquids on a solid surface. Part 1. Viscous flow. *Journal of Fluid Mechanics*, 168:169–194, 7 1986.

R. G. Cox. Inertial and viscous effects on dynamic contact angles. *Journal of Fluid Mechanics*, 357: 249–278, 2 1998.

M. Damsohn and H.-M. Prasser. High-speed liquid film sensor for two-phase flows with high spatial resolution based on electrical conductance. *Flow Measurement and Instrumentation*, 20(1):1–14, 2009.

J. R. de Bruyn. Growth of fingers at a driven three-phase contact line. *Physical Review A*, 46(8):R4500, 1992.

P.-G. de Gennes. Wetting: statics and dynamics. *Reviews of Modern Physics*, 57(3):827, 1985.

G. Della Rocca and G. Blanquart. Level set reinitialization at a contact line. *Journal of Computational Physics*, 265(0):34 – 49, 2014.

G. F. Dietze, F. Al-Sibai, and R. Kneer. Experimental study of flow separation in laminar falling liquid films. *Journal of Fluid Mechanics*, 637:73–104, 2009.

H. Ding, P. D. Spelt, and C. Shu. Diffuse interface model for incompressible two-phase flows with large density ratios. *Journal of Computational Physics*, 226(2):2078 – 2095, 2007.

H. Ding, E. Q. Li, F. H. Zhang, Y. Sui, P. D. M. Spelt, and S. T. Thoroddsen. Propagation of capillary waves and ejection of small droplets in rapid droplet spreading. *Journal of Fluid Mechanics*, 697: 92–114, 4 2012.

E. Drosos, S. Paras, and A. Karabelas. Characteristics of developing free falling films at intermediate Reynolds and high Kapitza numbers. *International Journal of Multiphase Flow*, 30(7):853–876, 2004.

E. Drosos, S. Paras, and A. Karabelas. Counter-current gas–liquid flow in a vertical narrow channel—liquid film characteristics and flooding phenomena. *International Journal of Multiphase Flow*, 32(1):51–81, 2006.

A. du Chéné, C. Min, and F. Gibou. Second-order accurate computation of curvatures in a level set framework using novel high-order reinitialization schemes. *Journal of Scientific Computing*, 35(2-3): 114–131, 2008.

J.-B. Dupont. *Étude des écoulements diphasiques dans les mini-canaux d'une pile à combustible*. PhD thesis, Toulouse, INPT, 2007.

J.-B. Dupont and D. Legendre. Numerical simulation of static and sliding drop with contact angle hysteresis. *Journal of Computational Physics*, 229(7):2453 – 2478, 2010.

E. B. Dussan V. On the spreading of liquids on solid surfaces: Static and dynamic contact lines. *Annual Review of Fluid Mechanics*, 11(1):371–400, 1979.

E. B. Dussan V., E. Ramé, and S. Garoff. On identifying the appropriate boundary conditions at a moving contact line: an experimental investigation. *Journal of Fluid Mechanics*, 230:97–116, 9 1991.

C. Fang, C. Hidrovo, F. min Wang, J. Eaton, and K. Goodson. 3-D numerical simulation of contact angle hysteresis for microscale two phase flow. *International Journal of Multiphase Flow*, 34(7):690 – 705, 2008.

R. P. Fedkiw, T. Aslam, B. Merriman, and S. Osher. A non-oscillatory Eulerian approach to interfaces in multimaterial flows (the ghost fluid method). *Journal of Computational Physics*, 152(2):457 – 492, 1999.

M. Fourati, V. Roig, and L. Raynal. Experimental study of liquid spreading in structured packings. *Chemical Engineering Science*, 80:1–15, 2012.

M. Fourati, V. Roig, and L. Raynal. Liquid dispersion in packed columns: experiments and numerical modeling. *Chemical Engineering Science*, 100:266–278, 2013.

M. M. Francois, S. J. Cummins, E. D. Dendy, D. B. Kothe, J. M. Sicilian, and M. W. Williams. A balanced-force algorithm for continuous and sharp interfacial surface tension models within a volume tracking framework. *Journal of Computational Physics*, 213(1):141 – 173, 2006.

P. Freund. Making deep reductions in CO_2 emissions from coal-fired power plant using capture and storage of CO_2. *Proceedings of the Institution of Mechanical Engineers, Part A: Journal of Power and Energy*, 217(1):1–7, 2003.

Glycerine Producers' Association. *Physical properties of glycerine and its solutions*. Glycerine Producers' Association, 1963.

A. Gosset and J. Buchlin. Techniques optiques pour la caractérisation de films liquides instables. *Congrès Francophone de Techniques Laser, CFTL*, 2008.

R. O. Grigoriev. Transient growth in driven contact lines. *Physica D: Nonlinear Phenomena*, 209(1): 105–116, 2005.

J.-L. Guermond and L. Quartapelle. A projection FEM for variable density incompressible flows. *Journal of Computational Physics*, 165(1):167 – 188, 2000.

Y. G. Guezennec, R. S. Brodkey, N. Trigui, and J. C. Kent. Algorithms for fully automated three-dimensional particle tracking velocimetry. *Experiments in Fluids*, 17(4):209–219, 1994.

Y. Han, N. Shikazono, and N. Kasagi. Measurement of liquid film thickness in a micro parallel channel with interferometer and laser focus displacement meter. *International Journal of Multiphase Flow*, 37 (1):36–45, 2011.

Y. Haroun. *Étude du transfert de masse réactif gaz-liquide le long de plans corrugués par simulation numérique avec suivi d'interface*. PhD thesis, Toulouse, INPT, 2008.

Y. Haroun, L. Raynal, and P. Alix. Prediction of effective area and liquid hold-up in structured packings by CFD. *Chemical Engineering Research and Design*, 92(11):2247–2254, 2014.

D. Hartmann, M. Meinke, and W. Schröder. The constrained reinitialization equation for level set methods. *Journal of Computational Physics*, 229(5):1514 – 1535, 2010.

C. W. Hirt and B. D. Nichols. Volume of fluid (VOF) method for the dynamics of free boundaries. *Journal of Computational Physics*, 39(1):201–225, 1981.

L. M. Hocking and A. D. Rivers. The spreading of a drop by capillary action. *Journal of Fluid Mechanics*, 121:425–442, 8 1982.

C. Huh and S. Mason. The steady movement of a liquid meniscus in a capillary tube. *Journal of Fluid Mechanics*, 81(03):401–419, 1977.

C. Huh and L. Scriven. Hydrodynamic model of steady movement of a solid/liquid/fluid contact line. *Journal of Colloid and Interface Science*, 35(1):85 – 101, 1971.

H. E. Huppert. Flow and instability of a viscous current down a slope. *Nature*, 300(5891):427–429, 1982.

I. Iliuta, C. Petre, and F. Larachi. Hydrodynamic continuum model for two-phase flow structured-packing-containing columns. *Chemical Engineering Science*, 59(4):879–888, 2004.

R. I. Issa. Solution of the implicitly discretised fluid flow equations by operator-splitting. *Journal of Computational Physics*, 62(1):40–65, 1985.

G.-S. Jiang and D. Peng. Weighted ENO schemes for Hamilton–Jacobi equations. *SIAM Journal on Scientific Computing*, 21(6):2126–2143, 2000.

G.-S. Jiang and C.-W. Shu. Efficient implementation of weighted ENO schemes. *Journal of Computational Physics*, 126(1):202 – 228, 1996.

M. Johnson, R. Schluter, M. Miksis, and S. Bankoff. Experimental study of rivulet formation on an inclined plate by fluorescent imaging. *Journal of Fluid Mechanics*, 394:339–354, 1999.

Joint Committee for Guides in Metrology. JCGM 100: Evaluation of measurement data - guide to the expression of uncertainty in measurement. Technical report, JCGM, 2008.

F. Y. Kafka and E. B. Dussan V. On the interpretation of dynamic contact angles in capillaries. *Journal of Fluid Mechanics*, 95:539–565, 12 1979.

S. Kalliadasis. Nonlinear instability of a contact line driven by gravity. *Journal of Fluid Mechanics*, 413: 355–378, 2000.

T. Kamei and A. Serizawa. Measurement of 2-dimensional local instantaneous liquid film thickness around simulated nuclear fuel rod by ultrasonic transmission technique. *Nuclear Engineering and Design*, 184(2):349–362, 1998.

J.-B. Kim and M.-H. Kim. A photochromic dye activation method for measuring the thickness of liquid films. *Bulletin of the Korean Chemical Society*, 26(6):966–970, 2005.

M. Kohrt, I. Ausner, G. Wozny, and J.-U. Repke. Texture influence on liquid-side mass transfer. *Chemical Engineering Research and Design*, 89(8):1405–1413, 2011.

L. Kondic and J. Diez. Pattern formation in the flow of thin films down an incline: Constant flux configuration. *Physics of Fluids (1994-present)*, 13(11):3168–3184, 2001.

G. Lagubeau, M. A. Fontelos, C. Josserand, A. Maurel, V. Pagneux, and P. Petitjeans. Spreading dynamics of drop impacts. *Journal of Fluid Mechanics*, 713:50–60, 2012.

C. Lam, N. Kim, D. Hui, D. Kwok, M. Hair, and A. Neumann. The effect of liquid properties to contact angle hysteresis. *Colloids and Surfaces A: Physicochemical and Engineering Aspects*, 189(1–3):265 – 278, 2001.

B. Lavi and A. Marmur. The exponential power law: partial wetting kinetics and dynamic contact angles. *Colloids and Surfaces A: Physicochemical and Engineering Aspects*, 250(1–3):409 – 414, 2004.

N. Le Grand, A. Daerr, and L. Limat. Shape and motion of drops sliding down an inclined plane. *Journal of Fluid Mechanics*, 541:293–315, 10 2005.

Y.-C. Lei, W.-H. Tien, J. Duncan, M. Paul, N. Ponchaut, C. Mouton, D. Dabiri, T. Rösgen, and J. Hove. A vision-based hybrid particle tracking velocimetry (PTV) technique using a modified cascade correlation peak-finding method. *Experiments in Fluids*, 53(5):1251–1268, 2012.

V. Lel, F. Al-Sibai, A. Leefken, and U. Renz. Local thickness and wave velocity measurement of wavy films with a chromatic confocal imaging method and a fluorescence intensity technique. *Experiments in fluids*, 39(5):856–864, 2005.

V. Linek, P. Petricek, P. Benes, and R. Braun. Effective interfacial area and liquid side mass transfer coefficients in absorption columns packed with hydrophilised and untreated plastic packings. *Chemical Engineering Research and Design*, 62(1):13–21, 1984.

S. Liu, J. Li, and Q. Chen. Visualization of flow pattern in thermosyphon by ECT. *Flow Measurement and Instrumentation*, 18(5):216–222, 2007.

J. Luo, X. Hu, and N. Adams. Curvature boundary condition for a moving contact line. *Journal of Computational Physics*, 310:329 – 341, 2016.

M. Maglio and D. Legendre. Numerical simulation of sliding drops on an inclined solid surface. In *Computational and Experimental Fluid Mechanics with Applications to Physics, Engineering and the Environment*, pages 47–69. Springer International Publishing, 2014.

B. Mahr and D. Mewes. CFD modelling and calculation of dynamic two-phase flow in columns equipped with structured packing. *Chemical Engineering Research and Design*, 85(8):1112–1122, 2007.

B. Mahr and D. Mewes. Two-phase flow in structured packings: Modeling and calculation on a macroscopic scale. *AIChE journal*, 54(3):614–626, 2008.

A. Maurel, P. Cobelli, V. Pagneux, and P. Petitjeans. Experimental and theoretical inspection of the phase-to-height relation in Fourier transform profilometry. *Applied Optics*, 48(2):380–392, 2009.

R. Meland, I. Gran, R. Olsen, and S. Munkejord. Reduction of parasitic currents in level-set calculations with a consistent discretization of the surface-tension force for the CSF model. In *16th Australasian Fluid Mechanics Conference (AFMC)*, pages 862–865. School of Engineering, The University of Queensland, 2007.

R. Menikoff, R. Mjolsness, D. Sharp, and C. Zemach. Unstable normal mode for Rayleigh–Taylor instability in viscous fluids. *Physics of Fluids (1958-1988)*, 20(12):2000–2004, 1977.

C. Min. On reinitializing level set functions. *Journal of Computational Physics*, 229(8):2764 – 2772, 2010. ISSN 0021-9991.

C. Min and F. Gibou. A second order accurate level set method on non-graded adaptive cartesian grids. *Journal of Computational Physics*, 225(1):300 – 321, 2007.

R. J. Moffat. Describing the uncertainties in experimental results. *Experimental Thermal and Fluid Science*, 1(1):3–17, 1988.

H. K. Moffatt. Viscous and resistive eddies near a sharp corner. *Journal of Fluid Mechanics*, 18:1–18, 1 1964.

F. Moisy, M. Rabaud, and K. Salsac. A synthetic schlieren method for the measurement of the topography of a liquid interface. *Experiments in Fluids*, 46(6):1021–1036, 2009.

K. Moran, J. Inumaru, and M. Kawaji. Instantaneous hydrodynamics of a laminar wavy liquid film. *International Journal of Multiphase Flow*, 28(5):731–755, 2002.

C. G. Ngan and E. B. Dussan V. On the dynamics of liquid spreading on solid surfaces. *Journal of Fluid Mechanics*, 209:191–226, 12 1989.

L. Ó Náraigh, P. Valluri, D. M. Scott, I. Bethune, and P. D. M. Spelt. Linear instability, nonlinear instability and ligament dynamics in three-dimensional laminar two-layer liquid-liquid flows. *Journal of Fluid Mechanics*, 750:464–506, 7 2014.

E. Olsson and G. Kreiss. A conservative level set method for two phase flow. *Journal of Computational Physics*, 210(1):225 – 246, 2005.

T. Onda, S. Shibuichi, N. Satoh, and K. Tsujii. Super-water-repellent fractal surfaces. *Langmuir*, 12(9): 2125–2127, 1996.

S. Osher and R. Fedkiw. *Level set methods and dynamic implicit surfaces*. Springer Science & Business Media, 2006.

C. F. Petre, F. Larachi, I. Iliuta, and B. Grandjean. Pressure drop through structured packings: Breakdown into the contributing mechanisms by CFD modeling. *Chemical Engineering Science*, 58(1):163–177, 2003.

T. Podgorski, J.-M. Flesselles, and L. Limat. Corners, cusps, and pearls in running drops. *Physical Review Letters*, 87:036102, Jun 2001.

M. N. Polyanskiy. Refractive index database. 2016. http:://refractiveindex.info.

S. Popinet. An accurate adaptive solver for surface-tension-driven interfacial flows. *Journal of Computational Physics*, 228(16):5838 – 5866, 2009.

C. Pozrikidis. The flow of a liquid film along a periodic wall. *Journal of Fluid Mechanics*, 188:275–300, 1988.

C. Pozrikidis. *Introduction to theoretical and computational fluid dynamics*. Oxford University Press, 2011.

A. Przadka, B. Cabane, V. Pagneux, A. Maurel, and P. Petitjeans. Fourier transform profilometry for water waves: how to achieve clean water attenuation with diffusive reflection at the water surface? *Experiments in Fluids*, 52(2):519–527, 2012.

D. Quéré. Wetting and roughness. *Annual Review of Materials Research*, 38:71–99, 2008.

M. Raffel, C. Willert, and J. Kompenhans. *Particle image velocimetry: a practical guide.* Springer, 1998.

E. Ramé, S. Garoff, and K. R. Willson. Characterizing the microscopic physics near moving contact lines using dynamic contact angle data. *Physical Review E*, 70:031608, Sep 2004.

L. Rayleigh. Investigation of the character of the equilibrium of an incompressible heavy fluid of variable density. *Proc. London Math. Soc*, 14(1):8, 1883.

L. Raynal and A. Royon-Lebeaud. A multi-scale approach for CFD calculations of gas–liquid flow within large size column equipped with structured packing. *Chemical Engineering Science*, 62(24):7196–7204, 2007.

L. Raynal, C. Boyer, and J.-P. Ballaguet. Liquid holdup and pressure drop determination in structured packing with CFD simulations. *The Canadian Journal of Chemical Engineering*, 82(5):871–879, 2004.

L. Raynal, P.-A. Bouillon, A. Gomez, and P. Broutin. From MEA to demixing solvents and future steps, a roadmap for lowering the cost of post-combustion carbon capture. *Chemical Engineering Journal*, 171 (3):742–752, 2011.

L. Raynal, A. Gomez, B. Caillat, and Y. Haroun. CO_2 capture cost reduction: Use of a multiscale simulations strategy for a multiscale issue. *Oil & Gas Science and Technology-Revue d'IFP Energies nouvelles*, 68(6):1093–1108, 2013.

Y. Renardy and M. Renardy. PROST: a parabolic reconstruction of surface tension for the volume-of-fluid method. *Journal of Computational Physics*, 183(2):400–421, 2002.

G. Russo and P. Smereka. A remark on computing distance functions. *Journal of Computational Physics*, 163(1):51 – 67, 2000.

W. Said, M. Nemer, and D. Clodic. Modeling of dry pressure drop for fully developed gas flow in structured packing using CFD simulations. *Chemical Engineering Science*, 66(10):2107–2117, 2011.

R. P. Salazar and E. Marschall. Thickness measurement in liquid film flow by laser scattering. *Review of Scientific Instruments*, 46(11):1539–1541, 1975.

N. Savva, G. A. Pavliotis, and S. Kalliadasis. Contact lines over random topographical substrates. Part 1. Statics. *Journal of Fluid Mechanics*, 672:358–383, 2011.

R. Scardovelli and S. Zaleski. Direct numerical simulation of free-surface and interfacial flow. *Annual Review of Fluid Mechanics*, 31(1):567–603, 1999.

P. Schmidt, L. Ó. Náraigh, M. Lucquiaud, and P. Valluri. Linear and nonlinear instability in vertical counter-current laminar gas-liquid flows. *Physics of Fluids (1994-present)*, 28(4):042102, 2016.

T. K. Sengupta and A. Dipankar. A comparative study of time advancement methods for solving navier–stokes equations. *Journal of Scientific Computing*, 21(2):225–250, 2004.

J. A. Sethian. Evolution, implementation, and application of level set and fast marching methods for advancing fronts. *Journal of Computational Physics*, 169(2):503–555, 2001.

C. Shen and D. W. Ruth. Experimental and numerical investigations of the interface profile close to a moving contact line. *Physics of Fluids*, 10(4):789–799, 1998.

P. Sheng and M. Zhou. Immiscible-fluid displacement: Contact-line dynamics and the velocity-dependent capillary pressure. *Physical Review A*, 45:5694–5708, Apr 1992.

C.-W. Shu and S. Osher. Efficient implementation of essentially non-oscillatory shock-capturing schemes. *Journal of Computational Physics*, 77(2):439 – 471, 1988.

D. N. Sibley, A. Nold, and S. Kalliadasis. The asymptotics of the moving contact line: cracking an old nut. *Journal of Fluid Mechanics*, 764:445–462, 2 2015.

R. Sidi-Boumedine and L. Raynal. Influence of the viscosity on the liquid hold-up in trickle-bed reactors with structured packings. *Catalysis Today*, 105(3):673–679, 2005.

J. H. Snoeijer and B. Andreotti. Moving contact lines: scales, regimes, and dynamical transitions. *Annual Review of Fluid Mechanics*, 45:269–292, 2013.

J. H. Snoeijer, E. Rio, N. Le Grand, and L. Limat. Self-similar flow and contact line geometry at the rear of cornered drops. *Physics of Fluids*, 17(7), 2005.

C. Soulaine. *Modélisation des écoulements dans les garnissages structurés : de l'échelle du pore á l'échelle de la colonne*. PhD thesis, Toulouse, INPT, 2012.

C. Soulaine, P. Horgue, J. Franc, and M. Quintard. Gas–liquid flow modeling in columns equipped with structured packing. *AIChE Journal*, 60(10):3665–3674, 2014.

P. D. M. Spelt. A level-set approach for simulations of flows with multiple moving contact lines with hysteresis. *Journal of Computational Physics*, 207(2):389 – 404, 2005.

L. Spiegel and W. Meier. A generalized pressure drop model for structured packings. In *Institution of Chemical Engineers Symposium Series*, volume 128, pages B85–B85. Hemsphere Publishing Corporation, 1992.

M. Stanislas, K. Okamoto, C. J. Kähler, J. Westerweel, and F. Scarano. Main results of the third international PIV challenge. *Experiments in Fluids*, 45(1):27–71, 2008.

P. Suess and L. Spiegel. Hold-up of Mellapak structured packings. *Chemical Engineering and Processing: Process Intensification*, 31(2):119–124, 1992.

Y. Sui and P. D. Spelt. Non-isothermal droplet spreading/dewetting and its reversal. *Journal of Fluid Mechanics*, 776:74–95, 2015.

Y. Sui and P. D. M. Spelt. Validation and modification of asymptotic analysis of slow and rapid droplet spreading by numerical simulation. *Journal of Fluid Mechanics*, 715:283–313, 1 2013a.

Y. Sui and P. D. M. Spelt. An efficient computational model for macroscale simulations of moving contact lines. *Journal of Computational Physics*, 242(0):37 – 52, 2013b.

Y. Sui, H. Ding, and P. D. Spelt. Numerical simulations of flows with moving contact lines. *Annual Review of Fluid Mechanics*, 46(1):97–119, 2014.

M. Sussman and E. Fatemi. An efficient, interface-preserving level set redistancing algorithm and its application to interfacial incompressible fluid flow. *SIAM Journal on Scientific Computing*, 20(4): 1165–1191, 1999.

M. Sussman and E. G. Puckett. A coupled level set and volume-of-fluid method for computing 3D and axisymmetric incompressible two-phase flows. *Journal of Computational Physics*, 162(2):301–337, 2000.

M. Sussman, P. Smereka, and S. Osher. A level set approach for computing solutions to incompressible two-phase flow. *Journal of Computational Physics*, 114(1):146 – 159, 1994.

M. Sussman, A. S. Almgren, J. B. Bell, P. Colella, L. H. Howell, and M. L. Welcome. An adaptive level set approach for incompressible two-phase flows. *Journal of Computational Physics*, 148(1):81 – 124, 1999.

P. S. Swain and R. Lipowsky. Contact angles on heterogeneous surfaces: A new look at Cassie's and Wenzel's laws. *Langmuir*, 14(23):6772–6780, 1998.

M. Takeda and K. Mutoh. Fourier transform profilometry for the automatic measurement of 3-D object shapes. *Applied Optics*, 22(24):3977–3982, 1983.

C. B. Tibiriçá, F. J. do Nascimento, and G. Ribatski. Film thickness measurement techniques applied to micro-scale two-phase flow systems. *Experimental Thermal and Fluid Science*, 34(4):463–473, 2010.

Y. Y. Trifonov. Viscous liquid film flows over a periodic surface. *IJMF*, 24(7):1139 – 1161, 1999.

Y. Y. Trifonov. Viscous film flow down corrugated surfaces. *Journal of Applied Mechanics and Technical Physics*, 45(3):389–400, 2004.

S. Troian, E. Herbolzheimer, S. Safran, and J. Joanny. Fingering instabilities of driven spreading films. *EPL (Europhysics Letters)*, 10(1):25, 1989.

G. Tryggvason. Numerical simulations of the rayleigh-taylor instability. *Journal of Computational Physics*, 75(2):253 – 282, 1988.

G. Tryggvason, R. Scardovelli, and S. Zaleski. *Direct numerical simulations of gas–liquid multiphase flows*. Cambridge University Press, 2011.

O. Ubbink and R. Issa. A method for capturing sharp fluid interfaces on arbitrary meshes. *Journal of Computational Physics*, 153(1):26–50, 1999.

D. Udrea, P. Bryanston-Cross, W. Lee, and M. Funes-Gallanzi. Two sub-pixel processing algorithms for high accuracy particle centre estimation in low seeding density particle image velocimetry. *Optics & Laser Technology*, 28(5):389–396, 1996.

P. Valluri, O. K. Matar, G. F. Hewitt, and M. Mendes. Thin film flow over structured packings at moderate Reynolds numbers. *Chemical Engineering Science*, 60(7):1965–1975, 2005.

I. Veretennikov, A. Indeikina, and H.-C. Chang. Front dynamics and fingering of a driven contact line. *Journal of Fluid Mechanics*, 373:81–110, 1998.

Y. Vitry. *Étude expérimentale des écoulements film mince sur plan incliné avec contrecourant gaz dans des conditions de similitude aux écoulements cryogéniques*. PhD thesis, Toulouse, INPT, 2011.

M. Vlachogiannis and V. Bontozoglou. Experiments on laminar film flow along a periodic wall. *Journal of Fluid Mechanics*, 457:133–156, 2002.

P. D. Welch. The use of fast Fourier transform for the estimation of power spectra: A method based on time averaging over short, modified periodograms. *IEEE Transactions on audio and electroacoustics*, 15(2):70–73, 1967.

R. N. Wenzel. Resistance of solid surfaces to wetting by water. *Industrial & Engineering Chemistry*, 28 (8):988–994, 1936.

S. Whitaker. The transport equations for multi-phase systems. *Chemical Engineering Science*, 28(1): 139–147, 1973.

G. Wolansky and A. Marmur. Apparent contact angles on rough surfaces: the Wenzel equation revisited. *Colloids and Surfaces A: Physicochemical and Engineering Aspects*, 156(1):381–388, 1999.

T. Young. An essay on the cohesion of fluids. *Philosophical Transactions of the Royal Society of London*, 95:65–87, 1805.

L.-Q. Yu, F. Wasden, A. Dukler, and V. Balakotaiah. Nonlinear evolution of waves on falling films at high Reynolds numbers. *Physics of Fluids (1994-present)*, 7(8):1886–1902, 1995.

I. Zadrazil, O. K. Matar, and C. N. Markides. An experimental characterization of downwards gas–liquid annular flow by laser-induced fluorescence: Flow regimes and film statistics. *International Journal of Multiphase Flow*, 60:87–102, 2014.

H. Zhao. A fast sweeping method for eikonal equations. *Mathematics of computation*, 74(250):603–627, 2005.

D. Zhou, T. Gambaryan-Roisman, and P. Stephan. Measurement of water falling film thickness to flat plate using confocal chromatic sensoring technique. *Experimental Thermal and Fluid Science*, 33(2): 273–283, 2009.

Appendix A

Discretization methods

Outline

This appendix presents the WENO5 scheme for the conservative advection equation, Runge-Kutta schemes for the reinitialization equation, the WENO5 scheme for Hamilton-Jacobi equations, and general discretization methods of Navier-Stokes equations based on that of the solver TPLS used in the thesis.

A.1 WENO5 scheme for the conservative advection equation

For an incompressible flow $\nabla \cdot \mathbf{u} = 0$, the advection equation can be recast in conservative form as

$$\frac{\partial \phi}{\partial t} + \nabla \cdot (\phi \mathbf{u}) = 0. \tag{A.1}$$

Integrating the one-dimensional form of (A.1) over a cell centered at x_i yields

$$\frac{\partial \bar{\phi}_i}{\partial t} + \frac{1}{h}(u_{i+\frac{1}{2}}\phi_{i+\frac{1}{2}} - u_{i-\frac{1}{2}}\phi_{i-\frac{1}{2}}) = 0, \tag{A.2}$$

with

$$\bar{\phi}_i = \frac{1}{h} \int_{x_{i-\frac{1}{2}}}^{x_{i+\frac{1}{2}}} \phi(x) dx. \tag{A.3}$$

The WENO5 scheme allows computing $\phi^{\pm}_{i+\frac{1}{2}}$ and $\phi^{\pm}_{i-\frac{1}{2}}$, where $+$ and $-$ stand for the upwind and downwind reconstruction, respectively. The value $\phi^{\pm}_{i+\frac{1}{2}}$ is a combination of three values $\phi^{(p)\pm}_{i+\frac{1}{2}}, p \in [\![1, 3]\!]$, obtained with a third-order essentially non-oscillatory (ENO) scheme (Shu and Osher, 1988), with three different stencils. Weights $\omega^{(p)\pm}_{i+\frac{1}{2}}, p \in [\![1, 3]\!]$, are computed in order to select the smoothest reconstruction. The fifth-order reconstruction reads

$$\phi^{\pm}_{i+\frac{1}{2}} = \omega^{(1)\pm}_{i+\frac{1}{2}} \phi^{(1)\pm}_{i+\frac{1}{2}} + \omega^{(2)\pm}_{i+\frac{1}{2}} \phi^{(2)\pm}_{i+\frac{1}{2}} + \omega^{(3)\pm}_{i+\frac{1}{2}} \phi^{(3)\pm}_{i+\frac{1}{2}}, \tag{A.4}$$

where $\phi^{(p)\pm}_{i+\frac{1}{2}}, p \in [\![1, 3]\!]$ are the third-order ENO reconstructions,

$$\begin{aligned} \phi^{(1)\pm}_{i+\frac{1}{2}} &= \tfrac{1}{3} c^{\pm}_1 - \tfrac{7}{6} c^{\pm}_2 + \tfrac{11}{6} c^{\pm}_3, \\ \phi^{(2)\pm}_{i+\frac{1}{2}} &= -\tfrac{1}{6} c^{\pm}_2 + \tfrac{5}{6} c^{\pm}_3 + \tfrac{1}{3} c^{\pm}_4, \\ \phi^{(3)\pm}_{i+\frac{1}{2}} &= \tfrac{1}{3} c^{\pm}_3 + \tfrac{5}{6} c^{\pm}_4 - \tfrac{1}{6} c^{\pm}_5, \end{aligned} \tag{A.5}$$

and coefficients $c^{\pm}_p, p \in [\![1, 5]\!]$, are obtained from three different stencils,

$$\begin{aligned} c^{-}_p &= \bar{\phi}_{i-2+(p-1)}, \qquad p \in [\![1, 5]\!], \\ c^{+}_p &= \bar{\phi}_{i+3-(p-1)}, \qquad p \in [\![1, 5]\!]. \end{aligned} \tag{A.6}$$

The smoothness indicators $s^{(p)}, p \in [\![1, 3]\!]$, are defined as

$$\begin{aligned} s^{(1)} &= \tfrac{13}{12}(c^{\pm}_1 - 2c^{\pm}_2 + c^{\pm}_3) + \tfrac{1}{4}(c^{\pm}_1 - 4c^{\pm}_2 + 3c^{\pm}_3)^2, \\ s^{(2)} &= \tfrac{13}{12}(c^{\pm}_2 - 2c^{\pm}_3 + c^{\pm}_4) + \tfrac{1}{4}(c^{\pm}_2 - c^{\pm}_4)^2, \\ s^{(3)} &= \tfrac{13}{12}(c^{\pm}_2 - 2c^{\pm}_4 + c^{\pm}_5) + \tfrac{1}{4}(3c^{\pm}_3 - 4c^{\pm}_4 + c^{\pm}_5)^2, \end{aligned} \tag{A.7}$$

and weights are computed as

$$\omega^{(p)\pm}_{i+\frac{1}{2}} = \frac{\alpha^{(p)\pm}_{i+\frac{1}{2}}}{\alpha^{(1)\pm}_{i+\frac{1}{2}} + \alpha^{(2)\pm}_{i+\frac{1}{2}} + \alpha^{(3)\pm}_{i+\frac{1}{2}}}, \qquad p \in [\![1, 3]\!], \tag{A.8}$$

with

$$\alpha^{(1)\pm}_{i+\frac{1}{2}} = \tfrac{1}{10}\left(\tfrac{1}{\epsilon + s^{(1)}}\right)^2, \alpha^{(2)\pm}_{i+\frac{1}{2}} = \tfrac{3}{5}\left(\tfrac{1}{\epsilon + s^{(2)}}\right)^2, \alpha^{(3)\pm}_{i+\frac{1}{2}} = \tfrac{3}{10}\left(\tfrac{1}{\epsilon + s^{(3)}}\right). \tag{A.9}$$

ϵ is set to 10^{-7} in this work.

A.2 Runge-Kutta schemes

The following Runge-Kutta schemes have been tested in the reinitialization step.

A.2.1 Forward Euler

The FE method is a one-step time integration:

$$\frac{\psi^{m+1}-\psi^m}{\Delta\tau}+\text{sign}(\psi^0)\big(|G\psi^m|-1\big)=0, \tag{A.10}$$

where $G\psi$ is a numerical approximation of $\nabla\psi$.

A.2.2 TVD RK2

The TVD RK2 method is a two-step time integration that consists of two FE steps,

$$\begin{aligned}\frac{\tilde{\psi}^{m+1}-\psi^m}{\Delta\tau}+\text{sign}(\psi^0)\big(|G\psi^m|-1\big)&=0,\\ \frac{\tilde{\psi}^{m+2}-\tilde{\psi}^{m+1}}{\Delta\tau}+\text{sign}(\psi^0)\big(|G\tilde{\psi}^{m+1}|-1\big)&=0,\end{aligned} \tag{A.11}$$

followed by averaging:

$$\psi^{m+1}=\tfrac{1}{2}(\psi^m+\tilde{\psi}^{m+2}). \tag{A.12}$$

A.2.3 TVD RK3

The TVD RK3 method is a three-step time integration. The first two steps are simply FE steps:

$$\begin{aligned}\frac{\tilde{\psi}^{m+1}-\psi^m}{\Delta\tau}+\text{sign}(\psi^0)\big(|G\psi^m|-1\big)&=0,\\ \frac{\tilde{\psi}^{m+2}-\tilde{\psi}^{m+1}}{\Delta\tau}+\text{sign}(\psi^0)\big(|G\tilde{\psi}^{m+1}|-1\big)&=0.\end{aligned} \tag{A.13}$$

Next, $\tilde{\psi}^{m+\frac{1}{2}}$ is obtained by linear interpolation:

$$\tilde{\psi}^{m+\frac{1}{2}}=\tfrac{3}{4}\psi^m+\tfrac{1}{4}\tilde{\psi}^{m+2}. \tag{A.14}$$

Finally, there is a FE step,

$$\frac{\tilde{\psi}^{m+\frac{3}{2}}-\tilde{\psi}^{m+\frac{1}{2}}}{\Delta\tau}+\text{sign}(\psi^0)\big(|G\tilde{\psi}^{m+\frac{1}{2}}|-1\big)=0, \tag{A.15}$$

followed by linear interpolation:

$$\psi^{m+1}=\tfrac{1}{3}\psi^m+\tfrac{2}{3}\tilde{\psi}^{m+\frac{3}{2}}. \tag{A.16}$$

A.3 WENO5 scheme for Hamilton-Jacobi equations

The fifth-order reconstruction for one-sided finite differences of spatial derivatives reads

$$D_x^{\pm}\psi_i=\omega_i^{(1)\pm}D_x^{\pm}\psi_i^{(1)}+\omega_i^{(2)\pm}D_x^{\pm}\psi_i^{(2)}+\omega_i^{(3)\pm}D_x^{\pm}\psi_i^{(3)}, \tag{A.17}$$

where $D_x\psi_i^{(p)\pm}, p\in[\![1,3]\!]$ are the third-order ENO reconstructions,

$$\begin{aligned}D_x^{\pm}\psi_i^{(1)}&=\tfrac{1}{3}c_1^{\pm}-\tfrac{7}{6}c_2^{\pm}+\tfrac{11}{6}c_3^{\pm},\\ D_x^{\pm}\psi_i^{(2)}&=-\tfrac{1}{6}c_2^{\pm}+\tfrac{5}{6}c_3^{\pm}+\tfrac{1}{3}c_4^{\pm},\\ D_x^{\pm}\psi_i^{(3)}&=\tfrac{1}{3}c_3^{\pm}+\tfrac{5}{6}c_4^{\pm}-\tfrac{1}{6}c_5^{\pm},\end{aligned} \tag{A.18}$$

and coefficients $c_p^{\pm}, p \in [\![1,5]\!]$ are computed from three different stencils,

$$\begin{aligned} c_p^- &= \frac{\bar{\psi}_{i-2+(p-1)} - \bar{\psi}_{i-3+(p-1)}}{h}, \qquad p \in [\![1,5]\!], \\ c_p^+ &= \frac{\bar{\psi}_{i+3-(p-1)} - \bar{\psi}_{i+2-(p-1)}}{h}, \qquad p \in [\![1,5]\!]. \end{aligned} \tag{A.19}$$

The smoothness indicators $s^{(p)}, p \in [\![1,3]\!]$ are defined as

$$\begin{aligned} s^{(1)} &= \tfrac{13}{12}(c_1^{\pm} - 2c_2^{\pm} + c_3^{\pm}) + \tfrac{1}{4}(c_1^{\pm} - 4c_2^{\pm} + 3c_3^{\pm})^2, \\ s^{(2)} &= \tfrac{13}{12}(c_2^{\pm} - 2c_3^{\pm} + c_4^{\pm}) + \tfrac{1}{4}(c_2^{\pm} - c_4^{\pm})^2, \\ s^{(3)} &= \tfrac{13}{12}(c_2^{\pm} - 2c_4^{\pm} + c_5^{\pm}) + \tfrac{1}{4}(3c_3^{\pm} - 4c_4^{\pm} + c_5^{\pm})^2, \end{aligned} \tag{A.20}$$

and weights are computed as

$$\omega_i^{(p)\pm} = \frac{\alpha_i^{(p)\pm}}{\alpha_i^{(1)\pm} + \alpha_i^{(2)\pm} + \alpha_i^{(3)\pm}}, \qquad p \in [\![1,3]\!], \tag{A.21}$$

with

$$\alpha_i^{(1)\pm} = \tfrac{1}{10}\left(\tfrac{1}{\epsilon + s^{(1)}}\right)^2, \alpha_i^{(2)\pm} = \tfrac{3}{5}\left(\tfrac{1}{\epsilon + s^{(2)}}\right)^2, \alpha_i^{(3)\pm} = \tfrac{3}{10}\left(\tfrac{1}{\epsilon + s^{(3)}}\right)^2. \tag{A.22}$$

A.4 Navier-Stokes solver

The Navier-Stokes equations, which read in a semi-discretized form,

$$\frac{\mathbf{u}^{n+1} - \mathbf{u}^n}{\Delta t} = \frac{1}{12}\big(23\mathbf{C}^n - 16\mathbf{C}^{n-1} + 5\mathbf{C}^{n-2}\big) + \frac{1}{2\rho^{n+\frac{1}{2}}}\big(\mathbf{D}^n + \mathbf{D}^* - 2\nabla p\big) + \frac{1}{2}\big(\mathbf{M}^{n+1} + \mathbf{M}^n\big), \tag{A.23}$$

$$\nabla \cdot \mathbf{u}^{n+1} = 0, \tag{A.24}$$

are solved with a standard projection method, with a semi-implicit viscous solve for the temporary velocity $\mathbf{u}^*$ (Tryggvason et al., 2011), such as the momentum equation recasts

$$\begin{aligned} \frac{\mathbf{u}^{n+1} - \mathbf{u}^n}{\Delta t} &= \frac{1}{12}\big(23\mathbf{C}^n - 16\mathbf{C}^{n-1} + 5\mathbf{C}^{n-2}\big) \\ &+ \frac{1}{2\rho^{n+\frac{1}{2}}}\big((\mathbf{D}^n + \mathbf{D}^{n+1}) + (\mathbf{D}^* - \mathbf{D}^{n+1}) - 2\nabla\zeta\big) \\ &+ \frac{1}{2}\big(\mathbf{M}^{n+1} + \mathbf{M}^n\big), \end{aligned} \tag{A.25}$$

where ζ is the artificial pressure, such as

$$\frac{1}{2}\big(\mathbf{D}^* - \mathbf{D}^{n+1}\big) - \nabla\zeta = -\nabla p. \tag{A.26}$$

In (A.23), $\mathbf{D}$ are the diffusive viscous terms, which are implicit in the temporary velocity $\mathbf{u}^*$, and $\mathbf{C}$ is the sum of the convective terms and the left-over viscous terms, which are treated explicitly with a third-order Adams-Bashforth method. Time averaging is used to compute the surface tension terms $\mathbf{M}$, as both ϕ^{n+1} and ϕ^n are known.

The two-step projection method consists in solving Helmholtz equation for the temporary velocity $\mathbf{u}^*$,

$$\frac{\mathbf{u}^* - \mathbf{u}^n}{\Delta t} = \frac{1}{12}\big(23\mathbf{C}^n - 16\mathbf{C}^{n-1} + 5\mathbf{C}^{n-2}\big) + \frac{1}{2\rho^{n+\frac{1}{2}}}\big(\mathbf{D}^n + \mathbf{D}^*\big) + \frac{1}{2}\big(\mathbf{M}^{n+1} + \mathbf{M}^n\big), \tag{A.27}$$

and then Poisson equation for the artificial pressure,

$$\nabla \cdot \left(\frac{\nabla \zeta}{\rho^{n+\frac{1}{2}}} \right) = \frac{\nabla \cdot \mathbf{u}^*}{\Delta t}, \tag{A.28}$$

in order to get a divergence-free velocity field at time $n+1$,

$$\mathbf{u}^{n+1} = \mathbf{u}^* - \Delta t \frac{\nabla \zeta}{\rho^{n+\frac{1}{2}}}, \tag{A.29}$$

that satisfies the continuity equation (A.24).

A.4.1 Diffusive viscous terms

The diffusive viscous terms are discretized in finite volumes, such as at $(i+1/2, j)$,

$$\begin{aligned} \mathrm{D}_{i+\frac{1}{2},j} = {} & \frac{1}{Re} \frac{\mu_{i+1,j} \dfrac{u_{i+\frac{3}{2},j} - u_{i+\frac{1}{2},j}}{\Delta x} - \mu_{i,j} \dfrac{u_{i+\frac{1}{2},j} - u_{i-\frac{1}{2},j}}{\Delta x}}{\Delta x} \\ & + \frac{1}{Re} \frac{\mu_{i+\frac{1}{2},j+\frac{1}{2}} \dfrac{u_{i+\frac{1}{2},j+1} - u_{i+\frac{1}{2},j}}{\Delta y} - \mu_{i+\frac{1}{2},j-\frac{1}{2}} \dfrac{u_{i+\frac{1}{2},j} - u_{i+\frac{1}{2},j-1}}{\Delta y}}{\Delta y}. \end{aligned} \tag{A.30}$$

A.4.2 Other viscous terms

C is a numerical approximation of the convective terms $\mathbf{C}^{\mathrm{c}}$ plus the left-over viscous terms $\mathbf{C}^{\mathrm{v}}$. The left-over viscous terms are discretized in finite volumes, such as at $(i+1/2, j)$,

$$\begin{aligned} \mathrm{C}^{\mathrm{v}}_{i+\frac{1}{2},j} = {} & \frac{1}{Re} \frac{\mu_{i+1,j} \dfrac{u_{i+\frac{3}{2},j} - u_{i+\frac{1}{2},j}}{\Delta x} - \mu_{i,j} \dfrac{u_{i+\frac{1}{2},j} - u_{i-\frac{1}{2},j}}{\Delta x}}{\Delta x} \\ & + \frac{1}{Re} \frac{\mu_{i+\frac{1}{2},j+\frac{1}{2}} \dfrac{v_{i+1,j+\frac{1}{2}} - v_{i,j+\frac{1}{2}}}{\Delta x} - \mu_{i+\frac{1}{2},j-\frac{1}{2}} \dfrac{v_{i+1,j-\frac{1}{2}} - v_{i,j-\frac{1}{2}}}{\Delta x}}{\Delta y}, \end{aligned} \tag{A.31}$$

with, for instance,

$$\mu_{i+\frac{1}{2},j+\frac{1}{2}} = \frac{1}{4} \big(\mu_{i,j} + \mu_{i+1,j} + \mu_{i,j+1} + \mu_{i+1,j+1} \big). \tag{A.32}$$

A.4.3 Convective terms

In x-direction, the convective term at $(i+1/2, j)$ reads

$$\mathrm{C}^{\mathrm{c}}_{i+\frac{1}{2},j} = -u_{i+\frac{1}{2},j} \left(\frac{u_{i+\frac{3}{2},j} - u_{i-\frac{1}{2},j}}{2\Delta x} \right) - v_{i+\frac{1}{2},j} \left(\frac{u_{i+\frac{1}{2},j+1} - u_{i+\frac{1}{2},j-1}}{2\Delta y} \right), \tag{A.33}$$

with

$$v_{i+\frac{1}{2},j} = \frac{1}{4} \Big(v_{i,j+\frac{1}{2}} + v_{i+1,j+\frac{1}{2}} + v_{i,j-\frac{1}{2}} + v_{i+1,j-\frac{1}{2}} \Big). \tag{A.34}$$

A.4.4 Curvature and capillary terms

The capillary term $\mathbf{M}$ is discretized using second-order centered finite differences so that its discretization is consistent with that of the pressure gradient:

$$M_{i+\frac{1}{2},j} = -\frac{1}{We}\frac{\kappa_{i+\frac{1}{2},j}}{\rho_{i+\frac{1}{2},j}}\frac{(H_\xi)_{i+1,j} - (H_\xi)_{i,j}}{\Delta x}, \tag{A.35}$$

with

$$\kappa_{i+\frac{1}{2},j} = \frac{1}{2}\big(\kappa_{i+1,j} + \kappa_{i,j}\big), \tag{A.36}$$

where $\kappa_{i,j}$ is computed as the divergence of the normal vector, with the cell-based discrete divergence operator (Sussman et al., 1999). In 2D:

$$\begin{aligned}\kappa_{i,j} = {} & \frac{1}{2}\left(\frac{n^1_{i+\frac{1}{2},j+\frac{1}{2}} - n^1_{i-\frac{1}{2},j+\frac{1}{2}}}{\Delta x} + \frac{n^1_{i+\frac{1}{2},j-\frac{1}{2}} - n^1_{i-\frac{1}{2},j-\frac{1}{2}}}{\Delta x}\right) \\ & + \frac{1}{2}\left(\frac{n^2_{i+\frac{1}{2},j+\frac{1}{2}} - n^2_{i+\frac{1}{2},j-\frac{1}{2}}}{\Delta y} + \frac{n^2_{i-\frac{1}{2},j+\frac{1}{2}} - n^2_{i-\frac{1}{2},j-\frac{1}{2}}}{\Delta y}\right),\end{aligned} \tag{A.37}$$

with $(n^1, n^2) = G\phi/|G\phi|$ an approximation of the normal vector, such as, for instance,

$$(G\phi)^1_{i+\frac{1}{2},j+\frac{1}{2}} = \frac{1}{2}\left(\frac{\phi_{i+1,j+1} - \phi_{i,j+1}}{\Delta x} + \frac{\phi_{i+1,j} - \phi_{i,j}}{\Delta x}\right). \tag{A.38}$$

A.4.5 Pressure equation

Poisson equation for the pressure (A.28) is discretized using second-order centered finite differences. For example, in 1D:

$$\frac{\dfrac{1}{\rho_{i+\frac{1}{2}}}\dfrac{\zeta_{i+1} - \zeta_i}{\Delta x} - \dfrac{1}{\rho_{i-\frac{1}{2}}}\dfrac{\zeta_i - \zeta_{i-1}}{\Delta x}}{\Delta x} = \frac{1}{\Delta t}\left(\frac{u^*_{i+\frac{1}{2}} - u^*_{i-\frac{1}{2}}}{\Delta x}\right). \tag{A.39}$$

A.4.6 Velocity field

Finally, the velocity field is obtained from (A.29), that is discretized with second-order centered finite differences, which reads, in 2D:

$$u_{i+\frac{1}{2},j} = u^*_{i+\frac{1}{2},j} - \frac{1}{\rho_{i+\frac{1}{2},j}}\frac{\zeta_{i+1,j} - \zeta_{i,j}}{\Delta x}. \tag{A.40}$$

Appendix B

Two-phase flows with moving contact lines in the volume-of-fluid framework

Outline

For industrial purposes, the macroscale models of Cox (1986, 1998) have been implemented in the commercial code ANSYS Fluent 15.0, that has been developed to simulate many flows that can be laminar, turbulent, multiphase, compressible, etc. Axisymmetric and three-dimensional flows are simulated to validate the implementation, and results are compared to that obtained with TPLS in Chapter 4.

B.1 Numerical methods

B.1.1 The volume-of-fluid method

The interesting option of the commercial software ANSYS Fluent is the volume-of-fluid (VOF) method of Hirt and Nichols (1981), which is another interface-capturing method that allows simulating two-phase flows with a one-fluid formulation, as level-set. It consists in locating the interface with the volume fraction function of one fluid, arbitrarily chosen, that varies from 0 to 1 over a few cells next to the interface. As the interface moves with the fluid, the evolution of the VOF function is given by the following advection equation:

$$\frac{\partial \alpha}{\partial t} + \mathbf{u} \cdot \nabla \alpha = 0. \tag{B.1}$$

As the VOF function is not continuous at the interface, a geometrical reconstruction of the interface is generally done in order to accurately compute the advection term (Scardovelli and Zaleski, 1999) in Equation (B.1). The VOF method does not suffer from mass conservation errors as some LS codes but the calculation of surface tension forces and the location of the interface are not necessarily as accurate as with LS methods. Hence some authors, such as Sussman and Puckett (2000), have developed a combined LS-VOF method in order to take advantage of both methods.

In the VOF framework, fluid properties are calculated with the VOF function that is the volume fraction of one fluid,

$$\begin{aligned}\rho(\alpha) &= \alpha\rho_1 + (1-\alpha)\rho_2,\\ \mu(\alpha) &= \alpha\mu_1 + (1-\alpha)\mu_2,\end{aligned} \tag{B.2}$$

and volume conservation yields

$$\alpha_1 + \alpha_2 = 1. \tag{B.3}$$

The single-fluid formulation of the Navier-Stokes equations for two fluids reads

$$\frac{\partial}{\partial t}(\rho\mathbf{u}) + (\mathbf{u}\cdot\nabla)(\rho\mathbf{u}) = -\nabla p + \nabla\cdot(2\mu\mathbf{S}) - \sigma\kappa\frac{\nabla\alpha}{|\nabla\alpha|} + \rho\mathbf{g}, \tag{B.4}$$

$$\frac{\partial\rho}{\partial t} + \nabla\cdot(\rho\mathbf{u}) = 0, \tag{B.5}$$

with $\mathbf{S}$ the rate-of-strain tensor, defined as

$$S_{i,j} = \frac{1}{2}\left(\frac{\partial u_i}{\partial x_j} + \frac{\partial u_j}{\partial x_i}\right) - \frac{\delta_{i,j}}{3}\nabla\cdot\mathbf{u}. \tag{B.6}$$

In Equation (B.4), capillary effects are taken into account with the Continuum Surface Force model of Brackbill et al. (1992), already presented in the previous Chapter 3.

B.1.2 Solution methods

Discretization is done in finite volumes on a collocated grid: all physical quantities such as velocity, pressure, viscosity, density and volume fraction function are defined at cell centers. The PISO (Pressure-Implicit wit Splitting Operator) algorithm of Issa (1985) is used for pressure-velocity coupling. Momentum equations are solved with a second-order upwind scheme in space. The advection term in (B.1) is computed with the CICSAM (Capturing Sharp Fluid Interfaces on Arbitrary Meshes) method of Ubbink and Issa (1999) as the methodology developed in this project will further be used for simulations with complex geometries.

B.1.3 Implementation of the macroscale model via UDFs

In ANSYS Fluent 15.0, the contact angle needs to be specified at wall boundaries. The contact-line speed is first computed by using the temporary velocity of the PISO algorithm and the gradient of the volume fraction. In 3D:

$$U^*_{CL} = -\frac{u^*\partial_x\alpha + v^*\partial_y\alpha}{\sqrt{(\partial_x\alpha)^2 + (\partial_y\alpha)^2}}. \tag{B.7}$$

where $\mathbf{u}^*$ is the intermediate velocity, solution of a Helmholtz equation (see Equation (17) of Issa (1985)). The corresponding contact angle obtained from the theory of Cox (1986, 1998) is then given to the solver via User-Defined Functions (UDFs), and is used to compute the direction of the capillary term at the contact line, $\hat{\mathbf{n}} = \cos\theta_d\hat{\mathbf{e}}_x + \sin\theta_d\hat{\mathbf{e}}_y$, which is normal to the interface.

Initial diameter (mm)	0.611
Impact speed (m.s^{-1})	0.079
μ_L (Pa.s)	$1.003 \cdot 10^{-3}$
ρ_L (kg.m^{-3})	998.2
μ_G (Pa.s)	$1.7894 \cdot 10^{-5}$
ρ_G (kg.m^{-3})	1.225
σ (kg.s^{-2})	0.0728
θ_w (°)	23
Slip parameter (m)	10^{-16}

Table B.1: Parameters used for the simulation of the experiment of Ding et al. (2012) with ANSYS Fluent.

B.2 Results and discussion

B.2.1 Axisymmetric droplet spreading in inertial regime

The case simulated here is the one that was simulated in Section 4.4.2, also simulated by Sui and Spelt (2013b) using the inertial theory of Cox (1986), and compared to the experiment of Ding et al. (2012). The computational domain is a square with a no-slip condition at the bottom, symmetry boundaries on the right-hand side and the top, and the left-hand side boundary is axisymmetric. The initial state is a sphere of radius R centered at $(0, R)$. Parameters of the simulation setup are gathered in Table B.1. Note that the contact-line dynamics can be modeled using an unrealistically small slip length and a constant wall angle; Sui and Spelt (2013b) obtained similar results using a realistic slip length and a dynamic wall angle. Below, lengths are normalized by the initial radius of the drop and the timestep, made dimensionless by the inertial-capillary time scale $\sqrt{\rho R^3/\sigma}$, is set equal to $2.5 \cdot 10^{-5}$.

Figure B.1 presents qualitative results obtained accounting for contact-line dynamics; a second-stage droplet pinch-off is observed, which is consistent with the experiment. Figure B.2 presents qualitative results without the contact-line model, with a constant angle equal to the wall angle; a first-stage droplet pinch-off is observed, in contrast with the experiment. Contact-line dynamics qualitatively affects the flow up to the macroscale.

Time signals of the capillary number based on the contact-line speed are reported in Figure B.3. With the macroscale model, grid convergence is achieved, and the physical events are well observed in the time signal of the contact-line speed: the first capillary wave, coming back from the top of the drop, reaches the contact-line around $t = 1.0$, and the second wave, coming from the re-expanding neck, gets to the contact line after $t = 2.0$. Time signals obtained in VOF simulations look time-shifted. This is thought to be due to the initial position of the center of the drop, which was actually different from that used with TPLS, where the initial position of the center of the drop was $\left(0, R(1 - 1/16)^{1/2}\right)$ against $(0, R)$ here in the VOF simulation. Indisputably, the pinch-off observed here is of second-stage type, not first-stage, and the same characteristic events can be read in time signals of the contact-line speed. For the record, time signals of the drop-base radius are presented in Figure B.4 for the case with macroscale model and the case with constant contact angle. As expected, spreading is overestimated if the contact-line dynamics is not taken into account.

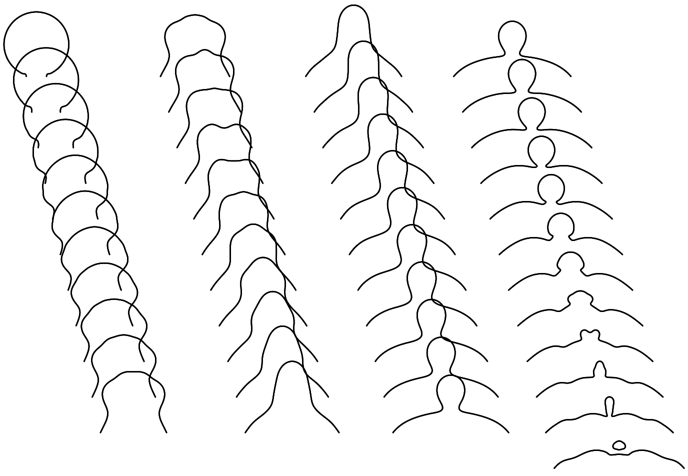

Figure B.1: Evolution of the shape using the dynamic contact angle model. A second-stage pinch-off is obtained, which is consistent with the experiment.

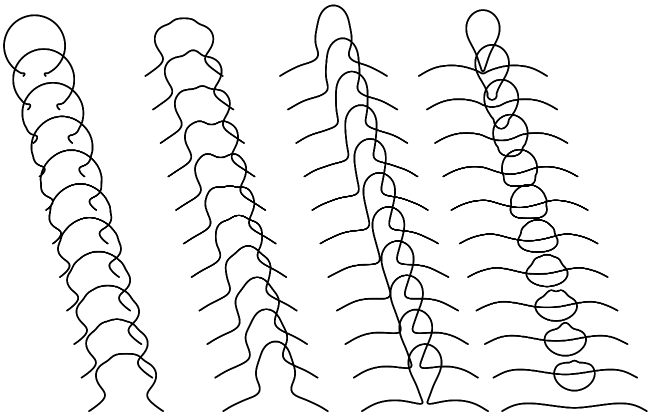

Figure B.2: Evolution of the shape using a constant contact angle. A first-stage pinch-off is obtained, which is not consistent with the experiment.

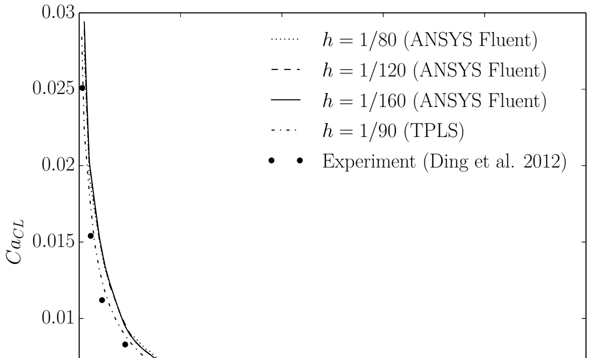

Figure B.3: Contact-line speed as a function of time for inertial spreading.

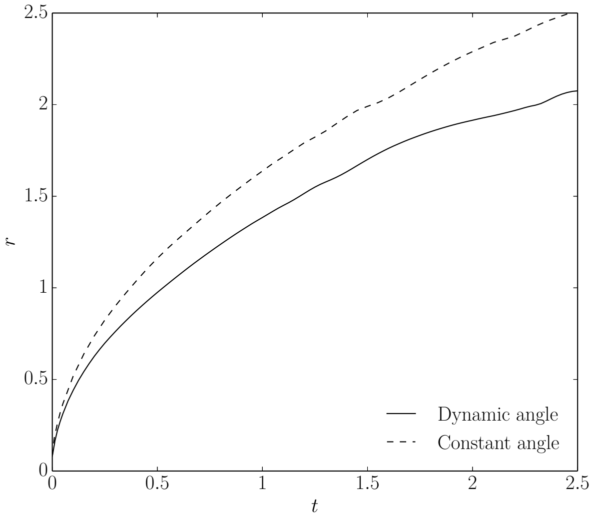

Figure B.4: Comparison of time signals of drop base radius between the case with dynamic contact angle and the case with constant contact angle for inertial spreading; $h = 1/120$.

B.2.2 Sliding drop in viscous regime

The purpose of this section is to validate the implementation of the macroscale model in 3D. The setup is exactly that of Section 4.4.3, with the governing parameter $Bo \sin \alpha$ set to 0.65, corresponding to the oval regime observed by Le Grand et al. (2005). The dynamic angle θ_d is obtained from the viscous theory of Cox (1986) (4.3) with $\theta_{w,A} = 50.5°$, $\theta_{w,R} = 45.5°$, a droplet volume $V = 6$ mm^3, a slip length $\lambda V^{1/3} = 10^{-9}$ m (consistent with the experiment), $Q_i = 0$, $r_\mu = 0.001$ and $r_\rho = 0.001$. Initially, the drop is a spherical cap with a contact angle equal to $\theta_{w,A} - 0.5°$. Lengths are scaled with $V^{1/3}$, where V is the drop volume, and time is normalized by the viscous time scale $\rho V^{2/3}/\mu$. Simulation results with a grid spacing $h = 1/32$ and a time step $\Delta t = 5 \cdot 10^{-6}$ were obtained.

A comparison with both experimental results of Le Grand et al. (2005) and numerical results obtained with TPLS in Section 4.4.3 is undertaken aiming to support the reliability of implementations of both codes. A top view of the oval drop is shown in Figure B.5, where the interface is colored by the height. As expected, an oval drop is observed, which is consistent with experiments. Qualitatively, results compare very well with those obtained with TPLS in Section 4.4.3. Time signals of the base length, the base width, the height and the speed of the drop are presented in Figure B.6, along with quantitative results obtained with TPLS in Section 4.4.3. A steady state is well achieved and quantitative results in terms of shape and sliding speed obtained are all within 20% from experimental data, which is satisfactory for such a coarse grid. Further convergence tests would have to be performed to assess the reliability of the results.

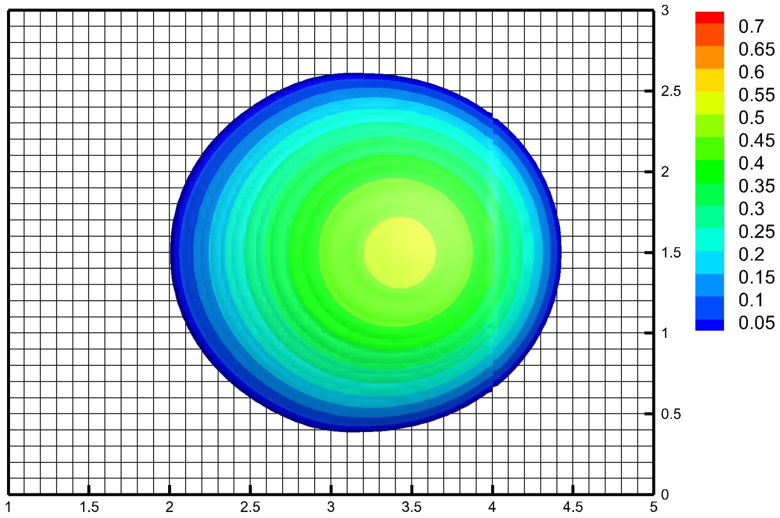

(a) Results obtained with ANSYS Fluent. The periodic boundary is at $x = 4$, the results have been duplicated and translated for representation.

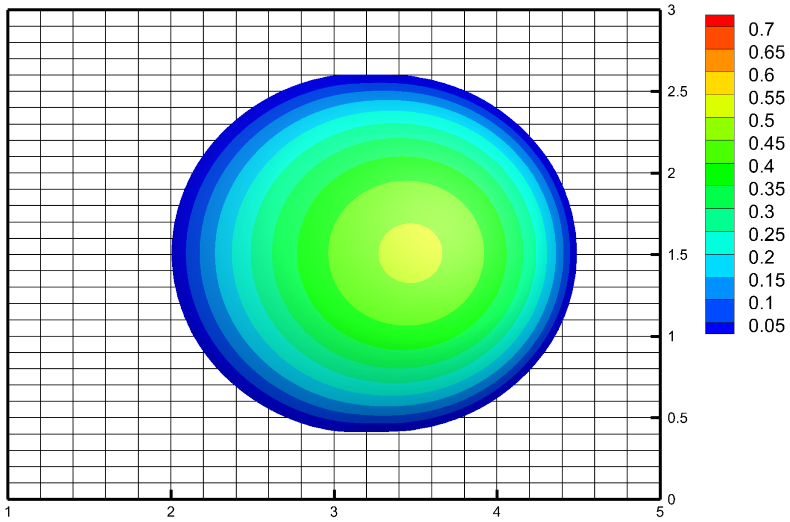

(b) Results obtained with TPLS.

Figure B.5: Top views of oval sliding drops obtained with the two codes; $(Bo \sin\alpha, t) = (0.65, 1.5)$. Flow is from left to right. The interface is colored by the height.

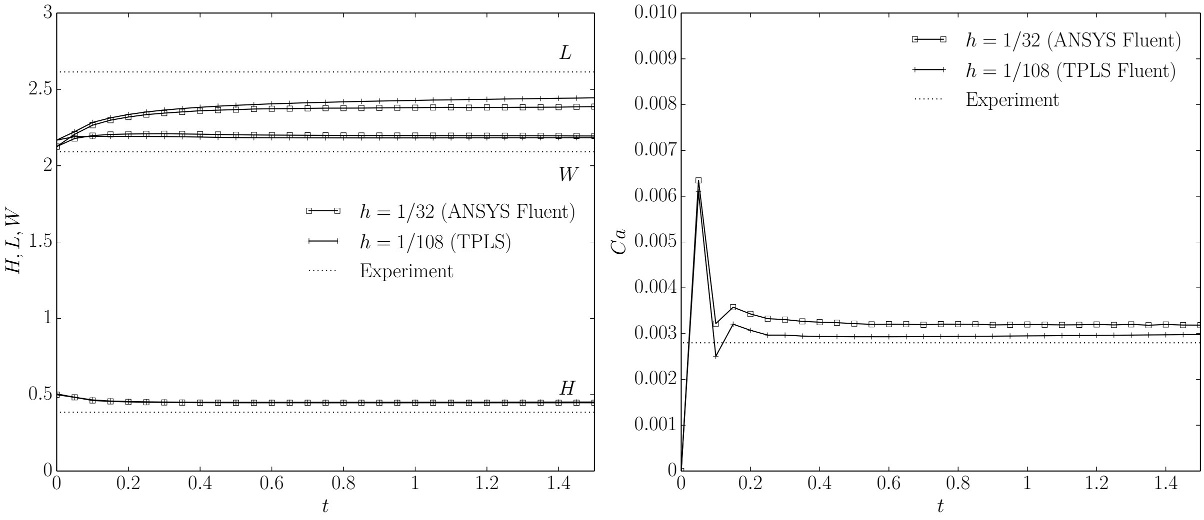

(a) Height, base length and base width against time.

(b) Speed against time.

Figure B.6: Quantitative results for the oval sliding drop; $Bo \sin \alpha = 0.65$.

B.3 Conclusion

The macroscale models for viscous regime (Cox, 1986) and inertial regime (Cox, 1998) were implemented in the VOF solver of ANSYS Fluent 15.0. Convergence tests were conducted for axisymmetric droplet spreading in inertial regime, for which good qualitative and quantitative agreement was achieved with the experiment and prior numerical work. The subgrid model was also implemented in 3D and tested on a coarse grid against drop sliding in viscous regime. Good qualitative agreement was obtained with the experiment and numerical results obtained with TPLS for the same test case.

Appendix C

Experimental uncertainties

Outline

This appendix first summarizes key aspects of uncertainty analysis and then presents, for each experimental setup, which errors are accounted for in measurement uncertainties.

C.1 Uncertainty analysis

Uncertainty analysis consists in identifying different sources of errors, systematic and random, in order to estimate the measurement uncertainty. Let consider the case of multiple-sample analysis: the result for the true value v is presented as the sum of a mean measured value $\bar{v}$ plus the measurement uncertainty δv for a set of M samples:

$$v = \bar{v} \pm \delta v. \tag{C.1}$$

The measurement uncertainty is an estimate of the combination of all measurement errors, systematic and random, and represents a confidence interval for the true value. For instance, for normally distributed random errors and in absence of any systematic error, the uncertainty would be 1.960σ, where σ is the standard deviation, the coefficient 1.960 corresponding to a probability of 95% for the true value to lie in the range $[\bar{v} - 1.960\sigma, \bar{v} + 1.960\sigma]$. But this is true only for an infinity of samples. For M samples, the true value v would read

$$v = \bar{v} \pm t_{(M,p)} \frac{S_M}{\sqrt{M}}, \tag{C.2}$$

with S_M the experimental standard deviation,

$$S_M(v) = \sqrt{\frac{1}{M-1} \sum_{i=1}^{M} (v_i - \bar{v})^2}, \tag{C.3}$$

and $t_{(M,p)}$ the Student multiplier of the two-tailed distribution, p being the probability for one v_i, $i \in [\![1, M]\!]$, to lie in the range $\left[\bar{v} - t_{(M,p)} S_M/\sqrt{M}, \bar{v} + t_{(M,p)} S_M/\sqrt{M}\right]$. Note that $\lim_{M\to\infty} t_{(M,.95)} = 1.960$, corresponding to a normal distribution.

In this work, the multiplier $t_{(60,.95)} = 2.000$ will be used in calculations of random uncertainties for a set of measurements with a number of samples greater than 60.

From the law of propagation of uncertainties (Joint Committee for Guides in Metrology, 2008), for a system of variables $(v^j)_{j\in[\![1,N]\!]}$, the overall uncertainty in a measurement of a variable v^k, $k \in [\![1, N]\!]$, is a combination of uncertainties due to each variable:

$$\delta v^k = \left(\sum_{j=1}^{N} \left(\frac{\partial v^k}{\partial v^j} \delta v^j \right)^2 \right)^{1/2}, \tag{C.4}$$

where $(\partial v^k / \partial v^j)_{j\in[\![1,N]\!]\setminus k}$ are the sensitivity coefficients. When the variable v^k can be recast in the form

$$v^k = \prod_{j\in[\![1,N]\!]\setminus\{k\}} (v^j)^{a_j},$$

the calculation of the relative uncertainty is straightforward (see Moffat (1988)):

$$\frac{\delta v}{v} = \left(\sum_{j\in[\![1,N]\!]\setminus\{k\}} \left(a_j \frac{\delta v^j}{v^j} \right)^2 \right)^{1/2}. \tag{C.5}$$

The overall uncertainty is calculated as the root mean square of systematic uncertainties $\delta^s v$ and random uncertainties $\delta^r v$, as they are independent:

$$\delta v = \sqrt{(\delta^s v)^2 + (\delta^r v)^2}. \tag{C.6}$$

The systematic uncertainty is generally a combination of uncertainties due to accuracy of sensors, calibration, positioning of sensors, post-processing, etc. The root-mean-square operator is always used to calculate a combination of uncertainties due to independent sources of uncertainty.

C.2 Contact angles

C.2.1 Scaling

The scaling procedure automatically determines the apparent size of a pixel from the knowledge of the outer diameter of the needle, which is $d = 206.0 \pm 0.5$ µm. The scaling factor α in the experiment was determined to be about 210 pix/mm. Let d_p be the outer diameter of the needle in pixels. The functional relationship is $\alpha = d_p/d$. The relative systematic uncertainty in the determination of the scale factor α reads

$$\frac{\delta^s \alpha}{\alpha} = \left(\left(\frac{\delta d_p}{d_p} \right)^2 + \left(\frac{\delta d}{d} \right)^2 \right)^{1/2}, \tag{C.7}$$

Considering an error of 0.1 pixel in locating the outer edges of the needle and estimating the sensitivity coefficients with the upper or lower limits of the confidence intervals that maximize uncertainties, the scaling factor reads $\alpha = 210.0 \pm 0.7$ pix/mm.

C.2.2 Apparent angles

For the determination of apparent angles, the interface shape next to the contact line is automatically fitted by the software to a general equation of the form $ax^2 + by^2 + cxy + dx + ey + f = 0$, or $f(x, y) = 0$. The software reports the mean square root error in micrometers. The tangent to this curve at the contact line yields the apparent angle. A normal vector of the tangent to the curve $f(x, y) = 0$, at a point (x_0, y_0), is $\nabla f(x_0, y_0)$. The resolution of $\nabla f(x_0, y_0) \cdot (t_1, t_2) = 0$ for the direction vector (t_1, t_2) yields the slope of the tangent, hence the apparent contact angle.

The software only reports the fit error in micrometers, which is basically lower than 1 µm. The upper limit, will be used for estimating the systematic error, such as $\delta x = \delta y = 1$ µm. The uncertainty in the measurement of θ reads

$$\delta^s \theta = \left(\left(\frac{\partial \theta}{\partial x} \delta x \right)^2 + \left(\frac{\partial \theta}{\partial y} \delta y \right)^2 \right)^{1/2}. \tag{C.8}$$

It is reasonable to consider that the apparent angle is estimated over a distance $d_p = 30$ pixels for estimating sensitivity coefficients, even though such a small distance may overestimate the uncertainty. In this case, sensitivity coefficients are equal to α/d_p, where α is the scale factor.

C.2.2.1 Advancing angle

Several sets of measurements of advancing angles have been performed. A result is presented as a mean plus a measurement uncertainty, that accounts for systematic and random errors. The uncertainty due to random errors is $\delta^r \theta = t_{(60,.95)} S_M / \sqrt{M}$ and the overall uncertainty is obtained from (C.6). Tables C.1 and C.2 give experimental uncertainties in measurements of advancing and receding angles, respectively.

C.2.2.2 Receding angle

The measurement uncertainty in the receding angle is estimated the same way as for the advancing angle, except, of course, that the Student t multiplier is greater than for advancing angles because of a lower number of samples.

	$\delta^s\theta_A$ (°)	$\delta^r\theta_A$ (°)	$\delta\theta_A$ (°)
Water on PMMA	0.8	3.6	3.7
Water on stainless steel	0.8	8.2	8.2
NaOH 0.1 mol/L on stainless steel	0.8	7.6	7.7

Table C.1: Experimental uncertainties in advancing angle measurements.

	$\delta^s\theta_R$ (°)	$\delta^r\theta_R$ (°)	$\delta\theta_R$ (°)
Water on PMMA	0.8	3.9	4.0
Water on stainless steel	0.8	10.5	10.5
NaOH 0.1 mol/L on stainless steel	0.8	8.8	8.8

Table C.2: Experimental uncertainties in receding angle measurements.

C.3 Inclined-plane experiment

C.3.1 Dynamic viscosity

Glycerine mixtures have here been characterized by dynamic viscosity measurements with a rheometer MCR72 from Anton Paar GmbH, in a cone-plate mode. Viscosity measurement are carried out at constant shear rate $\dot{\gamma} = \dot{\omega}/\alpha$, where $\dot{\omega}$ and α are the angular speed and the opening angle, respectively. The dynamic viscosity is just the shear stress $3T/(2\pi R^3)$, with a torque T and a radius R, divided by the shear rate, that is $\mu = 3\alpha T/(2\pi R^3\dot{\omega})$. The device returns the dynamic viscosity with an accuracy of 0.001 mPa.s. Many uncertainties are a priori involved in the determination of the dynamic viscosity: that in the temperature (controlled here and known with an accuracy of 0.1°C), that in the opening angle ($\delta\alpha$), that in the radius (δR), that in the shear rate ($\delta\dot{\gamma}$), and that in the torque (known with a resolution of 10^{-9} kg.m^2.s^{-2}). For the sake of clarity, the uncertainties presented in the manuscript are random uncertainties calculated from values of dynamic viscosity returned by the software.

C.3.2 Flow-rate

As stated in the manuscript, the flow rate is controlled with a volumetric pump with helical lobes, and measured with an electromagnetic flowmeter with an accuracy of 0.5 mL.s^{-1}. In the experiment, during a set of measurements, the flowmeter has measured changes in the volume flow rate of ± 1 mL.s^{-1}. A systematic uncertainty of 2 mL.s^{-1} shall be used in subsequent uncertainty calculations, that of the Reynolds number for instance.

C.3.3 Liquid density

The liquid density ρ has been determined by weighing some liquid volume $V = 20.0 \pm 0.1$ mL with an electronic weighing scale, accurate down to 10^{-3} g. The relative systematic uncertainty in that protocol is

$$\frac{\delta^s\rho}{\rho} = \left(\left(\frac{\delta m}{m}\right)^2 + \left(\frac{\delta V}{V}\right)^2\right)^{1/2}, \tag{C.9}$$

to which the random error must be added.

C.3.4 Reynolds number

The Reynolds number based on the volumetric flow rate is $Re = \rho Q/(\mu b)$, where b is the channel depth, yielding a relative uncertainty

$$\frac{\delta Re}{Re} = \left(\left(\frac{\delta \rho}{\rho} \right)^2 + \left(\frac{\delta Q}{Q} \right)^2 + \left(\frac{\delta \mu}{\mu} \right)^2 + \left(\frac{\delta b}{b} \right)^2 \right)^{1/2}. \tag{C.10}$$

C.3.5 Liquid film thickness

For the CCI system, the manufacturer reports an axial accuracy of $\delta^s d = 0.9$ µm in a distance measurement, hence an accuracy of $\delta^s h = 1.8$ µm in an indirect thickness measurement, as carried out in this work. This accuracy holds for a measurement in normal conditions. The sensor can receive a signal with a maximum tilt angle (with respect to the reflective object) $\theta_{\max} = 12°$. The sensor can still receive a signal for angles greater than $\theta_{\max}$ when the reflective surface is diffusive, but the value $\theta_{\max}$ specified by the manufacturer will be used in the calculations of uncertainties. This tilt angle introduces a relative systematic uncertainty

$$\frac{\delta^s h}{h} = \frac{1}{\cos \theta_{\max}} - 1. \tag{C.11}$$

In the flat-film configuration, an additional systematic uncertainty, due to uncertainties in the flow rate, fluid properties and inclination angle, must be taken into account, consistently with the flat-film solution $h = \big(3\mu Q/(b\rho g \sin \beta)\big)^{1/3}$, yielding an additional relative systematic uncertainty, that reads, making use of Equation (C.10):

$$\frac{\delta^s h}{h} = \frac{1}{3} \left(\left(\frac{\delta Re}{Re} \right)^2 + \left(\frac{\delta \beta}{\tan \beta} \right)^2 \right)^{1/2}. \tag{C.12}$$

The overall systematic uncertainty is the mean square root of the axial accuracy, the uncertainty due to the tilt angle, and the uncertainty in other variables. The uncertainty due to random errors is $\delta^r h = t_{(M,.95)} S_M \sqrt{M}$ and the overall uncertainty is obtained from (C.6).

C.3.6 Wavy-film amplitude

In this case, a 1D sinusoidal perturbation is introduced at the inlet and propagates downstream. The time signal is acquired during 30 periods and results are reported of the wavy-film amplitude.

C.3.6.1 CCI measurements

Distance measurement

The systematic uncertainty in the distance measurement is calculated accounting for the accuracy of the system and the maximum systematic error due to an eventual tilt angle.

Amplitudes of the time signal, A_0 and B_0

Calculations of the amplitudes from the time signal yields an additional systematic error. The time signal reads $s_0(t) = A_0 \cos(\omega t) + B_0 \sin(\omega t)$, and amplitudes are obtained by integrating the signal over n periods:

$$\begin{aligned} A_0 &= \frac{2}{nT} \int_{t_0}^{t_0+nT} s_0(t) \cos(\omega t) dt, \\ B_0 &= \frac{2}{nT} \int_{t_0}^{t_0+nT} s_0(t) \sin(\omega t) dt. \end{aligned} \tag{C.13}$$

Signals are integrated over $I = [t_0, t_0 + \Delta t]$ with the trapezium rule,

$$\begin{aligned} A_0 &= \frac{2}{nT} \sum_{i=0}^{N-2} \big(s_0(t_i) \cos(\omega t_i) + s_0(t_{i+1}) \cos(\omega t_{i+1}) \big) \frac{\Delta t}{2}, \\ B_0 &= \frac{2}{nT} \sum_{i=0}^{N-2} \big(s_0(t_i) \sin(\omega t_i) + s_0(t_{i+1}) \sin(\omega t_{i+1}) \big) \frac{\Delta t}{2}, \end{aligned} \tag{C.14}$$

with N the number of samples. For a function g continuous on $I = [t_i, t_{i+1}]$, the error in the integration of g over I using the trapezium rule is, at leading-order, $-(t_{i+1} - t_i)^3 g''(t_i)/12$, yielding systematic uncertainties in A_0 and B_0:

$$\begin{aligned} \delta^s A_0 &= \frac{2}{nT} \frac{\Delta t^3}{12} \left| \sum_{i=0}^{N-2} 2\omega^2 \big(A_0 \cos(2\omega t_i) + B_0 \sin(2\omega t_i) \big) \right|, \\ \delta^s B_0 &= \frac{2}{nT} \frac{\Delta t^3}{12} \left| \sum_{i=0}^{N-2} 2\omega^2 \big(A_0 \sin(2\omega t_i) - B_0 \cos(2\omega t_i) \big) \right|. \end{aligned} \tag{C.15}$$

Actual amplitude C_0

$C_0 = \sqrt{A_0^2 + B_0^2}$ so the systematic uncertainty in the amplitude is

$$\delta^s C_0 = \left(\left(\frac{A_0}{\sqrt{A_0^2 + B_0^2}} \delta A_0 \right)^2 + \left(\frac{B_0}{\sqrt{A_0^2 + B_0^2}} \delta B_0 \right)^2 \right)^{1/2}, \tag{C.16}$$

to which the axial accuracy and the eventual tilt of the CCI system must be added.

Phase ϕ_0

Knowing that $\phi_0 = \arctan(B_0/A_0)$, obtaining the uncertainty in the phase difference is straightforward:

$$\delta^s \phi_0 = \left(\left(- \frac{B_0}{A_0\sqrt{A_0^2 + B_0^2}} \delta A_0 \right)^2 + \left(\frac{\delta B_0}{\sqrt{A_0^2 + B_0^2}} \right)^2 \right)^{1/2}. \tag{C.17}$$

C.3.6.2 PSD measurements

Phase and amplitudes of the time signal

Amplitudes of the time signal, A_1, B_1 and ϕ_1 are calculated the same way as A_0, B_0 and ϕ_0.

$\delta^s\alpha/\alpha$	$\delta^r\alpha/\alpha$	$\delta\alpha/\alpha$
0.0167	0.0005	0.0168

Table C.3: Experimental uncertainties in the coefficient of proportionality of the PSD.

Distance between the two measurement points, Δx

The distance between the two measurement points is measured before starting a set of measurements, with a ruler. $\Delta x = 10.0 \pm 0.5$ mm in the sets of measurements carried out here.

Wavelength, λ

The wavelength is $\lambda = 2\pi\Delta x/(\phi_1 - \phi_0)$, so the relative systematic uncertainty is:

$$\frac{\delta^s\lambda}{\lambda} = \left(\left(\frac{\delta\Delta x}{\Delta x}\right)^2 + \left(\frac{\delta\phi_0}{\phi_0}\right)^2 + \left(\frac{\delta\phi_1}{\phi_1}\right)^2\right)^{1/2}. \tag{C.18}$$

Linearity of the PSD

The PSD returns the voltages at the terminals of the sensor corresponding to the coordinates of the Laser beam on the sensor. The PSD is a linear sensor and its coefficient of proportionality α, in mm.V^{-1}, is determined using a linear motorized stage with a 25-mm travel range and an accuracy in displacement $\delta d = 0.5$ µm. The accuracy in the position of the Laser beam on the sensor is $\delta X = 25$ µm and the resolution in the voltage is $\delta V = 5$ mV. The relative systematic uncertainty in the determination of the coefficient of proportionality is

$$\frac{\delta^s\alpha}{\alpha} = \left(\left(\frac{2\delta X}{\Delta X}\right)^2 + \left(\frac{2\delta d}{\Delta X}\right)^2 + \left(\frac{2\delta V}{\Delta V_X}\right)^2\right)^{1/2}, \tag{C.19}$$

where ΔV_X is the voltage at the terminals of the sensor corresponding to the two abscissas $X_{\min}$ and $X_{\max}$ of the Laser beam on the sensor. The additional random uncertainty due to fitting ΔX to αV_X is obtained with Student distribution, such as

$$\frac{\delta^r\alpha}{\alpha} = \frac{2S_M(X)}{\sqrt{M}\Delta X}, \tag{C.20}$$

with M the number of samples, and the overall relative uncertainty is just the combination of systematic and random uncertainties

$$\frac{\delta\alpha}{\alpha} = \left(\left(\frac{\delta^s\alpha}{\alpha}\right)^2 + \left(\frac{\delta^r\alpha}{\alpha}\right)^2\right)^{1/2}. \tag{C.21}$$

Relative uncertainties are gathered in Table C.3. Finally, the measured coefficient of proportionality is $\alpha = 0.1637 \pm 0.0027$ mm.V^{-1}.

Displacement on the PSD, ΔX

The additional uncertainty in the displacement ΔX on the PSD is due to the calibration procedure. Basically, the position on the sensor is $X(t) = \alpha s_1(t)$, with α the coefficient of proportionality. Therefore, the systematic uncertainty in the displacement is

$$\delta^s X = \left((A_1^2 + B_1^2)(\delta\alpha)^2 + \left(\frac{\alpha A_1}{\sqrt{A_1^2 + B_1^2}} \delta A_1 \right)^2 + \left(\frac{\alpha B_1}{\sqrt{A_1^2 + B_1^2}} \delta B_1 \right)^2 \right)^{1/2}. \tag{C.22}$$

Distance from the PSD to the interface, H

This has been measured with a measuring tape, $H = 18.0 \pm 0.5$ cm in the sets of measurements carried out here.

Refractive index

The refractive index has not been measured here. However, density and viscosity have been measured, and a corresponding value $n = 1.44 \pm 0.01$ has been selected, amongst the tabulated values gathered by the Glycerine Producers' Association (1963), and used in further calculations.

Wavy-film amplitude

The amplitude indirectly measured with the PSD is $C_1 = \lambda \Delta X / \big((n-1) 8 \pi H\big)$, so the relative systematic uncertainty is

$$\frac{\delta^s C_1}{C_1} = \left(\left(\frac{\delta\lambda}{\lambda} \right)^2 + \left(\frac{\delta \Delta X}{\Delta X} \right)^2 + \left(\frac{\delta n}{n-1} \right)^2 + \left(\frac{\delta H}{H} \right)^2 \right)^{1/2}. \tag{C.23}$$

C.3.7 Interface velocity

C.3.7.1 PIV

The different sources of uncertainties in PIV are identified below.

Scaling

The scaling procedure consists in determining the apparent size of a pixel by using a ruler. It is reasonable here to consider an accuracy δd_p of the order of 20 pixels in the procedure, yielding a relative systematic uncertainty in the scale factor $\delta^s \alpha / \alpha = \delta d_p / d_p$. In these sets of measurements d_p is of the order of 2000 pixels so the scale factor reads $\alpha = 7.0 \pm 0.5\%$. This introduces an uncertainty in a displacement d, of which the relative systematic uncertainty is

$$\frac{\delta^s d}{d} = \frac{\delta^s \alpha}{\alpha}, \tag{C.24}$$

and the relative uncertainty in the velocity component in the x-direction, $\delta^s \mathbf{u} \cdot \hat{\mathbf{e}}_x = \delta^s d / \Delta t$, is

$$\frac{\delta^s \mathbf{u} \cdot \hat{\mathbf{e}}_x}{\mathbf{u} \cdot \hat{\mathbf{e}}_x} = \frac{\delta^s \alpha}{\alpha}, \tag{C.25}$$

where Δt is the time difference between two successive frames. It will be considered here that the value of Δt is exact, although this is uncertain.

Cross-correlation algorithm

In PIV, the accuracy in the determination of the displacement of a pattern, δd, depends on the cross-correlation algorithm that is used, but is usually in the range 0.04 to 0.1 pixel (Stanislas et al., 2008). Therefore, the systematic uncertainty in a velocity component, in the x-direction for instance, is

$$\delta^s \mathbf{u} \cdot \hat{\mathbf{e}}_x = \frac{\mathbf{u} \cdot \hat{\mathbf{e}}_x}{|\mathbf{u}|} \frac{\delta d}{\Delta t}. \tag{C.26}$$

δd is here set to 0.1 pixel for uncertainty calculations. This must be combined with the uncertainty due to the scaling procedure.

Particular case of a flat film

For the flat film, an uncertainty must be taken into account, arising from uncertainties in parameters of the system. The analytical free-surface velocity is $U_{\text{th}} = \frac{3}{2}\left(Q^2 \rho g \sin\beta/(3\mu b^2)\right)^{1/3}$, and the corresponding systematic relative uncertainty is:

$$\frac{\delta^s U_{\text{th}}}{U_{\text{th}}} = \frac{1}{3}\left(\left(\frac{2\delta Q}{Q}\right)^2 + \left(\frac{\delta\rho}{\rho}\right)^2 + \left(\frac{\delta\beta}{\tan\beta}\right)^2 + \left(\frac{\delta\mu}{\mu}\right)^2 + \left(\frac{2\delta b}{b}\right)^2\right)^{1/2} \tag{C.27}$$

Sum of cross-correlation functions and space-averaging

In Section 5.2.3, results are presented of the free-surface velocity magnitude by space-averaging the mean velocity field obtained from the temporal summation of correlation functions. The uncertainty introduced in the summation of correlation functions cannot be quantified here and will be contained in random uncertainties due to the final space-averaging. The random uncertainty due to that space-averaging is quantified using Student distribution.

C.3.7.2 PTV

The uncertainty due to the scaling procedure and that from the analytical solution prevail. For PTV measurements, the cross-correlation-based algorithm of Brevis et al. (2011) is used. The accuracy in locating a particle will be taken equal to 0.1 pixel (Udrea et al., 1996; Lei et al., 2012), hence an accuracy in a displacement $\delta d = 0.2$ pixels. Additional sources of errors may arise due to overlaps of particles (Guezennec et al., 1994).

C.4 Complex-surface experiment

C.4.1 Liquid film thickness

As mentioned in Section C.3.5, components of systematic uncertainty in an indirect measurement of the liquid film thickness are due to the accuracy of the system, $\delta^s h = 1.8$ µm here, and the uncertainty due to the tilt of the sensor, that introduces a relative systematic uncertainty $\delta^s h/h = 1/\cos\theta_{\max} - 1$. The uncertainty due to random errors, $t_{(M,.95)} S_M \sqrt{M}$, must be added to systematic uncertainties to yield the overall uncertainty. The film thickness normalized by $(g \sin\alpha_c/\nu^2)^{-1/3}$, is denoted by h^*. The normalization introduces a further relative systematic uncertainty due to kinematic viscosity,

$$\frac{\delta^s h^*}{h^*} = \left(\left(\frac{\delta^s h}{h} \right)^2 + \left(\frac{3}{2} \frac{\delta^s \nu}{\nu} \right)^2 \right)^{1/2}, \tag{C.28}$$

to which the random uncertainty must be added. The dynamic viscosity of the fluid was not measured but was taken as $\nu_L = (1.0034 \pm 0.0248)10^{-6}$ m^2.s^{-1}, corresponding to a temperature of 20.0 ± 1.0 °C.

C.4.2 Liquid film thickness measurement through a transparent medium

The interposition of a glass of thickness t between the optical pen and its measuring range introduces a bias in distance measurement, that is actually function of the wavelength corresponding to the distance seen by the sensor. Let γ be the angle that the glass makes with the optical axis of the optical pen. We here want to correct that bias, or at least estimate its maximum and account for it in uncertainty calculations. Figure C.1 shows the configuration for that, with the origin O here chosen to coincide with the signal seen by the sensor. For a given wavelength, the bias due to the interposition of the glass thickness is unique: whatever the position of the glass, the optical path difference introduced by that transparent medium is the same, and only depends on the angle γ. The choice of the origin O is thus completely arbitrary and the calculation of the bias does not depend on the position of the origin. In Figure C.1, it can be seen that the fact that the transparent medium is not perpendicular to the optical axis deviates the measuring range from the optical axis, whereas the deviation would be along the optical axis in an orthogonal configuration (Dietze et al., 2009). The deviation, or the position of $M'(x', y')$ is wanted. For that, two intersection points of the light rays with the glass slide are introduced, I_k, $k \in \{d, u\}$. The lengths $\delta_k = |OI_k|$ are also introduced. For $k \in \{d, u\}$,

$$\delta_k = t(\tan i_k - \tan r_k), \tag{C.29}$$

hence, using the Snell-Descartes law of refraction,

$$\delta_k = t\left(\tan i_k - \frac{\sin i_k}{\sqrt{n^2 - \sin^2 i_k}} \right). \tag{C.30}$$

Points I_d and I_u thus have the coordinates

$$(x_k, y_k) = (-\delta_k \cos\gamma, -\delta_k \sin\gamma), k \in \{d, u\}, \tag{C.31}$$

and the straight lines (D_d) and (D_u) have equations

$$\begin{aligned} y - y_d &= -\tan(\omega - i_d)(x - x_d), \\ y - y_u &= \tan(i_u - \omega)(x - x_u), \end{aligned} \tag{C.32}$$

From there, the deviations in x and y direction are easily obtained, and for a distance x_0 seen by the sensor, the actual distance x' reads

$$x' = x_0 + \frac{y_d - y_u + x_d \tan(\omega - i_d) + x_u \tan(i_u - \omega)}{\tan(\omega - i_d) + \tan(i_u - \omega)}, \tag{C.33}$$

and the deviation from the optical axis is

$$y' = y_d - \tan(\omega - i_d)(x' - x_d). \tag{C.34}$$

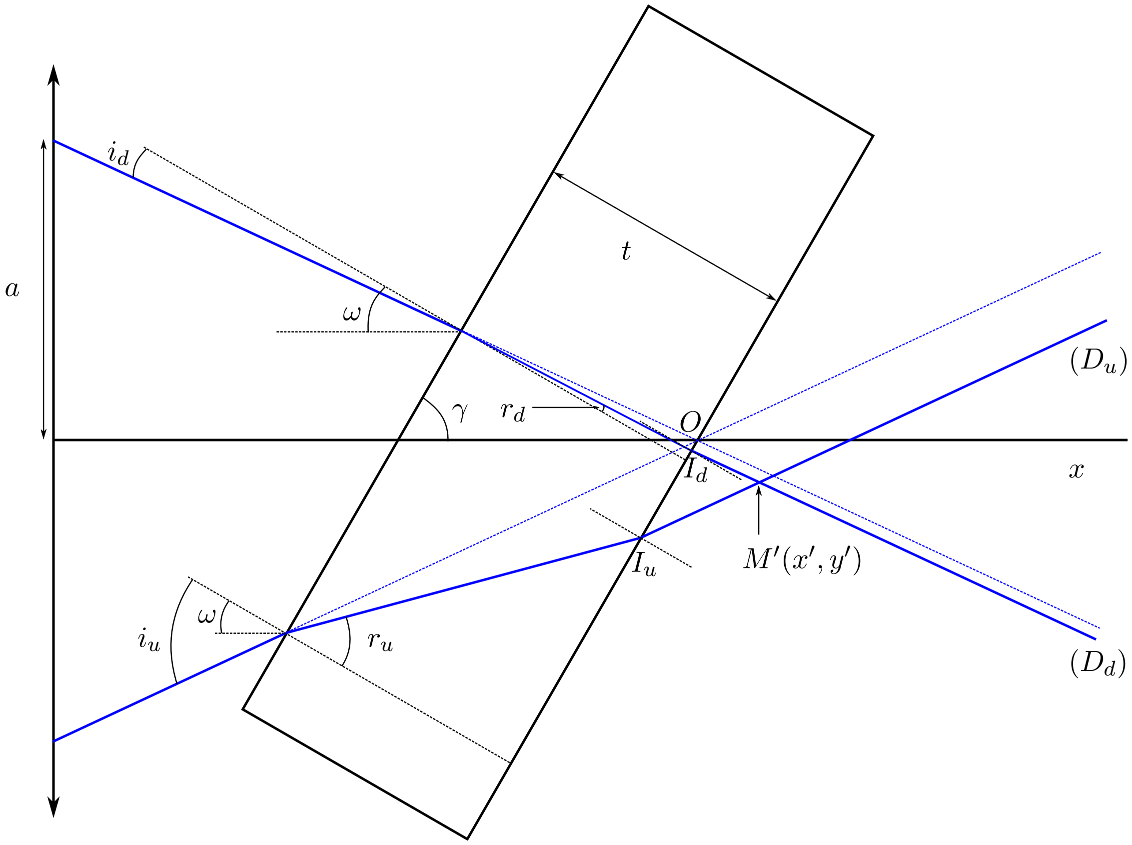

Figure C.1: Modification of the measuring range of the CCI system by interposition of a transparent medium of width t and refraction index n. a is the size of the chromatic lens. The axis Ox coincides with the optical axis of the optical pen.

Noting that $\omega - i_d = i_u - \omega$, $\gamma + \omega = \pi/2$, and making use of (C.30)–(C.31), (C.33) and (C.34) recast

$$\begin{aligned} x' &= x_0 + \frac{t}{2}\left(\frac{\sin\gamma}{\cot(\gamma+i_d)} + \cos\gamma\right)\left[\tan i_k - \frac{\sin i_k}{\sqrt{n^2-\sin^2 i_k}}\right]_{k=d}^{k=u}, \\ y' &= -\cot(\gamma+i_d)x' - t\left(\tan i_d - \frac{\sin i_d}{\sqrt{n^2-\sin^2 i_d}}\right)\big(\sin\gamma - \cot(\gamma+i_d)\cos\gamma\big). \end{aligned} \tag{C.35}$$

The glass is of BK7 type and the CCI sensor acquires a signal for wavelengths in the range 400–700 nm, corresponding to refractive indices $n_{\text{blue}} = 1.5308$ and $n_{\text{red}} = 1.5131$, respectively (Polyanskiy, 2016). The refractive index was actually determined experimentally for a wavelength 532 nm, by measuring deviations of a Laser beam spot. A value of $n = 1.5146$ with a thickness $t = 14.95$ mm were determined with the least-squares method. For information, the glass thickness is 15.0 millimeters-wide according to the manufacturer and the refractive index in the database of Polyanskiy (2016) corresponding to that wavelength is 1.5195. We now want the maximum biases $x' - x_0$ and y', corresponding to the wavelength the wavelengths 400 nm and 700 nm. For that, the angle $\omega - i_d$ can actually be calculated knowing the size of the lens, a (see Figure C.1), and the minimum working distance, $x_{\min}$, the measuring range, Δx. Here, $a = 15.0$ mm, $x_{\min} = 66.9$ mm and $\Delta x = 10000$ µm. The angles $\omega - i_{d,\text{blue}}$ are obtained from $\tan(\omega - i_{d,\text{blue}}) = a/x_{\min}$ and $\tan(\omega - i_{d,\text{red}}) = a/(x_{\min} + \Delta x)$, yielding

$$\cot(\gamma + i_{d,\text{blue}}) = \frac{a}{x_{\min}}, \tag{C.36}$$

Wavelength	$x' - x_0$	y'
400 nm	22.0 mm	-13.7 mm
700 nm	21.1 mm	-12.5 mm

Table C.4: Biases introduced in distance measurement by interposing a glass slide between the optical pen and the reflective interface. The numerical values are that obtained for given CCI system, glass thickness, and incidence angle.

and

$$\cot(\gamma + i_{d,\text{red}}) = \frac{a}{x_{\min} + \Delta x}. \tag{C.37}$$

The angle γ is determined by the triangular shape of large corrugations of the structured packing sheet,

$$\gamma = \arctan\left(\frac{2h_u}{\lambda_u}\right). \tag{C.38}$$

Numerical values of biases introduced by the glass thickness are gathered in Table C.4.

For an indirect thickness measurement (distance measurement for the reference and distance measurement with the liquid film), as carried out here, the sensor would measure a thickness equal to the measuring range Δx, corresponding to an actual thickness $(x' - x_0)_{\text{blue}} - (x' - x_0)_{\text{red}}$. Finally, as the functional relationship between the distance measured and the wavelength is not provided by the manufacturer, the experimental thickness reported in Section 6.4 will be that measured plus an additional positive uncertainty, corresponding to the mean value of the relative systematic uncertainty, calculated with the numerical values of Table C.4, that is

$$\frac{\delta^s h}{h} = \frac{(x' - x_0)_{\text{blue}} - (x' - x_0)_{\text{red}}}{\Delta x} - 1, \tag{C.39}$$

hence $\delta^s h/h = 0.083$. On the other hand, the mean difference in the deviation from the optical axis of the optical pen is, between two distance measurements, $(y'_{\text{red}} - y'_{\text{blue}})/\Delta x = 0.120$. The thicknesses measured in this experiment are lower than 275 µm, corresponding to a difference in y coordinate between the two measurement points lower than 33 µm, which first seems to be reasonable given that the amplitude of small corrugations is 2.8 mm. This is discussed further in Section 6.4.

dernière page de la thèse

AUTORISATION DE SOUTENANCE

Vu les dispositions de l'arrêté du 7 août 2006,

Vu la demande des Directeurs de Thèse

Monsieur P. SPELT et Monsieur M. LANCE

et les rapports de

M. A. BERLEMONT
Directeur de Recherche CNRS - UMR 6614 - CORIA - Université de Rouen
Site Universitaire de Madrillet - 675 avenue de l'Université - BP 12
76801 SAINT ETIENNE DU ROUVRAY cedex

et de

M. A. DAERR
Docteur HDR - Université Paris Diderot - Bât. Condorcet - cc 7056 - 75205 PARIS cedex 13

Monsieur SOLOMENKO Zlatko

est autorisé à soutenir une thèse pour l'obtention du grade de **DOCTEUR**

Ecole doctorale MECANIQUE, ENERGETIQUE, GENIE CIVIL ET ACOUSTIQUE

Fait à Ecully, le 25 novembre 2016

P/Le directeur de l'E.C.L.
La directrice des Etudes

ECOLE CENTRALE DE LYON
Service Scolarité
ECULLY

M-A. GALLAND